$M_{-}14$

203383

p 235

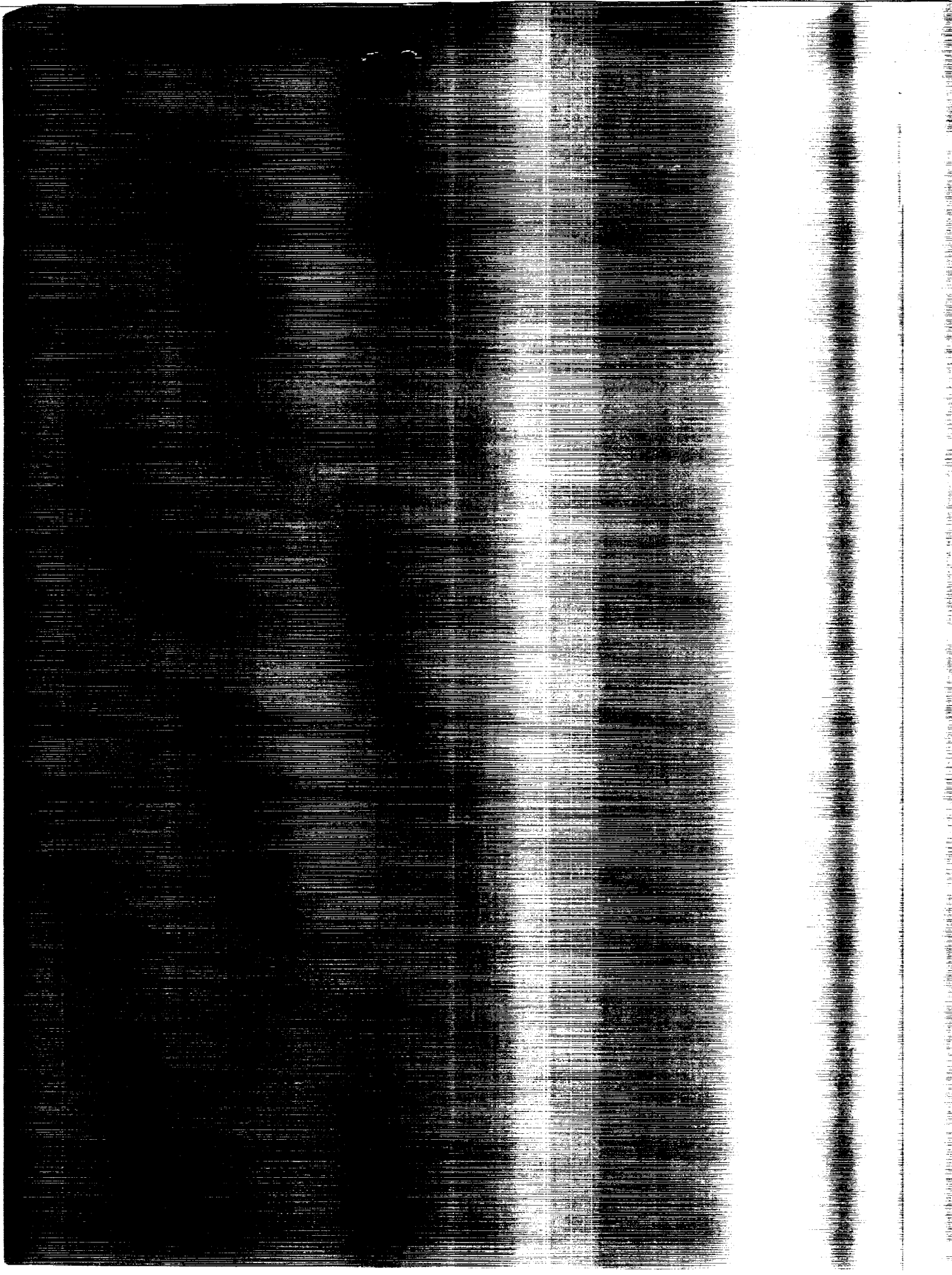# Spatiotemporal Behavior and Nonlinear Dynamics in a Phase Conjugate Resonator

Siuying Raymond Liu

NASA

NASA Contractor Report 4567

Spatiotemporal Behavior and Nonlinear Dynamics in a Phase Conjugate Resonator

Siuying Raymond Liu
Virginia Polytechnic Institute and State University
Blacksburg, Virginia

NASA

National Aeronautics and
Space Administration

Office of Management

Scientific and Technical
Information Program

1993

(NASA-CR-4567)   SPATIOTEMPORAL
BEHAVIOR AND NONLINEAR DYNAMICS IN
A PHASE CONJUGATE RESONATOR
(Virginia Polytechnic Inst. and
State Univ.)   225 p

N94-23529

Unclas

H1/74   0203383

Spatiotemporal behavior and nonlinear dynamics in a phase conjugate resonator

by

Siuying Raymond Liu

Committee Chairman: Prof. Guy Indebetouw

Department of Physics

ABSTRACT

The work described in this dissertation can be divided into two parts. The first part is an investigation of the transient behavior and stability property of a phase conjugate resonator (PCR) below threshold. The second part is an experimental and theoretical study of the PCR's spatiotemporal dynamics above threshold.

The time-dependent coupled wave equations for four-wave mixing (FWM) in a photorefractive crystal, with two distinct interaction regions caused by feedback from an ordinary mirror, was used to model the transient dynamics of a PCR below threshold. Analytical expressions of the steady state cavity's fields for the case of nondepleted pumps and an absorption free medium were derived and used to determine the self-oscillation conditions. The solutions, through simple frequency domain transformation techniques, were used to define the PCR's transfer function and analyse its stability.

Taking into account pump depletion and medium absorption, the transient buildup and decay times of the cavity's fields as well as the specularly reflected and phase conjugate reflected intensities were numerically calculated as functions of a number of system parameters such as the coupling parameter and the pump and probe ratios. General trends were unveiled and discussed in view of the possible use of the PCR in image storage or processing architectures. Experimental results for the buildup and decay times confirmed qualitatively the predicted behavior.

Experiments were carried out above threshold to study the spatiotemporal dynamics of the PCR as a function of the Bragg detuning achieved by misaligning one of the two pump beams and of the degree of transverse confinement controlled by varying

the resonator's Fresnel number. The temporal aspects of the beam's complexity were studied by local intensity time series, power spectra, and reconstructed pseudo phase portraits. An irregular time series was identified as deterministic chaos having a correlation dimension of 5.2 and a Kolmogorov entropy of $0.16\ \mathrm{s}^{-1}$. Experimental results varying both control parameters revealed the presence of two distinct frequencies in the power spectra in some regions of the parameter space. The existence of optical vortices in the wavefront were identified by interferometry. The spatial complexity of the beam was studied in terms of the spatial distributions of optical vortices, their trajectories and their relationship to the beam's spatial coherence.

The transverse dynamics and the spatiotemporal instabilities were also described by modeling the three dimensional coupled wave equations in photorefractive FWM, using a truncated modal expansion approach. Numerical solutions of the model revealed the presence and motion of optical vortices in the wavefront. Simulations using the Bragg detuning as a control parameter showed that optical vortices appear as long as a large enough modulation of the wavefront is brought about by local gain enhancement resulting from the small misalignment of one of the pump beams from the Bragg angle. Power spectra of simulated time series also contain two distinct frequencies for a certain range of the off-Bragg parameter. Maps of the spatial correlation index were found to be templates of the corresponding maps of the vortices' trajectories, indicating that the dynamics may be defect-mediated.

ACKNOWLEDGEMENTS

TABLE OF CONTENTS

LIST OF FIGURES

Chapter 1

Introduction

1.1 Background

Optical feedback has been widely used in image processing since the late 1970s. Its applications include image restoration and recovery, pattern recognition, and the implementation of optical associative memory. Historically, optical feedback in analog processors was first proposed to extend their range of optical operations and to increase their performance and accuracy. Systems with passive coherent feedback have been demonstrated in spatial filtering, computing the solutions of differential equations, image restoration, and the implementation of nonlinear operation [1]. Yet, the performance of these passive feedback systems is limited by the cavity losses and by the accumulation of phase errors in each round trip.

Theorectical work on optical feedback suggested that fast analog optical devices with feedback can implement slowly converging iterative algorithms [2, 3]. Iterative algorithms are often needed in problems such as image restoration and recovery as well as in recognition and associative recall. Efficient optical implementations of these algorithms, however, require active feedback with a regenerative feedback loop in which the signal energy and its phase after each iteration can be restored. In the feedback loop, to amplify the light, two type of gain devices have been experimen-

tally demonstrated in all-optical systems: dye amplification [4, 5] and photorefractive amplification [6, 7].

Amplified phase conjugation via four-wave mixing (FWM) with two antiparallel pump beams in a photorefractive medium can not only compensate for the cavity losses, but also cancel the aberrations and phase distortions acquired in each round trip. One advantage of photorefractive nonlinearities over other nonlinear mechanisms is that efficient beam interactions and large gain coefficients can now be achieved with a few tens of milliwatts of laser power in materials such as bismuth silicon oxide $Bi_{12}SiO_{20}$. Low-power cw phase conjugate resonator (PCR) oscillations were recently demonstrated using a barium titanate $BaTiO_3$ crystal as a phase conjugate mirror (PCM) [8].

Since the successful demonstration of the photorefractive oscillators, a variety of all-optical architectures was proposed for the realization of optical neural computers [9, 10, 11]. Most of the systems demonstrated so far are dealing with associative recall in which a partial information input can address the holographically stored images. The image having the highest correlation peak is selected and reconstructed. The PCMs in the systems are used to provide optical feedback, thresholding and gain, the three essential building blocks of a neural network system [12, 13, 14].

About a quarter of a century ago, an optical phenomenon now known as the photorefractive effect was discovered in lithium niobate $LiNbO_3$ and called at that time the "optical damage". The undesirable optical damage in nonlinear and electro-optical crystals turned out to be an advantage when using these materials as holographic optical memories. However, the interest in holographic memory in these media quickly declined because the stored information was being erased during the read-out process or lost subsequently after the pumps are turned off. For a while, as the basic understanding of the origin of the effect and its potential use in eliminating wavefront distortion became known, photorefractive wave mixing and phase conjugation has grown rapidly into a sub-discipline in the field of nonlinear optics. In the middle 1970s, the science of the photorefractive effect became mature. More knowledge of the electro-optic media and their characteristic properties was available. The

2

previously unwanted degradation of optical memories was recognized as exactly what is needed for real time holography. Up until a few years ago, most of the research in that field was concerned with the steady-state behavior of wave mixing in photorefractive media and its applications [15, 16]. Recently, however, there has been an increasing interest in the dynamics of these processes. As more practical devices are built exploiting photorefractive phase conjugation, we would like to know how these systems respond to the temporal variations of any of their parameters. Knowledge of the dynamical behaviors of such systems makes it possible to design devices and predict their performance. Also of interest, even for steady-state applications, is the stability of various wave-mixing schemes. For a device based on these principles, one would like to predict if the system will be stable for the ranges of parameter values over which the desired operations must be performed.

The dynamics of wave mixing in photorefractive media were first considered in early theorectical works of the transient behavior of two-wave mixing (TWM) [17]. They showed, for example, how the system approaches the steady state when only one of the input beams is present and the other is abruptly turned on. Later work examined the stability of photorefractive FWM processes [18, 19]. In addition, many groups have recently reported observations of temporal instabilities and chaos in photorefractive devices such as self-pumped PCMs [20, 21, 22], ring phase conjugators [23, 24], mutually pumped phase conjugators [25, 26], and PCRs [27, 28]. Several models have been put forward to explain the dynamics of optical phase conjugation found in photorefractive crystals [29, 30, 31, 32] and devices [33, 34, 35]. Different mechanisms have been suggested to explain the temporal photorefractive instabilities. In the model of reference [22], for example, the chaotic behavior of a photorefractive PCM in a FWM geometry is shown to be caused by the existence of multiple inter-action regions in the crystal. Instabilities also arise in PCMs having only a single grating and a single interaction region [31]. Here, the factor leading to the chaotic behavior is the presence of an external electric field causing a shift in the optical frequency of the phase conjugate wave (PCW). A more recent model [32] even predicts a chaotic behavior in the standard FWM geometry with a single interaction region

and no external electric field if two gratings, transmission and reflection, of similar strength take part in the process. In ref. [35], two coupled ring cavities provide a competition between nonlinear gain and loss which results in nonsteady oscillating beams. It is thought that the competition for energy between different cavities resembles the competition for energy between different channels inside the self-pumped PCM [21] when it becomes unstable.

Thus far, all these models are based on the well-known one dimensional coupled wave theory [36]. Therefore, they are incapable of describing the dynamics in the transverse plane observed in experiments such as those reported in refs. [27, 28]. Besides, effects such as strong light scattering (fanning) in the crystals, or various spatial effects of diffractions in resonators, all of which are found in real situations, result in non-uniform gain of the beam profiles. These kinds of considerations will require an extension of the one dimensional framework to a two or three dimensional framework in the coupled-wave theory. Indeed, the geometry of the self-pumped PCM has been considered in a three dimensional theory [37]. Furthermore, finite gaussian beams have recently been used to study the beam profile deformation in photorefractive TWM and FWM in a two dimensional framework [38]. These studies have been dealing with the steady-state aspect of the transverse beam profiles in photorefractive media. Yet, the transverse dynamics of nonlinear optical system is becoming an increasingly important topic of research [39].

1.2 Dissertation outline

In this thesis, the study of the nonlinear dynamics in a PCR has been divided into two parts. In the first part, we will investigate the transient behavior and stability property of a PCR below threshold. In the second part, we will study experimentally and theoretically the PCR's spatiotemporal dynamics above threshold.

In chapter 2, we will present the model and the steady state analysis of a PCR below threshold based on time-dependent coupled wave equations for FWM in a

photorefractive crystal with two distinct interaction regions caused by feedback from a slightly tilted ordinary mirror. The steady state equations for the cavity's field, taking into account nondepleted pumps and absorption free medium, will first be solved. The analytic solutions are used to discuss the threshold conditions. We also find the PCR's transfer function by applying simple frequency domain transformation techniques to the steady state equations. The transfer function is used to analyse the stability of the PCR.

In chapter 3, the study will be extended to the transient regime of the PCR. We will first apply a numerical scheme for integrating the coupled wave equations using an adiabatic elimination process. We calculate the cavity's buildup and decay times as well as the specularly reflected and phase conjugate reflected intensities as functions of a number of system parameters. Numerical results indicate that the cavity buildup and decay times can be tailored by varying several of the system parameters to assess the possible use of the PCR as an image processing element. Experimental measurements are shown to qualitatively confirm the numerical simulations.

In chapter 4, we will give a brief introduction to some of the terminlogy and methods of nonlinear and chaotic dynamics, which are applied to the analysis of experimental time series data and to the beam's spatial complexity in the dynamics of PCR above threshold.

In chapter 5, we will present experimental results for the dynamics of PCR above threshold. We study by experiments some aspects of the spatiotemporal behaviors of the PCR as a function of the resonator's Fresnel number by varying one of the two apertures inside the cavity. Temporal aspects of the beam's complexity will be studied analysing the local intensity time series, power spectra, and embedded phase space portraits. A range of parameters is found for which the time series exhibit chaotic variations. For the spatial aspects of the beam's complexity, we will give evidence for the presence of wavefront dislocations or vortices in the optical field by using video recording and interferometry. A rich variety of defect movements are recorded and analysed. The spatial complexity is characterized by the number of optical vortices and their variety of movements as well as their relationship with the beam's spatial

coherence.

In chapter 6, we will present and test a model based on a truncated modal expansion of the cavity modes, to investigate the spatiotemporal dynamics of the PCR. We find the optical vortices in the optical field's wavefront in the numerical solutions. Numerical calculations are performed using the Bragg detuning, achieved by misaligning one of two pump beams as a control parameter. Numerical results indicate that the loss of temporal coherence and the onset of temporal chaos in the local intensity fluctuations are correlated to the loss of spatial confinement of the vortices' trajectories and the spatial coherence. The validity of the model is verified by comparison with experimental data.

In chapter 7, a conclusion and a summary for this work are given. Some possible future investigations are suggested.

1.3 The photorefractive effect, wave mixing and real time holography

In the remainder of this chapter, we begin a brief introduction to the photorefractive effect, wave mixing and phase conjugation, and then go on to the transients of the PCR and the steady state analysis in the next chapter.

The photorefractive effect is a phenomenon in which the local index of refraction is changed by a spatially varying light intensity. The effect has been observed in crystals such as lithium niobate $LiNbO_3$, barium titanate $BaTiO_3$ and strontium barium niobate SBN as well as in cubic crystals of the sillenite family such as bismuth silicon oxide BSO.

Suppose that we illuminate a photorefractive crystal with two coherent plane electromagnetic waves as in fig. 1.1a. The waves will interfere with each other and produce a spatially varying (sinusoidal) light intensity pattern inside the crystal. Charge carriers are optically excited into the conduction band in the bright regions of the
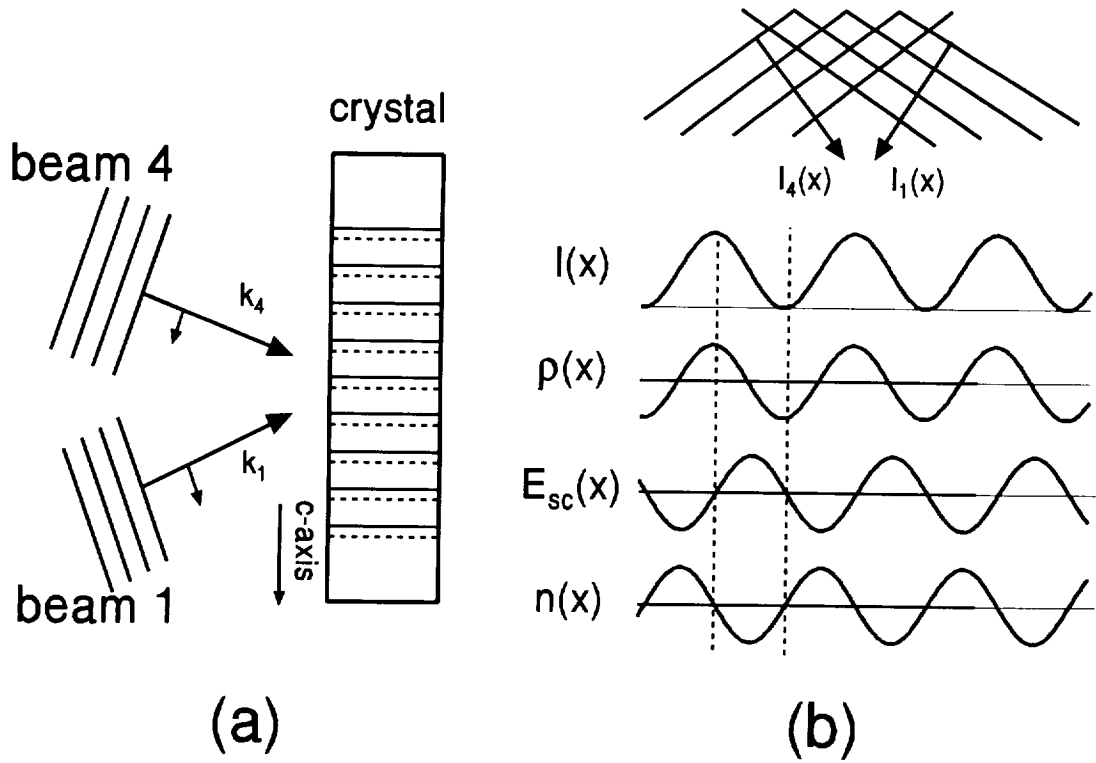
Figure 1.1: Pictorial illustration of the formation of a phase hologram in electro-optic crystals via the photorefractive effect. (a) Two coherent electromagnetic plane waves write a sinusodial grating inside the crystal, (b) Spatial variations of the light intensity $I(x)$, charge carrier distribution $\rho(x)$, space-charge field $\mathbf{E}(x)$ and refractive index $n(x)$. After Hall *et al.* [15]

interference pattern and move by drift (due to any internal and/or externally applied electric fields) and diffusion into the dark regions, where they are trapped. Thus, this sinusoidally varying space charge distribution creates a static, spatially periodic electric field $\mathbf{E}(x)$ inside the crystal as shown in fig. 1.1b, according to Poisson's equation:

$$\nabla \cdot \mathbf{E}(x) = (4\pi/\epsilon)\rho(x). \tag{1.1}$$

Here $\rho(x)$ is the charge density, ϵ is the dc dielectric constant. The electric field $\mathbf{E}(x)$ alters the crystal lattice and locally modulates the crystal's refractive index $n(x)$ via the linear electro-optic effect, generating a phase diffraction grating. (See fig. 1.1b). The amplitude $\Delta n(x)$ of the change in index of refraction is [40]

$$\Delta n(x) = -(n^3 r_{eff}/2)E(x). \tag{1.2}$$

Here r_{eff} is the effective Pockels coefficient of the crystal. (Pockels coefficients are linear combinations of elements of the crystal's third rank electro-optic tensor $\mathcal{R}_{ijk}$ [40].) Crystals having large Pockels coefficients such as $BaTiO_3$ and SBN can give rise to a significant photorefractive nonlinearity.

In a seminal series of papers, N. V. Kukhtarev et al. [41, 42, 43] showed that this refractive index grating interacts with the light waves and couples them together, so that their intensities I_1 and I_4 and their phases ϕ_1 and ϕ_4 change as the light waves propagate through the crystal:

$$\begin{aligned}
\frac{dI_1}{dz} &= -\mathrm{Re}(\gamma_o)\frac{I_1 I_4}{I_1 + I_4} - \alpha I_1, \\
\frac{dI_4}{dz} &= \mathrm{Re}(\gamma_o)\frac{I_1 I_4}{I_1 + I_4} - \alpha I_4, \\
\frac{d\phi_1}{dz} &= \frac{1}{2}\mathrm{Im}(\gamma_o)\frac{I_4}{I_1 + I_4}, \\
\frac{d\phi_4}{dz} &= \frac{1}{2}\mathrm{Im}(\gamma_o)\frac{I_1}{I_1 + I_4}.
\end{aligned} \tag{1.3}$$

Here α is the absorption coefficient of the crystal, and γ_o is the coupling strength (see eq. B.54), which is primarily determined by the crystal's Pockels coefficients,

dielectric constant and interacting geometry. In the absence of any external fields and if the charge migration in the crystal is dominated by diffusion, the resulting index grating will be shifted by 90° with respect to the interference pattern, as shown in fig. 1.1b, and the coupling strength γ_o will be purely real.

It is the occurrence of the phase shift between the index grating and the interference pattern that makes possible an asymmetric transfer of energy from one beam to the other. This two-beam coupling phenomenon is known as two wave mixing. According to equation 1.3, if the real part of the coupling strength, $\text{Re}(\gamma_o)$, is greater than zero (it depends on the interaction geometry and the sign of the charge of the charge carrier), the intensity I_4 will grow with propagation while I_1 will drop. Also, for purely real γ_o, the phases of both beams remain unchanged as they travel through the crystal.

Suppose now that a third weak beam (beam 2) is incident to the crystal, in a direction opposite to that of beam 1 as shown in fig. 1.2. This beam will be diffracted by the phase grating into the direction opposite to that of beam 4. It can be shown that this diffracted beam (beam 3) is the phase conjugate of beam 4. To see what this means physically, let the beam 4 amplitude be written as

$$E_4(r,t) = \frac{1}{2}\left[A_4(r)e^{i(\vec{k}\cdot\vec{r}-\omega t)} + A_4^*(r)e^{-i(\vec{k}\cdot\vec{r}-\omega t)} \right], \qquad (1.4)$$

The phase conjugate wave (PCW) is obtained by taking the complex conjugate of the spatial part of the wave in eq. 1.4:

$$E_{pc}(r,t) = \frac{1}{2}\left[A_4^*(r)e^{i(-\vec{k}\cdot\vec{r}-\omega t)} + A_4(r)e^{-i(-\vec{k}\cdot\vec{r}-\omega t)} \right], \qquad (1.5)$$

which can be rewritten as

$$E_{pc}(r,t) = \frac{1}{2}[A_4^*(r)e^{-i(\vec{k}\cdot\vec{r}+\omega t)} + A_4(r)e^{i(\vec{k}\cdot\vec{r}+\omega t)}], \qquad (1.6)$$

which is the time reversed version of the wave in eq. 1.4.

This generation of a time-reversal copy of the probe wave is called optical phase conjugation. A photorefractive crystal employed to produce such a phase conjugate
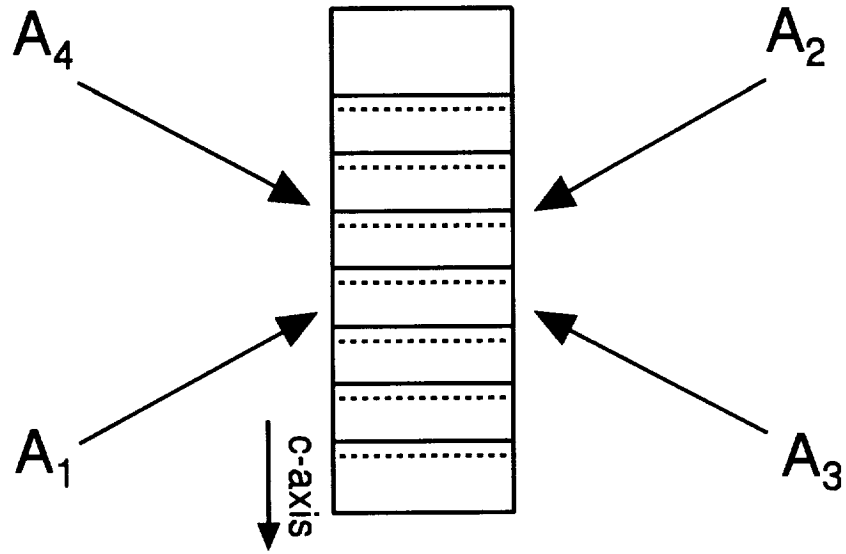
Figure 1.2: Schematic diagram of the four-wave mixing. Beam 1 and beam 4 write a phase grating inside the crystal. Beam 2, counterpropagating to beam 1, is incident on the crystal and diffracted into the direction opposite to that of beam 4. The diffracted beam, beam 3, is a phase conjugate replica of beam 4.

wave back to its source is called a "phase conjugate mirror". The process we just described involves four beams interacting and is referred to as "four-wave mixing".

H. Kogelnik, more than 25 years ago, demonstrated using conventional holography that a distorted image could be undistorted by first producing its phase conjugate replica and then sending it backward through the original distorter [44]. In conventional holography, this involves a two-step procedure in which a photographic plate is first used to store the interference pattern between the incoming distorted image and a reference wave. This hologram is developed and repositioned exactly in its original place. The hologram is then read out by a wave propagating in a direction opposite to that of the original reference wave and deflects the reading wave to produce the PCW.

Now, with the process of photorefractive FWM, the photorefractive crystal replaces the photographic plate to store the hologram which is being written by an image-bearing beam and a coherent reference beam. At the same time, the hologram can be read out by a reading beam incident at the Bragg angle inside the crystal. The simultaneous write and read processes eliminate the developing and fixing steps. So the FWM gives us a new method of storing dynamic holograms in real time image processing, which is often named "real-time holography".

Chapter 2

The PCR model: steady state analysis

2.1 Introduction

Phase conjugate resonators (PCRs) are resonators in which at least one of the mirrors is a phase conjugate mirror (PCM). The PCM, which acts both as a phase conjugator and as a gain element, confers to the resonator some unique properties (e.g. phase healing, transverse mode degeneracy, etc.) [45]. A number of applications of the PCR to image processing have been demonstrated or proposed [7, 46, 9, 11]. A class of these applications makes use of the regenerative feedback of the PCR to synthesize unusual transfer functions, perform nonlinear operations, or implement iterative algorithms [7, 46]. Another type of problem which has motivated this study more directly involves the implementation of discrete time algorithms for distributed parameter control systems [47]. A PCR could be used as a real-time holographic element for temporal image storage and delay operations. In all these, the PCR is below threshold (for self-oscillation) and functions as a regenerative amplifier.

In these applications, the way in which the PCR responds to time-varying signals is important for understanding the operation of the device. Therefore a theory is needed

to describe the transient effects in the PCR (such a theory is described in 2.2). Phase conjugate Fabry-Perot cavities have recently been studied both in the steady state case [48] and in the limit of a PCM with a fast response such as a Kerr material [49]. Fast response means that the time scale associated with the buildup of the polarization field in the medium is much shorter than other time scales in the problem. Thus, there is no difficulty in coupling the time dynamics of the material with the time dynamics of the optical field in a self-consistent manner. However, this is not the case in sluggish photorefractive materials such as in $BaTiO_3$ because the time scale of the grating formation is not shorter than other time scales in the problem. Equations for the transient behavior of the PCR with a sluggish medium must, therefore, include the material equations.

In section 2.3, we first solve the steady state equations for the PCR, for the conditions of nondepleted pumps and an absorption free medium. An analytic solution can be obtained and used to describe the threshold conditions of the PCR. In the quasi-steady state limit for a slow material, the steady state solution can also be used to derive a transfer function for the PCR (section 2.4). The transfer function is then used to analyse the transient response if there are some system operative ranges that could lead to instability of the device.

2.2 Model of the PCR below threshold

In this section, we develop a model for a phase conjugate Fabry-Perot resonator with a PCM consisting of a sluggish photorefractive material. The medium is modeled by the standard Kukhtarev theory. Equations for the fields in the cavity and in the medium, under the plane wave theory, are derived.

2.2.1 The Cavity

The geometry of the PCR is sketched in Figure 2.1. It consists of a conventional (dielectric) mirror and an externally pumped PCM . The input beam A_{IN} may make
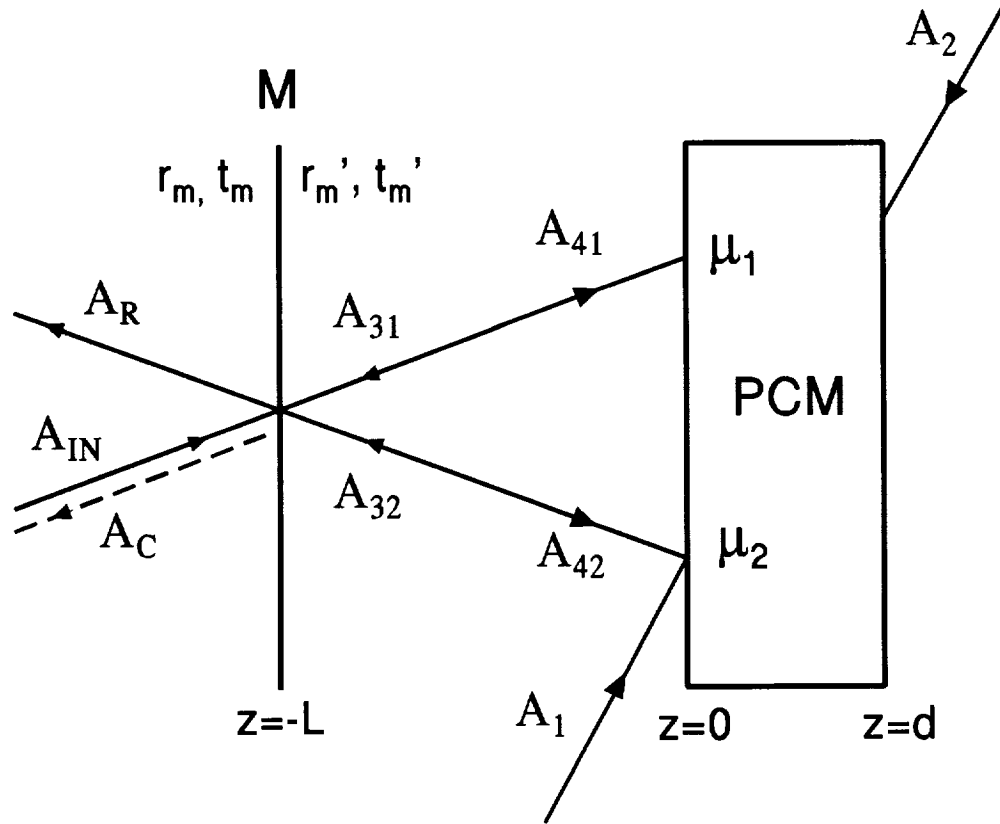
Figure 2.1: Schematic diagram of a phase conjugate resonator using an externally pumped phase conjugate mirror (PCM) and a conventional mirror (M). r_m, t_m, r'_m, t'_m are the reflection and transmission coefficients of the conventional mirror. μ_1, μ_2 are the PCM reflectivities at the two interaction regions. The angle of incidence of the input beam and the distance between the two interaction region are greatly exagerated

a small angle with the mirror normal so that in general two distinct interaction regions exist in the PCM. The presence of two distinct gratings can easily be verified experimentally.

A PCR formed by two PCMs has been investigated by others [50] and proposed for the holographic storage of images [51]. The only difference between the cavity of fig. 2.1 and the two-crystal cavity, as shown in figure 2.2, is that, in the two-crystal set up, the pumps' intensities can be varied independently. In a single-crystal cavity where the two interaction regions share the same pumps, the steady state PCM reflectivities μ_1 and μ_2 are equal, although they generally grow at different rates.

Within the framework of a plane wave theory, the fields' amplitudes in the cavity $(-L \leq z \leq 0)$, satisfy the self-consistency equations

$$A_{41}(z,t) = t_m A_{IN}(z,t) + r'_m A_{32}\left(z, t - \frac{2z}{c} - \frac{2L}{c}\right) e^{i\frac{\omega}{c}2(L+z)}, \tag{2.1}$$

$$A_{42}(z,t) = r'_m A_{31}\left(z, t - \frac{2z}{c} - \frac{2L}{c}\right) e^{i\frac{\omega}{c}2(L+z)}, \tag{2.2}$$

$$A_{31}(z,t) = \mu_1\left(t + \frac{z}{c}\right) A_{41}^*\left(z, t + \frac{2z}{c}\right), \tag{2.3}$$

$$A_{32}(z,t) = \mu_2\left(t + \frac{z}{c}\right) A_{42}^*\left(z, t + \frac{2z}{c}\right), \tag{2.4}$$

where L is the optical length of the cavity.

The PCM is assumed to be a sluggish photorefractive medium such as $BaTiO_3$. When the medium response time is much longer than the cavity round trip time, all the temporal delays in equations 2.1 to 2.4 can be discarded.

The specularly reflected output and the phase conjugate output are respectively

$$A_R(-L,t) = r_m A_{IN}(-L,t) + t'_m A_{32}(0,t) e^{i\frac{\omega}{c}L}, \tag{2.5}$$

and

$$A_C(-L,t) = t'_m A_{31}(0,t) e^{i\frac{\omega}{c}L}. \tag{2.6}$$

15
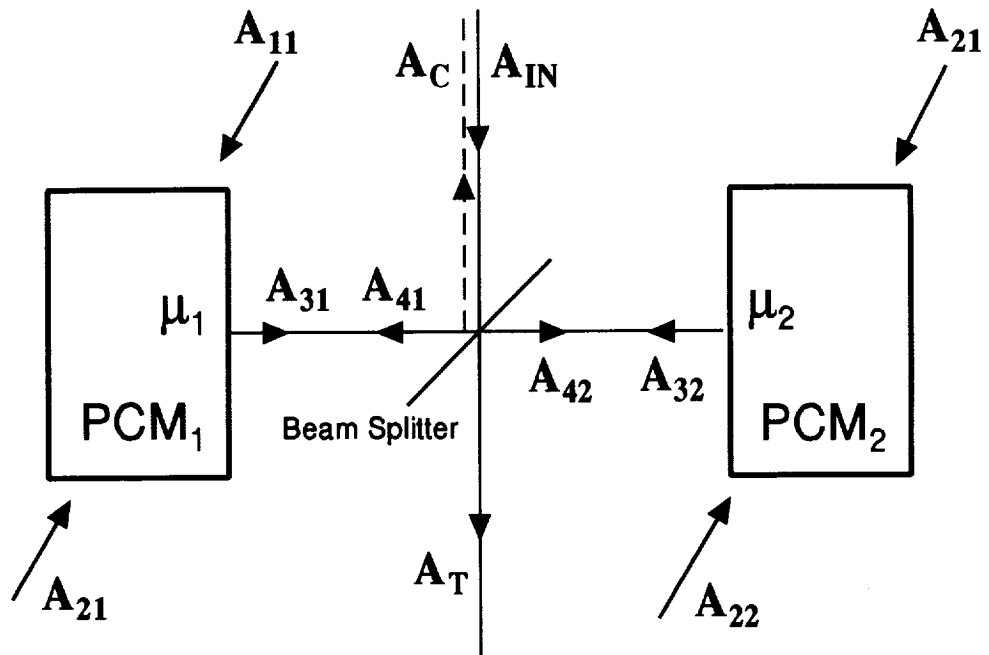
Figure 2.2: Two-crystal cavity comparable to the cavity with two interaction regions of figure 2.1.

2.2.2 The Four-wave mixing (FWM) equations

The standard model used to describe photorefractive wave mixing is based on the coupled wave formalism originally developed in the late 1960's by Kogelnik [36], and on the model due to Kukhtarev *et al.* [42] which describes how the index grating forms in the photorefractive medium. We first outline the coupled wave equations for the photorefractive FWM (the coupled wave equations are derived in Appendix A) and then combine them with Kukhtarev's equations to give a set of coupled partial differential equations which completely describe both the temporal and spatial variations of the fields in the FWM process.

The beams in the PCM are treated as plane waves with slowly varying envelopes (SVE approximation); i.e., the temporal and spatial rates of change of the fields and material polarization amplitudes are slow compared to the light frequency and coarse compared to its wavelength. The pump and input beams have all the same frequency and the same polarization state.

With these assumptions, the wave equation in the medium ($0 \leq z \leq d$) leads to the following standard coupled equations (see Appendix A) (the subscript $j = 1$ or 2 refers to either one of the two interaction regions):

$$\left(\frac{\partial}{\partial z} + \frac{\partial}{v\partial t}\right) A_{1j}(z,t) = -Q_j(z,t)A_{4j}(z,t) - \alpha_j A_{1j}(z,t), \qquad (2.7)$$

$$\left(\frac{\partial}{\partial z} - \frac{\partial}{v\partial t}\right) A_{2j}^*(z,t) = -Q_j(z,t)A_{3j}^*(z,t) + \alpha_j A_{2j}^*(z,t), \qquad (2.8)$$

$$\left(\frac{\partial}{\partial z} - \frac{\partial}{v\partial t}\right) A_{3j}(z,t) = Q_j(z,t)A_{2j}(z,t) + \alpha_j A_{3j}(z,t), \qquad (2.9)$$

$$\left(\frac{\partial}{\partial z} + \frac{\partial}{v\partial t}\right) A_{4j}^*(z,t) = Q_j(z,t)A_{1j}^*(z,t) - \alpha_j A_{4j}^*(z,t), \qquad (2.10)$$

where α_j is the linear amplitude absorption coefficient, Q_j is the complex amplitude of the material grating and v is the speed of light in the medium. The angular dependence of the spatial derivatives has been neglected, which is consistent with the assumption of a small angle between the pump beams and the cavity axis.

17

If the medium response time is much longer than the transit time through the PCM, as is assumed here, the temporal derivatives can be dropped from the LHS of equations 2.7– 2.10. The equations then describe a quasi steady state situation in which the fields' amplitudes follow adiabatically the medium changes.

Futhermore, it was assumed that only one index grating is operative in both regions. For example, with a geometry utilizing the extraordinary polarization to take advantage of the large electro-optic coefficient of $BaTiO_3$, the dominant grating is the one formed by the interference of A_1 with A_4 and A_2 with A_3. Its wave number is $\vec{k}_1 - \vec{k}_4 = \vec{k}_3 - \vec{k}_2$, where $\vec{k}_j$ is the wave vector of beam j.

The dynamics of the grating formation can be derived from the Kukhtarev equations and has the following form (see Appendix B where the details of the Kukhtarev theory and its underlying assumptions are summarized):

$$\tau_j \frac{\partial}{\partial t} Q_j(z,t) = Q_{oj}(z) - Q_j(z,t), \qquad j = 1, 2, \qquad (2.11)$$

where τ_j is a possibly complex time constant and Q_{oj} is the steady state grating. These two quantities can be evaluated from the parameters in the Kukhtarev model as shown in section 2.2.3. From Appendix B, the steady state grating has the form

$$Q_{oj}(z) = \gamma_{oj} \frac{A_{1j}(z)A_{4j}^*(z) + A_{2j}^*(z)A_{3j}(z)}{I_{oj}}, \qquad j = 1, 2, \qquad (2.12)$$

where I_{oj} is the local average intensity in region j : $I_{oj}(z,t) = \sum |A_{kj}(z,t)|^2$. The second factor in the RHS of equation 2.12 is the modulation depth of the interference fringes of beam A_1 with A_4 and beam A_2 with A_3. γ_{oj} is the coupling coefficient and has the form

$$\gamma_{oj} = \frac{i\omega n_o^3}{4c} r_{eff} E_{sc}^s, \qquad (2.13)$$

where r_{eff} is an effective Pockels coefficient which depends on the geometry and the

beams' polarization, and E_{sc}^s is the complex amplitude of the space-charge field modulation (see Appendix B). The effective Pockels coefficient r_{eff} for barium titanate (point group 4mm) can be written [7] as

$$r_{eff} = n_o^4 r_{13} \cos \beta,$$

(2.14)

for ordinary polarized beams, and as

$$r_{eff} = \frac{1}{2} \left[n_o^4 r_{13} (\cos 2\theta - \cos 2\beta) + 4 n_e^2 n_o^2 r_{42} \sin^2 \beta + n_e^4 r_{33} (\cos 2\beta + \cos 2\theta) \right] \cos \beta,$$

(2.15)

for extraordinary polarized beams, where n_o and n_e are the respective ordinary and extraordinary indices of refraction at wavelength $\lambda = 2\pi c/\omega$, r_{ij} are the elements of the linear electro-optic tensor (Pockels coefficients) [40], and θ and β are the angles inside the crystal defined as in Figure 2.3.

If the small angular difference for the beams interacting in regions 1 and 2 is neglected, γ_o and α have the same values in both interaction regions.

2.2.3 The material's constants

According to the Kukhtarev band transport model, a mathematical description of the grating formation process is given by the equations

$$\frac{\partial n}{\partial t} = \frac{\partial N_D^+}{\partial t} - \frac{1}{q} \nabla \cdot \vec{j} \qquad \text{(continuity)},$$

(2.16)

$$\frac{\partial N_D^+}{\partial t} = (SI + \beta)(N_D - N_D^+) - \gamma_R n N_D^+ \qquad \text{(rate equation)},$$

(2.17)

$$\vec{j} = q\mu n \vec{E} - k_B T \mu \nabla n + pI\hat{e}_c \qquad \text{(current equation)},$$

(2.18)

$$\nabla \cdot \vec{E} = \frac{q}{\epsilon} \left(n + N_A - N_D^+ \right) \qquad \text{(Poisson's law)},$$

(2.19)

where
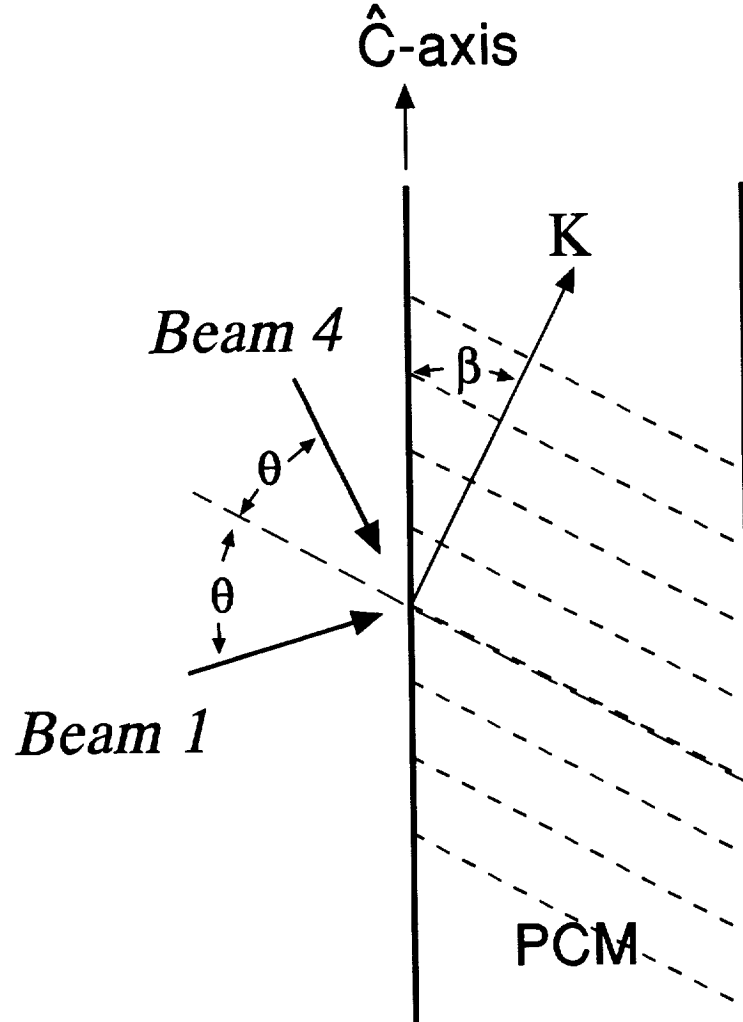
Figure 2.3: Geometrical configuration of two-wave mixing in a photorefractive material. K is the wave vector of the induced grating; $\hat{c}$ is the optical axis of the crystal; 2θ is the angle between two beams inside the crystal; β is the angle of K with the $\hat{c}$-axis.

$n(\vec{r}, t)$	is the free charge carrier (single species) number density,
N_D	is the total number density of the dopant (single species) (Fe for example),
$N_D^+(\vec{r}, t)$	is the number density of the ionized donors (traps) (Fe^{3+} for example),
N_A	is the number density of the acceptors,
$N_D - N_D^+$	is the number density of neutral (filled) donors (Fe^{2+} for example),
j	is the current density,
S	is the photoionization cross section,
I	is the intensity of the optical wave,
γ_R	is the recombination rate coefficient,
μ	is the mobility of the charge carriers,
E	is the total local electric field,
k_B	is Boltzmann's constant,
T	is the temperature,
p	is the photovoltaic coefficient,
q	is the charge of the charge carriers, and
ϵ	is the static dielectric constant.

After linearization in the grating modulation index and in the steady state limit, equations (2.16)–(2.19) can be solved and the steady state space-charge field is found to be (see Appendix B):

$$E_{sc}^s = -iE_q \left[\frac{(E_o + E_p) + iE_D}{E_o + i(E_q + E_D)} \right], \tag{2.20}$$

where E_o is the external applied field, E_p, E_D and E_q are characteristic fields of the material:

$$E_p = \frac{pI_o}{q\mu n_o} \quad \text{(photovoltaic field)}, \tag{2.21}$$

$$E_D = \frac{k_B T |\mathbf{K}|}{q} \quad \text{(diffusion field)},$$

$$E_q = \frac{qN_e}{\epsilon|\mathbf{K}|} \qquad \text{(saturation space charge field)}.$$

Here I_o is the zero order of the light intensity, N_e is the effective trap number density, $\mathbf{K}$ is the grating vector and p is the photovoltaic coefficient [52].

With no external field ($E_o = 0$) and negligible photovoltaic field ($E_p \sim 0$), the steady state space-charge field is simply given by

$$E_{sc}^s = \frac{-iE_qE_D}{E_q + E_D}. \tag{2.22}$$

In this case of a diffusion dominated process, the index grating in equation B.52 leads the light interference fringes by a $\pi/2$ phase shift and the coupling constant γ_o in equation 2.13 becomes real. The model also predicts a complex response time constant of the form (see Appendix B)

$$\tau_g = \tau_e + i\frac{1}{\omega_g}, \tag{2.23}$$

where the material response time is

$$\tau_e = \tau_{di} \frac{\left(1 + \frac{\tau_R}{\tau_D}\right)^2 + \left(\frac{\tau_R}{\tau_E}\right)^2}{\left(1 + \frac{\tau_R\tau_{di}}{\tau_D\tau_I}\right)\left(1 + \frac{\tau_R}{\tau_D}\right) + \left(\frac{\tau_R}{\tau_E}\right)^2\left(\frac{\tau_{di}}{\tau_I}\right)}, \tag{2.24}$$

and the material frequency is

$$\omega_g = \frac{1}{\tau_{di}} \frac{\left(\frac{\tau_R}{\tau_E}\right)\left(\frac{\tau_{di}}{\tau_I} - 1\right)}{\left(1 + \frac{\tau_R}{\tau_D}\right)^2 + \left(\frac{\tau_R}{\tau_E}\right)^2}. \tag{2.25}$$

The various time scales in equations 2.24 and 2.25 are defined by

$$\tau_{di} = \frac{\epsilon}{q\mu n_o} \qquad \text{(dielectric relaxation time)}, \tag{2.26}$$

$$\tau_E = (\mu|\mathbf{K}|E_o)^{-1} \qquad \text{(drift time)}, \tag{2.27}$$

$$\tau_D = (\mu|\mathbf{K}|E_D)^{-1} \qquad \text{(diffusion time)}, \tag{2.28}$$

$$\tau_R = (\gamma_R N_A)^{-1} \qquad \text{(recombination time)}, \qquad (2.29)$$

$$\tau_I = (SI_o)^{-1} \qquad \text{(inverse of photoexcitation rate)}, \qquad (2.30)$$

and the free carrier average density is

$$n_o = \frac{SI_o(N_D - N_A)}{\gamma_R N_A}. \qquad (2.31)$$

All the material constants involved in these relationships are of great interest to the material physicist whose objective is to make materials with optimal properties [53]. It is apparent that different applications require different material properties. For instance, in order to demonstrate high speed, low write laser power and long-lived memory, or large gain, it is necessary to use several different types of materials. It has been observed that BSO is a fast photorefractive material but of low efficiency due to a small electro-optic coefficient while $BaTiO_3$ has by far the largest electro-optic coefficient leading to high diffraction efficiency but with a slow response time. The research for improving photorefractive materials has a goal to overcome the trade off between speed and sensitivity as well as to enlarge the materials' performance over a wider operative range of device exploiting these materials, which is essential to the new optical computing technologies.

For photorefractive materials, one important attribute of the the grating response time is its dependence on the total intensity incident on the crystal. The one-species model of the Kukhtarev theory predicts an inversely linear dependence ($\tau \propto I_o^{-1}$). In $BaTiO_3$, this dependence is experimentally found to be sublinear with an exponent $0.5 < x < 1$. This behavior can be accounted for by assuming that two different species of traps take part in the photorefractive process [54]. For our study, it is however sufficient to use a normalized response time of the form

$$\tau_e \sim \tau_{di} = \frac{\epsilon \gamma_R}{q\mu S} \left(\frac{N_A}{N_D - N_A} \right) \frac{1}{I_o} = \frac{A}{I_o}, \qquad (2.32)$$

which is valid when the recombination time τ_R is short compared to the other time scales of the model. This happens to be the case for $BaTiO_3$. In the calculations of

the next chapter, we used a normalized time scale $\tau_o = I_o^{-1}$. This normalized time scale can be related to the real time scale for a particular material by evaluating the constant A. Typical numbers for $BaTiO_3$ are given in Ref. [53]:

$$\gamma_R = 5 \times 10^{-8} cm^3/s, \qquad (2.33)$$

$$N_A \sim 2 \times 10^{16} cm^{-3},$$

$$\mu \sim 0.5 cm^2/V \cdot s,$$

$$S(N_D - N_A) \sim \alpha \sim 0.3 cm^{-1},$$

$$q = 1.6 \times 10^{-19} C,$$

$$\epsilon_o = 8.85 \times 10^{-14} F cm^{-1}.$$

The relative dielectric constant is given by

$$\epsilon_R = \epsilon_\parallel \sin^2 \beta + \epsilon_\perp \cos^2 \beta, \qquad (2.34)$$

with $\epsilon_\parallel = 4300$, $\epsilon_\perp = 168$ and β is the angle between the grating wave vector and the c-axis of the crystal (Figure 2.3). For the experiment we had $\beta \sim 10°$, which gives $\epsilon_R \sim 300$. With these numbers, we find $A = 1.1 \times 10^{18}$ cm^{-2}.

In equation 2.32, I_o is expressed in number of photons per cm^2 per sec. In the calculations of the next chapter, the unit of intensity was chosen to be 1 mW/mm^2. At a wavelength $\lambda = 0.514\mu$m (photon energy $= 3.87 \times 10^{-19} J$), this corresponds to a photon flux of $2.58 \times 10^{17} s^{-1} cm^{-2}$. The normalized time scale used is thus given by

$$\tau_o(\text{Normalized}) = [I_o(\text{in mW/mm}^2)]^{-1} = \frac{\tau(\text{in sec})}{A'}, \qquad (2.35)$$

with

$$A' = \frac{1.1 \times 10^{18}}{2.58 \times 10^{17}} = 4.26(s \text{ mW/mm}^2). \qquad (2.36)$$

2.3 Steady-state analysis

The main reason for seeking an analytic steady state solution to the PCR's equations is that in the quasi steady state case (slow medium such as $BaTiO_3$) such a

solution can be used (as shown in section 2.4) to define a transfer function from which the stability of the solution can be analyzed. Furthermore, the steady state solutions determine the threshold for self-oscillations of the PCR.

2.3.1 Steady-state equations and their solutions

The steady state equations are obtained simply by setting all the time derivatives equal to zero. At steady state, an analytic solution can easily be found in the case of nondepleted pumps and negligible absorption, i.e. $A_1(z) = A_1(0) = A_1$, $A_2(z) = A_2(d) = A_2$, and $\alpha_{1,2} = 0$. Equations (2.7– 2.12) then reduce to

$$\frac{d}{dz}A_{3j}(z) = \frac{\gamma_o}{I_o}\left[A_1 A_{4j}^*(z) + A_2^* A_{3j}(z)\right] A_2, \tag{2.37}$$

$$\frac{d}{dz}A_{4j}^*(z) = \frac{\gamma_o}{I_o}\left[A_1 A_{4j}^*(z) + A_2^* A_{3j}(z)\right] A_1^* \qquad j = 1, 2, \tag{2.38}$$

where

$$I_o \simeq |A_1|^2 + |A_2|^2. \tag{2.39}$$

The boundary conditions are, from equations (2.1– 2.4),

$$A_{41}(0) = t_m A_{IN}(0) + r_m' A_{32}(0)e^{i\frac{\omega}{c}2L}, \tag{2.40}$$

$$A_{42}(0) = r_m' A_{31}(0)e^{i\frac{\omega}{c}2L}, \tag{2.41}$$

$$A_{31}(d) = A_{32}(d) = 0. \tag{2.42}$$

To solve the steady state equations 2.37 and 2.38, one may proceed as follows. Multiply equation 2.37 by $p \equiv A_2^*/A_1$ and we have

$$\frac{d}{dz}(pA_{3j}(z)) = \frac{\gamma_o|A_2|^2}{I_o}\left[A_{4j}^*(z) + pA_{3j}(z)\right], \qquad p = \frac{A_2^*}{A_1}, \tag{2.43}$$

$$\frac{d}{dz}A_{4j}^*(z) = \gamma_o\left(1 - \frac{|A_2|^2}{I_o}\right)\left[A_{4j}^*(z) + pA_{3j}(z)\right], \tag{2.44}$$

Adding equations 2.43 and 2.44 and integrating, gives

$$pA_{3j}(z) + A^*_{4j}(z) = [pA_{3j}(0) + A^*_{4j}(0)]e^{\gamma_o z}. \tag{2.45}$$

Substituting this equation into equation 2.43 and 2.44 and integrating, gives, respectively

$$A^*_{4j}(z) = \frac{|A_1|^2}{I_o} \left[pA_{3j}(0) + A^*_{4j}(0) \right] (e^{\gamma_o z} - 1) + A^*_{4j}(0), \tag{2.46}$$

and

$$A_{3j}(z) = \frac{|A_2|^2}{I_o p} \left[pA_{3j}(0) + A^*_{4j}(0) \right] (e^{\gamma_o z} - 1) + A_{3j}(0). \tag{2.47}$$

Using the boundary conditions 2.42 in equation 2.47, we find

$$A_{3j}(0) = p^* \frac{e^{-\gamma_o d} - 1}{e^{-\gamma_o d} + R_p} A^*_{4j}(0), \qquad R_p = \frac{I_2}{I_1}. \tag{2.48}$$

Substituting this in equation 2.40 and 2.41, we find

$$A_{41}(0) = t_m A_{IN}(0) + r'_m p^* \frac{e^{-\gamma_o d} - 1}{e^{-\gamma d} + R_p} A^*_{42}(0) e^{i\frac{\omega}{c} 2L}, \tag{2.49}$$

and

$$A_{42}(0) = r'_m p^* \frac{e^{-\gamma_o d} - 1}{e^{-\gamma d} + R_p} A^*_{41}(0) e^{i\frac{\omega}{c} 2L}. \tag{2.50}$$

Equations 2.49 and 2.50 are combined to give

$$A_{41}(0) = \frac{t_m A_{IN}(0)}{1 - \beta}, \tag{2.51}$$

with

$$\beta = |r_m|^2 R_p \left| \frac{e^{-\gamma_o d} - 1}{e^{-\gamma_o d} + R_p} \right|^2 \qquad \text{(feedback parameter)}, \tag{2.52}$$

and

$$R_p = \left| \frac{A_2}{A_1} \right|^2 \qquad \text{(pump ratio)}. \tag{2.53}$$

Using this result in equations 2.46 and 2.47 and making use of the relationship between $A_{42}(0)$ and $A_{41}(0)$ derived in equations 2.49 and 2.50, we finally find the steady state fields in the crystal ($0 \le z \le d$):

$$A_{41}^*(z) = \frac{e^{\gamma_o(z-d)} + R_p}{e^{-\gamma_o d} + R_p} \left(\frac{t_m A_{IN}(0)}{1-\beta} \right)^*, \tag{2.54}$$

$$A_{42}^*(z) = r_m'^* p e^{-i\frac{\omega}{c}2L} \frac{(e^{\gamma_o(z-d)} + R_p)(e^{-\gamma_o d} - 1)^*}{|e^{-\gamma_o d} + R_p|^2} \left(\frac{t_m A_{IN}(0)}{1-\beta} \right), \tag{2.55}$$

$$A_{31}(z) = p^* \frac{e^{\gamma_o(z-d)} - 1}{e^{-\gamma_o d} + R_p} \left(\frac{t_m A_{IN}(0)}{1-\beta} \right)^*, \tag{2.56}$$

$$A_{32}(z) = r_m'^* R_p e^{-i\frac{\omega}{c}2L} \frac{(e^{\gamma_o(z-d)} - 1)(e^{-\gamma_o d} - 1)^*}{|e^{-\gamma_o d} + R_p|^2} \left(\frac{t_m A_{IN}(0)}{1-\beta} \right). \tag{2.57}$$

The cavity fields and the outputs can then be found by using equations (2.54–2.57) in equations (2.1– 2.6).

2.3.2 Threshold for self-oscillation

The PCM steady state reflectivities are defined, from equations 2.3 and 2.4, as

$$\mu_j = \frac{A_{3j}(0)}{A_{4j}^*(0)}, \qquad j = 1,2. \tag{2.58}$$

Using equations (2.54– 2.57), we find

$$\mu_1 = \mu_2 = \mu = p^* \frac{e^{-\gamma_o d} - 1}{e^{-\gamma_o d} + R_p}, \tag{2.59}$$

and the feedback parameter takes the form

$$\beta = |r_m \mu|^2. \tag{2.60}$$

If the two interaction regions share the same pumps, they have equal steady state reflectivity. In a diffusion dominated medium with a stationary grating, the coupling parameter γ_o is real. The phase of the PCM reflectivity is thus simply the sum of

27
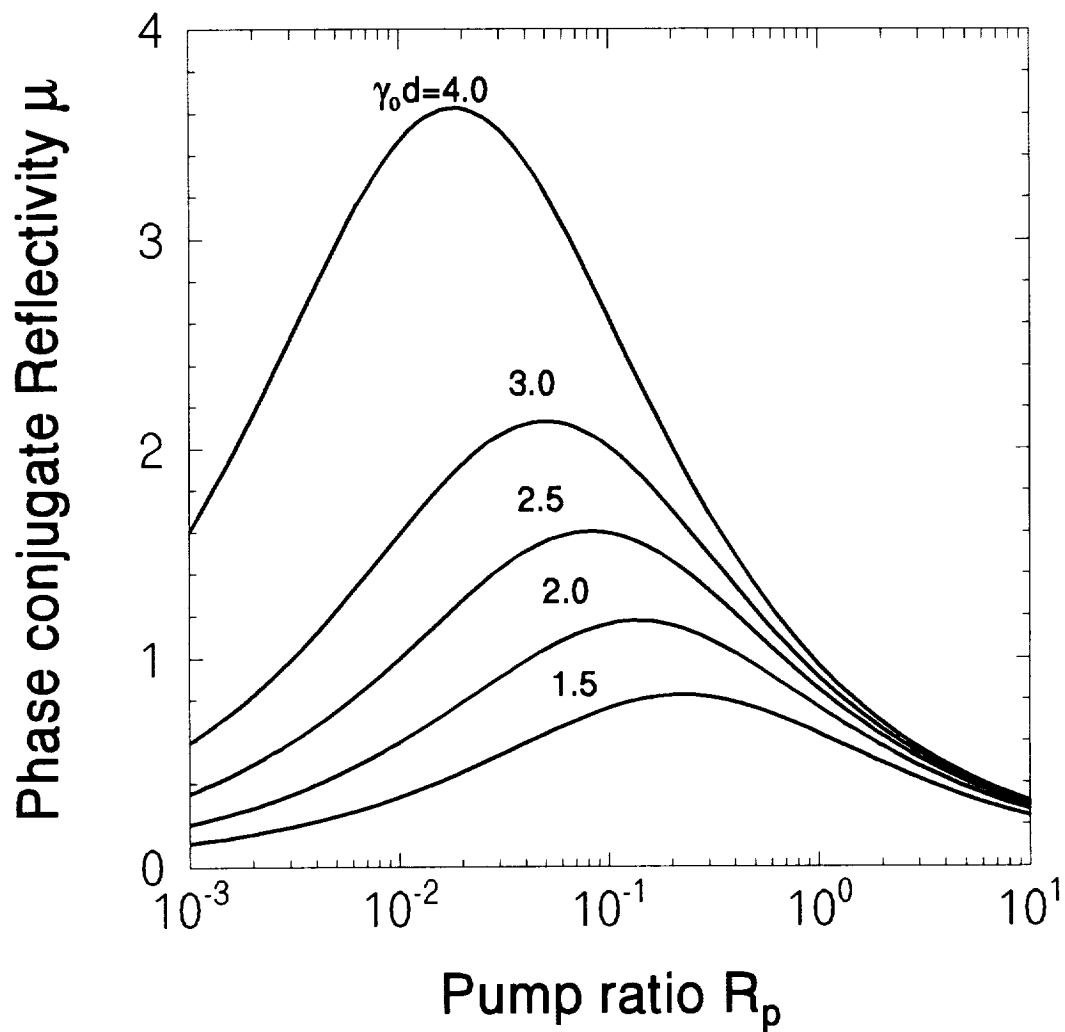
Figure 2.4: Steady state PCM reflectivity as a function of the pump ratio for various values of the coupling parameter

the phases of the pump beams: $\text{Arg}[\mu] = \phi_1(0) + \phi_2(d)$, $\phi_1(0) = \text{Arg}[A_1(0)]$, $\phi_2(d) = \text{Arg}[A_2(d)]$.

Figure 2.4 shows the magnitude of the PCM reflectivity as a function of the pump ratio for various values of the coupling constant $\gamma_o d$. For the pump ratio $R_p \ll e^{-\gamma_o d}$, $|\mu|$ increases as $\sqrt{R_p}$. For $R_p \gg e^{-\gamma_o d}$, $|\mu|$ drops as $1/\sqrt{R_p}$ almost independently of the coupling constant. Also, the reflectivities all converge to zero as the power of pump 2 becomes much greater than that of pump 1. This is because the index grating written by pump 1 and the input is erased by the large power of pump 2. Equation 2.60 shows that the feedback parameter is proportional to $|\mu|^2$. Care must be taken, however, in interpreting this result. It is clear that the steady state solution of equations (2.54– 2.57) is valid only below threshold, i.e. $\beta < 1$. The condition $\beta = 1$, which corresponds to a feedback system in which the gain exactly compensates the losses, defines the threshold for self-oscillations of the PCR (i.e. no external input needed to establish the cavity fields). Figure 2.5 shows β calculated from equation 2.60 with a mirror reflectivity $|r_m|^2 = 0.95$. It is seen that for small coupling ($\gamma_o d \simeq 1.8$), the resonator is stable for the entire range of pump ratios. For larger coupling constant, there is a range of pump ratios around $R_p \sim 0.1$ which would have $\beta > 1$. This is of course not physical. As one approaches threshold, the cavity fields increase, the undepleted pump assumption ceases to be valid, saturation takes place and β remains equal to unity even if the coupling constant is increased.

2.4 Transfer function of the PCR and its stability analysis

In this section, we develop a method to derive a transfer function of the PCR and we use it for the analysis of the device's frequency response and possible instabilities.

2.4.1 Frequency domain transformation of the PCR's equations

To derive the transfer function, we begin with the time-dependent FWM equations (2.7– 2.11) in section 2.2.2. In the undepleted pumps and negligible absorption
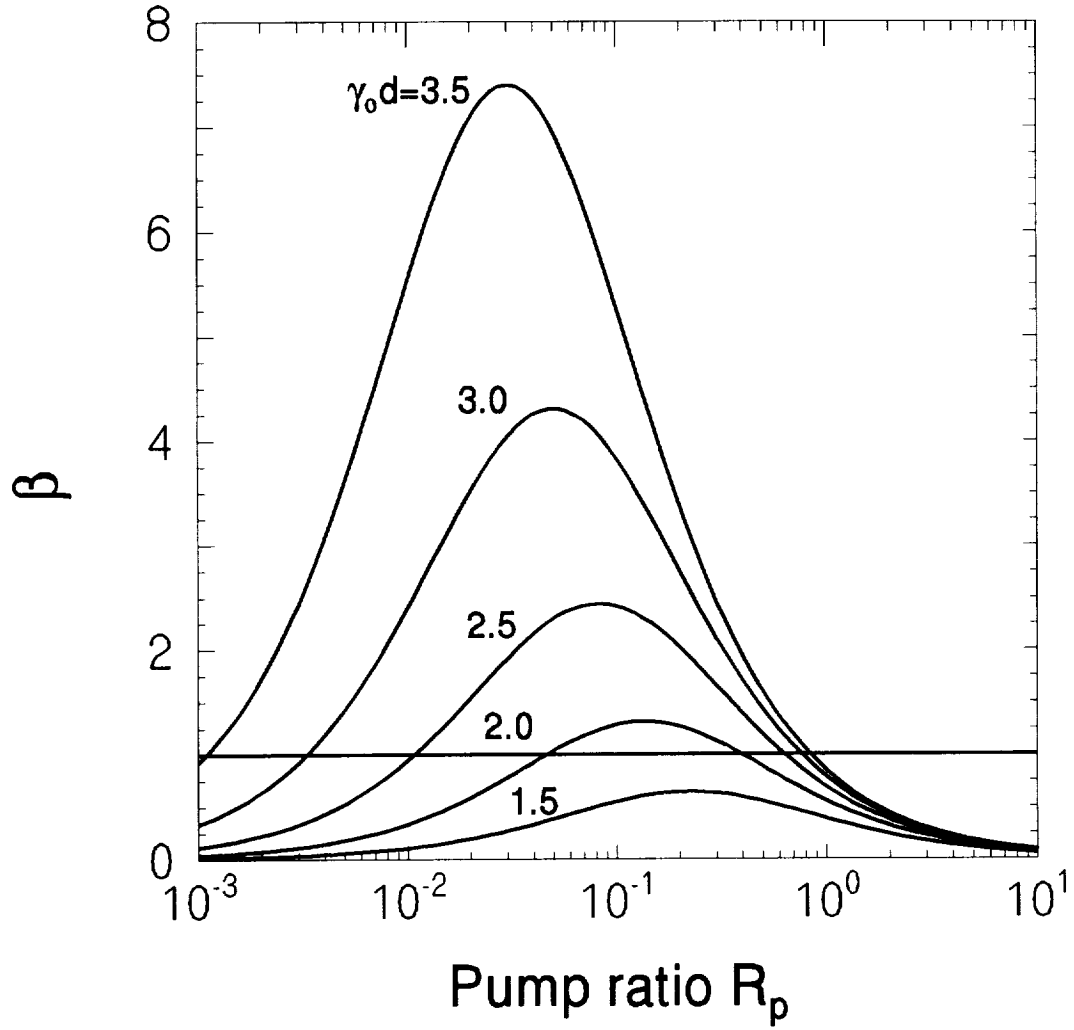
Figure 2.5: Feedback parameter as a function of the pump ratio for various values of the coupling parameter. The steady state solution is valid only below threshold: $\beta < 1$.

approximation, they read:

$$\left(\frac{\partial}{\partial z} + \frac{\partial}{v\partial t}\right) A_{3j}(z,t) = Q_j(z,t)A_2, \tag{2.61}$$

$$\left(\frac{\partial}{\partial z} - \frac{\partial}{v\partial t}\right) A_{4j}^*(z,t) = Q_j(z,t)A_1^*, \tag{2.62}$$

$$\tau\frac{\partial}{\partial t}Q_j(z,t) + Q_j(z,t) = \gamma_o\frac{A_1 A_{4j}^*(z,t) + A_2^* A_{3j}(z,t)}{I_o}. \tag{2.63}$$

We define $a_{3j}(z,\Omega)$, $\tilde{a}_{4j}(z,\Omega)$ and $q_j(z,\Omega)$ as the complex Fourier transforms (or double sided Laplace transforms) of $A_{3j}(z,t)$, $A_{4j}^*(z,t)$ and $Q_j(z,t)$, respectively, i.e.

$$f(\Omega) = \int_{-\infty}^{+\infty} F(t)e^{-i\Omega t}dt, \tag{2.64}$$

$$F(t) = \frac{1}{2\pi}\int_{-\infty+ic}^{+\infty+ic} f(\Omega)e^{i\Omega t}d\Omega, \tag{2.65}$$

so that $\tilde{a}_4(z,\Omega) = a_4^*(z,-\Omega)$. Equations (2.61– 2.63) become

$$\left(\frac{\partial}{\partial z} + i\frac{\Omega}{v}\right) a_{3j}(z,\Omega) = q_j(z,\Omega)A_2, \tag{2.66}$$

$$\left(\frac{\partial}{\partial z} - i\frac{\Omega}{v}\right) \tilde{a}_{4j}(z,\Omega) = q_j(z,\Omega)A_1^*, \tag{2.67}$$

$$(1 + i\Omega\tau)q_j(z,\Omega) = \frac{\gamma_o}{I_o}[A_1\tilde{a}_{4j}(z,\Omega) + A_2^* a_{3j}(z,\Omega)]. \tag{2.68}$$

Thus, the complex amplitudes of a_{3j} and $\tilde{a}_{4j}$ satisfy

$$\left(\frac{\partial}{\partial z} + i\frac{\Omega}{v}\right) a_{3j}(z,\Omega) = \frac{\gamma_o}{1 + i\Omega\tau}\frac{A_1 a_{4j}^*(z,-\Omega) + A_2^* a_{3j}(z,\Omega)}{I_o}A_2, \tag{2.69}$$

$$\left(\frac{\partial}{\partial z} - i\frac{\Omega}{v}\right) a_{4j}^*(z,-\Omega) = \frac{\gamma_o}{1 + i\Omega\tau}\frac{A_1 a_{4j}^*(z,-\Omega) + A_2^* a_{3j}(z,\Omega)}{I_o}A_1^*. \tag{2.70}$$

For a slow medium, the transit time through the PCM is much shorter than the medium response time ($\tau \gg d/v$) and the terms $i\Omega/v$ can thus be neglected.

Equations 2.69 and 2.70 are then identical to the differential equations 2.37 and 2.38 used to derive the steady state solutions if the substitution

$$\gamma = \frac{\gamma_o}{1 + i\Omega\tau}, \tag{2.71}$$

is made. With a slow medium ($\tau \gg$ cavity round trip time), the boundary conditions for a_3 and a_4 also have the same form as equations (2.40– 2.42). The solutions of equations 2.69 and 2.70 are thus identical to the solutions of equations 2.37 and 2.38 respectively, with the substitution of equation 2.71.

2.4.2 Transient response and its stability

From the results of the previous section, we can now define a transfer function for the phase conjugate cavity beam,

$$\begin{aligned} H(\Omega) &= \frac{a_{31}(0, \Omega)}{\tilde{a}_{IN}(0, \Omega)} \\ &= \left(\frac{t_m p}{1 - \beta(\Omega)}\right)^* \frac{e^{-\gamma d} - 1}{e^{-\gamma d} + R_p}, \end{aligned} \tag{2.72}$$

with

$$\beta(\Omega) = |r'_m|^2 R_p \left|\frac{e^{-\gamma d} - 1}{e^{-\gamma d} + R_p}\right|^2, \tag{2.73}$$

where $p = A_2^*/A_1$ and $R_p = |A_2/A_1|^2$.

From the definition of the complex Fourier transform given in equations 2.64 and 2.65, the system is unstable when the transfer function has poles with negative imaginary parts. Figures (2.6– 2.8) show contour plots (on a log scale) and 3D plots (on a linear scale) of the transfer function for three different values of the coupling parameter. The shaded areas outline the region in which $\beta > 1$ and in which the definition of a transfer function becomes meaningless. The poles are located along the boundary $\beta = 1$.

For a weak coupling parameter, all the poles are above the real axis and the system is stable (Figure 2.6). From equation 2.73 and the parameter values given in
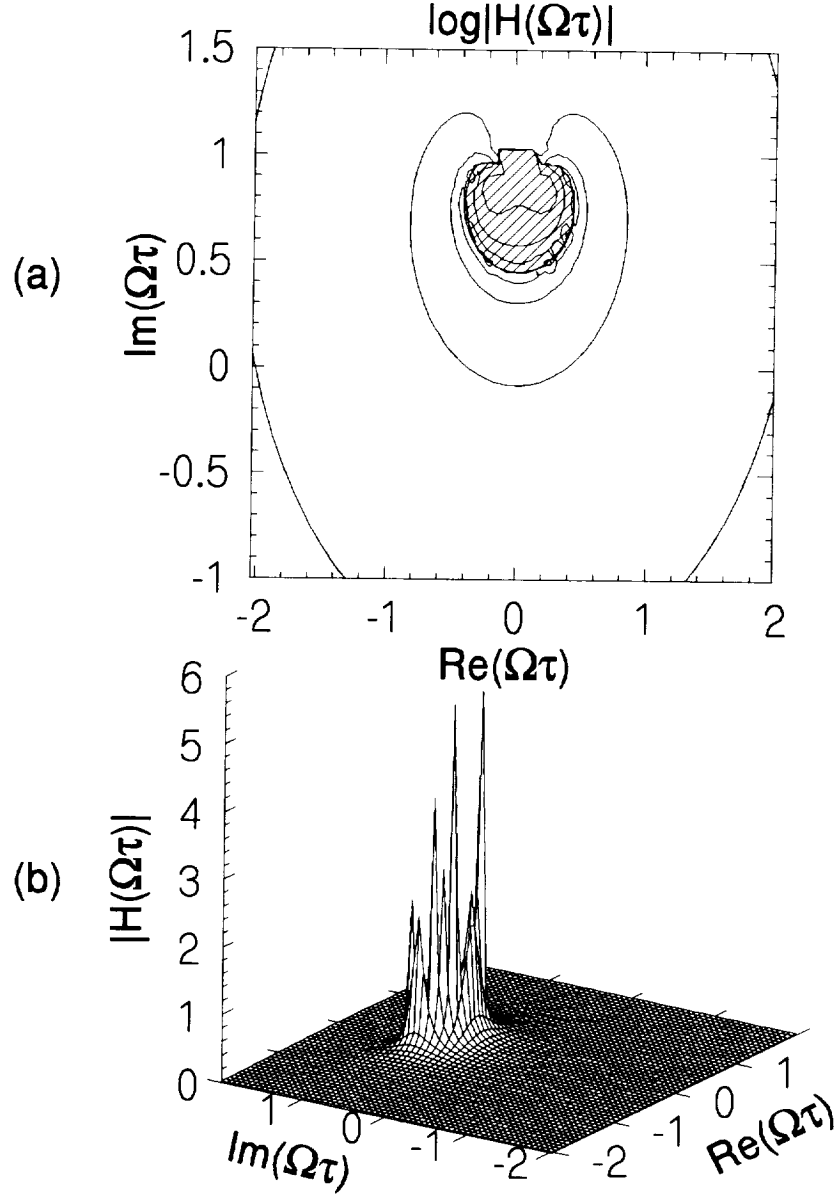
Figure 2.6: (a)Contour plot in the complex plane (log scale) and (b)3D plot (linear scale) of the transfer function of the PCR with a sluggish medium, in the limit of negligible absorption and no pump depletion. The relevant parameter values are $\gamma_o d = 1.0, R_p = 0.1, R_m = 0.95$. The shaded region outlines the domain $\beta > 1$.
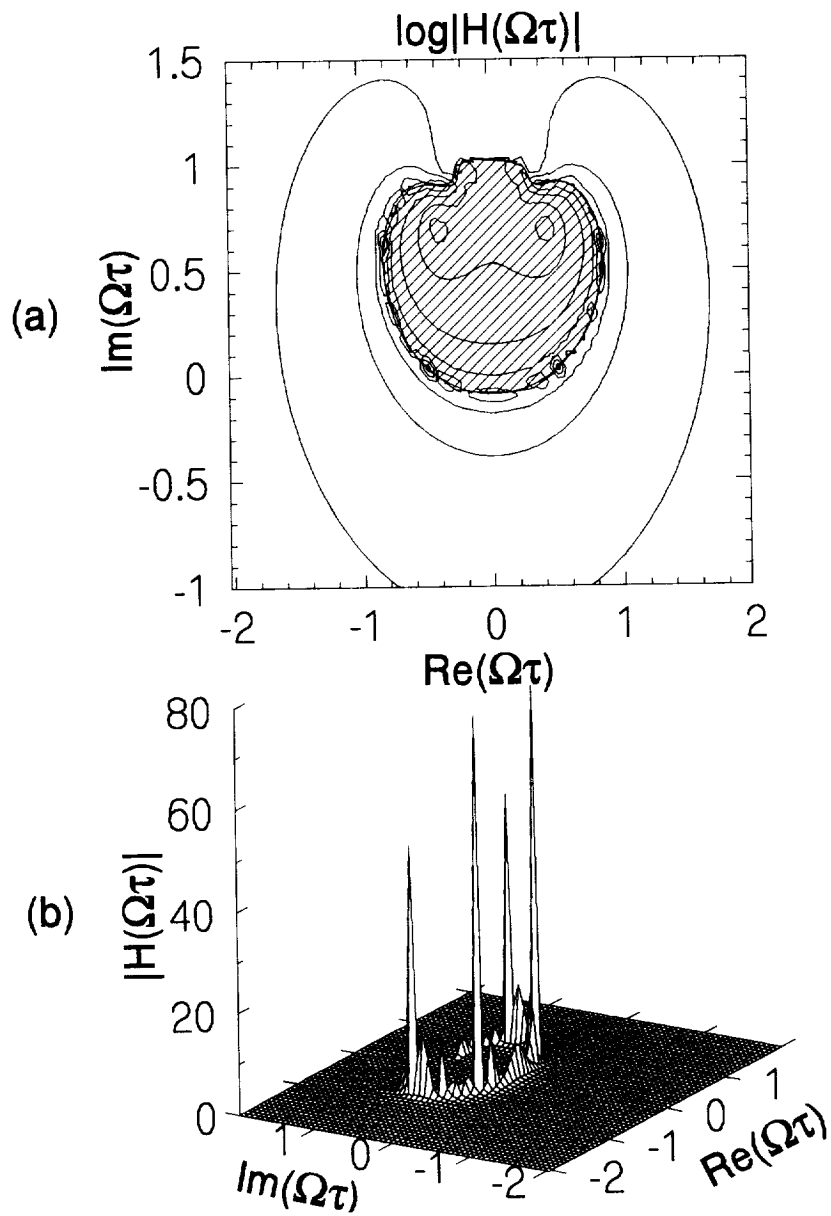
Figure 2.7: Same as Figure 2.6 with $\gamma_o d = 2.0$. The cavity has just reached threshold.
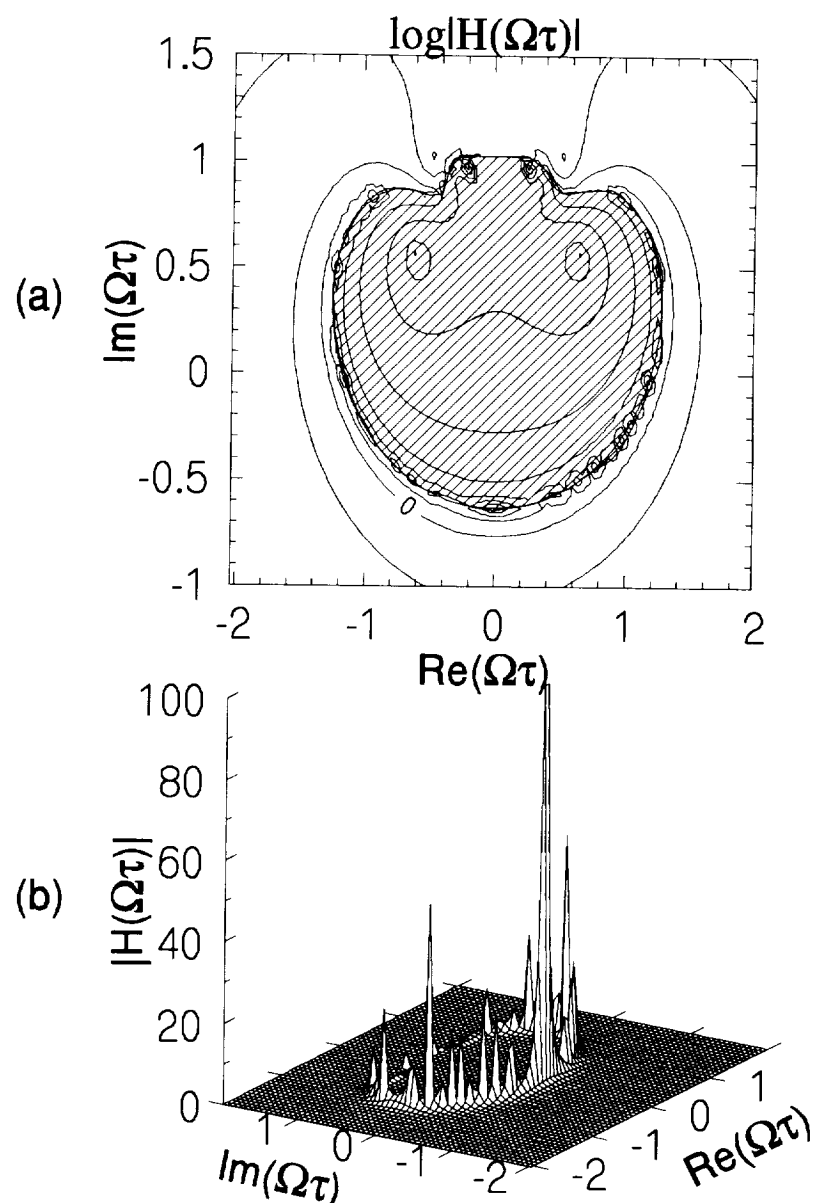
Figure 2.8: Same as Figure 2.6 and 2.7 with $\gamma_o d = 3.0$ showing additional unstable conjugate pairs of poles.

the caption of Figure 2.6, it can be calculated that the intersection of the boundary $\beta = 1$ with the imaginary axis crosses to the lower half plane for $\gamma_o d = 1.87$ (Figure 2.7). This is, of course, precisely the coupling parameter needed to reach threshold for these parameter values, as can be verified in Figure 2.5. At this point, the resonator self-oscillates and has a stable steady state output. As the coupling parameter increases further, additional complex conjugate poles may cross the real axis and become unstable. (Figure 2.8).

2.5 Conclusion

We have presented a model and the steady state analysis of the PCR in the framework of the plane wave representation. A steady state analysis of the FWM process of the PCR is performed and analytic solutions are derived in the case of nondepleted pump, an absorption free medium and real coupling constant. Stability analysis of the solutions is also discussed with the use of the transfer function in the frequency domain. We find that dynamic instabilities start to come in when the resonator self-oscillates, i.e. when the feedback parameter $\beta = 1$.

Chapter 3

Transient behavior of a PCR: numerical study

The theory of the photorefractive phase conjugate Fabry-Perot cavity formulated in chapter 2 was used to find steady state solutions. The analytic results and the analysis of the stability under quasi steady-state conditions have been presented in that chapter. For practical applications, it is also crucial to understand the transient dynamics of the device. In this chapter, the transient regime of a PCR under the plane wave assumption is studied numerically. In particular we are concerned with the cavity's response time as a function of the system's parameters. In section 3.1 we review the time-dependent equations for the waves in a PCR and describe a numerical method for their solution. In section 3.2 we present the numerical results as functions of the coupling parameter, the pump ratio, the probe ratio, the dielectric mirror's reflectivity, and the absorption constant of the medium. The general trends are discussed in view of the possible use of the system in image processing. In section 3.3 we describe an experimental setup used to study the transient dynamics of a PCR and discuss the experimental results. A summary of the study is given in section 3.4.

3.1   A numerical approach

In this section we begin with the time-dependent equations derived in chapter 2, including the pump depletion and medium absorption. We then apply an adiabatic elimination method to integrate the partial differential equations separately in the space and time domains to obtain the final steady state of the cavity fields.

3.1.1   The start of the transients

The time-dependent equations derived in section 2.2.2 for the plane wave model of four wave mixing in a slow photorefractive medium are (figure 2.1):

$$\frac{\partial}{\partial z}A_{1j}(z,t) = -Q_j(z,t)A_{4j}(z,t) - \alpha_j A_{1j}(z,t), \tag{3.1}$$

$$\frac{\partial}{\partial z}A_{2j}^*(z,t) = -Q_j(z,t)A_{3j}^*(z,t) + \alpha_j A_{2j}^*(z,t), \tag{3.2}$$

$$\frac{\partial}{\partial z}A_{3j}(z,t) = Q_j(z,t)A_{2j}(z,t) + \alpha_j A_{3j}(z,t), \tag{3.3}$$

$$\frac{\partial}{\partial z}A_{4j}^*(z,t) = Q_j(z,t)A_{1j}^*(z,t) - \alpha_j A_{4j}^*(z,t), \tag{3.4}$$

and

$$\tau\frac{\partial}{\partial t}Q_j(z,t) + Q_j(z,t) = \frac{\gamma_o}{I_o(z,t)}[A_{1j}(z,t)A_{4j}^*(z,t) + A_{2j}^*(z,t)A_{3j}(z,t)]. \tag{3.5}$$

The boundary conditions for the cavity fields are:

$$A_{41}(0,t) = t_m A_{IN} + r_m' A_{32}(0,t)e^{i\frac{\omega}{c}2L}, \tag{3.6}$$

$$A_{42}(0,t) = r_m' A_{31}(0,t)e^{i\frac{\omega}{c}2L}, \tag{3.7}$$

$$A_{31}(d,t) = A_{32}(d,t) = 0, \tag{3.8}$$

$$A_{11}(0,t) = A_{12}(0,t) = A_{1o}, \tag{3.9}$$

$$A_{21}(d,t) = A_{22}(d,t) = A_{2o}. \tag{3.10}$$

38

For the initial state of the PCR, we assume that only the two pump beams A_1 and A_2 are present. We further assume that there is no scattered noise so that even if the cavity is above threshold (gain > loss), self-oscillations do not start spontaneously without an input beam. Since the interaction between the two pumps is neglected, their initial spatial distributions in the crystal assume a simple exponential dependence of the form $e^{\pm \alpha z}$.

The signal beam is then abruptly turned on to a constant value A_{IN}. Since no interaction takes place yet, it also assumes an exponential distribution:

$$A_{41}(z,0) = t_m A_{IN} e^{-\alpha z}, \tag{3.11}$$

$$A_{31}(z,0) = A_{42}(z,0) = A_{32}(z,0) = 0. \tag{3.12}$$

After a first short lapse of time, a grating is being formed in region 1, driven by the interference between A_{41} and A_1 only. The scattering of A_2 by this grating produces a phase conjugate beam A_{31}. After reflection on the mirror, this beam produces a probe beam A_{42} in the region 2. The three beams A_{42}, A_1 and A_2 in region 2 vary exponentially in space since there exists no interaction yet, and their interference triggers the formation of a grating in exactly the same way as in region 1. After a second lapse of time, this grating generates a phase conjugate beam A_{32} which adds up coherently to the input A_{IN} to define the new probe beam A_{41} in region 1. The process goes on with the two gratings driving each other's growth and building up the cavity fields until a steady state is reached.

3.1.2 Adiabatic elimination algorithm

For a slow medium such as BaTiO$_3$, the time derivatives in equations (3.1–3.4) have been eliminated since the propagation delays in the cavity and in the medium are short compared with the time needed for grating formation. Under this quasi steady-state condition, one can regard the field amplitudes inside the crystal as following the slow grating changes adiabatically. This method was proposed by Heaton *et al.*

in [17] for the integration of the time-dependent photorefractive equations separately in the space and time domain and is known as the adiabatic elimination method. The numerical recipe includes the following steps [55]. At time t_N, $Q_j(z, t_N)$ modulates the field amplitudes inside the crystal. The spatial distributions of the fields are calculated by solving the ordinary differential equations (3.1–3.4) with the boundary conditions (3.6–3.10), by using a fourth order Runge-Kutta method. The boundary conditions allow one to separate these equations into two independent sets. First, equations 3.2 and 3.3 are solved simultaneously with the boundary values $A_{3j}(d, t_N) = 0$; $A_{2j}(d, t_N) = A_{2j}(0) = A_{2o}$. The solution of this first set of equations is then used to find the boundary values $A_{4j}(0, t_N)$. These, together with the boundary values $A_{1j}(0, t_N) = A_{1j}(0) = A_{1o}$, are used to solve equations 3.1 and 3.4. All the fields inside the crystal at t_N are then known.

The medium then responds to these fields according to equation 3.5 to produce a new grating $Q_j(z, t_{N+1})$. A second order Runge-Kutta method is used to integrate this temporal equation, giving

$$Q_j(z, t_{N+1}) \approx Q_j(z, t_N) + (\Delta t_N / \tau)\{\gamma_o m_j(z, t_N + \Delta t_N / 2) - [Q_j(z, t_N) + (1/2)K^{(N)}]\},$$
$$(3.13)$$

where

$$K^{(N)} = (\Delta t_N / \tau)[\gamma_o m_j(z, t_N) - Q_j(z, t_N)], \qquad (3.14)$$

and

$$m_j(z, t_N) = \frac{A_{1j}(z, t_N)A_{4j}^*(z, t_N) + A_{2j}^*(z, t_N)A_{3j}(z, t_N)}{I_{oj}(z, t_N)}, \qquad (3.15)$$

with $t_{N+1} = t_N + \Delta t_N$. The new grating is then used to find the new spatial distribution of the fields at time t_{N+1} which is again calculated from equations 3.1 and 3.4. The process is repeated for a fixed number of steps or until a steady state is reached.

For the calculation to be valid, the time step Δt_N must be small enough compared to the time constant $\tau(t_N)$ of the grating. Since this constant is a function of the

intensity incident on the crystal and therefore changes in time, the temporal step was not taken as a constant but rather each step was chosen equal to 1/10 the instantaneous time constant $\tau(t_N)$ of the grating.

Since, according to the standard Kukhtarev model, the grating time constant is inversely proportional to the total intensity I_o incident on the crystal, we chose a relative time scale of the form $\tau = I_o^{-1}$ for the calculations. This time scale can be related to the actual time scale $T = AI_o^{-1}$ by evaluating the constant A for a particular material [53]. Typical values of parameters for BaTiO$_3$ give $A \approx 4.3$ s $\times$ mW/mm^2 (see section 2.2.3). The time appearing in the graphs discussed in the next section is normalized to the medium response time with a total incident I_o of 1 mW/mm^2 (e.g., $\sim$ 4.3s for BaTiO$_3$).

3.2 Numerical analysis

In this section, the numerical procedure just discussed is used to find the transient behaviors of the cavity fields as functions of the system's parameters. Particular attention is given to the system response time and the PCR's reflectivity because of their importance in the design of practical devices.

3.2.1 Response curves for the cavity fields

The system's parameters used in this and the following sections are the coupling parameter $\gamma_o d$, the pump ratio $R_p \equiv I_2/I_1$, the probe ratio $R_s = I_{IN}/(I_1 + I_2)$, the input mirror reflectivity $R_m = |r_m|^2$, and the absorption parameter αd. Figures (3.1–3.5) show the results of sample calculations of the temporal evolution of the cavity field intensity $I_{31}(0, t/\tau_o)$. The other fields experience similar growth. The normalized intensity of the phase conjugate cavity field intensity $I_{31}/(I_1 + I_2)$ is plotted as a function of time, for a square pulse input. The length of the pulse was chosen long enough to allow the PCR to reach a steady state.
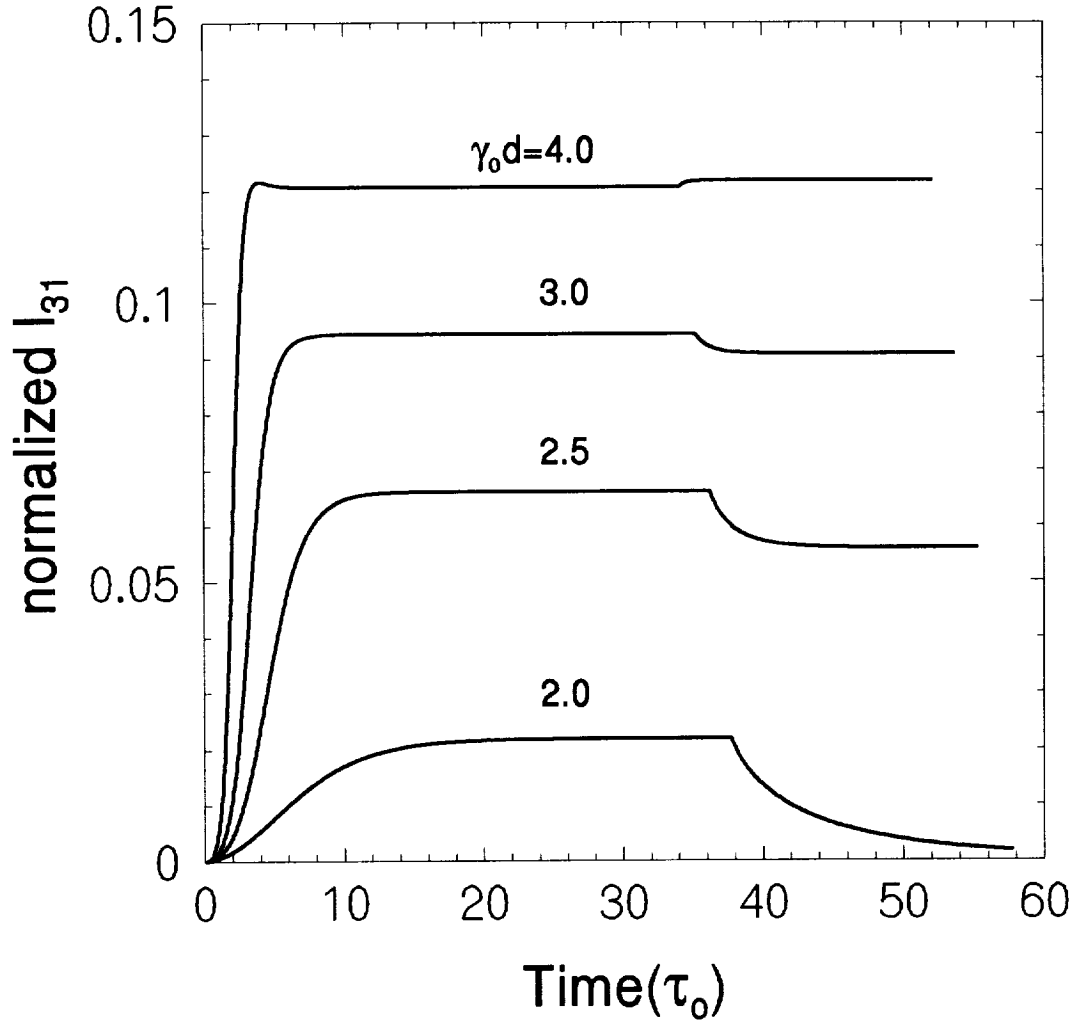
Figure 3.1: Normalized cavity field intensity $I_{31}/(I_1 + I_2)$ showing the response of the PCR to a square pulse input for various values of the coupling parameter and $R_s = 0.02$, $R_p = 0.3$, $R_m = 0.95$, $\alpha d = 0.15$. Time is normalized to the response time τ_o of the medium with $I_o = 1\text{mW/mm}^2$. The cavity is above threshold for $\gamma_o d \geq 2.5$.

Figure 3.1 shows the response for various values of the coupling parameter. The other parameters are $R_s = 0.02$, $R_p = 0.3$, $R_m = 0.95$ and $\alpha d = 0.15$. Larger values of the coupling parameter lead to larger cavity fields, as expected, to faster growth rates and to shorter buildup times. For $\gamma_o d \sim 2.2$, the cavity is above threshold and a self-oscillating field remains in the cavity even after the input has been cut off. This is consistent with the result of figure 2.5 which indicates that at $R_p \sim 3$, the cavity reaches threshold for $\gamma_o d \sim 2$ without absorption.

Figure 3.2 shows the response for various pump ratios. In varying R_p the pump intensity I_1 was maintained constant, and I_2 was varied. The other parameters are $\gamma_o d = 2$, $R_s = 0.02$, $R_m = 0.95$ and $\alpha d = 0.15$. With these parameter values, the cavity remains below threshold for all values of R_p, as shown in figure 2.5. It is seen that at first, the steady state cavity field intensity increases with increasing pump ratios and then drops. This is consistent with the result of figure 2.4 which shows that the PCM reflectivity also reaches a maximum. The buildup and decay rates follow similar trends but the total buildup time does not vary much with the pump ratio.

Figure 3.3 shows the PCR response for various probe ratios. The other parameters are $R_p = 0.5$, $\gamma_o d = 2.5$, $R_m = 0.95$, and $\alpha d = 0.15$. The steady state cavity intensity increases monotonically with the probe ratio, the buildup rate increases and the buildup time becomes shorter. The decay time, however, is fairly constant. In this example, the cavity was slightly above threshold. As the input is cut off, the cavity field evolves toward a final self-oscillating steady state intensity in a time which does not depend much on the initial input intensity. This behavior could be found useful in an optical processor, as it is seen that seeding the PCR with inputs of various intensities changes the buildup time but does not affect the threshold condition.

Figure 3.4 shows the response for different mirror reflectivies and for $\gamma_o d = 2$, $R_p = 0.5$, $R_s = 0.1$. In this case, lowering the input mirror reflectivity increases the steady-state PCM reflectivity product $|\mu_1 \mu_2|$. Consequently, the increased PCM gain overcomes the additional losses of the input mirror and leads to a larger steady state cavity field. The buildup and decay times slowly increase with smaller input mirror
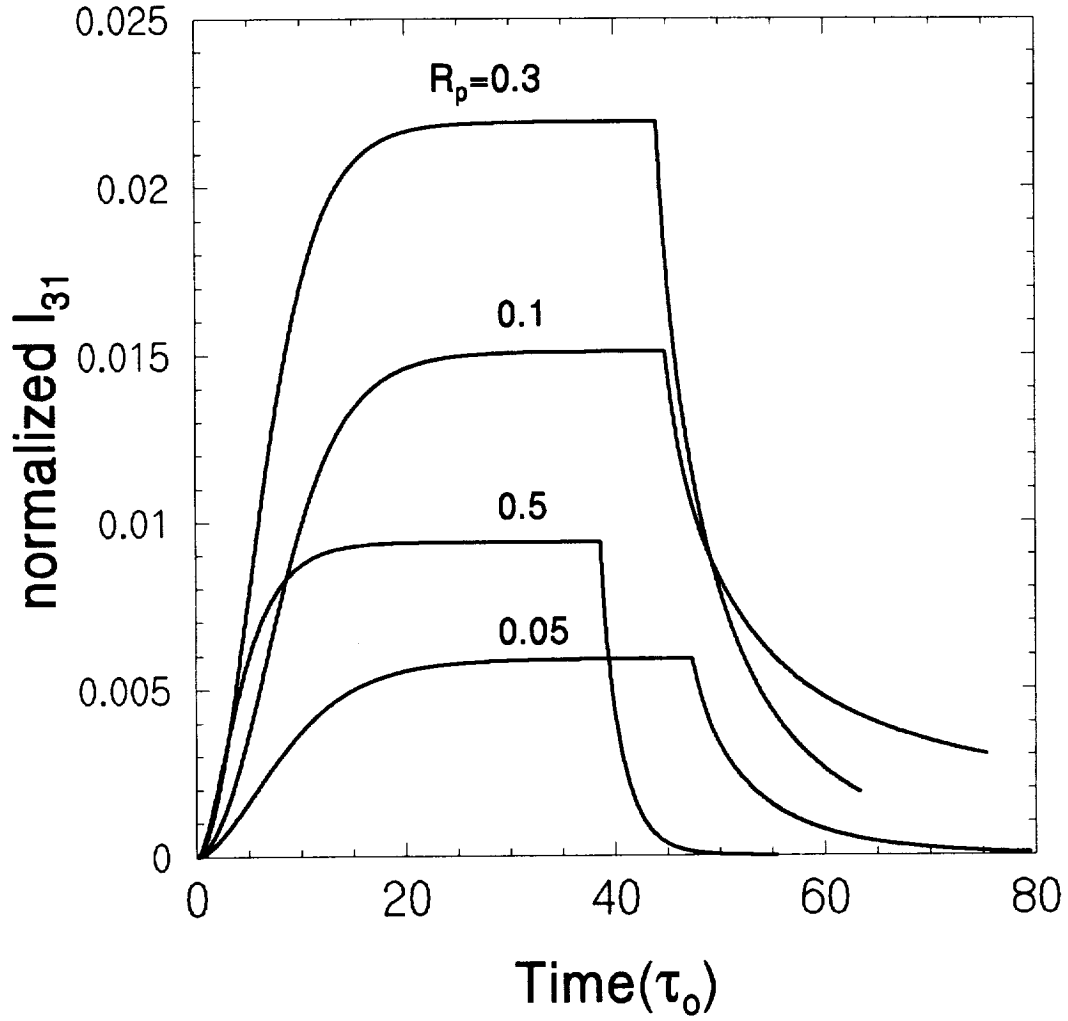
Figure 3.2: Normalized cavity field intensity $I_{31}/(I_1 + I_2)$ showing the response of the PCR to a square pulse input for various values of the pump ratio and $\gamma_o d = 2.0$, $R_s = 0.02$, $R_m = 0.95$, $\alpha d = 0.15$.
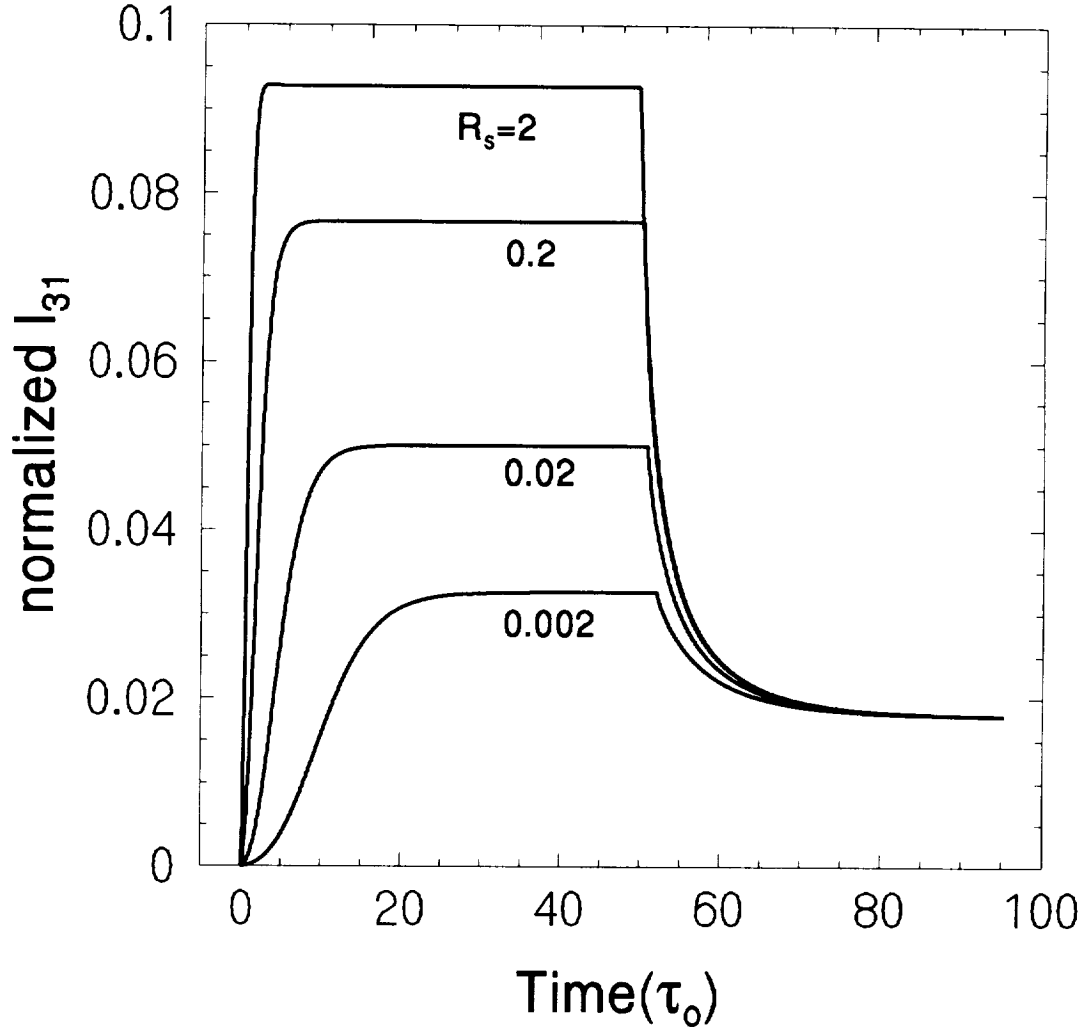
Figure 3.3: Normalized cavity field intensity $I_{31}/(I_1 + I_2)$ showing the response of the PCR to a square pulse input for various values of the probe ratio and $\gamma_o d = 2.5$, $R_p = 0.5$, $R_m = 0.95$, $\alpha d = 0.15$.
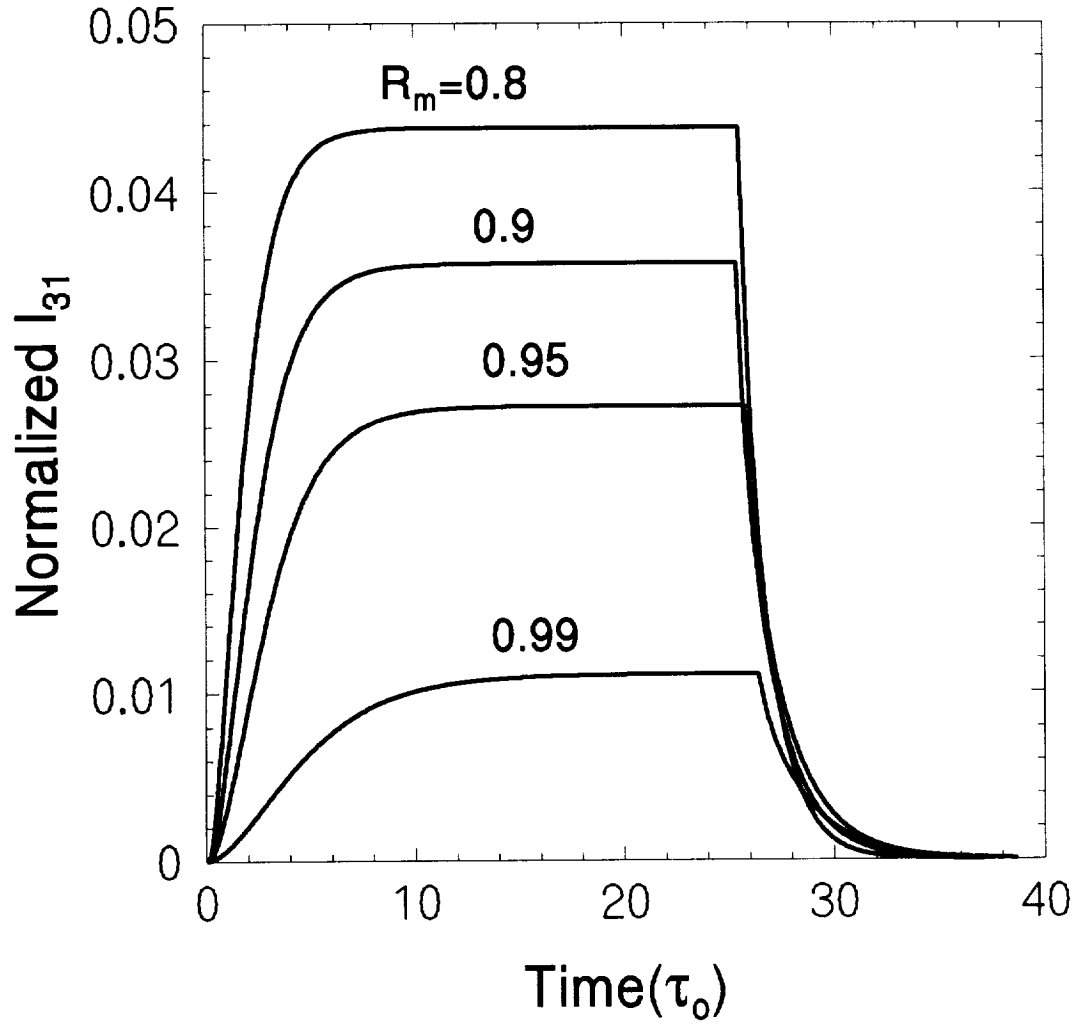
Figure 3.4: Normalized cavity field intensity $I_{31}/(I_1 + I_2)$ showing the response of the PCR to a square pulse input for various values of the input mirror's reflectivity and $\gamma_o d = 2.0$, $R_p = 0.5$, $R_s = 0.1$, $\alpha d = 0.15$.
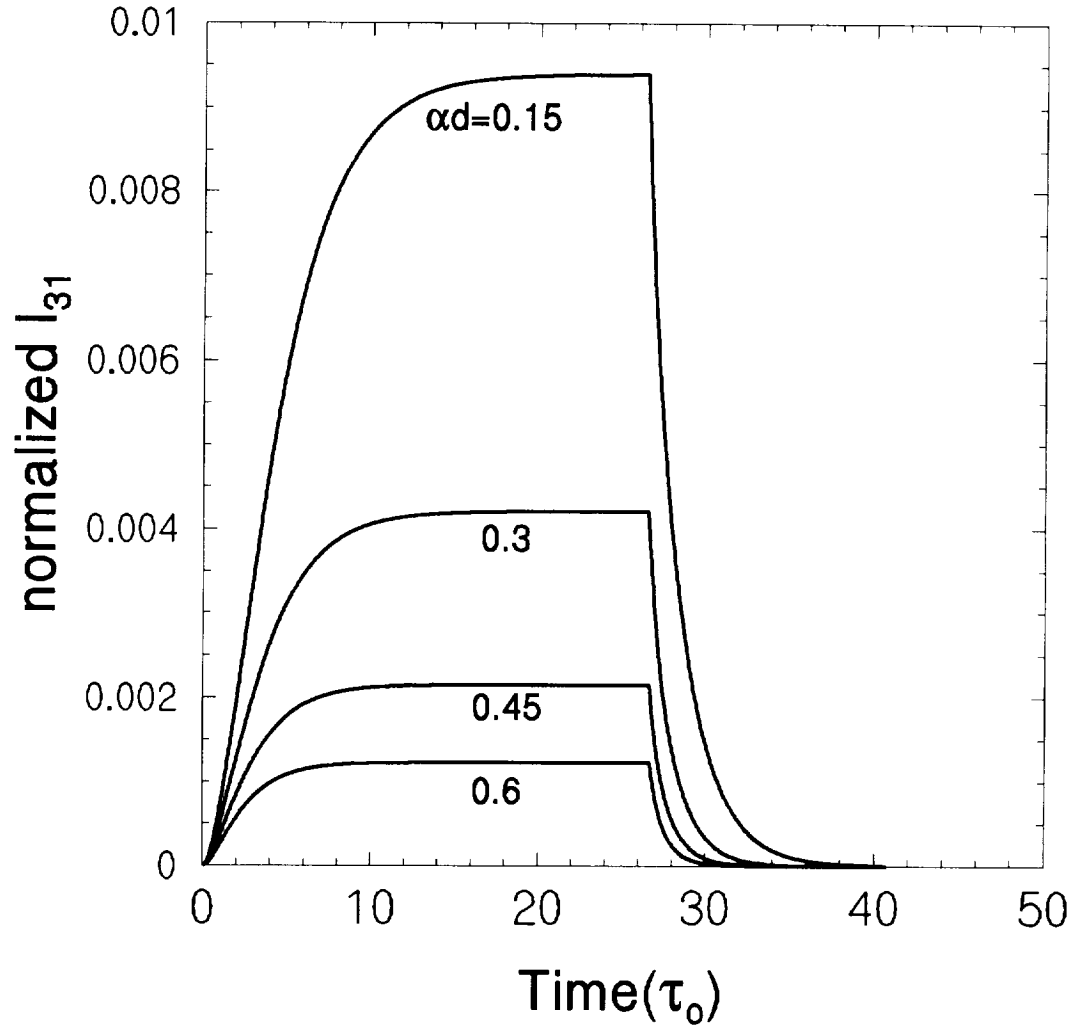
Figure 3.5: Normalized cavity field intensity $I_{31}/(I_1 + I_2)$ showing the response of the PCR to a square pulse input for various values of the medium's absorption parameter and $\gamma_o d = 2.0$, $R_p = 0.5$, $R_s = 0.02$, $R_m = 0.95$.

47

reflectivity, since this brings the cavity closer to threshold.

Figure 3.5 shows the response for different values of the absorption parameter. Increasing the absorption losses reduces the cavity field amplitude, everything else being equal. Here, $\gamma_o d = 2$, $R_p = 0.5$, $R_s = 0.02$, and $R_m = 0.95$. The buildup and decay rates also drop with increasing absorption.

Most of the response curves shown in figures (3.1–3.5) exhibit smooth and monotonic growth to steady state and monotonic decays. With large coupling constant and especially if the resonator is far above threshold, overshooting and damped oscillations can also be seen.

3.2.2 Cavity response time

The cavity buildup and decay times were measured from a large number of plots similar to those shown in figures (3.1–3.5). These times were then plotted as functions of the pump ratio and the probe ratio, which ratios appear to be the two most important parameters in determing the system's behavior.

Since some of the buildup curves exhibit overshooting for large $\gamma_o d$, the buildup time was defined as the time it takes for the cavity intensity to grow from 10% to 90% of its maximum (which is not necessarily the steady state in case of overshooting). The decay time was defined as the time it takes for the cavity intensity to drop from 90% to 10% of its steady state value.

Figures 3.6 and 3.7 show the buildup and the decay times, respectively, as functions of the pump ratio for (a) $R_m = 0.8$, (b) $R_m = 0.95$ and $R_s = 0.1$. For weak coupling, the buildup time increases with increasing pump ratios for small R_p, reaches a maximum and drops for larger R_p. This can be correlated with the behavior of the PCM reflectivity and the cavity field intensity which follow similar trends with varying R_p, as seen in figures 2.4 and 3.2. For stronger coupling, there is a range of values of R_p within which the cavity is above threshold. In this region, the initial gain of the cavity is large (larger than the losses) and the transient buildup is fast, sometimes
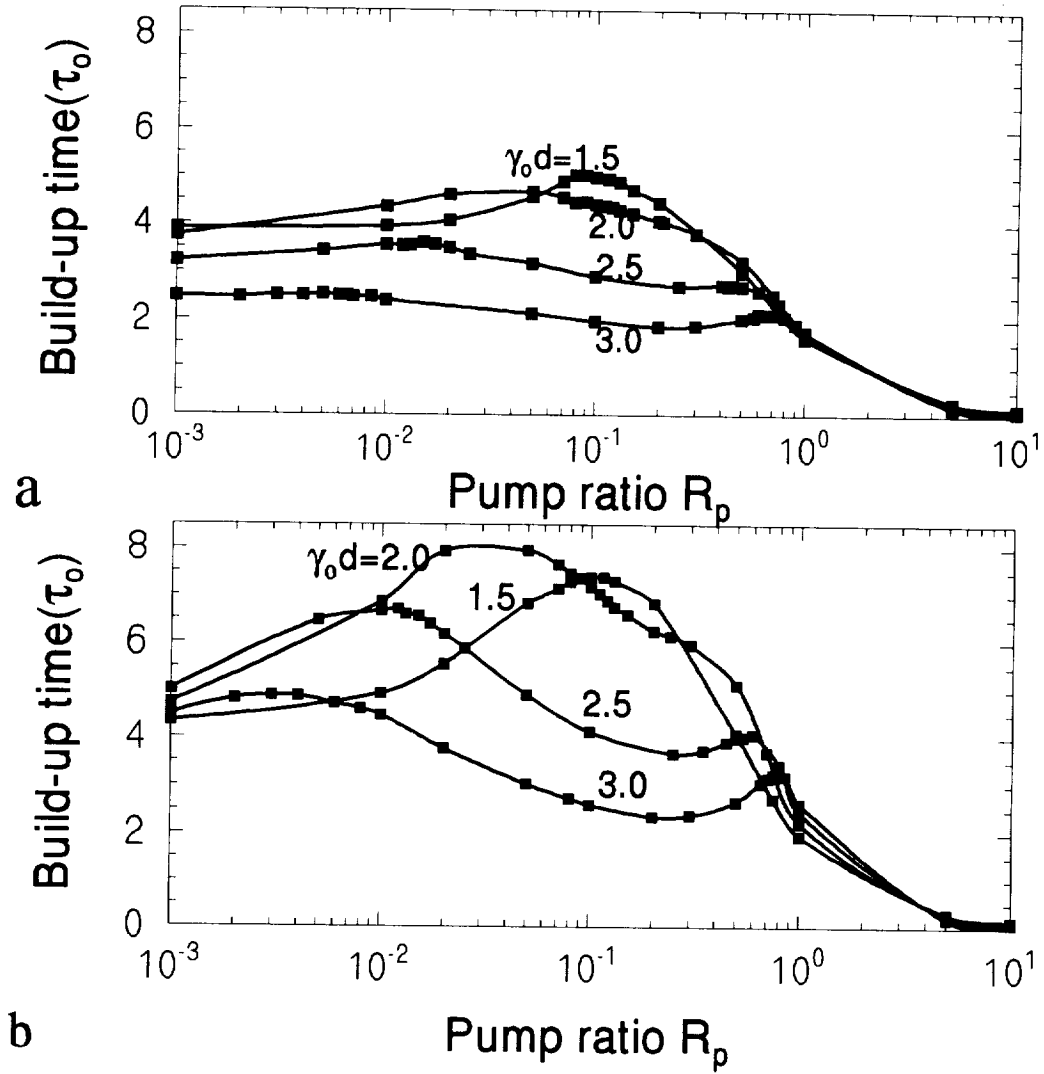
Figure 3.6: **a** Buildup time versus pump ratio for various values of the coupling parameter and $R_m = 0.8$, $R_s = 0.1$, $\alpha d = 0.15$. For $\gamma_o d \geq 2.5$, the cavity is above threshold for a range of values of the pump ratio around 10^{-1}. **b** Same as figure 3.6a except that $R_m = 0.95$.

exhibiting overshooting. This explains the central dip in the curves (figure 3.6) for $\gamma_o d > 2$.

In figure 3.7, the decay time is plotted as a function of the pump ratio. The divergence of the decay time as threshold is approached is clearly shown. The pump ratios at which divergence occurs correspond to the ratios at which the feedback parameter β reaches unity in figure 2.5.

Figures 3.8 and 3.9 show respectively the buildup time and the decay time as functions of the probe ratio for various values of the pump ratio and for $\gamma_o d = 2.5$, $R_m = 0.95$, $\alpha d = 0.15$. For these values of parameters, the resonator is above threshold for pump ratios ranging from about 0.02 to 0.5. Far below threshold ($R_p \sim 1$), figure 3.8 shows that the buildup time does not change much for a wide range of probe ratios. As one approaches threshold ($R_p \approx 0.01$ and 0.55), the buildup time varies significantly with the probe ratio especially for small probe beam intensity. Figure 3.9 shows a similar behavior for the decay time. Below threshold, the decay time does not change with the probe ratio while close to threshold, it varies significantly with that parameter. This may bear some important consequences in applications making use of the cavity for image storage or processing. If a large dynamic range input is imaged in the PCM, the weaker parts of the input will take considerably more time to buildup and to decay than the more intense parts, giving rise to contrast enhancement during buildup and contrast reduction during decay. The phenomenon could also be used to produce momentary time varying spatial filtering if the input spatial spectrum rather than the input itself is projected in the PCM.

To simulate the buildup of self-oscillation in a cavity above threshold, we calculated the cavity response to a very weak input pulse of short duration. In the physical system, this type of seed is provided by scattered noise. The result is shown in figure 3.10. In figure 3.10a, the cavity is below threshold. A very weak phase conjugate beam appears and remains in the cavity as long as the seed is present. It then rapidly decays when the seed is removed. In figure 3.10b, the cavity is above threshold. The cavity field remains in the cavity even after the seed is removed and it grows very slowly (note the different intensity and time scales of figure 3.10a and b). After a
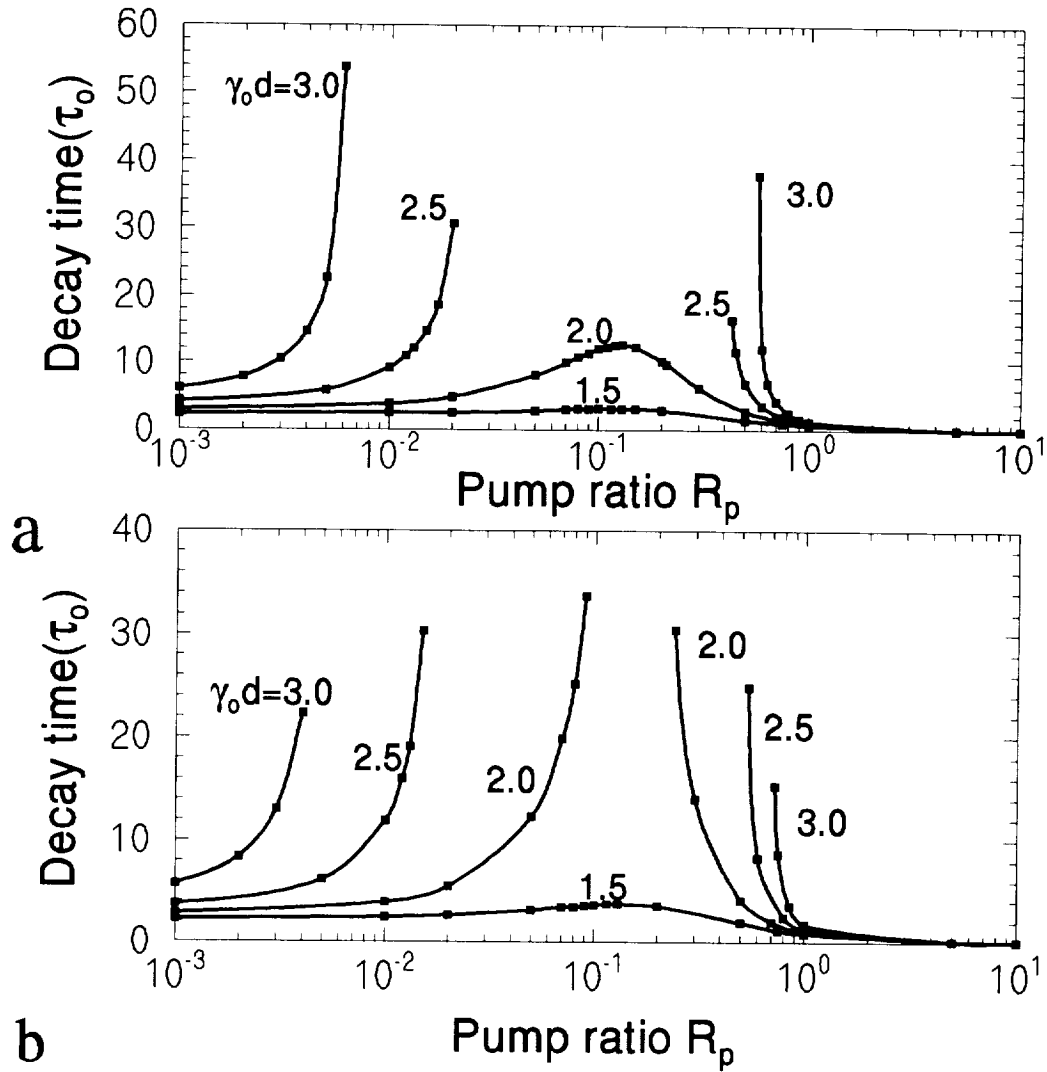
Figure 3.7: **a** Decay time versus pump ratio for various values of the coupling parameter showing the range of values of pump ratio for which the cavity is above threshold. The parameter values are the same as for figure 3.6a ($R_m = 0.8$). **b** Same as figure 3.7a but for the same parameter values as for figure 3.6b ($R_m = 0.95$).
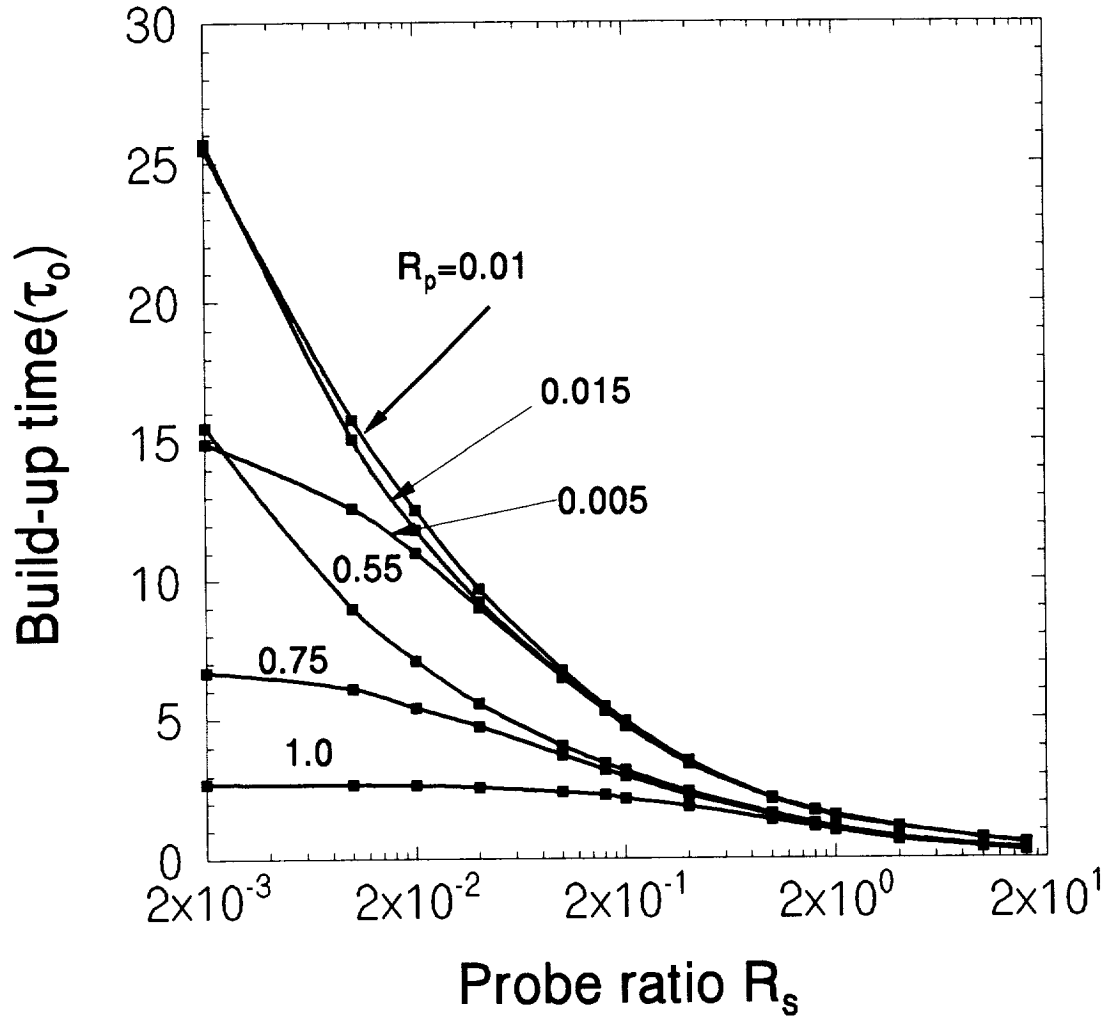
Figure 3.8: Buildup time versus probe ratio for various values of the pump ratio and $\gamma_o d = 2.5$, $\alpha d = 0.15$, $R_m = 0.95$.
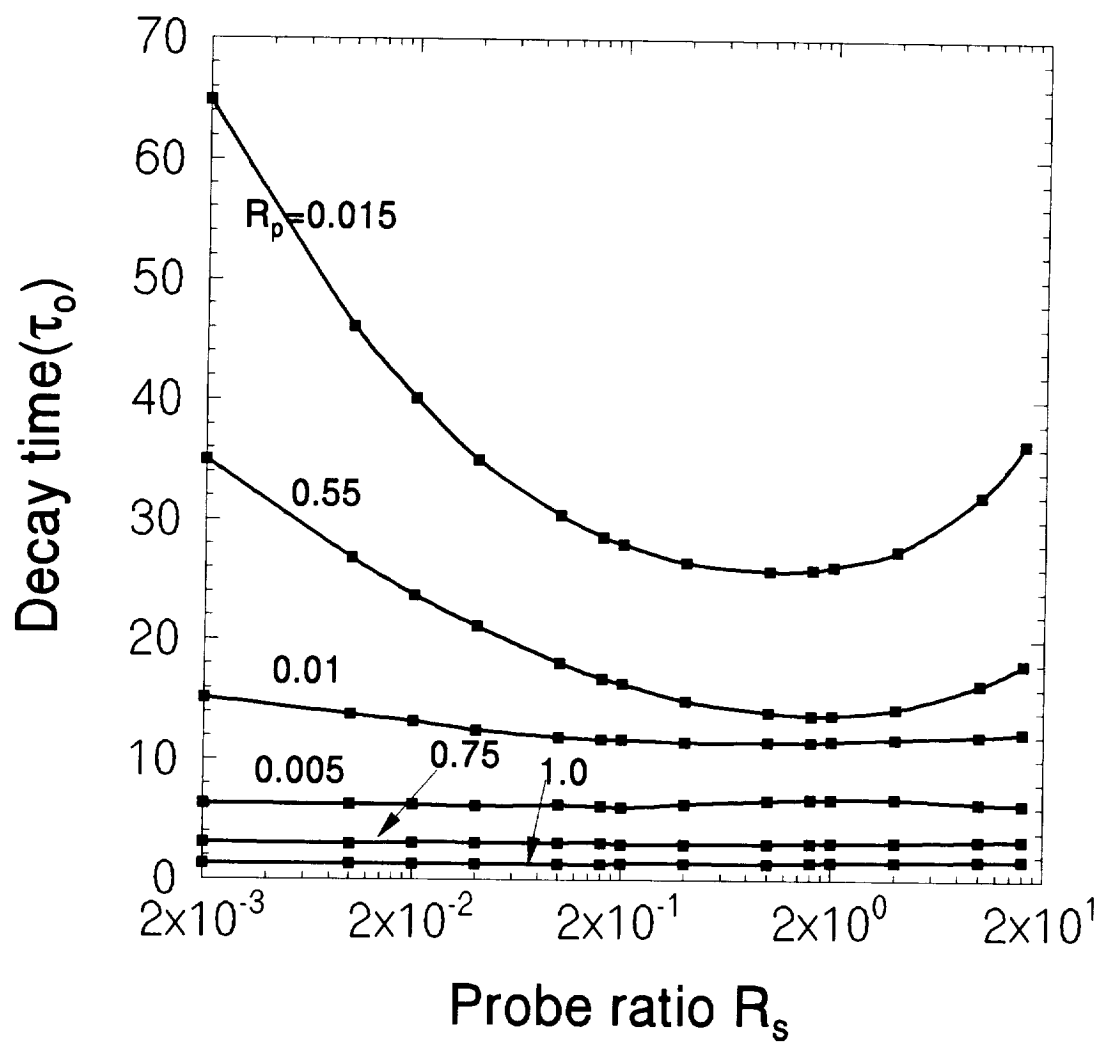
Figure 3.9: Decay time versus probe ratio for various values of the pump ratio and the same parameter values as for figure 3.8.

relatively long time, the cavity field builds up more rapidly to a final steady state value.

3.2.3 Specular and conjugate reflections

We now use the numerical method described in the preceding sections to investigate the temporal response of the two reflected outputs, $I_R = |A_R|^2$ and $I_C = |A_C|^2$. Figures 3.11 and 3.12 show the two outputs normalized to the total pump intensity $I_1 + I_2$, as functions of time for a normalized input $R_s = 5 \times 10^{-3}$. The results of figure 3.11 correspond to a pump ratio of 0.5 and a modest coupling parameter $\gamma_o d = 2.5$. Three different values of the input mirror reflectance R_m were used (figures 3.11a–c). It is seen that with a smaller input mirror reflectance, the total PCM steady state reflectivity product $|\mu_1 \mu_2|$ increases, approaching unity. Consequently, the steady state specular reflection almost drops to zero, leaving only the phase conjugate reflected wave counter propagating to the input beam.

With a higher coupling parameter (figure 3.12), the PCM steady state reflectivity exceeds unity. In this case (figure 3.12a) the specular reflection is seen to drop to zero and then to settle at a finite steady state value which is small compared to the conjugate reflection. The situation is that of a cavity which is not too far from threshold. Similar temporal conjugate reflection was reported in [49] for a PCM having an instantaneous response and a fixed reflectivity. Decreasing the input mirror reflectance again increases the PCM reflectivity, bringing the cavity above threshold (figure 3.12b). In this case, the specular reflection drops to zero and then grows to a large steady state value.

3.3 Experimental results

An experimental setup was built to study the temporal response of the PCR as a function of the pump ratio, the probe ratio and other parameters. Measurements of
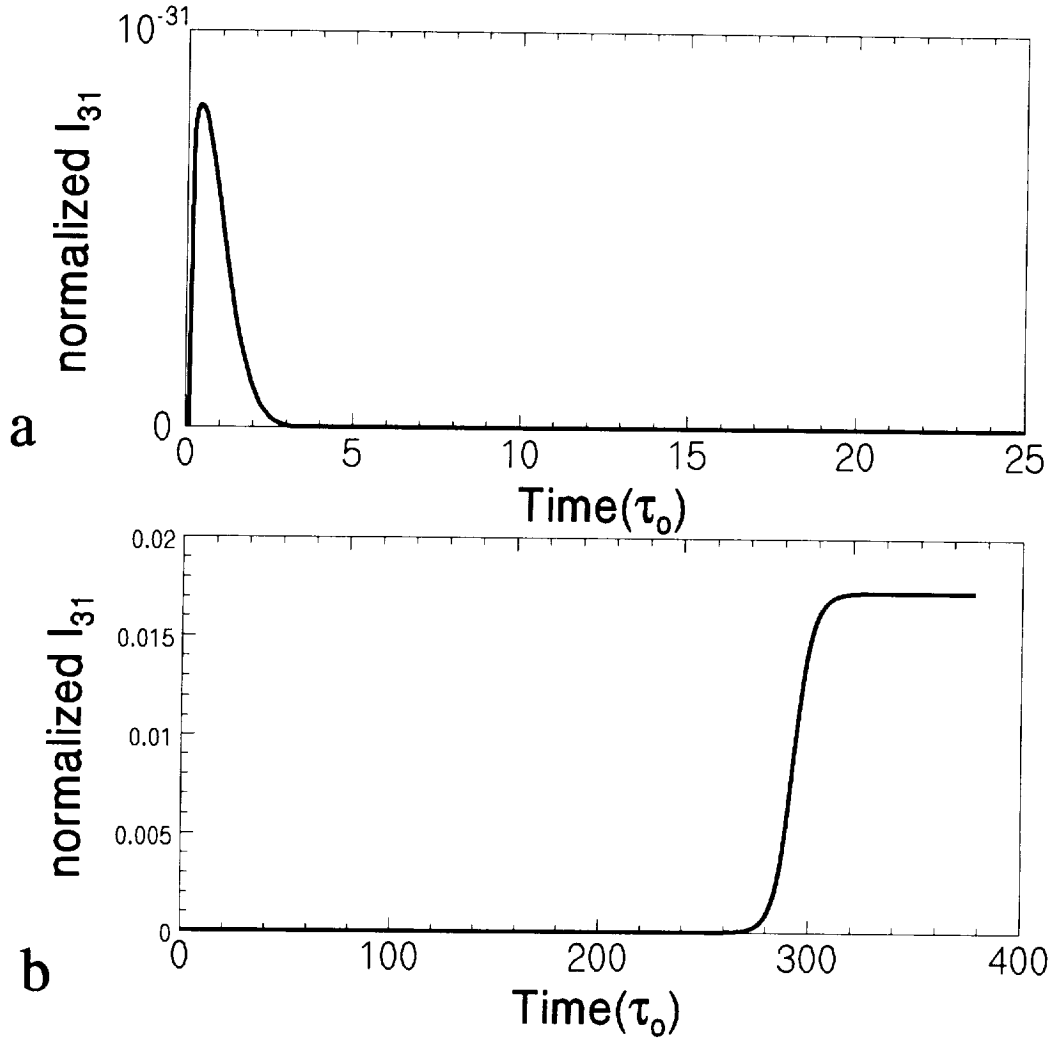
Figure 3.10: Response of the PCR to a short seed pulse of intensity corresponding to $R_s = 10^{-24}$. Normalized cavity field I_{31} versus normalized time for $R_p = 0.1$, $R_m = 0.95$, $\alpha d = 0.15$. **a** Cavity below threshold with $\gamma_o d = 2.0$; **b** Cavity above threshold with $\gamma_o d = 2.2$. (Note the different scales).
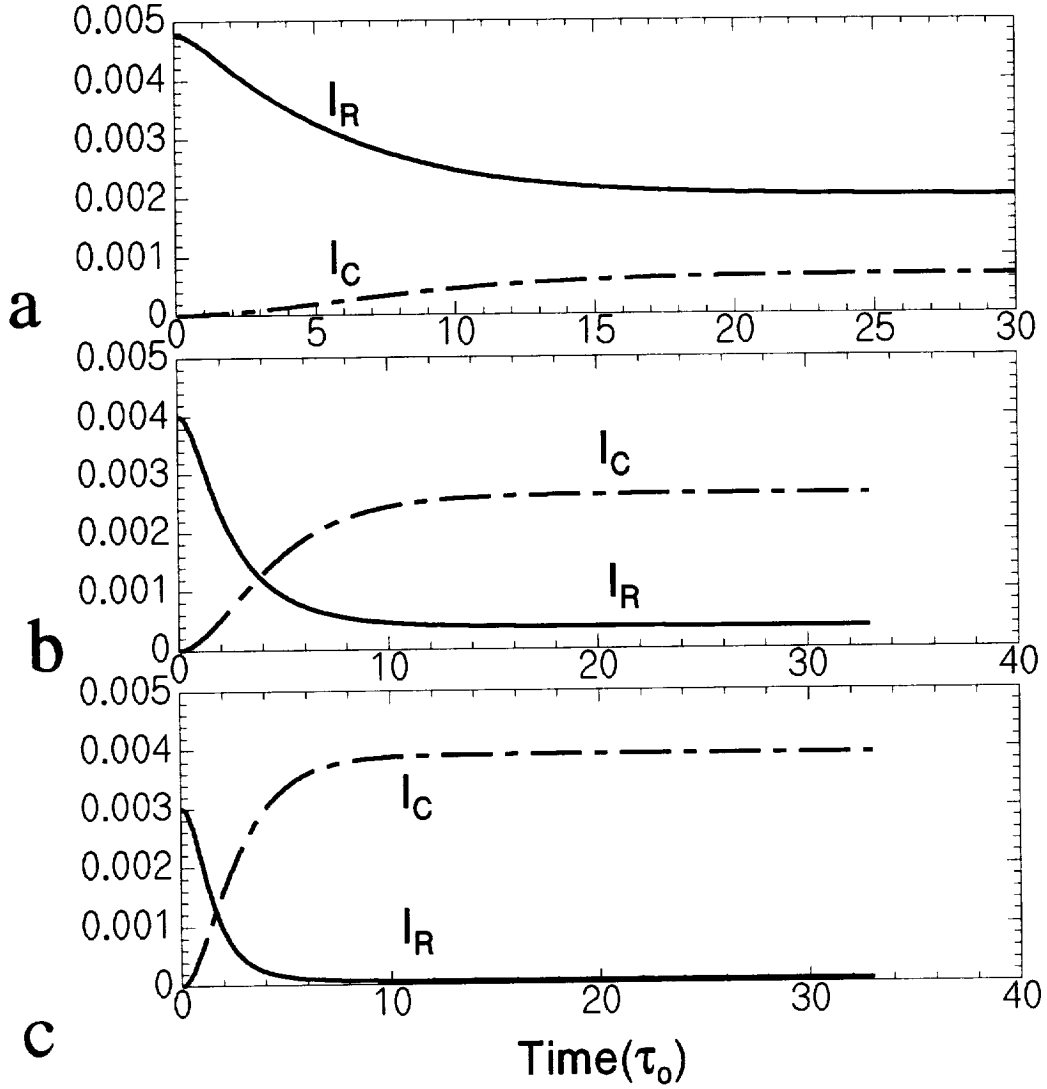
Figure 3.11: Time evolution of the normalized intensity of the specular $I_R/(I_1 + I_2)$ and conjugate $I_C/(I_1 + I_2)$ reflection with a constant normalized input of $R_s = 0.005$, $R_p = 0.5$, $\gamma_o d = 3.0$. **a**, $R_m = 0.95$ resulting in a steady state PCM reflectivity product $|\mu_1\mu_2| = 0.915$; **b**, $R_m = 0.8$, $|\mu_1\mu_2| = 0.921$; **c**, $R_m = 0.6$, $|\mu_1\mu_2| = 0.939$.
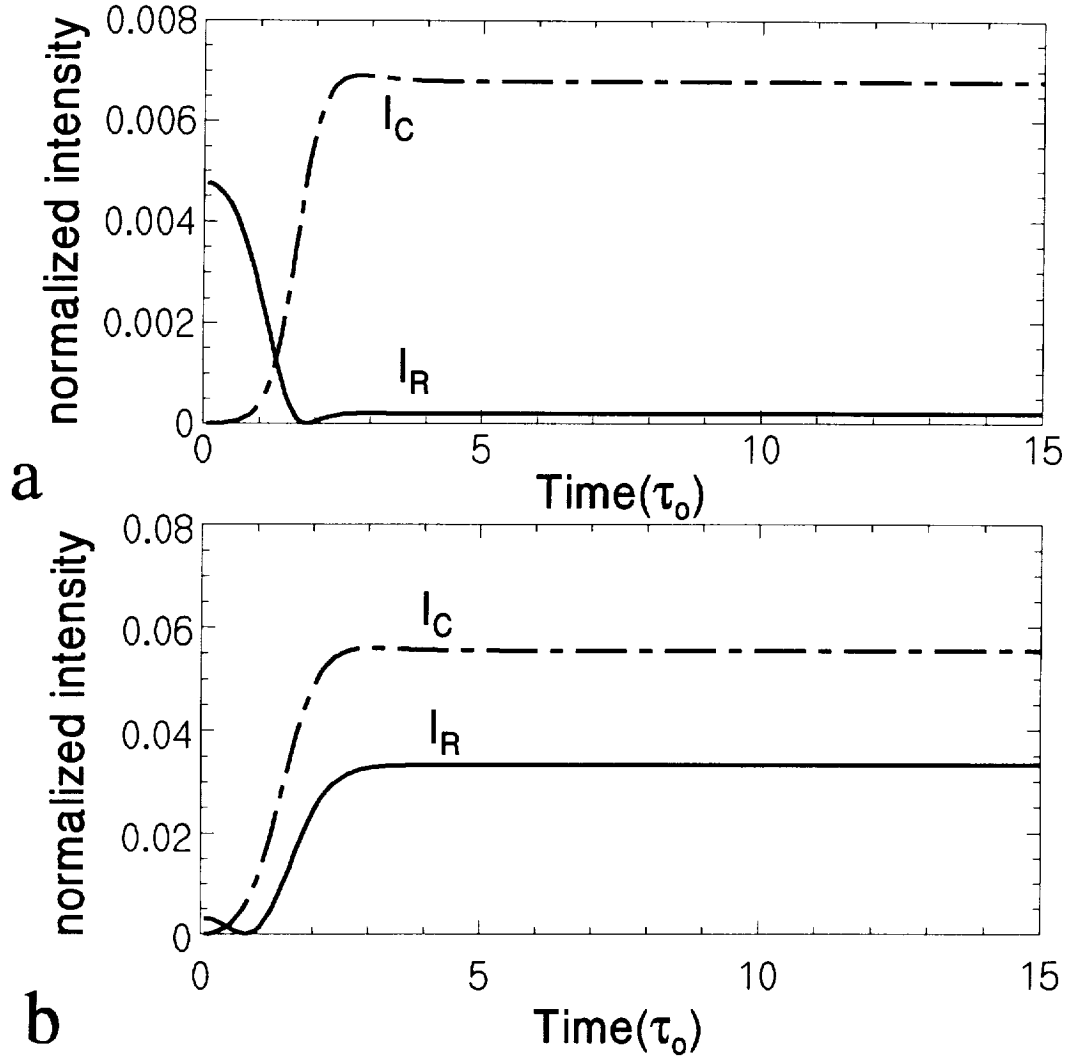
Figure 3.12: Same as figure 3.11 with larger coupling parameter $\gamma_o d = 6.0$. **a** $R_m = 0.95$ resulting in $|\mu_1\mu_2| = 1.008$; **b** $R_m = 0.6$, resulting in $|\mu_1\mu_2| = 1.444$ which brings the cavity above the threshold.

the cavity's response times are described and compared, qualitatively, with theoretical predictions in this section.

3.3.1 Experimental setup

A diagram of the experimental setup is shown in figure 3.13. The PCM is an externally pumped single crystal of $BaTiO_3$. The laser is a single mode Ar^+, operating at $\lambda = 514nm$. The two pump beams and the input beam are each equipped with a halfwave plate/polarizer assembly used as a variable attenuator. All polarizations are extraordinary (in the plane of the figure). The pump and the probe beams made angles of about 49° and 15°, respectively, with the normal to the crystal surface. The input mirror (dielectric) had a reflectivity of 95%. It made a small angle with the input beam in order to produce two distinct interaction regions in the crystal.

The phase conjugate cavity beam was extracted from the cavity by a pellicle beam splitter *PBS* having about 5% reflectance. The lens *Le* reimaged the interaction regions in the plane of a slit which was positioned to select the cavity beam I_{31} and isolate it from the other beam I_{32}. The beam intensity I_{31} was measured by a photodetector, recorded and stored in a PC. A shutter was used to turn the input on and off and produce a square pulse, as in the simulation.

3.3.2 Measurement of the cavity response time

Two sets of data were collected – the first for as high a coupling constant as we could achieve with this particular geometry and the other for a lower coupling constant, spoiled by rotating the crystal by a few degrees. In both cases, the response to the input pulse was recorded and the buildup time and the decay time were estimated from the curve. A typical experimental record of the cavity field intensity I_{31} is shown in figure 3.14.

The results are shown in figures (3.15–3.18). The error bars in these figures are qualitative and are intended only to give an indication of the level of confidence
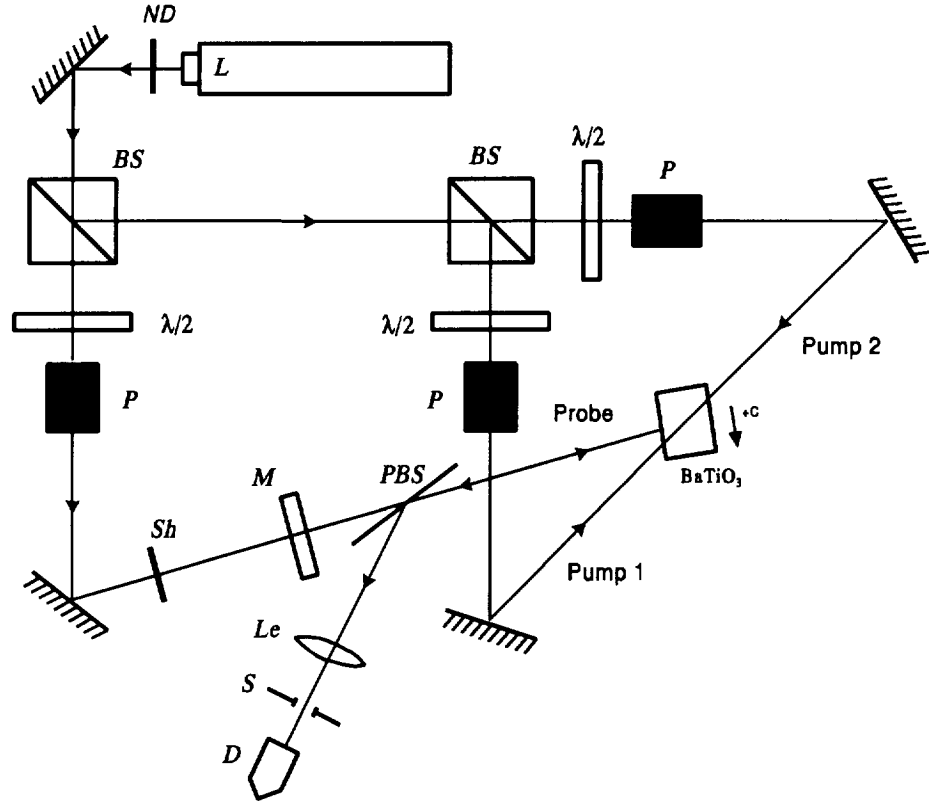
Figure 3.13: Diagram of the experimental setup. L: Ar$^+$ laser (514nm), $\lambda/2$-P: halfwave plate/polarizer assembly, Sh: shutter, M: 95% dielectric mirror, PBS: pellicle beam splitter, Le: imaging lens, S: slit, D: photodetector.
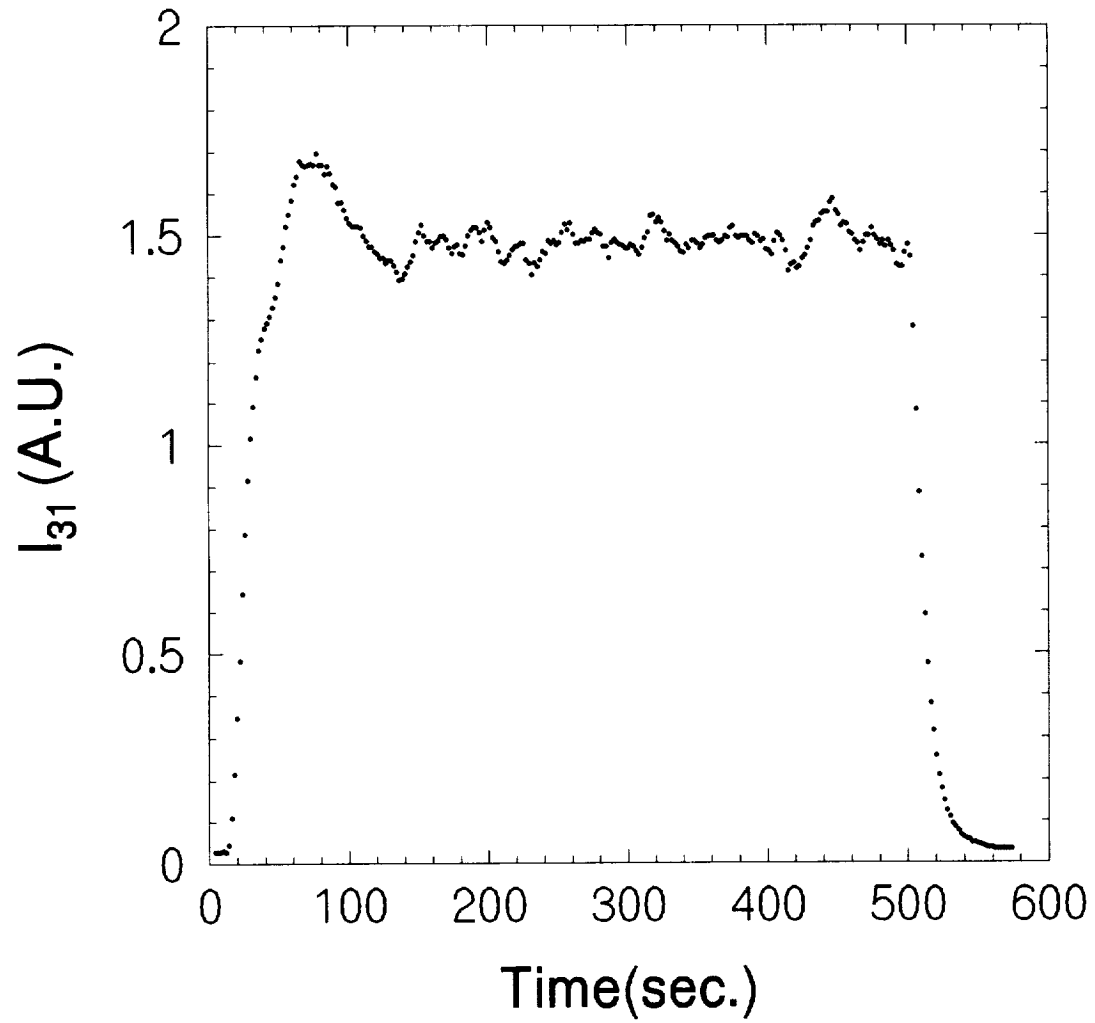
Figure 3.14: Typical cavity field response to a square pulse input from which the buildup and decay times were measured.

that was attributed to the eyeball estimation of the characteristic times from the response curves. Some data were noiser than others and thus were assigned larger error bars. The lines are visual aids. Above threshold, the PCR response often exhibits overshooting and sometimes damped oscillations. This made it more difficult to measure the characteristic times, and larger errors are expected as threshold is approached.

There were many other possible sources of errors more difficult to quantify. For example, close to threshold the system is extremely sensitive to any external perturbation. In this region, small mechanical or acoustical perturbations can give rise to large differences in the PCR transient response.

Figure 3.15 shows the buildup time as a function of the pump ratio. Pump I_1 was maintained constant at 0.5mW with a beam diameter of about 1mm inside the crystal, and pump I_2 was varied. The probe ratio was $R_s = 0.02$. The general behavior is qualitatively similar to that of figure 3.6 obtained from the simulation. At low pump ratios, the buildup time increases with R_p and with the coupling parameter. It reaches a maximum for $0.1 < R_p < 0.2$ and then drops. At high pump ratios, the buildup time is nearly independent of the coupling parameter. The two lower data points near the center of the high coupling curve are dubious. They could represent the drop of the buildup time predicted in figure 3.6 above threshold or their lower value could be due to some external perturbations giving rise to large errors near threshold.

Figure 3.16 shows the decay time as a function of the pump ratio. This also is qualitatively similar to the result of the simulation shown in figure 3.7. By comparing the range of pump ratios within which the experimental PCR is above threshold with the curves of figure 3.7b, which corresponds to the same values of parameters, one can estimate that the coupling parameter achieved in the experiment was of the order of $\gamma_o d \sim 2$.

Figures 3.17 and 3.18 show the buildup and decay times, respectively, as functions of the probe ratio for $\gamma_o d \sim 2$, $R_p \sim 1$. The buildup time decreases monotonically with R_s in a manner quite similiar to that shown in figure 3.8. The decay time
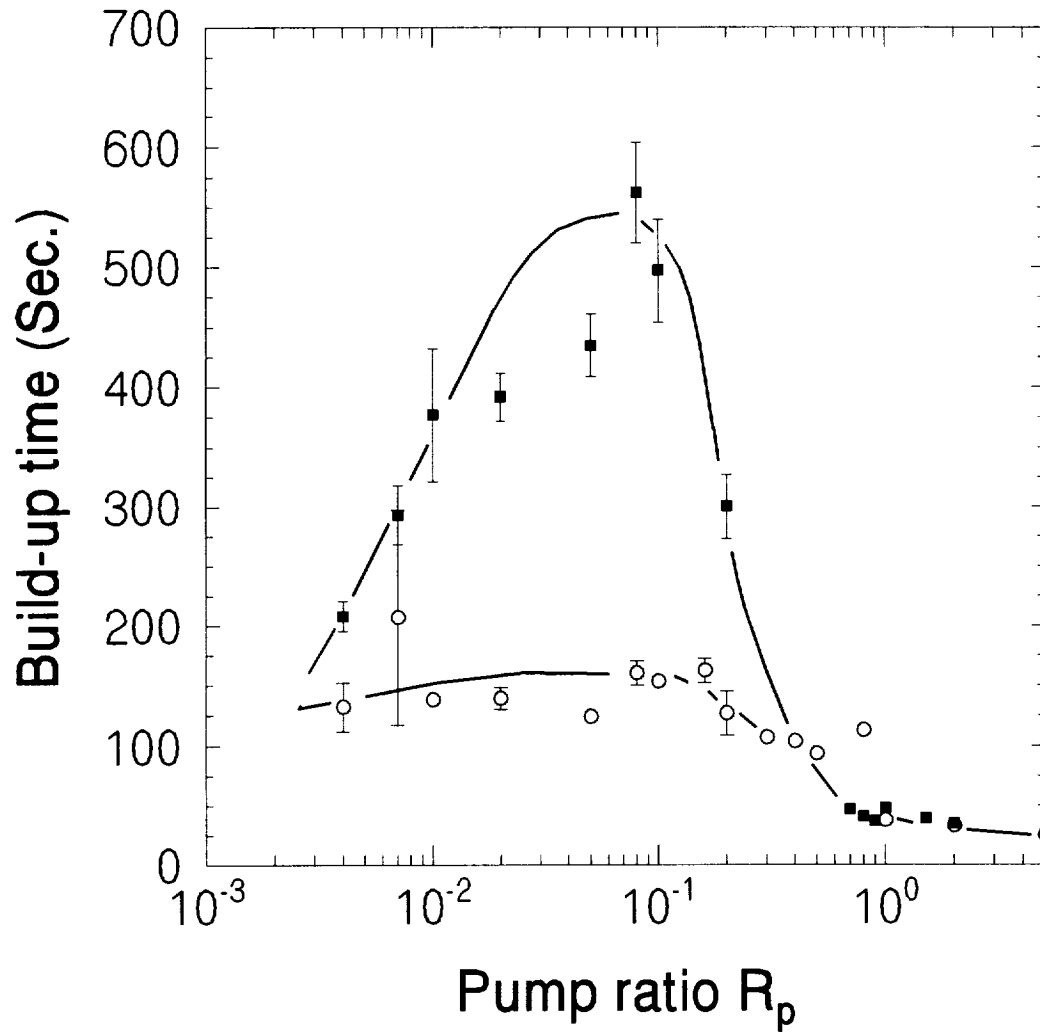
Figure 3.15: Experimental buildup time versus pump ratio for two values of the coupling parameter and $R_m = 0.95$, $R_s = 0.02$. The error bars only indicate the level of confidence to be given to different data points. The solid lines are for visual aid. (The circles are data points for a low coupling parameter; the squares are data points for a high coupling parameter)
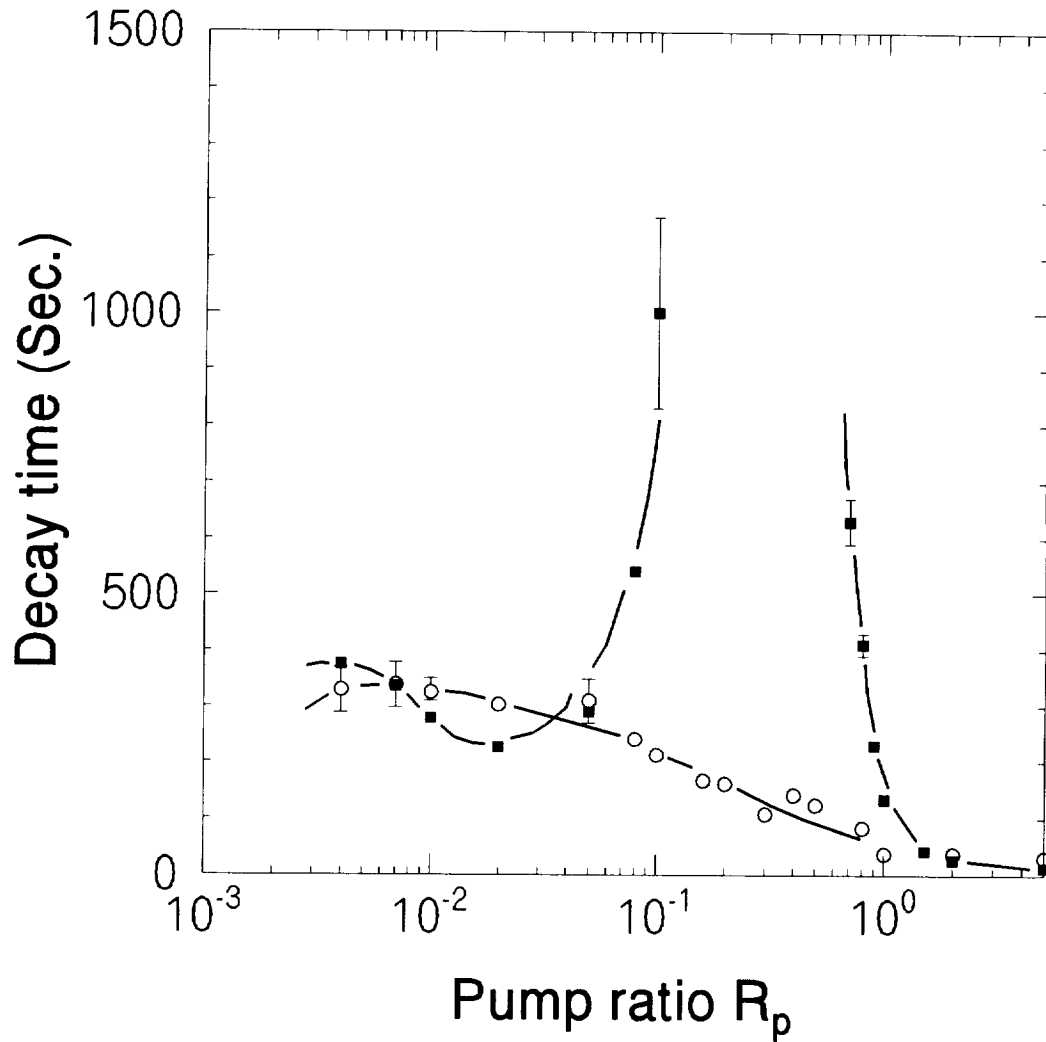
Figure 3.16: Experimental decay time versus pump ratio for two values of the coupling parameter and $R_m = 0.95$, $R_s = 0.02$. (The circles are data points for a low coupling parameters; the squares are data points for a high coupling parameter)

behavior is also qualitatively similar to that shown in figure 3.9.

3.4 Conclusion

In this chapter we have presented a numerical scheme for integrating the photorefractive equations separately in the space and time domains using the adiabatic elimination process. With this numerical scheme, the transient dynamics of a PCR was described in the limit of a plane wave model and a sluggish photorefractive medium, but taking into account both the pump depletion and medium's absorption. The dependence of the cavity buildup and decay times on parameters such as the pump ratio, the probe ratio, the coupling parameter, the input mirror's reflectivity and the medium absorption constant were discussed. The numerical results show that the parameters affecting the threshold most directly are the coupling parameter and the pump ratio. We find that the higher the coupling parameter, the wider the range of pump ratio values for which the PCR is above threshold. Results also indicate that the cavity buildup and decay times can be tailored by varying several of the system parameters. This may be of importance to image processing applications. For example, the PCR would, in principle, perform contrast enhancement during buildup and contrast reduction during decay. This same feature could be used to implement a time varying spatial filter if the projected field in the PCM is the spatial spectrum of an image rather than the input image itself.

The numerical simulations also reveal the unusual reflection property of a phase conjugate Fabry-Perot. For example, we find that when the steady state value of the phase conjugate reflectivity approaches unity, the specular reflection is completely extinguished, leaving only the phase conjugate reflection output.

An experimental setup was built to study the transients in a PCR and the experimental results are in general qualitative agreement with the results of the numerical simulations. In real situations, the material's parameter values may vary considerably between crystals. In our case, the parameter values for the $BaTiO_3$ crystal are chosen from the literature [53]. Futhermore, it seems likely that quantitative agreement
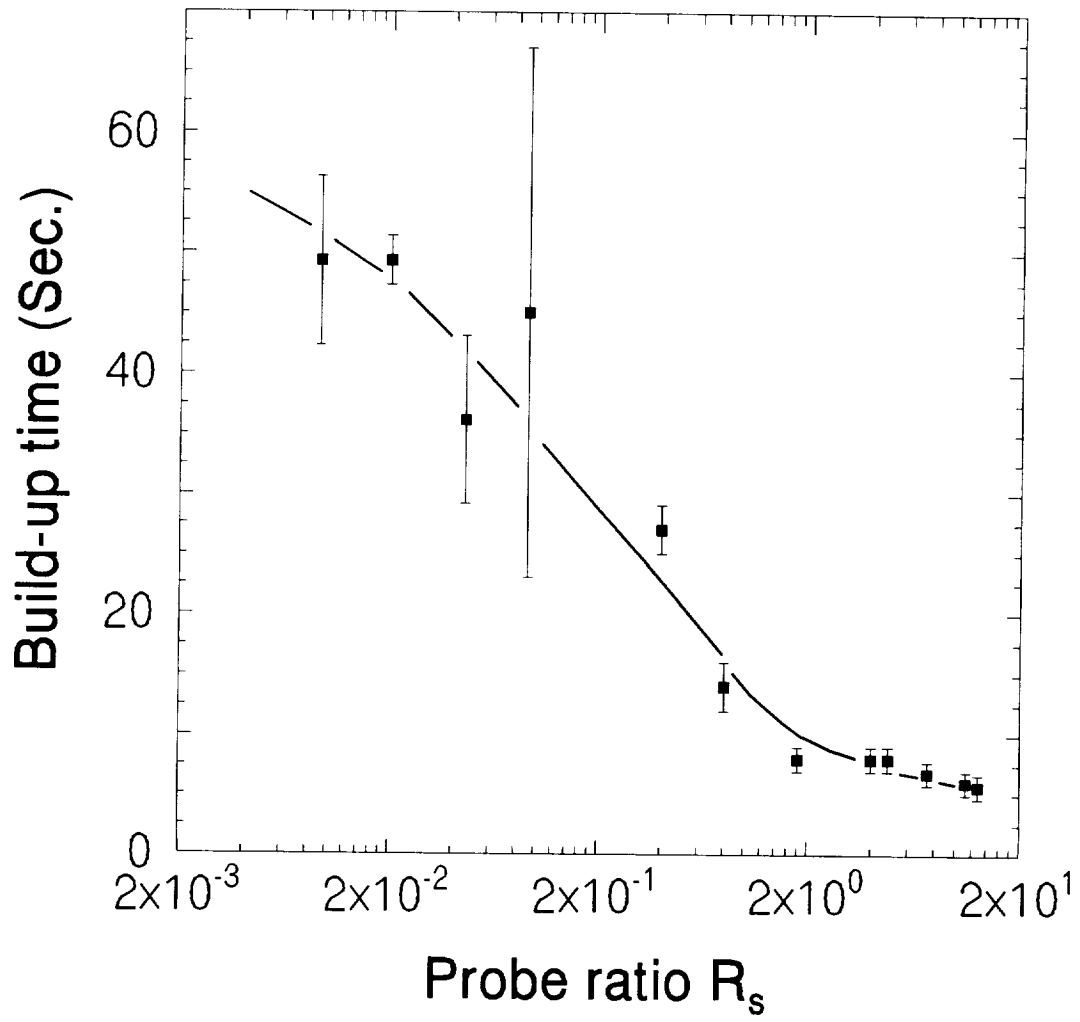
Figure 3.17: Experimental buildup time versus probe ratio for $R_p = 1$, $R_m = 0.95$.
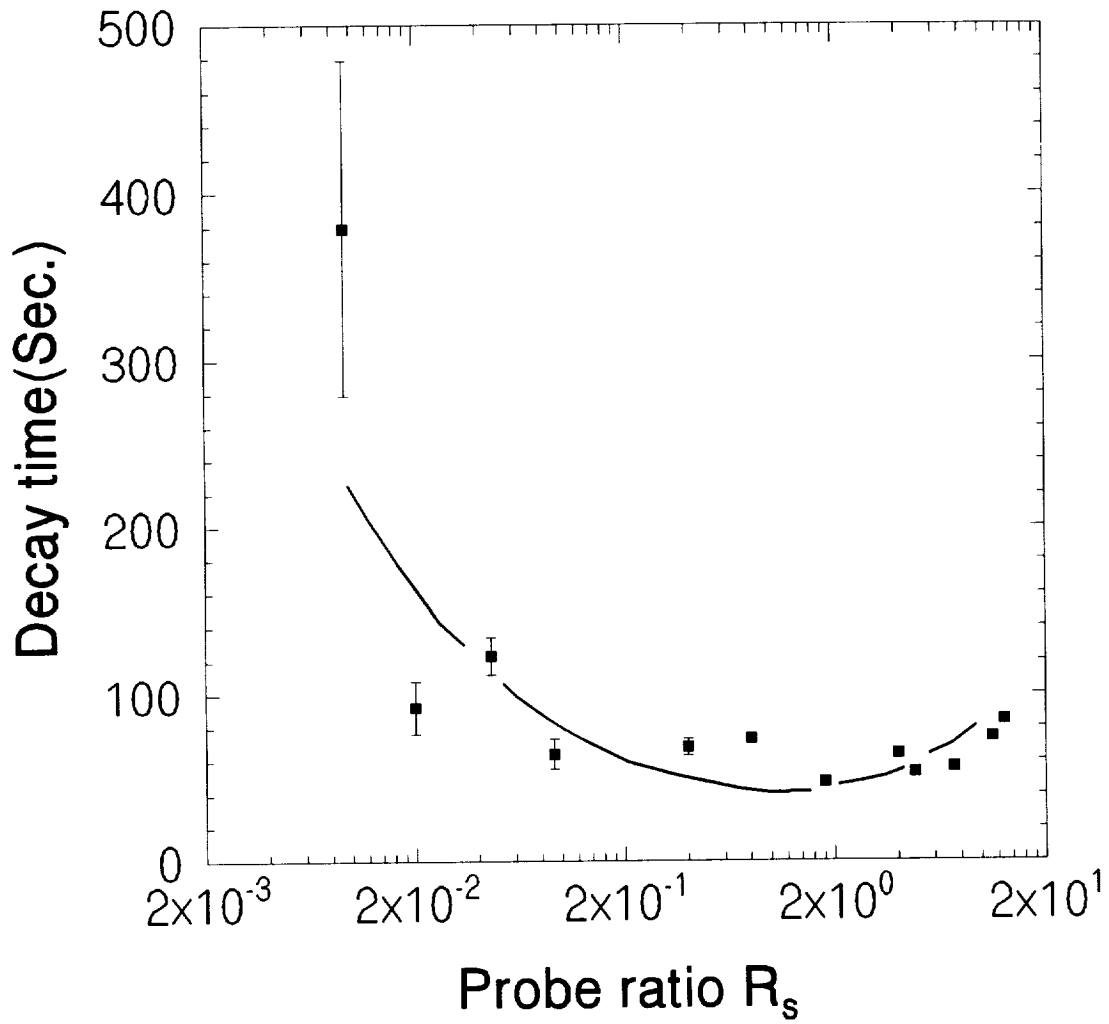
Figure 3.18: Experimental decay time versus probe ratio for $R_p = 1$, $R_m = 0.95$.

would require some refinement of the simplified Kukhtarev model by including, at least, multiple species of traps taking part in the photorefractive process.

Chapter 4

Temporal and spatial instabilities

So far we have demonstrated how the PCR below threshold responds to the temporal change of an input. In the remaining part of this thesis we will study another mode of operation of the PCR: emphasis will be given to the characterization of the spatial structure of the cavity beams above threshold. In this chapter, we first give a brief introduction to some of the terminology and methods of chaotic dynamics, which will be applied to the study of the spatiotemporal dynamics of the PCR above threshold in the following two chapters. The first part of this introduction will be devoted to chaos in nonlinear dynamics. This includes the discussion of qualitative methods in nonlinear dynamics such as the uses of power spectra, phase space portraits and the notion of attractors. Regarding the quantitative methods for the characterization of chaotic dynamics, we give a brief introduction to the notion of dimensions and to the calculation of the correlation integral function as well as the Kolmogorov entropy. We also describe a method used for the reconstruction of a pseudo phase space portrait from an experimental time series. In the second part, we will briefly mention some recent studies of spatial pattern evolutions and instabilities, which is currently an active area of investigation [56]. The discussion will focus on wavefront dislocations and optical vortices because they are found to appear in the PCR's beams and probably mediate the observed dynamics.

4.0.1 Nonlinear systems

In general, the dynamics of physical systems can be described by means of differential equations. In cases of nonlinear systems, the equations which govern their behaviors will contain nonlinear terms. Linearization of the nonlinear terms in some regions of parameter space where their effects are small often provides simple solutions and a sufficiently clear picture of the system's dynamics. A classic example of this is the simple pendulum in the small angle approximation. There are some nonlinear systems, however, where the nonlinear terms dominate in the physically interesting region of parameter space. In those cases, the linearization of the system's equations results in the loss of significant knowledge about the system's behavior. The variety of responses of nonlinear systems is often found to be much richer than that of linear systems, as illustrated in figure 4.1 for two systems driven by a sinusoidally varying input. The output of the linear system must also be sinusoidal, with the same frequency as the input. The output in the nonlinear system can be periodic (not necessary sinusoidal); or periodic with subharmonics with frequencies ω/n, where n is an integer. Another possibility is the occurrence of quasi-periodic motion with an output of the form $c_1 \cos(\omega_1 t) + c_2 \cos(\omega_2 t)$, where the ratio ω_1/ω_2 is an irrational number if ω_1 and ω_2 are incommensurate; or the output can be chaotic, fluctuating erratically in time.

Now, let us look at one example of nonlinear system which is at the origin of the science of chaos. Chaos was first discovered by E. N. Lorenz [58] in the early 1960s. Lorenz considered a rather typical problem of fluid dynamics which is called the convection instability or Rayleigh-Benard instability (his purpose was to analyze the motion of the atmosphere). The motion of the fluid is described by the Navier-Stokes equations which are nonlinear, partial differential equations. In order to cut down the complexity of the problem of solving these equations, Lorenz introduced a Fourier decomposition. He expanded the velocity and temperature fields of the fluid into spatial Fourier series. The Fourier coefficients were still time dependent variables. Lorenz truncated the infinite series to only three terms representing three
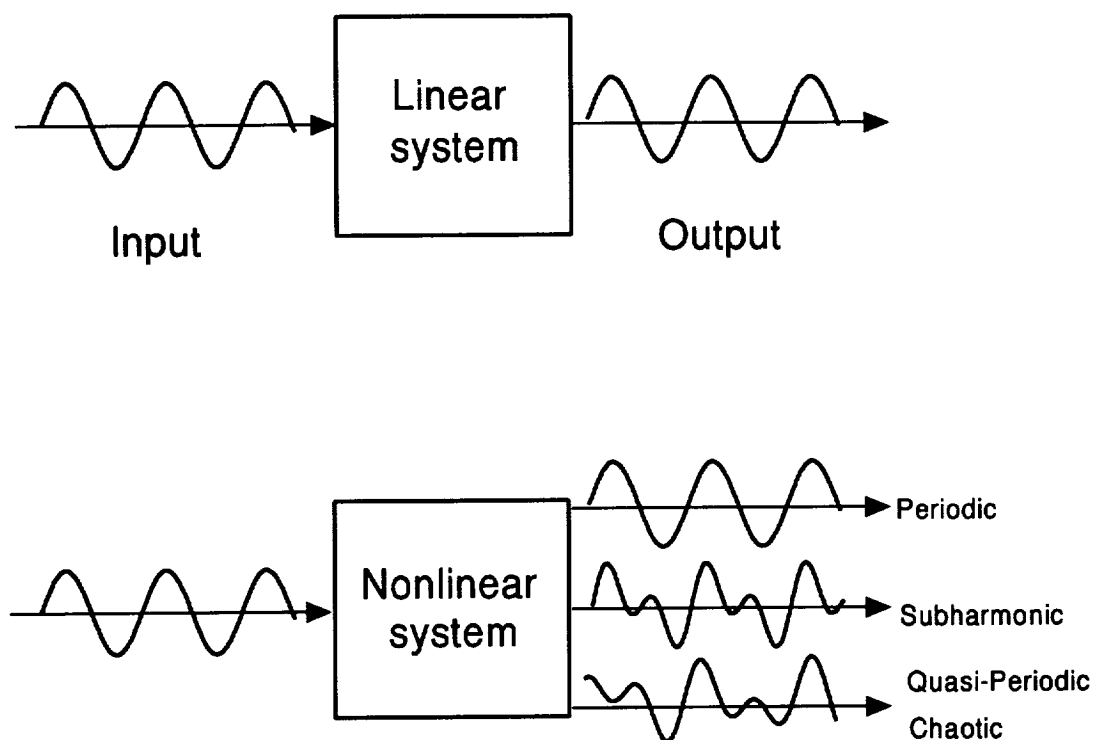
Figure 4.1: Schematic diagram showing the possible outputs of a linear and a non-linear system for a sinusoidal input. In a linear system, the output must be also sinusoidal. In a nonlinear system, the output can be either periodic, periodic with subharmonics, quasiperiodic or chaotic. (After [57])

individual modes to save computing effort while still keeping the important physics of the problem. In this way he derived three coupled differential equations for three variables. The equations of the Lorenz model are usually written in the following form:

$$\frac{dX}{dt} = \sigma(Y - X), \tag{4.1}$$

$$\frac{dY}{dt} = -XZ + rX - Y, \tag{4.2}$$

$$\frac{dZ}{dt} = XY - bZ. \tag{4.3}$$

X represents the amplitude of the fundamental velocity mode; Y represents the fundamental temperature mode and Z represents the temperature second harmonic. σ is the Prandtl number, $r \equiv R/R_c$ is the normalized Rayleigh number relative to the critical Rayleigh number R_c at which the onset of convection occurs, and $b = 4\pi^2/(\pi^2+k_1^2)$, where k_1 is a dimensionless wave number. The equations 4.1–4.3 are of quite simple structure. They are ordinary differential equations and contain only two nonlinear terms in XZ and XY. To the great surprise of many physicists and mathematicians, Lorenz found that the numerical solutions for some parameter values (e.g. $\sigma = 10$, $b = 8/3$, $r = 28$) can exhibit, in addition to stationary and periodic states, irregular behaviors. Figure 4.2 illustrates the rapid divergence, characteristic of chaotic behavior, of two solutions which start from initial conditions differing only by about 1 part in a thousand. Figure 4.3 shows the plots of X versus Y and X versus Z where the trajectories stay most of the time around certain zones although the trajectories are never closed.

4.1 Characterization of chaotic dynamics

4.1.1 Fourier spectra

One method of examining the dynamics of a nonlinear system is by Fourier spectral analysis. Consider the temporal behavior of a function $y(t)$. It is quasiperiodic if its
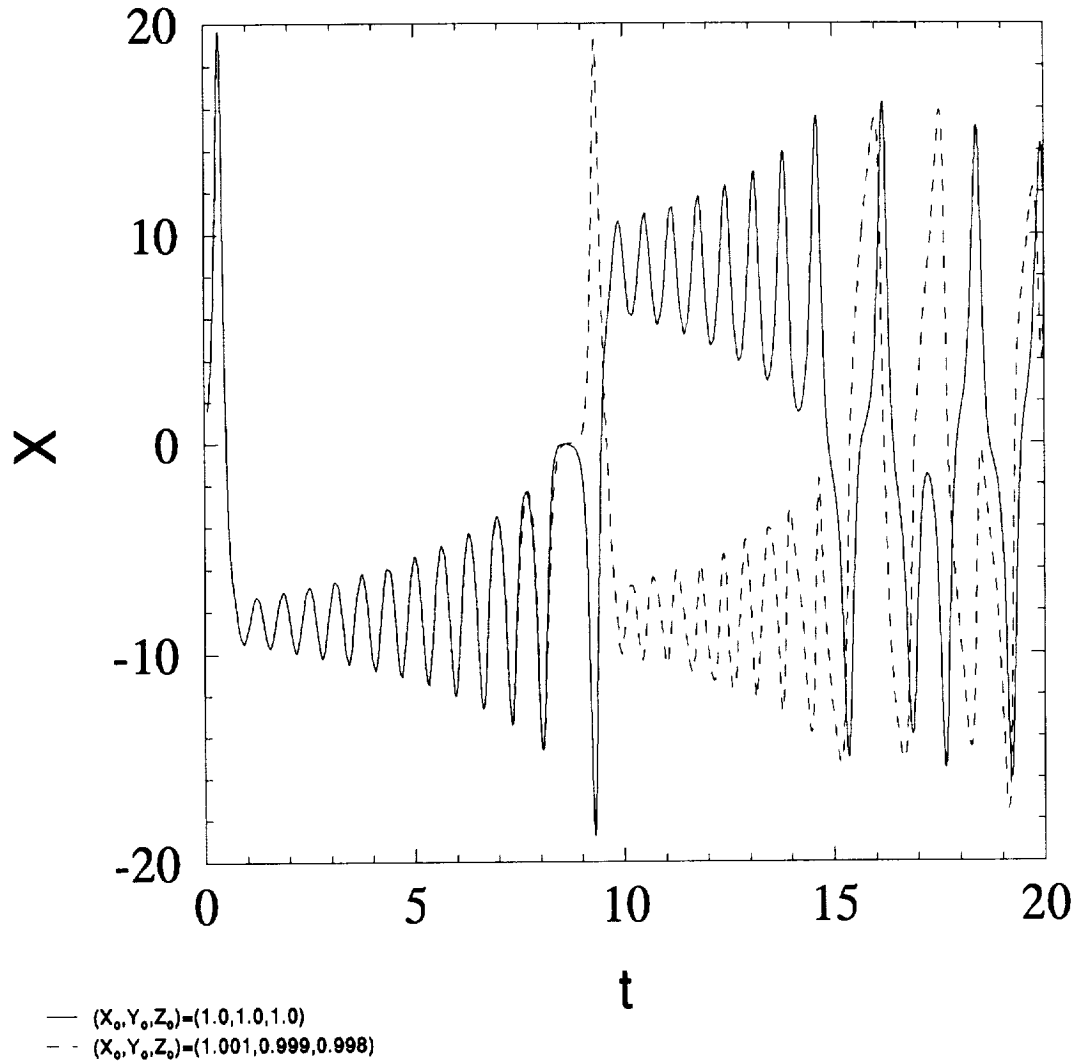
Figure 4.2: Graphs of chaotic fluctuations in time of the variable X of the Lorenz's convective equations. Values of parameters are: $\sigma = 10$, $b = 8/3$, and $r = 28$. This shows a chaotic solution very sensitive to initial conditions, i.e. two points which start out close can grow expontentially apart in time.
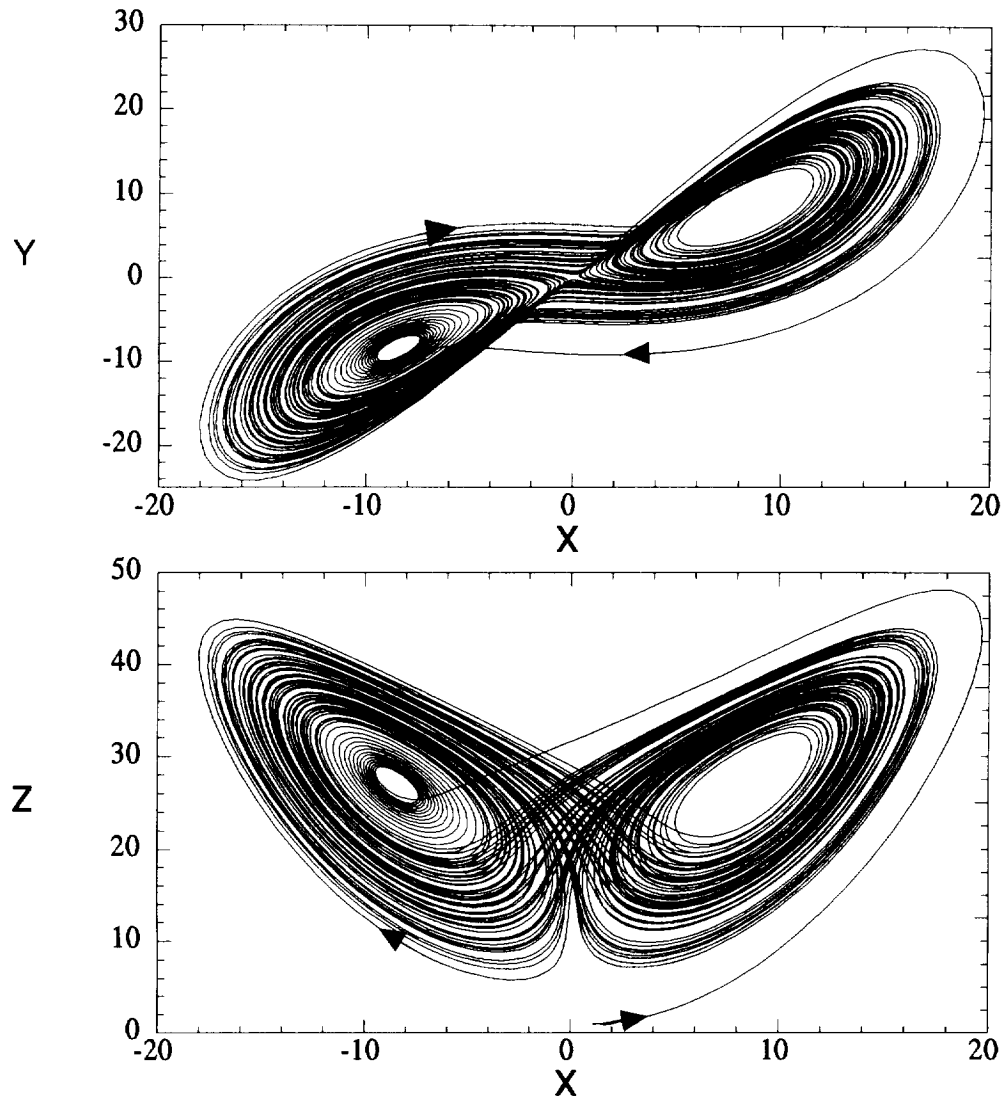
Figure 4.3: Trajectories of a chaotic solution of Lorenz's convective equations projected on the plane $X - Y$ (above) and on the plane $X - Z$ (below). The trajectories trace out certain regions of the planes although they are never closed. (Parameters' values are the same as in figure 4.2.)

Fourier transform consists of sharp spikes, i.e. if

$$y(t) = \sum_{j=1}^{n} c_j e^{i\omega_j t}. \tag{4.4}$$

The characteristic recurrence feature of quasiperiodicity may be stated formally as follows: for any $\epsilon > 0$ there exists a $T(\epsilon)$ such that any interval of length $T(\epsilon)$ of the real line contains at least one point t' such that $|y(t) - y(t')| < \epsilon$ for any t [59]. Given $y(t)$, we can always find a t' such that $y(t')$ is as close to $y(t)$ as we wish, and there are an infinite number of such times t'. Periodic functions are quasiperiodic, but of course quasiperiodicity does not imply periodicity. Thus the function

$$y(t) = c_1 \cos \omega_1 t + c_2 \cos \omega_2 t \tag{4.5}$$

is quasiperiodic, but it is not periodic unless ω_1 and ω_2 are commensurate frequencies, i.e. unless ω_1/ω_2 is a rational number.

Quasiperiodic motion can certainly look very complicated and irregular, but it cannot be truly chaotic in the sense of exponential sensitivity to initial conditions. In particular, the difference between two quasiperiodic trajectories is itself quasiperiodic, and so we cannot have the exponential separation of initially close trajectories that is the hallmark of chaos.

Since quasiperiodicity implies order, it follows that chaos implies non-quasiperiodic motions. Thus chaotic motion does not have a purely discrete Fourier spectrum as in 4.4, but must have a broadband, continuous component in its spectrum. Fourier analysis is therefore a very useful tool in distinguishing regular from chaotic motion.

Caution has to be taken here because a broadband spectrum can arise from stochastic behavior as well as from deterministic chaos. Additional analyses are therefore needed. For example, for a process governed by stochastic mechanisms, the spectral power at high frequencies follows a power law. In contrast, for a process governed by deterministic mechanisms, the power spectrum falls off exponentially [60]. Therefore, a linear behavior on the semilogarithmic plot of a power spectrum indicates that the broadband noise arises from a deterministic rather than a stochastic process.

4.1.2 Phase space portraits and attractors

A dynamical system consists of two parts: the state which describes the essential information about the system, and the dynamics which is a rule that describes how the state evolves with time. The evolution can be visualized in phase space, an abstract space whose coordinates are the components of the state. Therefore, the phase space provides a powerful tool for inspecting the behavior of chaotic systems. The phase space represents the behavior in a geometric form. For example, a pendulum that moves with friction eventually comes to a rest, which in phase space means that the orbit approaches a stationary point called a fixed point. Since it attracts nearby orbits, it is known as an attractor.

Some systems do not come to rest in the long term but cycle periodically through a sequence of states. An example is the pendulum clock (driven pendulum), in which energy lost to friction is supplied by an external force. The pendulum clock repeats the same motion over and over again. In phase space such a motion corresponds to a cycle, or periodic orbit. Such attractors are called limit cycles.

A system may have several attractors. If that is the case, different initial conditions may evolve to different attractors. The set of points that evolve to an attractor is called its basin of attraction. The pendulum clock has two such basins. A very small displacement of the pendulum from its rest position results in a return to rest. With a larger displacement, however, the clock begins to tick as the pendulum executes a stable oscillation.

Another type of attractor in phase space is a torus or quasiperiodic attractor, which resembles the surface of a doughnut. This shape describes motion made up of two independent oscillating frequencies such as in driven electrical oscillators. One frequency determines how fast the orbit circles the doughnut in the short direction and the other regulates how fast the orbit circles the long way around. If motion is represented by the combination of more than two oscillating frequencies, the attractor becomes a higher-dimensional torus.

The important feature of a quasiperiodic attractor is that in spite of its complexity

it is predictable. Even though the orbit may never exactly repeat itself, i.e if two frequencies are incommensurate, the motion still remains regular. Orbits that start on the torus near one another remain near one another, and long term predictability is guaranteed.

Since the first example of a chaotic or strange attractor discovered by Lorenz, now known as the Lorenz attractor, interest in looking for this special type of attractor in phase space has been growing rapidly. A chaotic attractor has a much more complicated structure than a predictable attractor such as a fixed point, a limit cycle or a torus. For a chaotic attractor, two orbits with nearby initial conditions diverge exponentially and then come back close together for only a short time. Stretching and folding operations which take place in phase space are the key to understanding the chaotic behavior on these attractors. Exponential divergence is a local feature because attractors have finite size so that two orbits on a chaotic attractor cannot diverge exponentially forever. As a result, the attractor must fold over onto itself. Although orbits diverge and follow increasingly different paths, they eventually must pass close to one another again. The process of stretching and folding happens repeatedly, creating folds within folds indefinitely. A chaotic attractor is, therefore, much like a fractal: an object that reveals more details but self similar as it is increasingly magnified.

4.2 Dimensions

To distinguish deterministic chaos from stochastic noise, other quantitative means are needed. A chaotic attractor can be quantitatively characterized by its geometric properties. A suitable quantity characterizing the attractor as a metric structure is its dimension.

There are several alternative ways of defining the dimension of a set of points [61]. We shall give what we feel to be the most intuitive one here, called the fractal or capacity dimension D_C [62]. Referring to figure 4.4, we consider a set of points

$$N \sim 1/\varepsilon$$

$$N \sim 1/\varepsilon^2$$
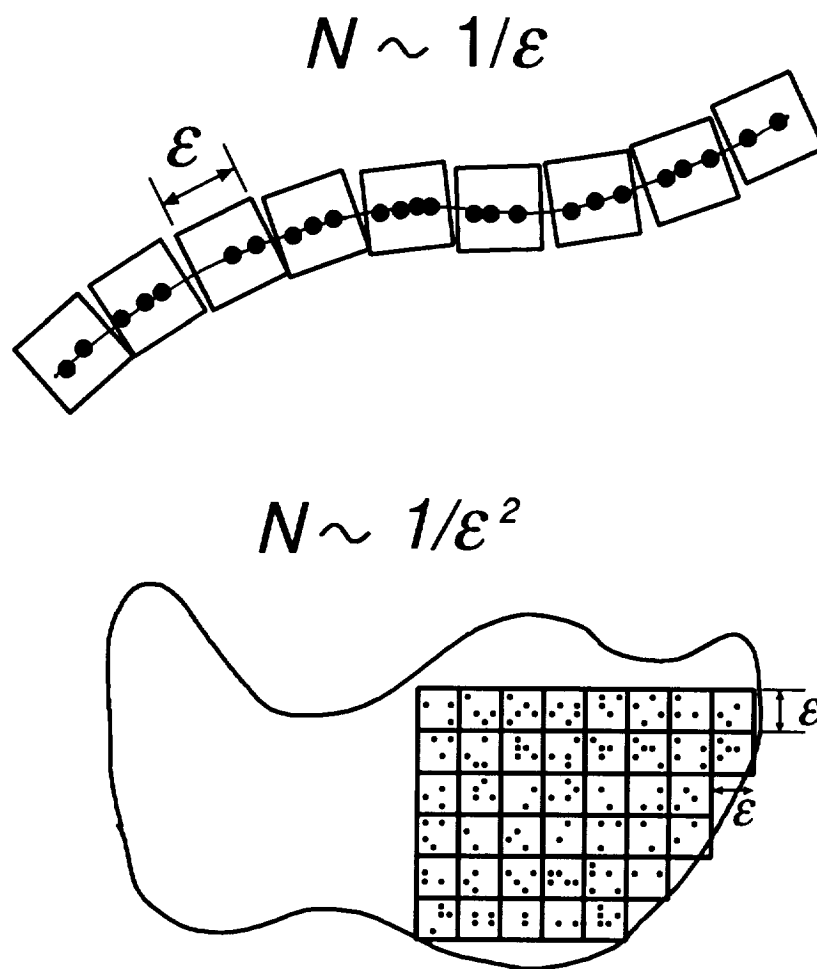
Figure 4.4: Illustration of the method of covering a 1- and 2-dimensional sets of points using small squares. This can lead to an intuitive definition of the capacity dimension (see the text). (After [57]).

uniformly distributed along a line as in the above half of the figure. We want to find out how many small squares of side length ϵ are needed to completely cover the set of points. If the line is of length l, then this number will clearly be $N(\epsilon) = l/\epsilon$. Similarly, we can consider a two-dimensional set of points as shown in the bottom half of the figure, and find that the number of small squares needed to cover the area A is $N(\epsilon) = A/\epsilon^2$. Extrapolating this procedure to sets of points in higher dimensions, we find the following scaling rule:

$$N(\epsilon) = \frac{l^d}{\epsilon^d}, \tag{4.6}$$

where d is the dimension of the set of points. From this we can define the capacity dimension D_C as

$$D_C = \frac{\log N(\epsilon)}{\log l + \log(1/\epsilon)}, \tag{4.7}$$

and in the limit of small ϵ, the term containing l becomes negligible, i.e.

$$D_C \sim \lim_{\epsilon \to 0} \frac{\log N(\epsilon)}{\log(1/\epsilon)}. \tag{4.8}$$

If the dimension of a set of points as defined in equation 4.7 is non-integer, then the set is a fractal set.

The structure of the strange attractor does not tell us anything about the frequency with which different points on the attractor are visited in the course of the flow. It is therefore useful to modify the definition of eq. 4.8 by covering the attractor with cells and weighting the jth cell by its visitation probability P_j. This gives the information dimension

$$D_I = \lim_{\epsilon \to 0} I(\epsilon)/\log(1/\epsilon), \tag{4.9}$$

where

$$I(\epsilon) \equiv -\sum_{j=1}^{N(\epsilon)} P_j \log P_j. \tag{4.10}$$

Note that if each cell has the same visitation probability, so that $P_j = 1/N(\epsilon)$ for all j, then $I(\epsilon) = N(\epsilon)$ and D_I reduces to D_C. In general, though, $D_I \leq D_C$.

To generalize, it is convenient to define an infinite set of dimensions. Let $\vec{X}(t) = (x_1(t), x_2(t), \cdots, x_d(t))$ denote a trajectory in a d-dimensional phase space and construct from the trajectory a sequence of points $\vec{X}(0), \vec{X}(\tau), \vec{X}(2\tau), \cdots, \vec{X}(M\tau)$ in

phase space, where M is large. Partition the phase space into $N(\epsilon)$ cells of side ϵ and let M_i be the number of points appearing in cell i. Define $P_i = M_i/M$ as the probability of finding a point in cell i. Then the dimensions D_n are defined by

$$D_n = \lim_{\epsilon \to 0} \left(\frac{1}{n-1} \right) \log \left(\sum_{i=1}^{N(\epsilon)} P_i^n \right) / \log \epsilon. \tag{4.11}$$

Note that

$$D_0 = -\lim_{\epsilon \to 0} \log N(\epsilon) / \log \epsilon = D_C, \tag{4.12}$$

and

$$D_1 = \lim_{\epsilon \to 0} \left(\sum_{i=1}^{N(\epsilon)} P_i \log P_i \right) / \log \epsilon = D_I. \tag{4.13}$$

That is, D_0 and D_1 reduce to the fractal and information dimensions defined earlier. For the total set of generalized dimensions it can be shown that $D_n \leq D_m$ for $n \geq m$, where the equality holds for a completely homogeneous probability distribution, i.e. $P_i = 1/N(\epsilon)$. Hence, the difference between dimensions of different order measures the degree of inhomogeneity of the attractor due to the variation of visitation frequency of each cell.

The dimension D_2 is related to the correlation integral function

$$C_2(\epsilon, d) = \lim_{M \to \infty} \frac{1}{M^2} \sum_{\substack{i,j=1 \\ (i \neq j)}}^{M} \theta(\epsilon - z_{ij}), \tag{4.14}$$

where z_{ij} is the separation of two of the points such that $z_{ij} = [\sum_{k=1}^{d}(x_k(t_j) - x_k(t_j))^2]^{1/2}$ and $\theta(x)$ is the step function such that

$$\theta(x) = \begin{cases} 0 \,, & \text{if} \quad x \leq 0 \\ 1 \,, & \text{otherwise.} \end{cases} \tag{4.15}$$

To see this, note that $\sum P_i^2$ is the probability that any two points lie in the same cell. This is approximately the probability that two points on the attractor are within a distance ϵ of each other, which is given by eq. 4.14. Thus, the correlation dimension is

$$D_2(d) = \lim_{\epsilon \to 0} \frac{\log C_2(\epsilon, d)}{\log \epsilon}. \tag{4.16}$$

4.2.1 Kolmogorov entropy

Another useful quantity to characterize a chaotic attractor is the Kolmogorov entropy, which involves a concept with a strong analogy to the entropy concept in information theory. In information theory, we know that the maximum information content for a system with two possible states is 1 binary bit. It is 2 bits for a system with four possible states and so on. In general, the maximum information content is $\log_2 N$ bits for N possible states.

Suppose a system has N states, and the ith state is known to occur with probability P_i. The entropy of the system is defined as

$$S = -\sum_{i=1}^{N} P_i \log_2 P_i. \tag{4.17}$$

Here, entropy is a measure of the amount of information necessary to determine the state of the system. Consider now a trajectory $x(t_i) = (x_1(t_i), x_2(t_i), \ldots, x_n(t_i))$ and partition phase space into n hypercubes of side ϵ. Let $P(i_1, i_2, \ldots, i_n)$ be the joint probability that the point $x(i\tau)$ lies in the i_ith cell. Then, from the above discussion,

$$K_n \equiv -\sum_{i_1,\ldots,i_n} P(i_1, i_2, \ldots, i_n) \log_2 P(i_1, i_2, \ldots, i_n) \tag{4.18}$$

is a measure of the amount of information necessary to specify the trajectory to within a precision ϵ. It follows that $K_{n+1} - K_n$ is the additional amount of information required to specify which cell $x(n\tau + \tau)$ will fall in. The Kolmogorov entropy may be defined as [63]

$$K \equiv \lim_{\tau \to 0} \lim_{\epsilon \to 0} \lim_{N \to \infty} \left(\frac{1}{N\tau}\right) \sum_{n=1}^{N} (K_{n+1} - K_n) \tag{4.19}$$

$$= -\lim_{\tau \to 0} \lim_{\epsilon \to 0} \lim_{N \to \infty} \left(\frac{1}{N\tau}\right) \sum_{i_1,i_2,\ldots,i_n} P(i_1, i_2, \ldots, i_n)$$

$$\times \log_2 P(i_1, i_2, \ldots, i_n). \tag{4.20}$$

We see that K is the average rate of the information loss. Hence, $K = 0$ in an ordered system; $K = \infty$ in a random system; and K is positive constant $\neq 0$ in a chaotic

system. To generalize, we define the order-q Renyi entropy as

$$K_q \equiv - \lim_{\tau \to 0} \lim_{\epsilon \to 0} \lim_{N \to \infty} \left(\frac{1}{N\tau(q-1)} \right) \log_2 \sum_{i_1,i_2,\ldots,i_n} P^q(i_1,i_2,\ldots,i_n), \qquad (4.21)$$

with $P^q = P \exp(q-1) \log_2 P$. Of all the order-$q$ quantities K_q, K_2 is the easiest quantity to calculate. It can be shown to be a lower bound to the Kolmogorov entropy [63].

4.2.2 Dimensions and phase space portraits from an experimental time series

In the discussion of the preceding section, we made no mention of how one can construct a phase space portrait of a dynamic system with only time series data for one variable. For example, in our experiments with the PCR, the data is the temporal fluctuation of an intensity. According to the Takens embedding theorem [64], the topology of an attractor can be reconstructed in an artificial phase space derived from a single experimental time series. The procedure in such cases is to construct a pseudo phase space, for example by plotting the value of the measured variable at time t on one axis and successively time-delayed values on other axes. For example, we denote the measured quantity at time t by $x(t)$. Then, for a two-dimensional phase space, we plot $x(t + \tau)$ on the second axis, where τ is a small interval of time. Construction of a d embedding dimensional phase space follows in the same manner by using $\vec{X} = (x(t), x(t + \tau), \cdots, x(t + d\tau))$. The choice of τ is a debated subject [56]. There is a certain amount of trial-and-error involved in finding the best τ for a particular problem. If τ is made too large, one loses the correlation between the data points, with the result that the plot is just a randomly moving wiggly line. One the other hand, if too small a value is chosen, the plot shows strong dependence among points and no structure can be resolved.

To calculate the correlation dimension and the Kolmogrov entropy from an experimental time series data, we simply apply the calculation methods discussed in the preceding sections to the embedding phase spaces made up of those vector points $\vec{X}$.

The second order Renyi entropy is given by

$$K_2 = \tau^{-1}[\log C_2(\epsilon, d) - \log C_2(\epsilon, d+1)]. \tag{4.22}$$

For small ϵ and large embedding dimension d it is found that

$$C_2(\epsilon, d) \sim \epsilon^{D_2(d)} \exp(-d\tau K_2), \tag{4.23}$$

so that in practice K_2 can be obtained by calculating $C_2(\epsilon, d)$ for different values of d. As K_2 is a lower bound to the Kolmogorov entropy, the condition $K_2 > 0$ is sufficient for the existence of chaos.

4.3 Background on spatiotemporal chaos

4.3.1 Extended systems. Weak turbulence

Chaos, as discussed in the preceding sections, is a temporal phenomenon as long as there are no spatial counterpart involved. This limitation has to be reconsidered if the degrees of freedom in a dynamical system have a spatial significance. Indeed, in nonlinear nonequilibrium states, as in fluid convection, there appear structures, which have been called dissipative structures by I. Prigogine [65]. Examples of these states having structures include:

(1) patterns with steady structures which vary purely in space (e.g. convection of fluids, chemical reactions, etc.);

(2) states with homogeneous structures which vary periodically purely in time (e.g. chemical oscillations, heartbeat etc.);

(3) quasiperiodic states (similar to (2)), which vary quasiperiodically in time;

(4) chaotic states which vary chaotically in time;

(5) turbulent states which vary chaotically both in time and in space.

Some physical systems may only exhibit one of these examples while others can have all these, such as Rayleigh-Benard convections and Taylor-Couette flows [66]. Regarding the nonequilibrium states involving spatial structures, one of the tasks of

C·2

spatiotemporal chaos is to find out how the local/global instability mechanisms are manifested in the physical space rather than in the phase space portraits.

The notion of temporal chaos discussed in this thesis applies to a situation where the confinement effects are so strong that the degrees of freedom in a dynamical system one studies do not have any spatial significance. In that case, one deals only with the temporal aspect of the dynamics. When systems are weakly confined, i.e. the boundary effects are less stringent, the instability mechanisms can be then manifested in the structural modulations. The word pattern will then be a key to the associated disorder, which has now a space-time meaning.

A much studied example of a confined system is that of a fluid layer contained in a small box heated from the bottom [67]. At the beginning of the experiment, the liquid is static. The heat flows across the layer cell via conduction. As the temperature gradient reaches a critical value, a convection flow sets in. The hot and less dense liquid rises in the middle while the cool liquid flows down at the sides. So, there appear two convective rolls. As the temperature gradient is increased further, the rolls suddenly become unstable in a specific way. A wave (mode) starts running along the roll (see figure 4.5) periodically. As the temperature gradient is increased further, an additional new wave (mode) is observed. The temperature monitored locally fluctuates periodically and quasiperiodically until it becomes chaotic. This early work has shown how the confinement effects affect the dynamics. From the physical dimensions of the container, the aspect ratio Γ can be defined to be the ratio of the laterial extension l to the height which is comparable to the radii of the rolls, λ_r, i.e. $\Gamma = l/\lambda_r$. When Γ is small, the spatial structure is stablized by the lateral confinement effects. In constrast, when $\Gamma \gg 1$, the system is called weakly confined or extended, where the size of ordered states is down to a local scale only. The overall structure is then to better understood in terms of pattern or textures. As the complexity level increases, structural defects may often appear. The role played by such defects in the turbulent system is a currently active area of research [68].

If now the layer of fluid considered above is contained in a box of much larger aspect ratios, i.e. the lateral extension is much larger than that of the radii of the
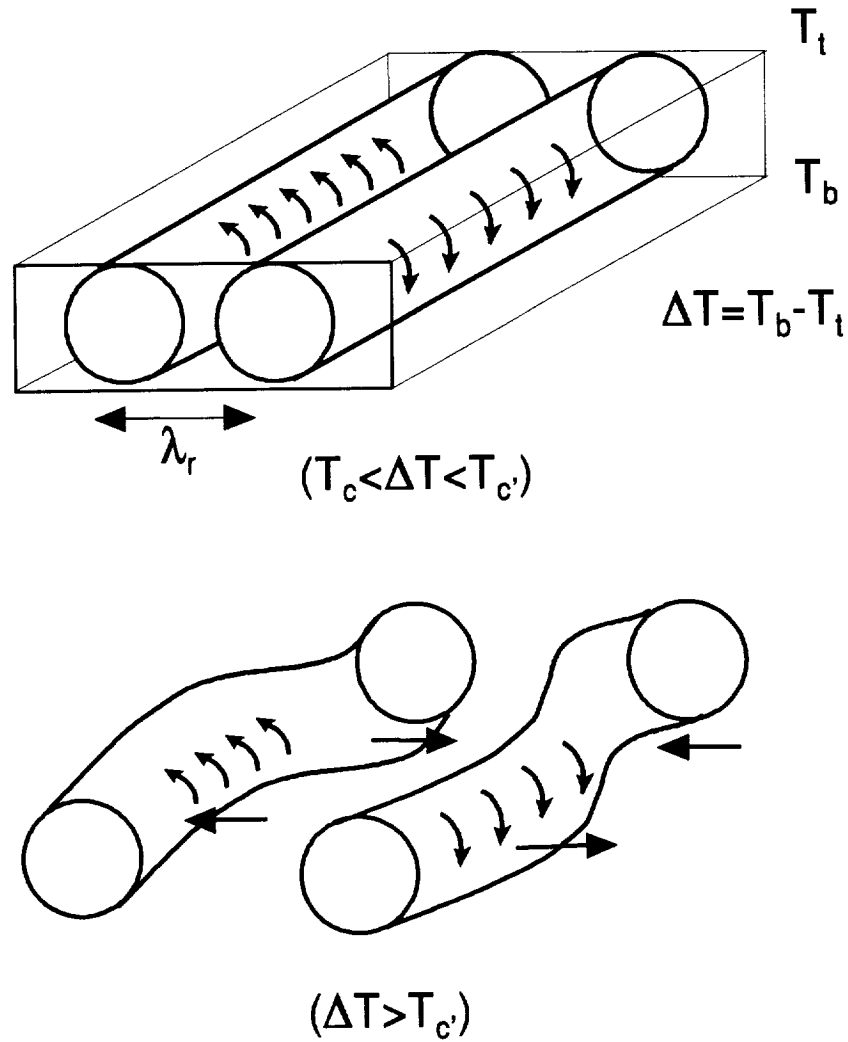
Figure 4.5: Schematic diagram of the Rayleigh-Benard convection. A thin layer of fluid in a small box is heated from the bottom. Two convective rolls rotate as indicated by the arrows when the temperature gradient reaches a critical value. As the temperature gradient further increases, waves are excited and run along the lateral direction of the rolls.

rolls, a continuous spectrum of excited waves (modes) can be present. When many of them with comparable wavelength can be present independently with nearly equal amplitude, their mutual interferences can induce large scale modulations. These kinds of modulation have been associated closely with the so called the Benjamin-Feir instability [69]. To describe such modulations or instability mechanisms, the basic idea of spatiotemporal chaos is to extend the notion of an amplitude that is time-dependent-only, as in temporal chaos, to account also for spatial dependence. In other words, the amplitude of the wave has to be described by the two variables of time and space. In fact, such an idea of using envelop functions for the amplitudes of the excited waves leads to a complex Ginzburg-Landau equation to describe the dynamics of the dissipative structures in hydrodynamics [68].

4.3.2 Topological turbulence

The last few years have witnessed very extensive explorations of the spatial behavior of laser beams which may display spatial structures similar to those seen in hydrodynamics [70, 71, 72, 73, 74, 75] . A series of investigations of transverse effects in laser dynamics by Lugiato and co-workers shows that, just as temporal chaos results from the presence of at least a few competiting frequencies in a nonlinear system, instability mechanisms of the spatial structures in a laser may be governed by the interactions and competitions among a few chosen transverse cavity modes. The solutions of Maxwell-Block equations including diffraction [70] display families of transverse patterns containing regularly distributed dark spots called phase singularities [76, 77]. Also, recently, in their analysis of laser cavities with large Fresnel number, P. Coullet et al. reduced the Maxwell-Block equations to a single equation of the form of the complex Ginzburg-Landau equation [78]. In the two-dimensional space of the Ginzburg-Landau equation, they found singular solutions in the form of spirals. As the spiral waves bear some analogy with the vortices in hydrodynamics, they are now named optical vortices. In the stable case, these solutions persist indefinitely owing to their character of topological defect. In the unstable case, they

nucleate spontaneously as temporary singularities of the moving wavefront. The spatiotemporal chaotic regime that sets in has been called defect-mediated turbulence or topological turbulence [79, 80]. Defect-mediated turbulence is currently an active area of investigation across many disciplines of nonlinear science. The role of defects in mediating turbulence in nonequilibrium systems with large aspect ratios is an important matter of interest. Therefore, some knowledge of defects [81] becomes necessary. Before discussing some of the structures and characteristics of defects, let us close this brief introduction on spatiotemporal chaos with some mention of the methodologies commonly used for its analysis.

4.3.3 Methodologies of spatiotemporal complexity

At present, there are still no well-established methods for studying spatiotemporal chaos, in particular the fully developed turbulence. However, we may see emerging some important paradigms or methods for the study of the spatiotemporal dynamics. We now describe briefly some of these methods.

One of the oldest examples of a dynamical system which may evolve both in space and time are cellular automata. Cellular automata were invented in the late 40s by J. von Neumann to mimic the behavior of complex, spatially extended structures. W. Burke gave a good overview of the work of von Neumann [82]. In cellular automata, space is divided into discrete small units called cells or sites. The cells take on numerical values. Consider a one-dimensional cellular automaton consisting of a row of cells. Each cell is assigned a set of initial numbers. A set of rules specifies how these numbers are to be changed at every clock step. Suppose that the automaton initially is filled with 0's except for a single cell which is occupied by a 1:

$$\ldots 010000000 \ldots$$

And suppose that the rule states that the number in each cell is to be replaced by the sum of itself and its left neighbor. Thus, after one clock step, the state of the automaton will be as follows:

$$\ldots 011000000 \ldots$$

Another clock step later the state will be

$$\ldots 012100000 \ldots$$

followed by

$$\ldots 013310000 \ldots$$

$$\ldots 014641000 \ldots$$

etc. In fact, this cellular automaton is one of the early von Neumann machines used to compute the binominal coefficient of $(a+b)^n$. Cellular automata can be applied to one, two and higher dimensional problems. The fixed rules which specify the change of the cells' values carry out local interactions between neighboring cells, reflecting the dynamics of the system in question. Cellular automata have been used to model the complexity in biological systems from the level of cell activity to the levels of clusters of cells and populations of organisms. In chemistry, cellular automata have been used to model kinetics of molecular systems and crystal growth. In physics, they have been used to study dynamical systems such as the clustering of galaxies.

Another model for studying spatiotemporal chaos in spatially extended systems are the coupled map lattices introduced by K. Kaneko [83]. Coupled map lattices are dynamical systems discrete in both time and space. Although their modeling structure looks similar to that of cellular automata, the change of the state of each site is done by a local mapping function rather than by a set of rules. One example of coupled map lattices has the form

$$x_{n+1}(i) = (1 - D)f(x_n(i)) + D[f(x_n(i+1) + f(x_n(i-1))], \qquad (4.24)$$

where n represents the time step, i represents a lattice site, and D represents the diffusive coupling between nearest neighbors. The function $f(x)$ is chosen to be $ax(1-x)$ (i.e. coupled logistic lattice) or $x + A\sin(2\pi x) + c$ (i.e. coupled circle lattice). It has been shown that transitions to turbulence via spatiotemporal intermittency arise in these systems [84]. At the same time, studies of spatiotemporal chaos by

coupled map lattices have been growing rapidly because calculations are efficient and they lend themselves to the generalization of some of the quantitative methods used to characterize temporal chaos (e.g. Lyapunov spectra and Kolmogorov entropy density). This approach is also one of the very few known approaches providing means for the diagnosis of experimental data of spatially extended systems [84].

A third possible approach to the study of spatiotemporal dynamics is called the modal expansion of fields with transverse structures, as used in laser systems by Lugiato and co-workers. As is well known, spatiotemporal problems of continuous variables are mostly described by partial differential equations (PDEs). The solutions often rely on numerical methods. Sometimes, PDEs can be formidably demanding in computing power. Lugiato and co-workers demonstrated an alternative way of solving the PDEs of lasers by expanding the dynamical quantities in a series of normal modes. The PDEs are then reduced to a set of coupled ordinary differential equations (ODEs) in the limit of the mean-field approximation. The basic idea of this approach is to represent the envelop functions of the fields' amplitudes by the space-dependent-only normal modes and the corresponding time-dependent-only coefficient if it is validly allowed. This method is highly efficient and yet the essential dynamics of the spatial structures can still be captured.

A last approach to a description of the turbulent state in a nonequilibrium system is to characterize it by the presence of topological defects. As mentioned before, this approach of topological turbulence was first introduced by P. Coullet *et al.* for laser systems [80]. They used numerical solutions of the Ginzburg-Landau equation to illustrate a mechanism of defect formation, annihilation and dynamics in dissipative structures. Another possible theoretical approach to describe defect formation and turbulence in large aspect ratio systems has recently been proposed by I. Procaccia [85]. In the study of nematic electroconvection, the ordered state of the convective rolls before the appearance of defects is well described by the envelope equations. However, how the modulations are affected by the defects is not clear. Procaccia concluded in his study of nematics that a field theory might be necessary to describe the dynamics and the interaction forces between defects. On the experimental side,

several examples have already demonstrated defect formation in nonequilibrium systems of large aspect ratios, as in surface waves, in thermal convection, and in the transverse patterns of lasers and nonlinear optical systems [56, 86]. In fact, the dynamics that we observe in the PCR above threshold also provide evidence for such defect-mediated transitions [87, 88]. This will be demonstrated in the following chapters. But we first introduce in the next section some of the concepts related to the definitions of defects and in particular the phase defects or wavefront dislocations observed in electromagnetic waves.

4.4 Wavefront dislocations/phase defects

In this concluding section, we will define the singularities found in electromagnetic waves and the corresponding terminology used later on in our discussions of the PCR's dynamics. The discussion given here follows closely that of a paper by M. Berry [89].

Wavefront dislocations or phase defects were first discovered by Nye and Berry in their study of ultrasound reflected from a rough surface [90]. Wave dislocations appear ubiquitously in optical fields, acoustics, and quantum mechanics as well as water waves [81, 91]. Wavefront dislocations are just one kind of singulary that can appear in scalar waves (for vector or tensor waves, see [92]). Ray caustics are another kind of wave singularity with a different length scale. On a caustic, rays of light (in a geometrical optics sense) are all focused to a point and thus the intensity is infinite. On a phase defect, the intensity is zero. To be observable, the phase defects of a wavefront must be explored on the wavelength's scale, for example by interferometry. Caustic singularities, in constrast, are visible to the naked eye (e.g. the reflection of sunlight from a wavy water surface).

As is well known, singularities are present in many complicated systems, such as solids, liquid crystals, and hydrodynamics as well as in nonlinear optics. When considered as geometric structures, singularities are forms rather than materials. Waves are also forms. Therefore, dislocations in wavefronts are forms of forms. Despite their "double" abstract nature, they are directly observable phenomena.

Another important nature of wavefront dislocations is their singular character. Consider a travelling wave $\psi(r,t)$ with complex amplitude $\rho(r,t)$ and phase $\chi(r,t)$ defined by

$$\psi = \rho \exp(i\chi). \tag{4.25}$$

For the waves in which we are interested, ψ is a smooth single-valued function of position and time. When traversing a loop in the wavefront, χ may change by $2m\pi$, where m is an integer. Let us shrink the path to a very small loop while the amount of variation in χ does not change. Thus, a singularity is enclosed because χ is varying infinitely fast. And yet the smoothness of ψ has to be preserved. It implies that this can happen only where $\psi = 0$, i.e. χ is indeterminate. As ψ is null, both $\mathrm{Re}\psi$ and $\mathrm{Im}\psi$ vanish (i.e. $\mathrm{Re}\psi = \mathrm{Im}\psi = 0$). Thus, phase singularities are points in planes and lines in space, analogous to crystal dislocations in solids.

Before we illustrate the possible structural forms of the wavefront dislocations by examples, we would like to ask how they happen. Since the singularities happen only where $\psi = 0$, i.e. the intensity ρ^2 vanishes, they might be confused with the dark fringes often discussed in elementary treatments of interference. The dark fringes are, however, conceived as surfaces rather than lines. Wavefront singularities result from the destructive interferences of the different rays contributing to ψ at a crossing region of waves scattered from different objects. The crossing can be a point in a plane or a line in space.

Now we will illustrate some of the possible structural forms of the dislocations of a wave ψ satisfying the wave equation in a uniform static isotropic medium:

$$\nabla^2 \psi = \frac{1}{c^2} \frac{\partial^2 \psi}{\partial t^2}. \tag{4.26}$$

Suppose that ψ travels only in the z-direction, i.e. $\psi = \rho \exp(i\xi)$, $\xi = z - ct$. The first case considered is a dislocation moving rigidly with the host wavefront. The wave for such a case must satisfy

$$\psi = \psi(x,y,\xi), \qquad \frac{\partial^2 \psi}{\partial x^2} + \frac{\partial^2 \psi}{\partial y^2} = 0. \tag{4.27}$$

Consider as an example, $\psi = A(kx + i\beta k\xi)e^{ik\xi}$, where A and β are real constants.
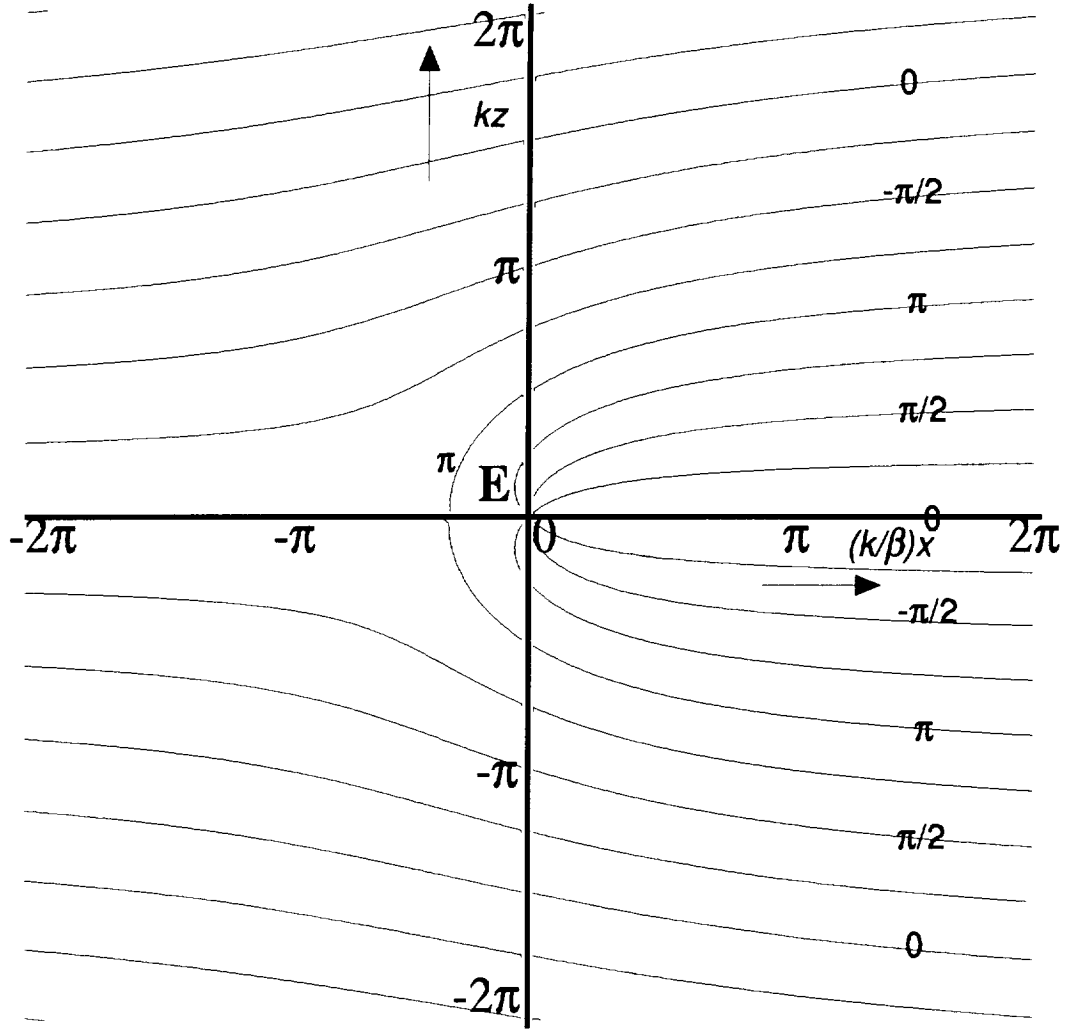
Figure 4.6: Phase contours of a travelling wave containing a pure edge dislocation. The wave moves upwards. Notice the wavecrest ending at the origin E. This singularity is an edge dislocation bearing some analogy with an edge dislocation in solids.

Figure 4.6 shows the contours of ξ, i.e. wavefronts of ψ moving upwards. The dislocation is located at E. In crystallographic terms, this is a pure edge dislocation. The next example of dislocation is the pure screw dislocation, which for strength s has a wave function

$$\psi = A(kx \pm iky)^s e^{ik\xi}. \tag{4.28}$$

Figure 4.7 shows the typical plot of pure screw dislocation with strength $s = 2$. The sign $\pm$ determines the helicity of the screw and the charge s its pitch. Negative charge of a screw dislocation means that the phase increases counterclockwise around the dislocation. There is also a mixed type of dislocation, i.e. edge-screw dislocation with waves of the form

$$\psi = A(kx + i\beta(k\xi\cos\delta - ky\sin\delta))e^{ik\xi}, \tag{4.29}$$

for example, $\delta = 0$ and $\delta = \pi/2$ correspond to pure edge and pure screw respectively.

Now consider the modulation of the wave in equation 4.25 with quadratic terms in x, y and which also satisfy equation 4.27. In this way, it would have curved dislocation lines that move rigidly with the host wave. An example is $\psi = [(x - iy)^2 + i\beta k\xi]e^{ik\xi}$ whose dislocation lines have the form of two parabolas orthogonal to each other, as shown in figure 4.8a.

We now consider examples showing dislocations moving relative to the wavefront as the host wave propagates. A simple example of these is

$$\psi = A[\alpha kx + k^2 x^2 + i(\beta k\xi + kz)]e^{ik\xi}, \tag{4.30}$$

where α is real constant. This has two edge dislocations at $x = 0$ and $x = -\alpha/k$, moving parallel to the propagating axis (see figure 4.8b). In a crystallographic term, such motion is glide. Another kind of movement is made possible if the term in ξ is made quadratic, i.e. if

$$\psi = A[\alpha kx + k^2 x^2 + i(\beta k^2 \xi^2 + kz)]e^{ik\xi}, \tag{4.31}$$

Now two pairs of edge dislocations are located at $x = 0$, and $x = -\alpha/k$. If $\beta > 0$, members of each pair approach, collide and annihilate while if $\beta \leq 0$ they appear and
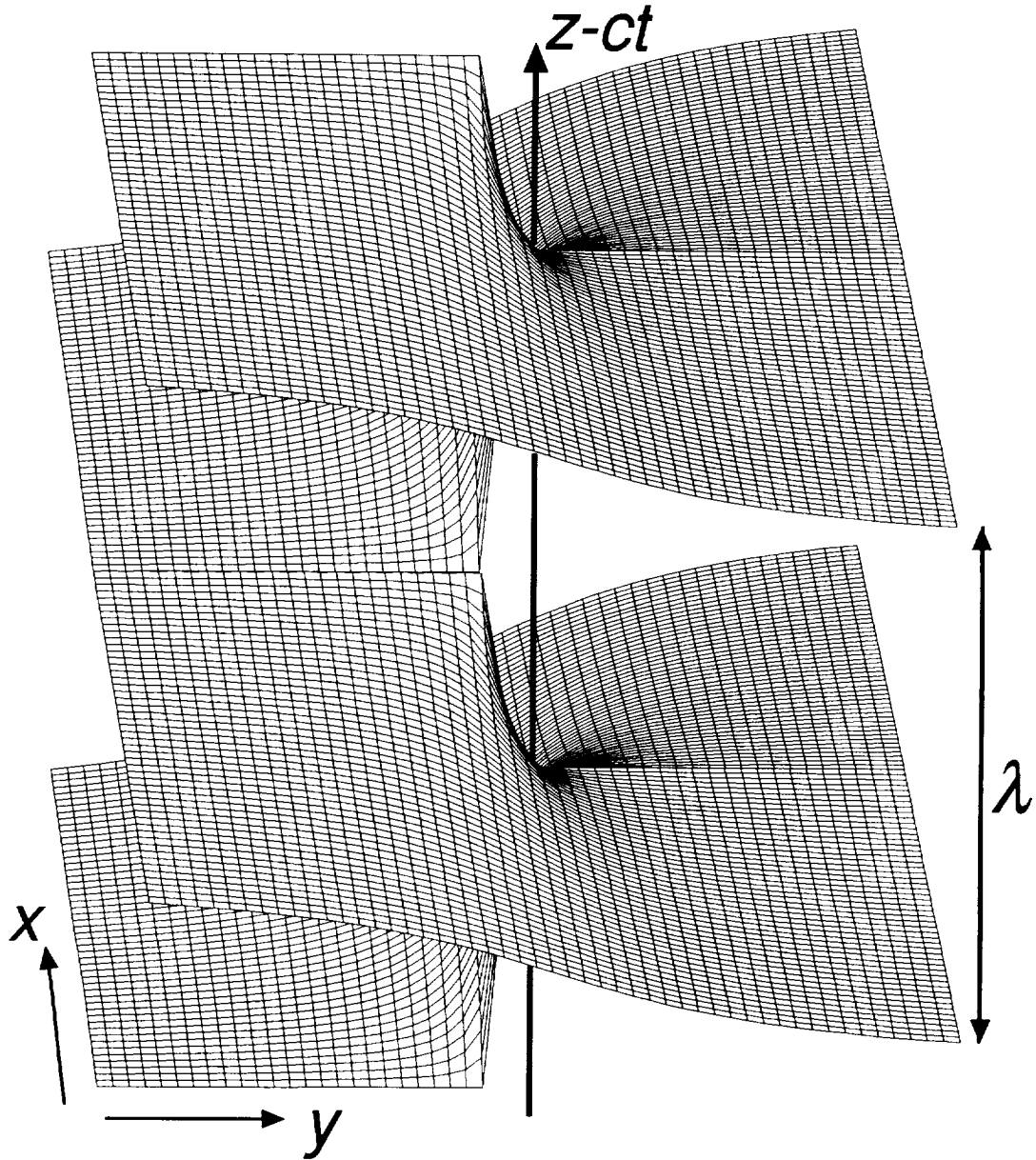
Figure 4.7: Wavefronts of a travelling wave containing a pure screw dislocation. This helical wavefront with the dislocation along the axis of propagation rotates in clockwise. The direction of rotation determines the sign or charge of the screw dislocation. Clockwise rotation means a positive charge and vice versa.
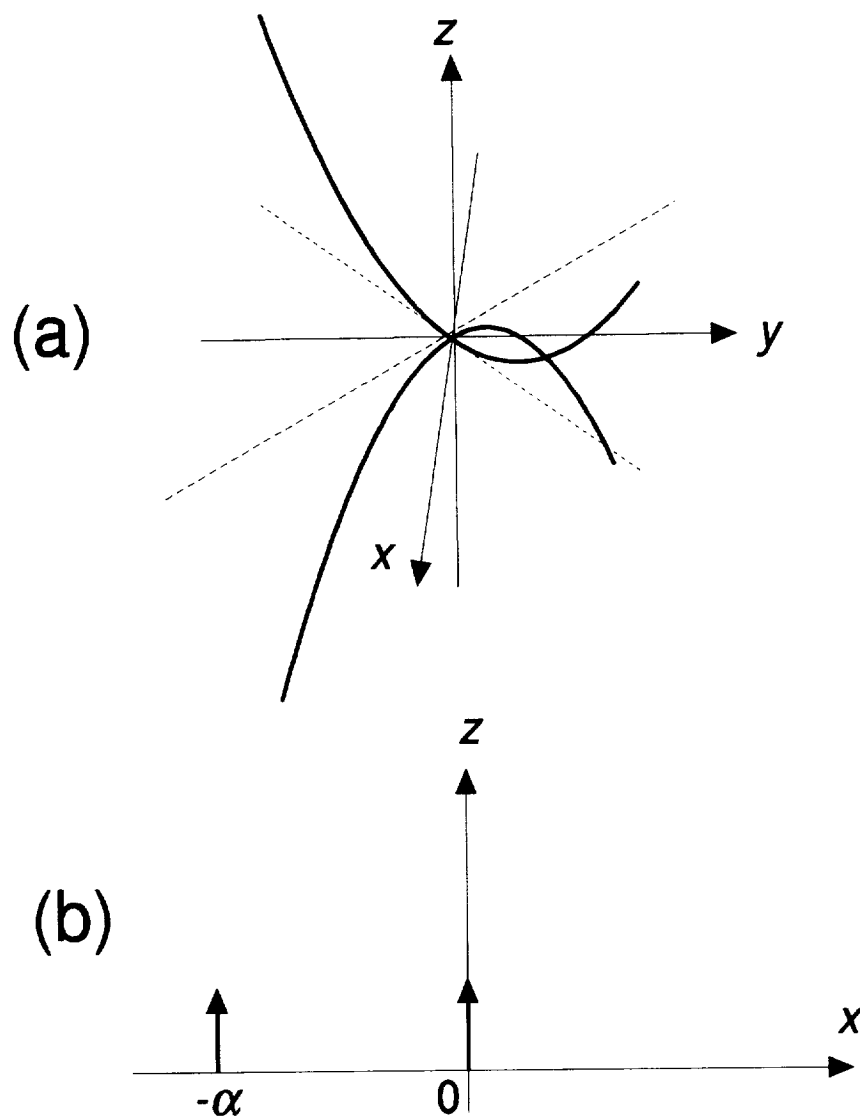
Figure 4.8: Examples of dislocations' motion in a travelling wave. The wave travels upwards (see text for details).
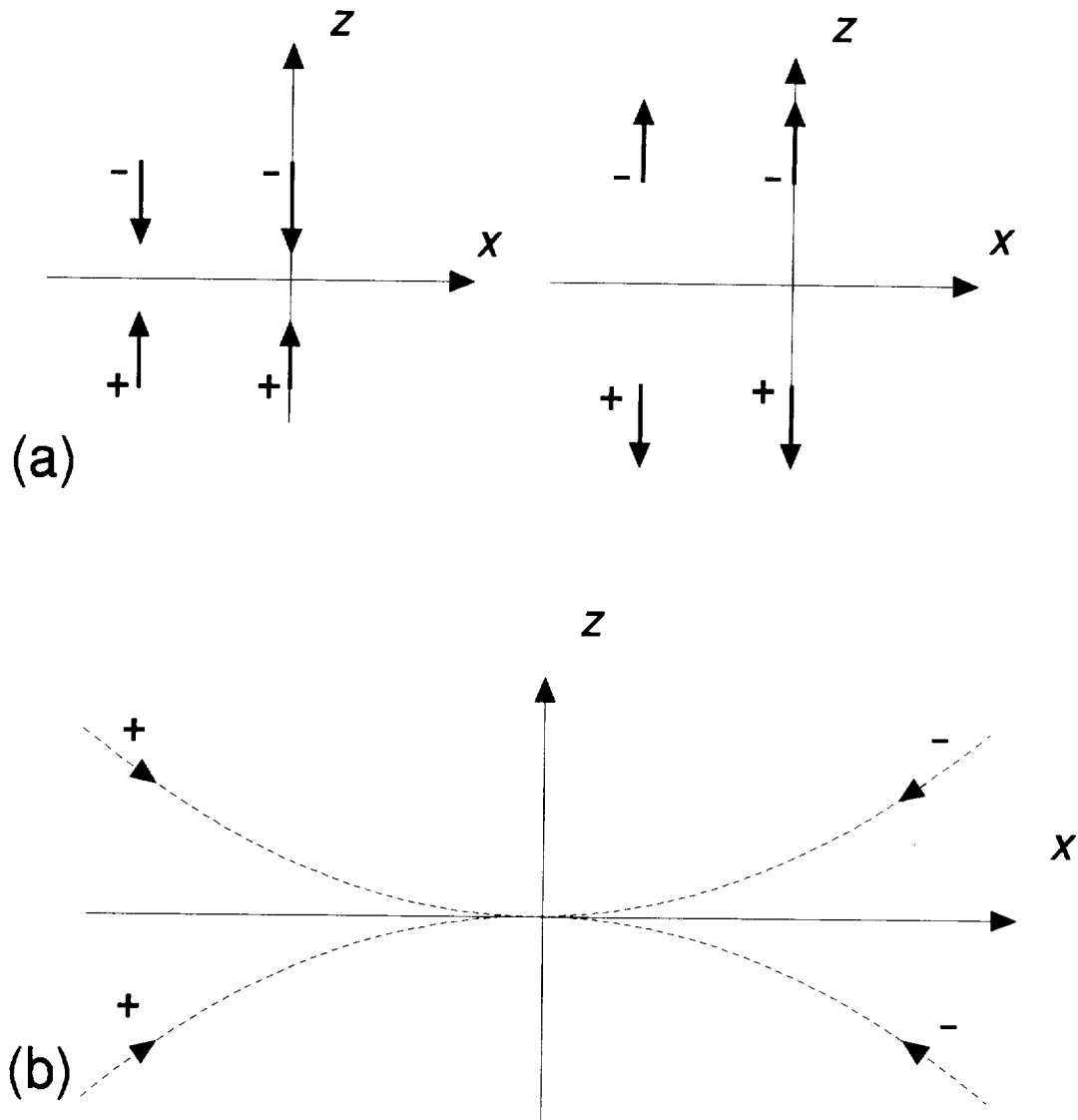
Figure 4.9: More examples of dislocations' movements in a travelling wave. The wave travels upwards (see text for details).

then glide apart (see figure 4.9a). If a slight change of form is made in equation 4.31, for example, if it becomes

$$\psi = A[k^2 x^2 + i(\beta - i\gamma)k^2 \xi^2 + ikz]e^{ik\xi}, \qquad (4.32)$$

where γ is a real constant, two pairs of edge dislocations approach each other along parabolic trajectories and annihilate when they meet (see figure 4.9b). Such motion, called climb, corresponds to the spontaneous recovery of a tear in a wavefront. Above are a few of many possible structural forms and movements that the wavefront dislocation or phase defects can have. Many other interesting examples can be found in references [90, 93, 89].

In conclusion, we have presented a brief introduction of nonlinear dynamics and spatiotemporal as well as temporal chaos. Of particular interest are the definitions of topological turbulence and the role played by the wavefront dislocations or phase defects in mediating the dynamics. Some aspects of these phenomena will be illustrated in the study of the PCR's dynamics above threshold, described in the following chapters.

Chapter 5

Experiments: spatiotemporal dynamics in PCRs

In this and the following chapter we present the results of an experimental study of spatiotemporal structures in the PCR's beams above threshold. In this chapter, the emergence of spatiotemporal structures as the degree of transverse confinement is varied by changing the Fresnel number will be described in detail. A theoretical model of the spatiotemporal dynamics of the PCR will be presented in the next chapter.

This chapter is organized as follows: In section 5.1, the experimental arrangement for the study of the spatiotemporal dynamics of the PCR will be described. The experimental results and their analyses are presented in the following five sections. The dynamics of the local intensity measured at one point in the beam will be analysed in section 5.2 with the aid of experimental time series, power spectra and phase space portraits. An attempt at quantifying the chaotic dynamics by calculating the correlation dimension and the Kolmogorov entropy will be presented in section 5.3. The spatial instabilities of structures across the PCR's beams will be discussed in sections 5.4 and 5.5, where it is indicated that the spatiotemporal dynamics observed has some the characteristics of a topological or defect-mediated turbulence. Finally, in section 5.6, it is shown that the superposition of a few simple empty cavity TEM

modes with different frequencies have a dynamical behavior compatible with the observed phenomena. Additional discussion and conclusions are presented in the concluding section 5.7.

5.1 Experimental setup

The linear phase-conjugate resonator under study is sketched schematically in figure 5.1. The resonator consists of a flat dielectric mirror M (95 % reflectance) and a phase-conjugate mirror. The phase-conjugate mirror is a single crystal of $BaTiO_3$ 5mm×5mm×7mm in size. It is pumped externally by two counterpropagating beams from a single-mode Argon ion laser tuned to 514nm. The beam diameter is about 1.5mm. The intensity and polarization direction of each pump beam are controlled independently by assemblies consisting of a half-wave plate and a crystal polarizer. In all experiments reported in this chapter, both beams' polarization directions were extraordinary, i.e. in the same plane as the ĉ-axis of the crystal, which lies in the plane of the figure.

The resonator contains two apertures, H_1 and H_2. The aperture H_2 is located as close as possible to the mirror M and in the front focal plane of a 16 cm focal length lens. The aperture H_1 is in the back focal plane of that lens, about 3 cm away from the phase-conjugate mirror. The degree of transverse confinement of the system can be varied by changing the apertures sizes. A quantitaive measure of this confinement is given by the resonator Fresnel number defined as

$$F = \frac{D_1 D_2}{\lambda f}, \qquad (5.1)$$

where D_1 and D_2 are the diameters of the apertures H_1 and H_2 respectively, λ is the wavelength and f is the focal length of the lens. D_1 is small enough to ensure that the interaction region in the crystal is smaller than the area of pump overlap. The Fresnel number has a concrete physical meaning [94]. A simple argument based on scalar diffraction theory shows that the transverse dimension of a speckle near the aperture H_1 is given by $\lambda f/D_2$. F is, therefore, a measure of the number of speckles
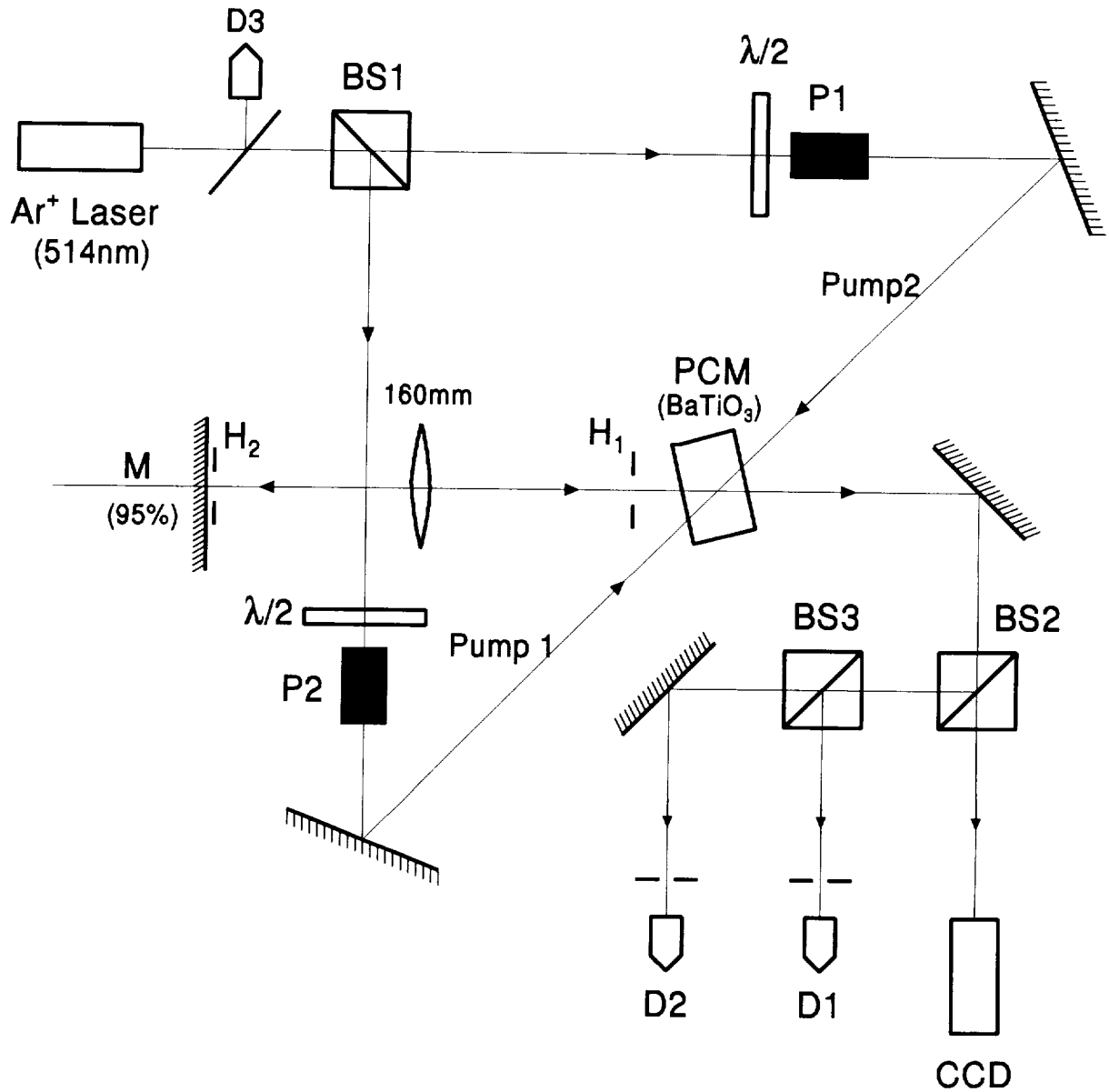
Figure 5.1: Schematic diagram of the phase-conjugate resonator setup: $\lambda/2$-P are half-wave plate – polarizer assemblies used to vary the intensity of the beams individually. All beams' polarizations are extraordinary. The two apertures H_1, H_2 are one focal length away from the lens (f=16cm). The Ar^+ laser operates in a single mode at 514nm. The phase-conjugate mirror is a single crystal of $BaTiO_3$. D1, D2 are photomultiplier tubes measuring the local intensity at two different locations; D3 monitors the laser output and the CCD camera is used to capture the dynamics of the intensity distribution.

99

along any transverse diameter in the resonator field. In all the experiments reported here, except for the measurements made with $F < 3$, the aperture H_1 was fixed with $D_1 = 0.69$mm.

The Fresnel number is the control parameter used in the experiments. The Bragg detuning achieved by misaligning one of the two pumps is another significant parameter, which will be considered in the next chapter. Both appear to be the parameters that most directly affect the spatiotemporal dynamics of the system. Two other parameters have been observed to affect the dynamics as well, but to a much lesser degree. The first is the total intensity I_o incident on the crystal. The response time associated with the photorefractive effect is roughly inversely proportional to the intensity in the range used (10mW/mm^2 $\sim$ 100 mW/mm^2). For our crystal, the response time was of the order of 1s mm^2/mW. The second factor influencing the dynamics is the pump ratio, defined as $R_p = I_2/I_1$, where I_2 and I_1 are pump 2 and pump 1 intensities, respectively (see figure 5.1). The pump ratio can be used to vary the departure of the cavity from threshold, which affects the buildup and decay rates of the cavity [34]. It has been seen in chapter 2 that the decay time diverges for the values of the pump ratio at which the cavity reaches threshold for self-oscillation. From chapter 3 (fig. 3.10), it is seen that the cavity is above threshold for $0.1 < R_p <$ 1. The departure from threshold can then be varied by choosing a pump ratio within that range. With a better alignment of the crystal, and thus a higher gain coefficient, that range could be extended to $R_p < 2$ for the experiments described in this chapter.

With a tight confinement ($F = 1.8$), giving a stationary output, we measured the intensity and the buildup times of the phase conjugate beam I_3 against the pump ratio for various values of the total pump power. The goal was to determine what values of these two parameters gave rates of change of the observed phenomena compatible with visual observation and standard video recording. The results are shown in figure 5.2. For all the experiments reported here, the pump ratio was fixed at 1 and the total power of the two pumps was kept at 60mW. Other parameters such as alignments, four-wave-mixing geometry, etc., were fixed for all the measurements.

The field distribution in aperture H_1 was imaged (with lenses not shown in Fig. 5.1)
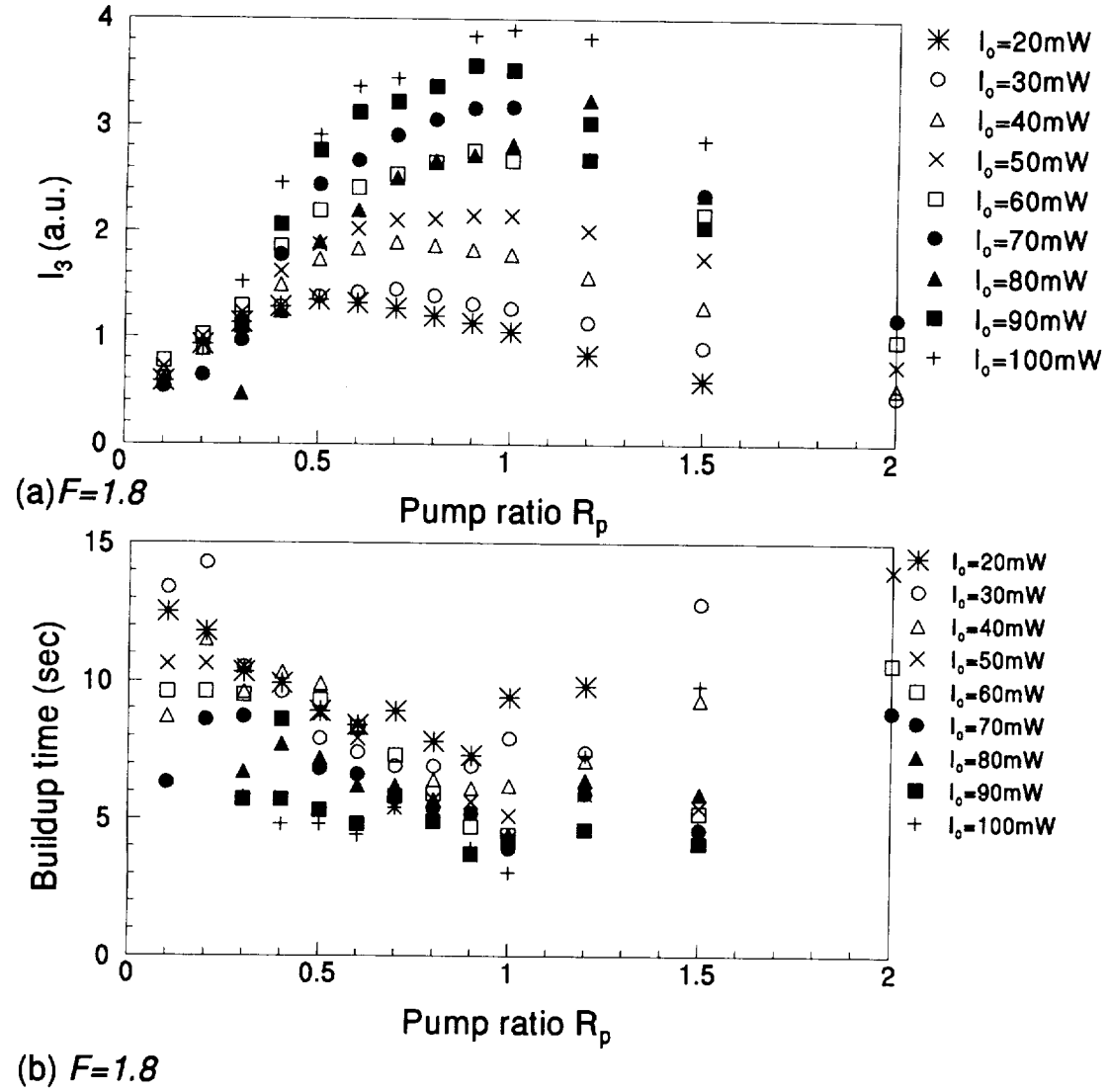
Figure 5.2: (a) Phase conjugate intensity I_3 versus the pump ratio for various values of the total pump power. (b) Buildup time of I_3 versus pump ratio for various values of the total pump power

through the crystal onto three output planes. The local intensities at two different locations in H_1 were measured through ports 1 and 2 by two photomultipliers D1 and D2. The points at which the intensities are measured were selected by two pinholes. Both photomultiplier currents were sent to current-to-voltage amplifiers and to analog filters before being digitized and recorded by a PC based system.

The transverse intensity distribution and its dynamics was recorded via port 3, either by a motorized 35mm camera or a CCD camera connected to a video-tape recorder. The same port and the same modes of recording were also used to record interferograms of the wavefront. To do this, the field in the image plane at port 3 was made to interfere with a tilted plane wave from the same laser.

The cavity output through the phase-conjugate mirror was chosen because of its higher intensity. It is amplified in the crystal. The transverse beam profile and its dynamics were found to be the same in the entire volume of the cavity. This was verified by extracting the left and right propagating cavity beams with the aid of a low loss pellicle beam splitter, and comparing the profiles of these beams with that of the output used for the measurments. The phase conjugate beam exiting the cavity via the conventional mirror had also a similar transverse profile and exhibited the same dynamical behavior.

An additional detector D3 was used to monitor the laser output and check for any spurious correlation between the measured time series and the laser output fluctuations. The output was found to be stable with occasional but very rare mode hops. Since such events would affect the cavity dynamics unpredictably, the data would be trashed when a mode hop occurred during the recording of a time series.

5.2   Time series, Power spectra and Phase space portraits

As we have seen in section 4.1, the state of a dynamical system changes with the value of the control parameters, and, in some cases, the system may become chaotic. Time series, power spectra and phase space portraits are useful tools for examining

the dynamics of a nonlinear system.

In our experiments, time series of the local intensity containing 8,000 data points each were recorded for various values of the Fresnel number. Some representative examples are shown in figure 5.3. A number of characteristic transitions from order to chaos can be identified in this figure.

For tight confinements($F \leq 2$), the irradiance distribution in aperture H_1 observed through the phase-conjugate mirror is uniform and the local intensity is stationary. A first bifurcation occurs near $2 \leq F \leq 2.2$, leading to stable periodic oscillations. As the confinement is relaxed further ($2.2 \leq F \leq 3.5$), more bifurcations occur, leading to more complex but still periodic motions. An example is shown for $F = 3.2$. Eventually, these higher order bifurcations lead the system to a chaotic state near $F \approx 4$. At higher Fresnel numbers ($F \geq 4$), the nature of the dynamics appears to change. At $F = 5.8$ for example, a quasiperiodic state interrupted by chaotic bursts is being observed. Finally, at $F \geq 7$, a new chaotic state sets in.

Time series of 8,000 points may be considered as short, especially near bifurcation or threshold points where critical slowing down might take place. Longer time series, however, would have had a much higher probability of corruption from laser instability, instrumental drift, and mechanical relaxation.

The power spectra of the time series of figure 5.3 are shown in figure 5.4. These spectra reveal information complementing that contained in the time series.

At $F = 2.2$, the motion is clearly periodic with a fundamental frequency f_1=0.106Hz and its higher harmonics. At $F = 3.2$, the spectrum contains, in addition to the fundamental frequency f_1=0.132Hz, all the multiples of the subharmonic $f_1/3$. This is the spectrum of a period three motion. The corresponding time series indeed shows three peaks per period.

As F is increased further and the transverse confinement is relaxed, additional subharmonics appear. At $F \approx 4$ however, a dramatic change occurs. The main feature of the spectrum is now a broadband continuum, a clear sign of an irregular signal. At low frequencies, near 0.055Hz where some new feature seems to have
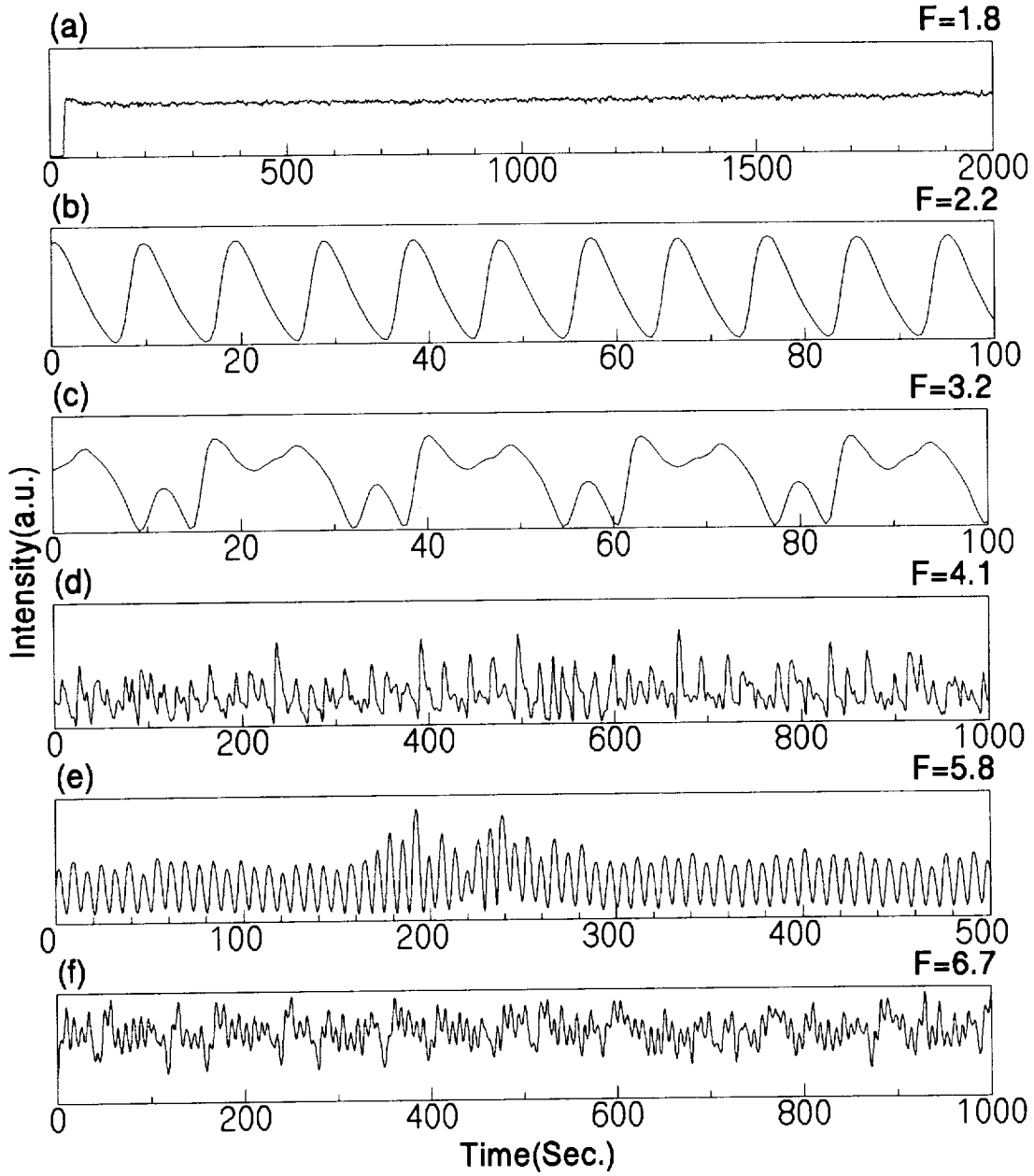
Figure 5.3: Output intensity versus time at a point within aperture H_1, for different values of the Fresnel number F. The total power of the two pumps is 60mW and the pump ratio is 1. The time series shows (a) a stationary output, (b) stable oscillations, (c) the emergence of subharmonics, (d) the development of chaotic oscillations, (e) unstable oscillatory motions with intermittant bursts, and (f) another chaotic motion.
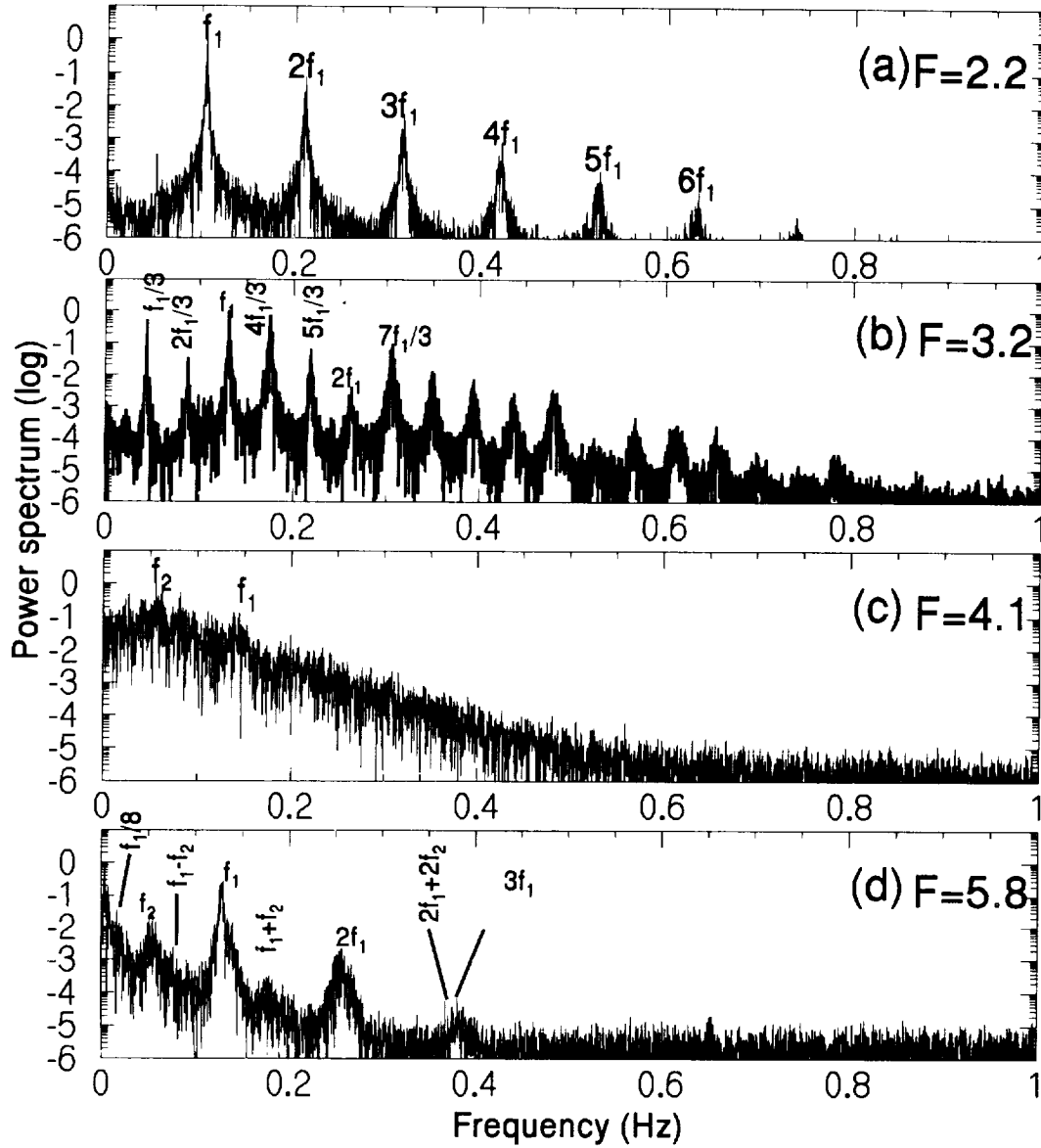
Figure 5.4: Normalized power spectra calculated from the data of Fig 5.3 showing (a) a fundamental frequency and its higher harmonics, (b) a fundamental frequency and its subharmonics multiples of 1/3, (c) a broadband spectrum with the emergence of two frequency peaks, and (d) two broadened frequency peaks and their linear combinations.

appeared in the spectrum, the background is nearly three orders of magnitude above the noise floor. One can thus rule out random noise external to the system and safely attribute the appearance of the continuum to the intrinsic dynamics of the system. At higher frequencies, the power is seen to drop linearly in the semilog plot. This indicates an exponential decay of the power spectrum. Such a spectral feature has been recognised as a signature of deterministic chaos [95].

At $F = 5.8$, the spectral energy is mostly confined near two different frequencies, f_1=0.128Hz and f_2=0.055Hz, and their linear combinations. The continuous background has not entirely disappeared, however. It is interesting to note that these two frequencies can already be seen to emerge from the background at $F = 4.1$. This identification of two frequencies, one of them being the frequency of the original limit cycles and another, apparently unrelated, suggests a route to chaos following the Ruelle-Takens-Newhouse scenario.

As seen in section 4.1.2, the pseudo phase space portraits provide additional information on the dynamical state of the system. According to the Takens's embedding theorem, a pseudo phase space portrait having the same geometrical properties as the original one can be reconstructed from a single time series of experimental data (section 4.2.2). Some examples of pseudo phase space portraits are shown in figure 5.5.

At $F = 1.8$, the phase space portrait is a simple fixed point. A limit cycle is the portrait at $F = 2.2$ as shown in figure 5.5a. The width of the attractor may be attributed to stochastic noise. At $F = 3.2$, a stable period three cycle appears (figure 5.5b). The phase space portrait at $F = 4.1$ is an irregular distribution of points filling up the phase space more or less uniformly (figure 5.5c). The phase space portrait at $F = 5.8$ (figure 5.5d) exhibits some very interesting features indicative of what appears to be an unstable limit cycle surrounded by a cloud of scattered points. As seen in figure 5.6, this phase space portrait corresponds to a time series which is nearly periodic with occasional interruptions by irregular bursts. This behavior is compatible with the Ruelle-Taken-Newhouse scenario in which additional frequencies, unrelated to that of the original limit cycle appear in the spectrum. In this scenario, the bursts are interpreted as a manifestation of type III intermittency [60]. Indeed
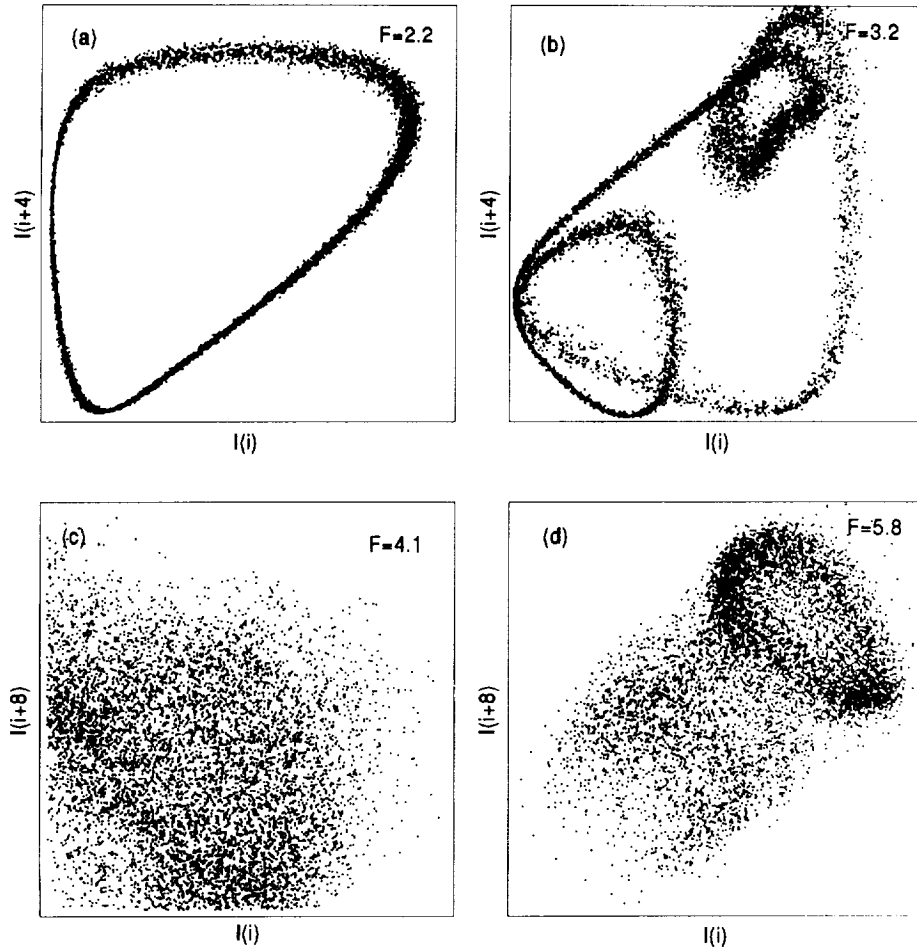
Figure 5.5: Phase space portraits of time series containing N=8000 data points. $I(i)$ is plotted versus $I(i + n)$, with a time delay given by $\Delta t = n\tau$. τ is the sampling interval. One can identify (a)a limit cycle, (b)a stable period 3 motion, (c)an irregular filling of phase space; and (d)an unstable limit cycle smeared by a cloud of irregularly distributed points.
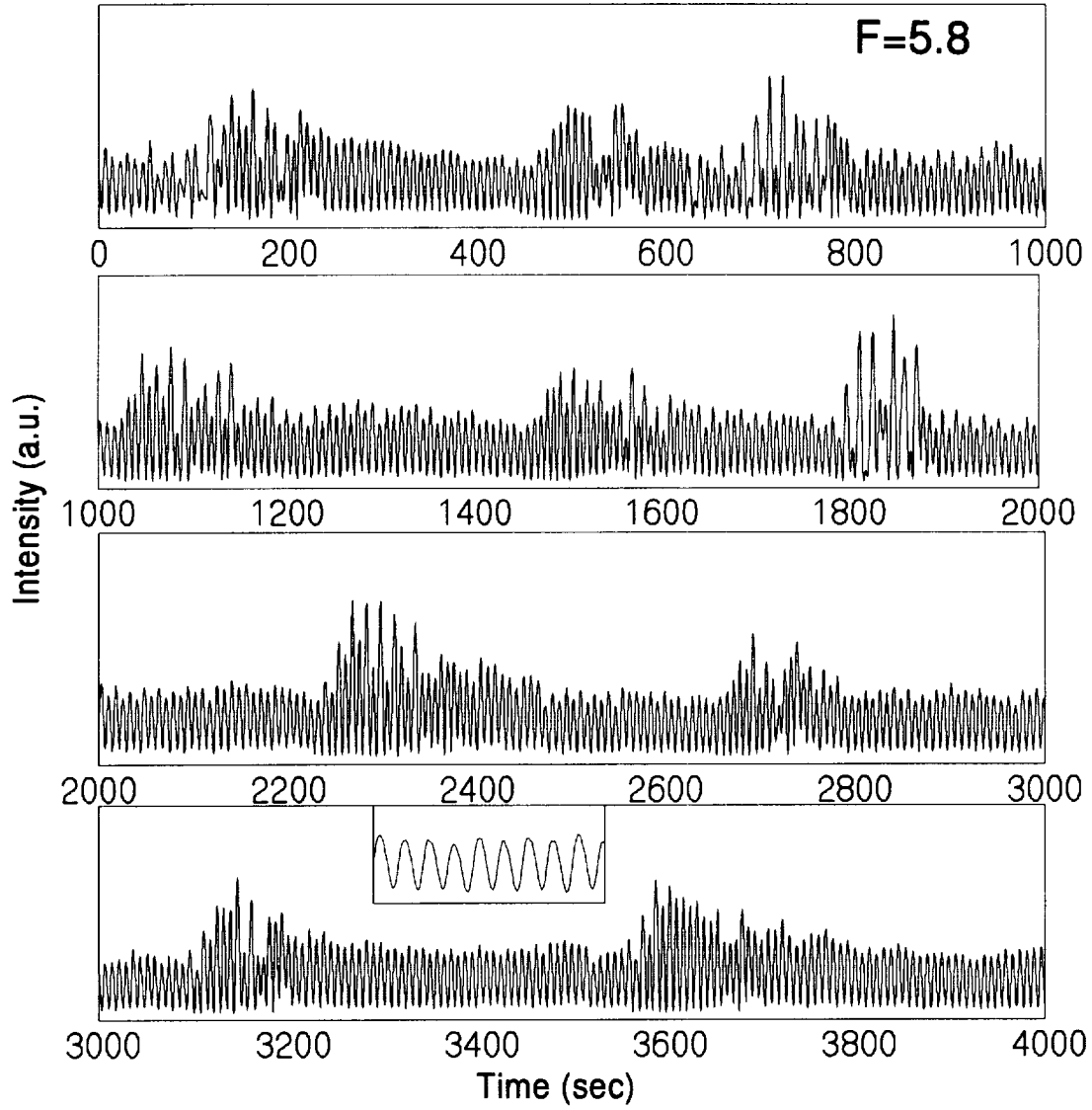
Figure 5.6: Time series of the local intensity for $F = 5.8$ showing a quasiperiodic motion interrupted by intermittent bursts.

some of the intermittent bursts appear to show an increase and then a sudden drop of the amplitude of a subharmonic, which is a signature of type III intermittency.

5.3 Correlation dimension and Kolmogorov entropy

We have seen in section 4.1 that a number of quantitative methods have been established for studing dynamical systems and distinguishing deterministic chaos from random noise. In the following, we analyse quantitatively the nature of the chaotic motion observed with a Fresnel number $F = 4.1$ by calculating the correlation dimension and the corresponding entropy, using the corresponding time series, a section of which is shown in figure 5.3d.

The Grassberger-Procaccia algorithm was used to calculate the correlation dimension of the experimental chaotic time series [96]. This algorithm is based on the Takens embedding theorem according to which N vectors $\vec{X}(t_n) = [X(t_n), X(t_n + \Delta t), \ldots, X(t_n + (d-1)\Delta t)]$ of length d (the embedding dimension) can be extracted from the time series and used to reconstruct the attractor in a pseudo d-dimensional phase space. The delay $\Delta t = i\tau$, where τ is the sampling interval, is chosen such that the choice of τ is made according to the remarks explained in section 4.2.2.

The correlation function or second order correlation integral is then calculated as (see section 4.2):

$$C_2(\epsilon, d) = \frac{1}{N^2} \sum_{m,n=1}^{N} \theta(\epsilon - z_{m,n}),$$ (5.2)

where θ is a step function and $z_{m,n} = \sum_{i=0}^{d-1} |X_{n+i} - X_{m+i}|^2$ is the Euclidean distance between the pair of vectors m, n and d is the embedding dimension. The correlation integral thus measures the number of pairs of vectors with a distance smaller than ϵ. From equation 4.23, the correlation integral scales with the embedding dimension as

$$C_2(\epsilon, d) \propto \epsilon^\nu \exp(-d\tau K_2).$$ (5.3)

For large enough d and small ϵ, the correlation exponent ν becomes the correlation dimension D_2. K_2 is the second order Renyi entropy. These two quantities are lower

bounds to the fractal (Hausdorff) dimension D_o of the attractor and to the information dimension D_1 ($D_o \geq D_1 \geq D_2$), and to the Kolmogorov entropy K_1 ($K_1 > K_2$), respectively (see section 4.1).

Figure 5.7 shows log-log plots of the correlation integral for values of the embedding dimension ranging from 7 to 27. The slope of the curves, which is the correlation exponent according to eq. 5.2, appears to converge toward what is believed to be the value of the correlation dimension D_2. The local slope, calculated using a seven point local average of the slope of the data of figure 5.7, is shown in figure 5.8 for different values of d. Although the plateau, which should indicate the value of D_2, is not very broad, it does seem to converge, for $d \geq 20$, toward a value approximately equal to 5.2, as shown in figure 5.9.

According to eq. 5.3, a lower bound to the Kolmogorov entropy can also be extracted from the data of figure 5.7 by calculating the rate at which the correlation integral drops with increasing values of the embedding dimension. In section 4.2.1 we discussed briefly that the Kolmogorov entropy measures the rate of information flow in the dynamical system and is an indication of the system's sensitivity to initial conditions. In an ordered system, it is expected to be zero, while in a stochastic system, it should be infinite. For a deterministic chaos, its value would be finite and positive. Figure 5.10 shows a plot of K_2 versus d. Again, for $d \geq 20$, the entropy appears to converge toward a value approximately equal to 0.16 s^{-1}.

Although the relatively large value found for the correlation dimension may possibly put in doubt the validity of the algorithm used to calculate it, both the finite positive lower bound to the Kolmogrov entropy and the non-integer value of the correlation dimension seem to provide some evidence for the existence of a strange attractor for the time series at $F = 4.1$.
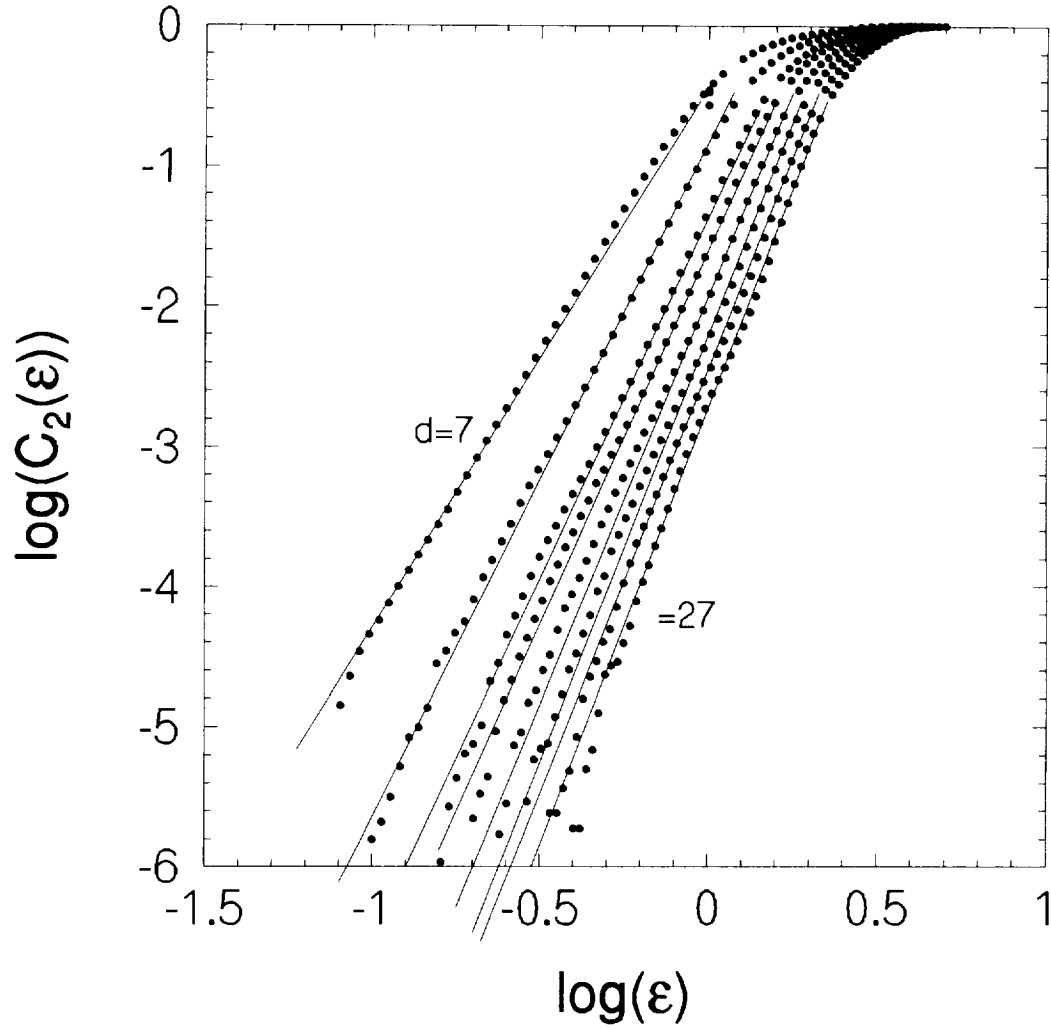
Figure 5.7: Log-log plots of the correlation integral $C_2(\epsilon)$ versus distance ϵ, with increasing values of the embedding dimension d, for the chaotic output of Fig 5.7.
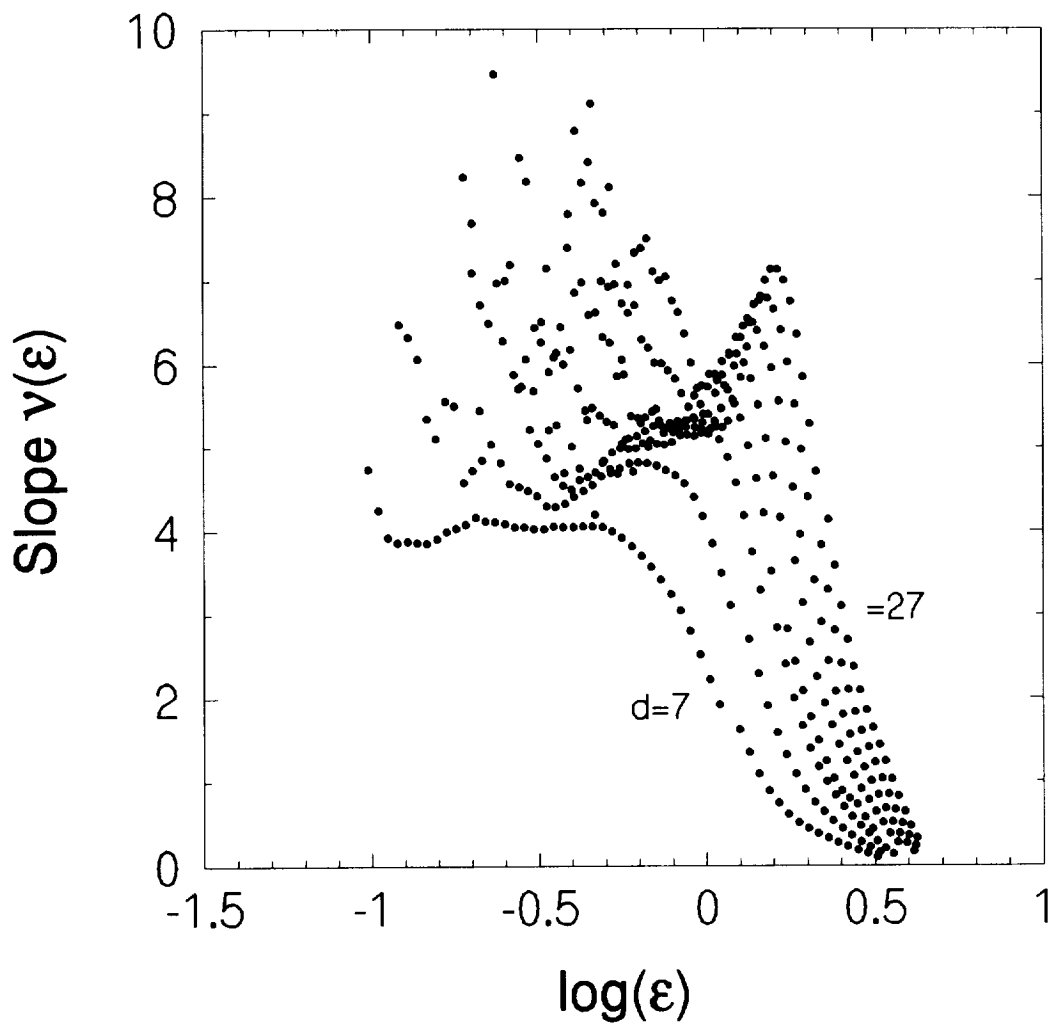
Figure 5.8: Local slope $\nu(\epsilon)$ of the correlation integral of Fig 5.7. versus $\log \epsilon$. The slopes are averaged over 7 local points. The plateau indicates the range of linear scaling for each d. The slope in the region of the plateau converges toward the correlation dimension D_2.
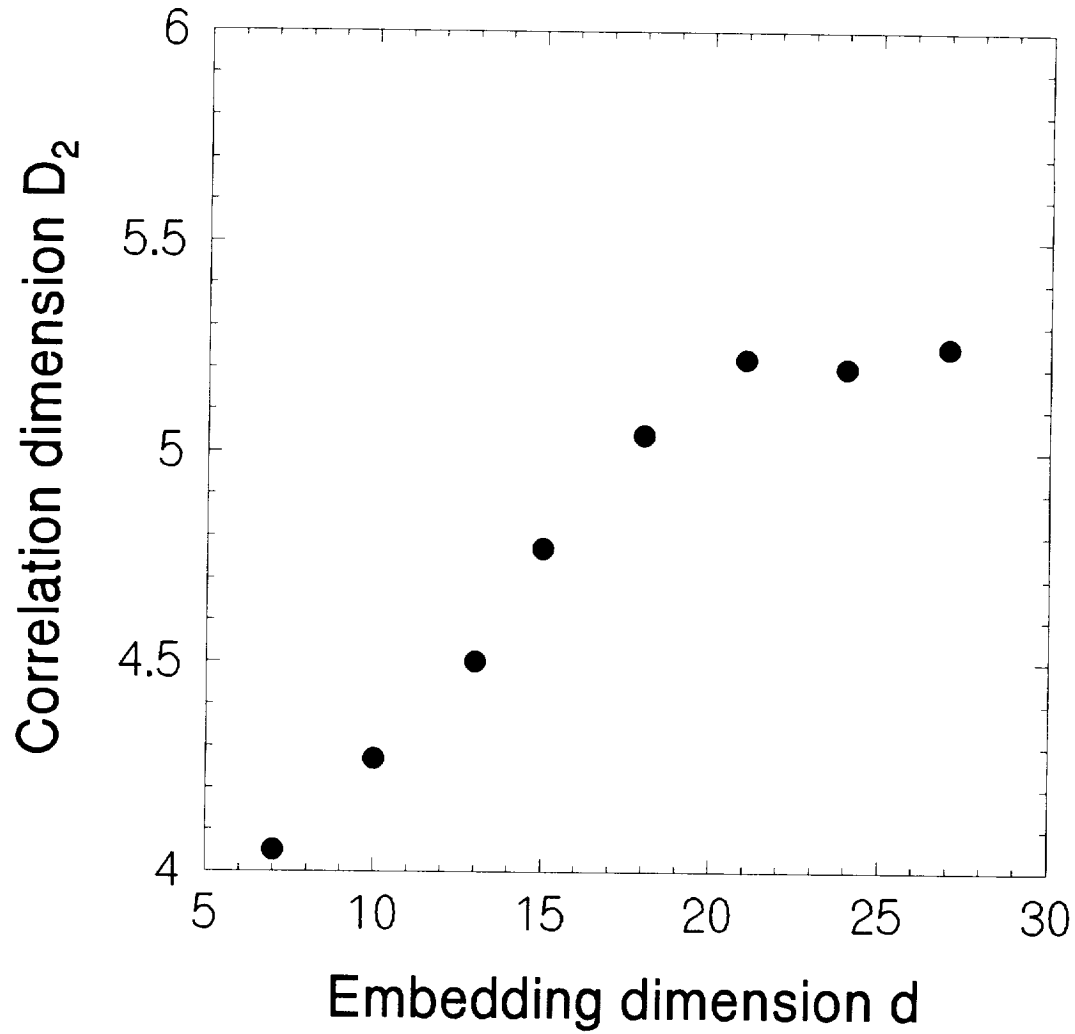
Figure 5.9: Plot of the correlation dimension for each embedding dimension d of Fig 5.7. The correlation dimension appears to converge to a value $D_2 \approx 5.2$.
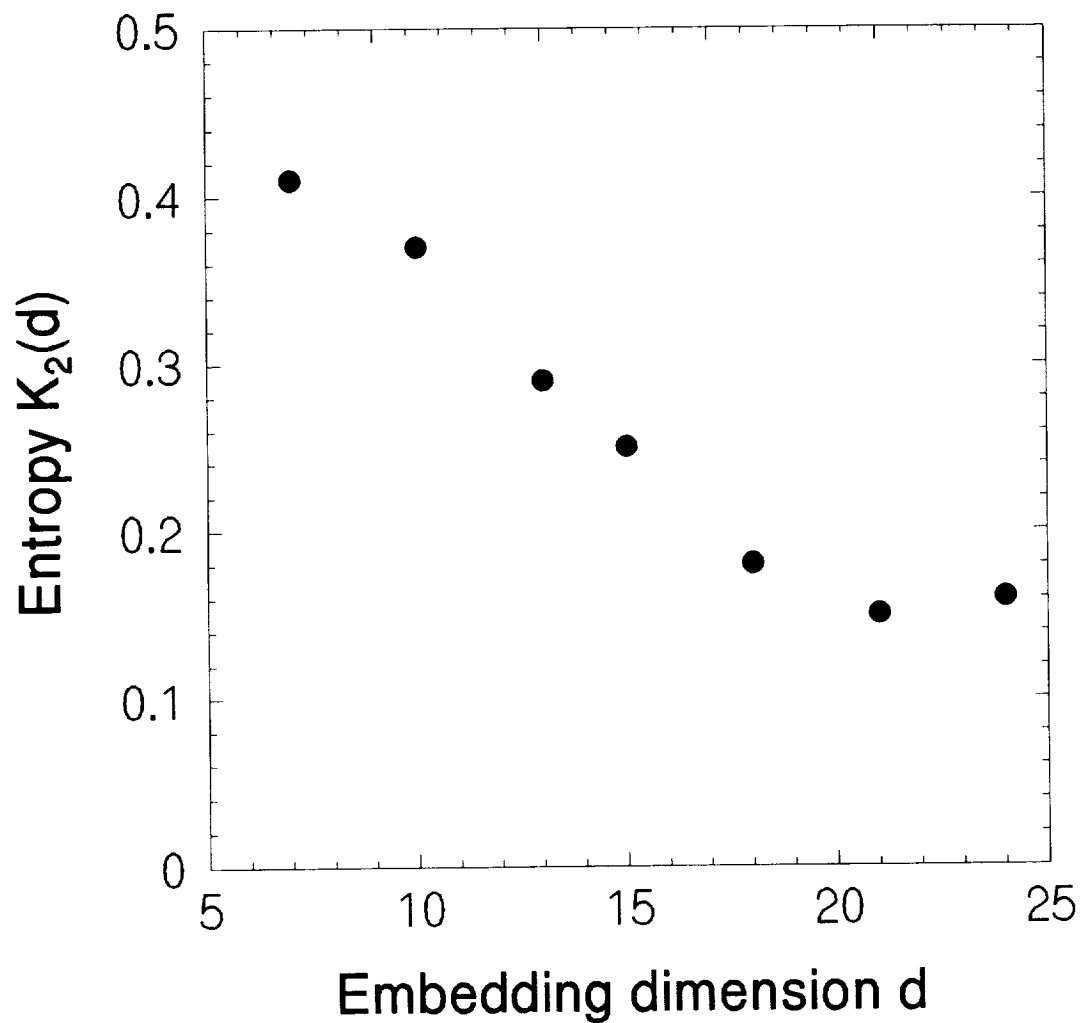
Figure 5.10: Value of the entropy $K_{2,d}$ calculated from the data of Fig 5.7, versus the embedding dimension d, averaged over the linear scaling region in ϵ. The asymptotic value $K_2 \approx 0.16s^{-1}$, is a lower bound to the Kolmogorov entropy.

5.4 Wavefront dislocations

The transverse irradiance distribution within the aperture H_1 as seen through the PCM was recorded as a function of time. As the transverse confinement of the system is relaxed, the distribution of structures across the PCR's beams becomes more complex, containing more and more bright lobes and dark lines around them. At the same time, the motion of the structures also increases in complexity, changing from a simple periodic motion to an apparently chaotic dance.

Interferograms of the wavefront were recorded to reveal the presence of wavefront dislocations or vortices [87] (also see section 4.4). In the interferograms, the defects should appear as a discontinuity in the interference fringes and thus should be easily identifiable. The number of defects and the complexity of their motions in time were found to be strongly correlated to the temporal dynamics of the time series described in section 5.2 as well as to the spatial decorrelation of the pattern. This suggests that the topological defects may indeed act as the catalyst for the observed spatiotemporal dynamics and induce the observed turbulence in a manner similar to that of the so-called topological turbulence (see section 4.3.2). In this section, we will describe how the transverse pattern changes when the Fresnel number, and thus the transverse confinement of the cavity, is varied.

After a first bifurcation at $2 \leq F \leq 2.2$, the transverse pattern varies in time in a simple and periodic way. Some snapshots of the irradiance distribution, taken at a half second interval between frames, are shown in figure 5.11. The irradiance distribution is at first uniform, both in amplitude and phase. This lasts for about eight seconds, after which time a folding of the phase appears at the center of the pattern. This is manifested by a darkening of the area. Very rapidly, a pair of defects of opposite charge develops from this fold at the center of the pattern. The two defects split and repel each other, swiftly moving away along diametrically opposite directions. They finally disappear at the boundary. The presence of the defects lasts only about two seconds or so. The wavefront then quickly recovers and remains stable for a period of time. Then, the sequence repeats itself. Figure 5.12 is an enlarged
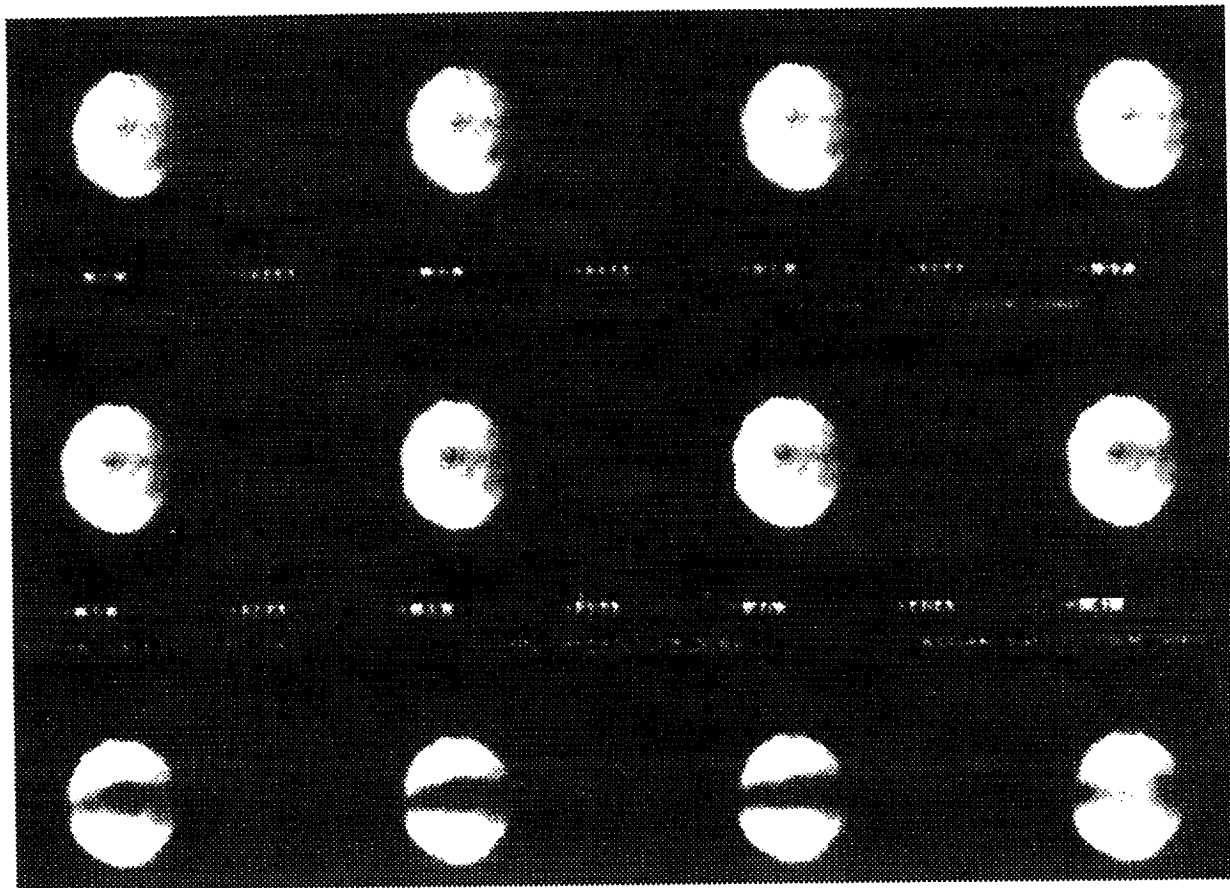
Figure 5.11: Sequence of snapshots of the irradiance distribution in aperture H_1 with $F = 2.2$. The time interval between sanpshots is 0.5 second.
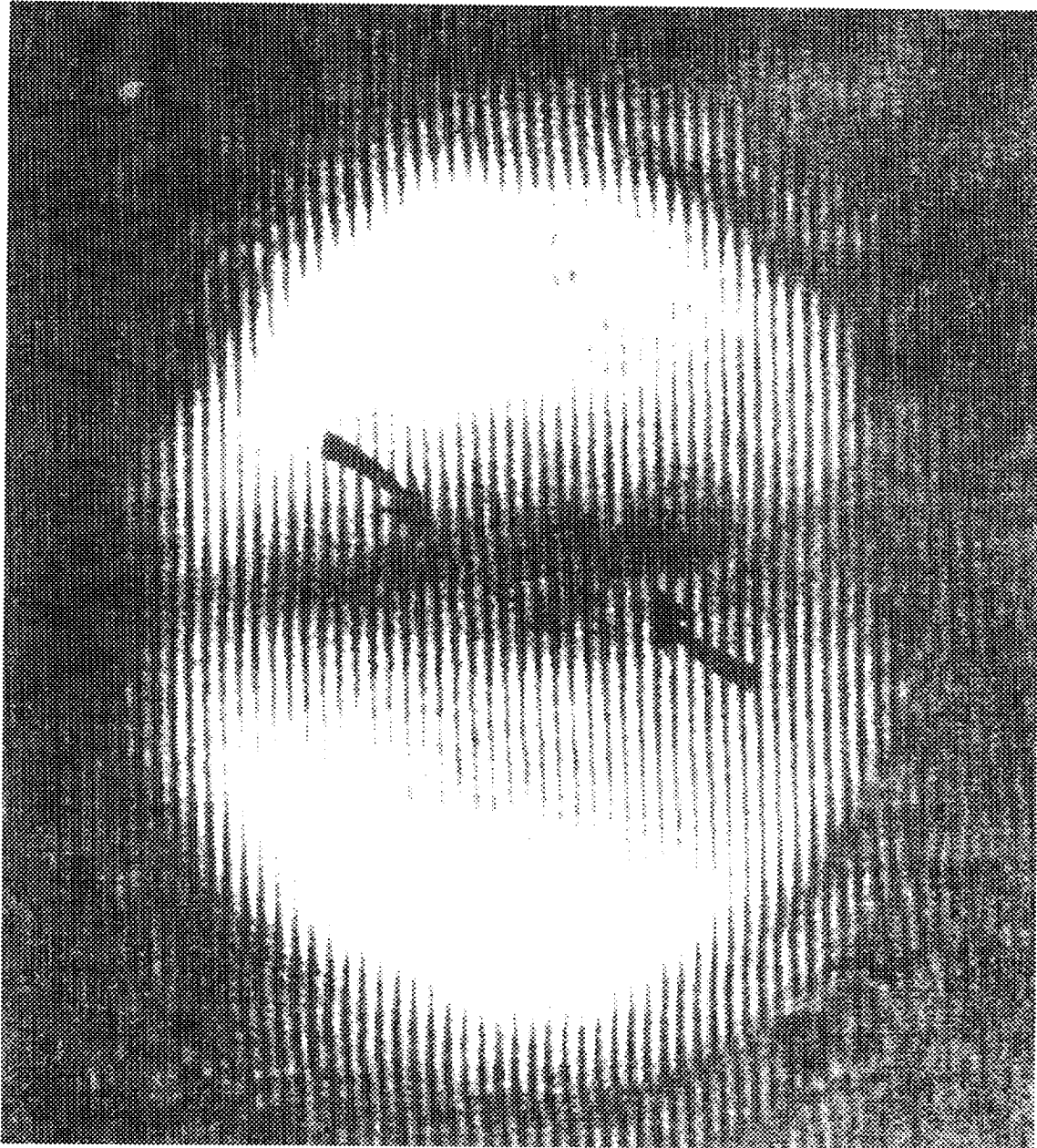
Figure 5.12: Instantaneous interferogram with $F = 2.2$ showing a pair of defects of opposite charge.

snapshot of an interferogram obtained by interfering the output distribution with a tilted plane wave and showing the pair of defects of opposite charge moving away from each other and along a horizontal diameter.

As the transverse confinement of the system is relaxed, more complex behaviors are observed. At $F = 3.6$, for example, the motion of the transverse pattern is more complex but still periodic. This explains the appearance of the subharmonics in the time series of the local intensity (Fig. 5.3). A sequence of snapshots taken at half second intervals is shown in figure 5.13. Figure 5.14 is an enlarged interferogram showing three pairs of defects of opposite charge.

A number of characteristic motions of the defects were observed for $2.2 \leq F \leq 5$. Some of them are illustrated schematically in figure 5.15. Figure 5.15a corresponds to the motion described in figure 5.11. In fig. 5.15b, the two defects of a pair are seen to spiral outward, away from each other, and then inward toward each other, along trajectories of alternating handedness. Figure 5.15c describes a motion similar to that of figure 5.13. Pairs of defects are generated at two diametrically opposite locations. The two inner defects spiral toward each other while the other two spiral outward and die at the boundary. The two inner defects may rebound, repel each other and accelerate outward along a diameter. The sequence then repeats itself with other pairs of defects originating at conjugate locations and with trajectories of opposite handedness. Figure 5.15d shows another dance of similar nature, where several pairs of defects are generated, move, rotate, collide, rebound or annihilate each other.

The motions described in the preceding paragraph may appear in sequence, when the dynamics is periodic. They may also appear in an apparently random order. This is the case for $F = 4.1$, which, as seen in section 5.2, corresponds to a chaotic time series. Figure 5.16 shows some snapshots (0.5 second interval) of the nonperiodic motion at $F = 4.1$. Figure 5.17 is an enlarged interferogram showing the presence of four pairs of defects.

All the patterns with low enough Fresnel numbers have a center of symmetry. We believe that this is a result of the particular geometry of the cavity and of the nature
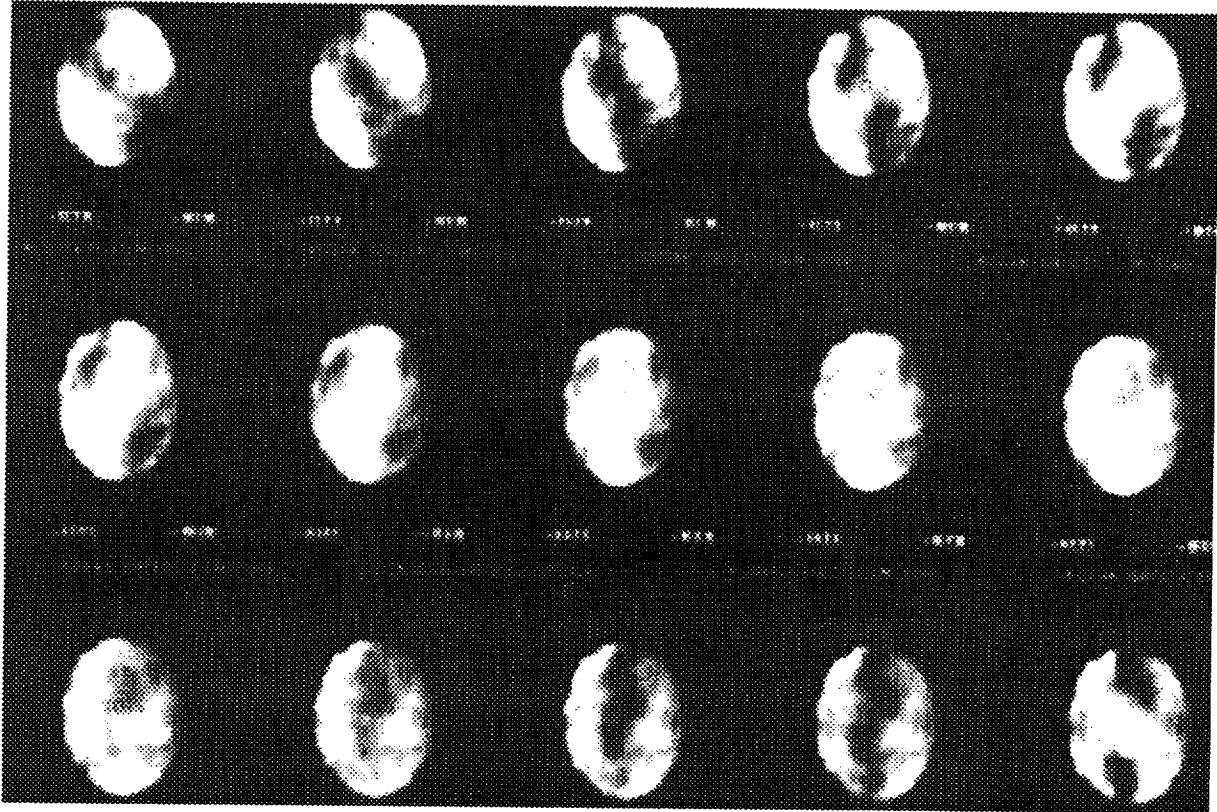
Figure 5.13: Sequence of snapshots with $F = 3.6$ (time interval $= 0.5$s) revealing a more complicated but still periodic motion.

Figure 5.14: Instantaneous interferogram with $F = 3.6$ showing three pairs of defects.
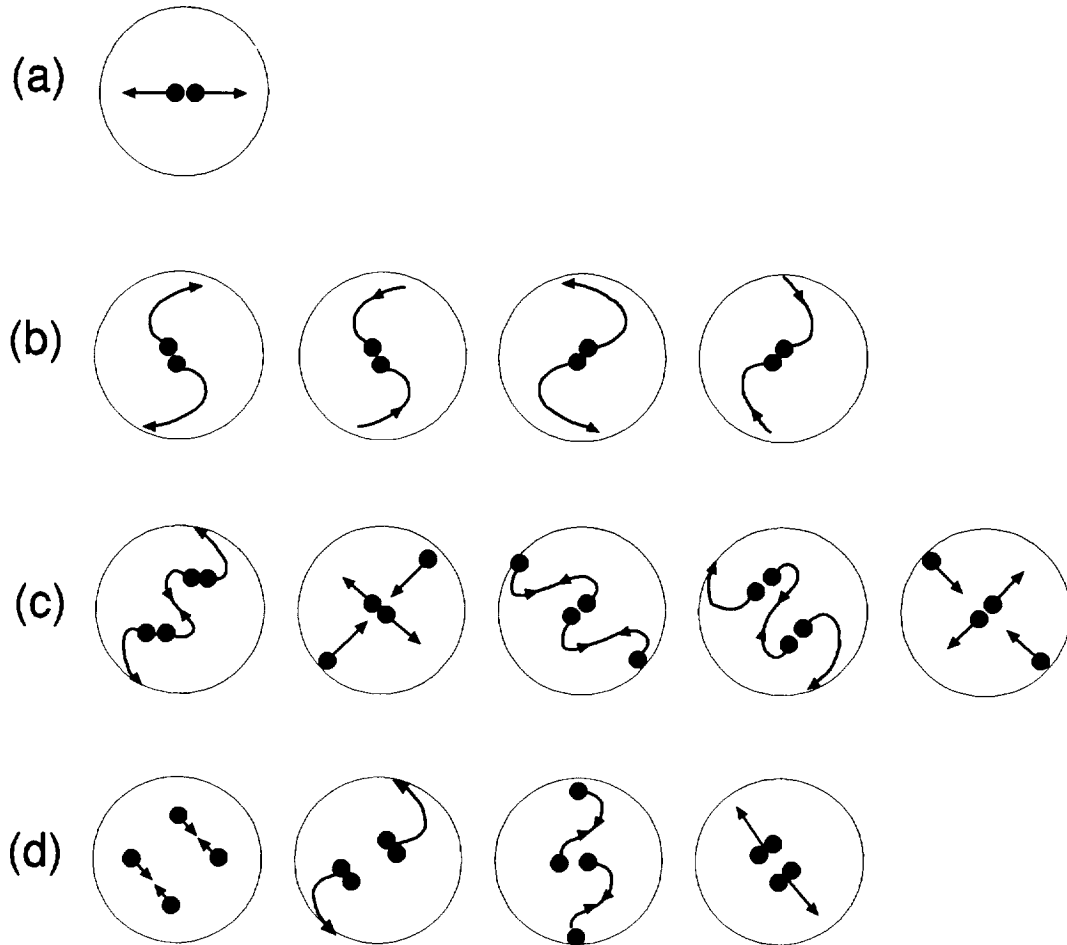
Figure 5.15: Sketches of some typical motions of the defects observed with $2 \leq F \leq 5$. See text for details.
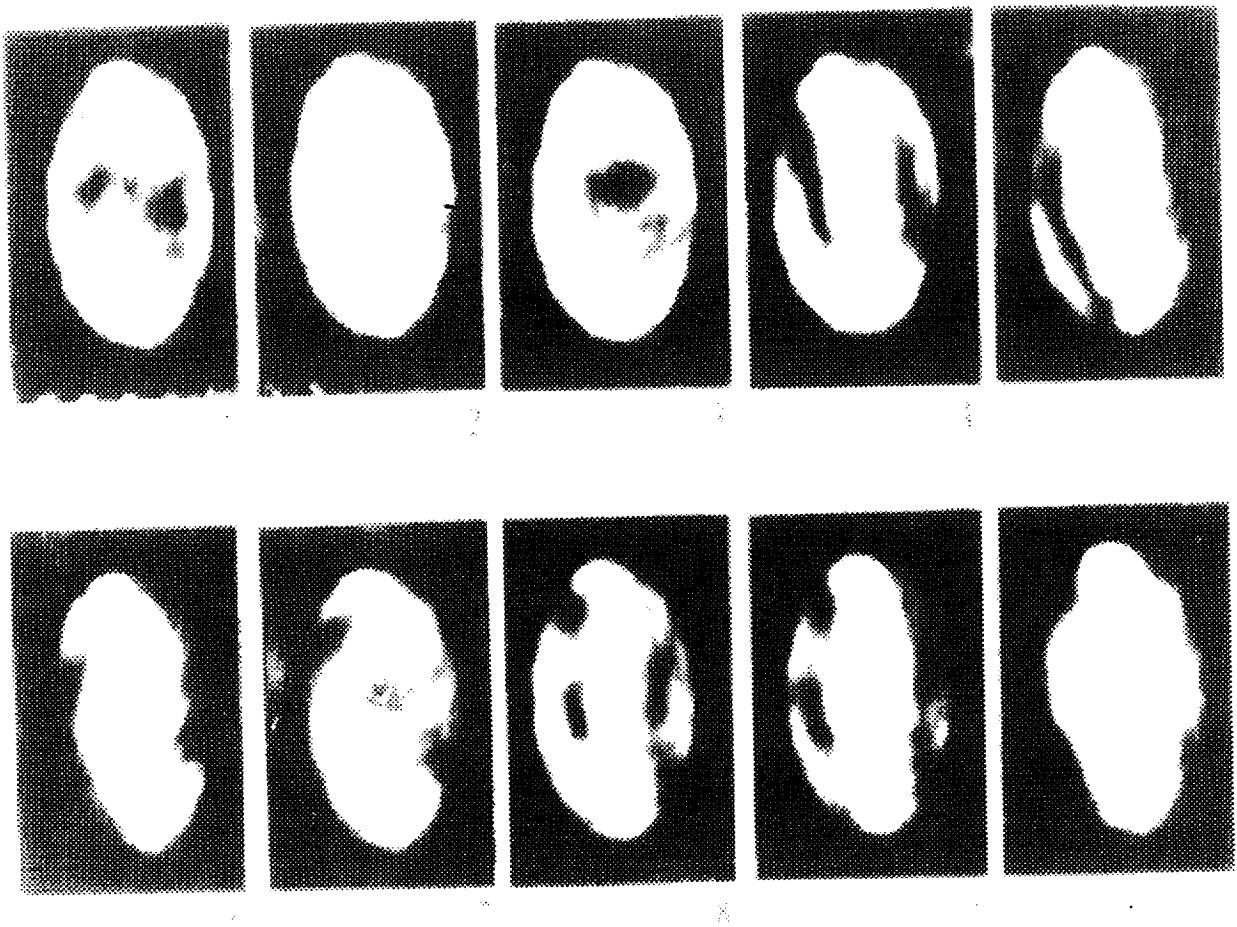
Figure 5.16: Sequence of snapshots with $F = 4.1$ (time interval $=0.5$s) revealing a nonperiodic motion (horizontal scale compressed).

Figure 5.17: Instantaneous interferogram with $F = 4.1$ showing four pairs of defects.

of the PCM. Indeed, one round trip in the cavity involves two operations: phase conjugation and imaging with unit magnification and inversion. Thus, if a certain distribution $f(\vec{r})$ exists in the cavity, another $f^*(-\vec{r})$ should also be present, at least in steady state.

In the range $5 \leq F \leq 6$, drastic changes in the dynamics of the local intensity time series were observed. Similar changes are also found in the behavior of the defects. At $F = 5.8$, for example, the spatial distribution shown in the sequence of figure 5.18 is rather complex and indeed shows more structure than the pattern at $F = 4.1$ (Fig. 5.17), which corresponds to a chaotic motion. However, not all the dark lines in figure 5.18 contains true zeros. Thus, when $F = 5.8$, the number of defects is actually smaller on average and the spatiotemporal complexity is lower than when $F = 4.1$. The motion for interferograms at $F = 5.8$ is also simpler in appearance. Figure 5.19 shows an instantaneous interferogram at $F = 5.8$, where only one pair of defects is visible. When the transverse confinement is further relaxed, the motion becomes chaotic again (Fig. 5.3f). Figure 5.20 shows an interferogram obtained with a Fresnel number $F = 8.6$ and in which about eight pairs of defects are seen as they execute a chaotic dance.

5.5 Defect-mediated turbulence

It appears, from the observations described in figures 5.11 to 5.20 and the corresponding results of section 5.2, that the presence and the motion of singular points in the wavefront (the phase defects or vortices), where both the real and the imaginary parts of the field vanish and the phase is indeterminate (see section 4.4), may be responsible for the loss of spatiotemporal coherence. According to the Coullet conjecture, this in turn may induce turbulence in weakly coupled systems [79, 78, 80, 97]. In order to further illustrate the correlation between the number of defects and the spatiotemporal dynamical behavior of the system, the following two measurements were made.

The temporal evolution of the interferograms obtained with increasing Fresnel
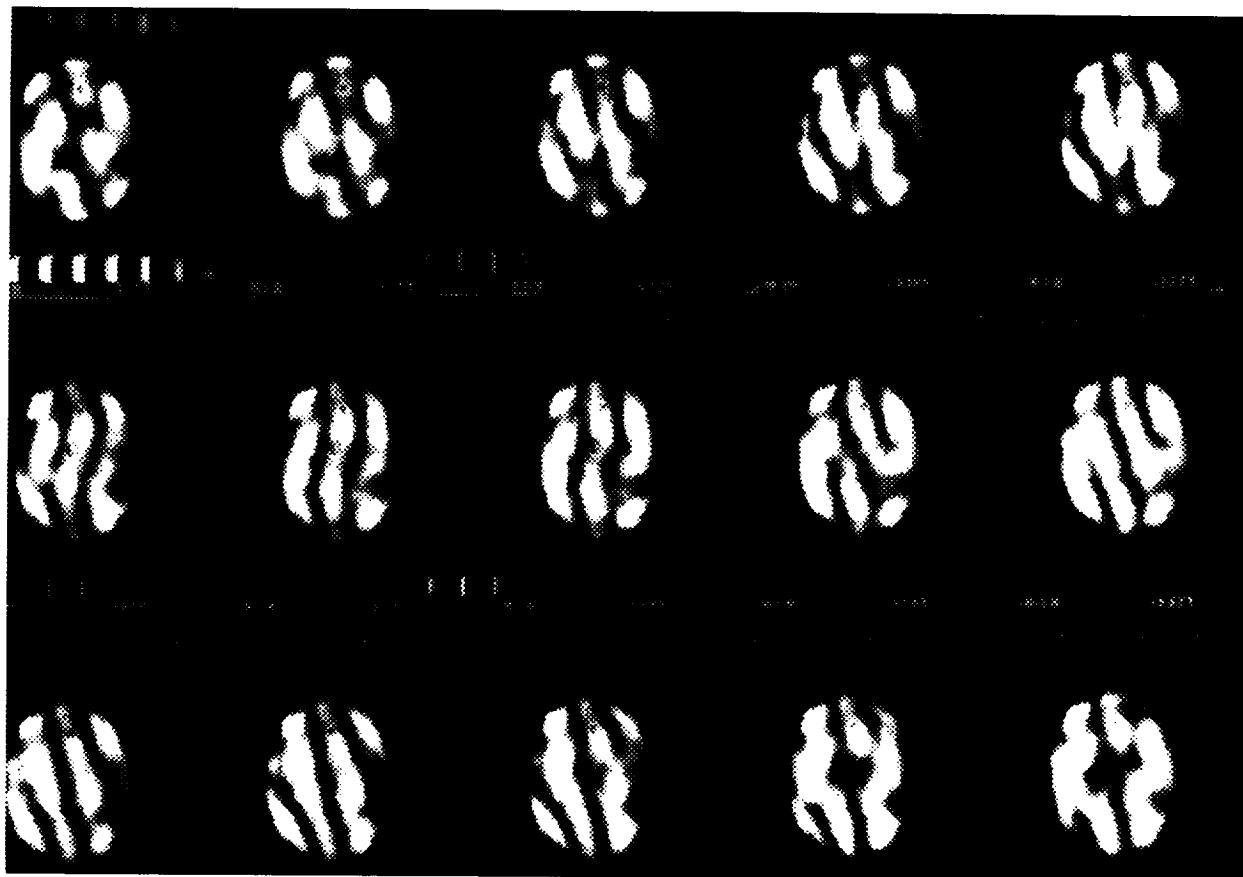
Figure 5.18: Sequence of snapshots with $F = 5.8$ (time interval $= 0.5$s) revealing a more complicated pattern but executing a simpler motion
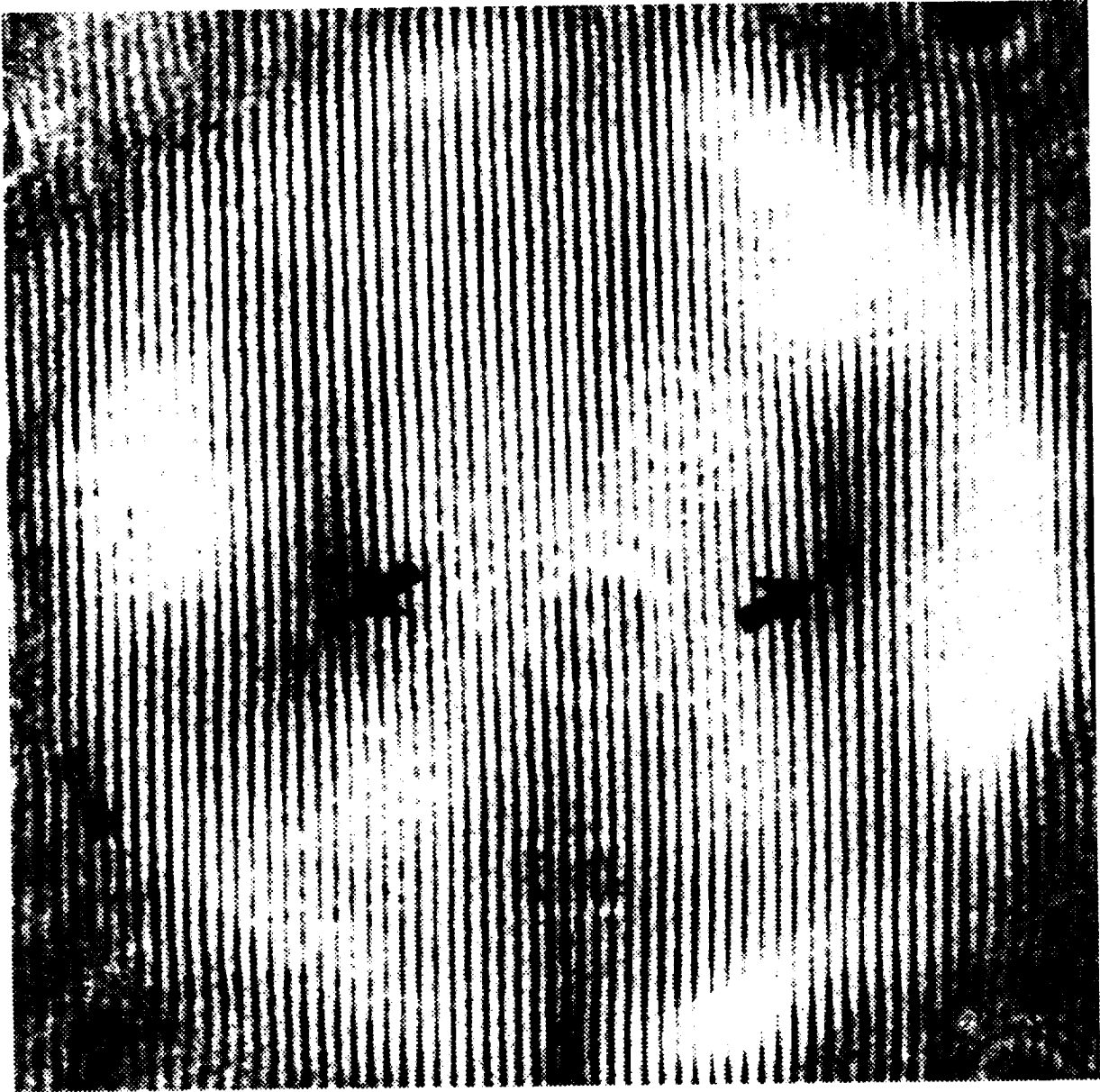
Figure 5.19: Instantaneous interferogram with $F = 5.8$, showing only one pair of defects.
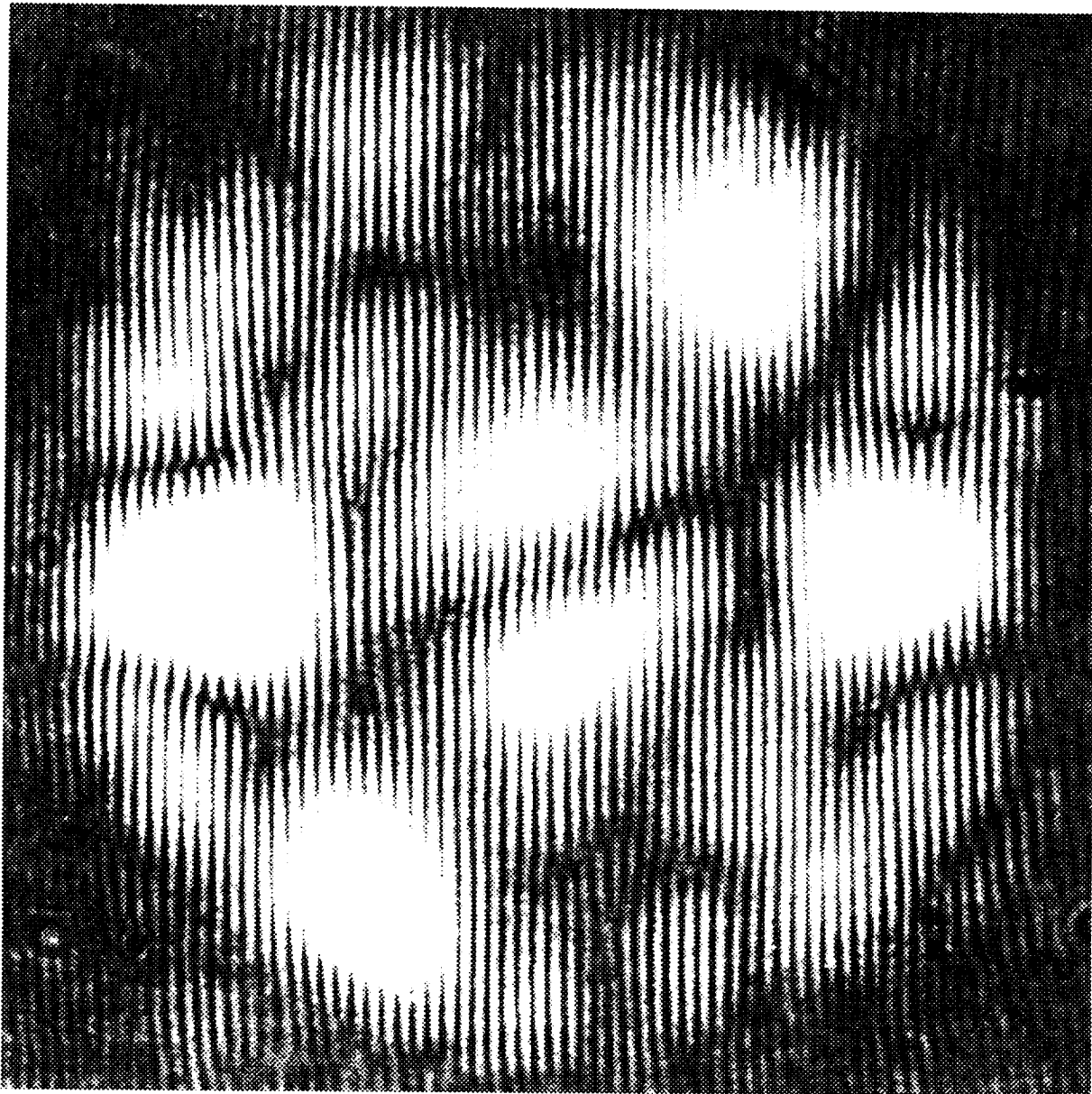
Figure 5.20: Instantaneous interferogram with $F = 8.6$ showing at least 8 pairs of defects executing a chaotic dance.
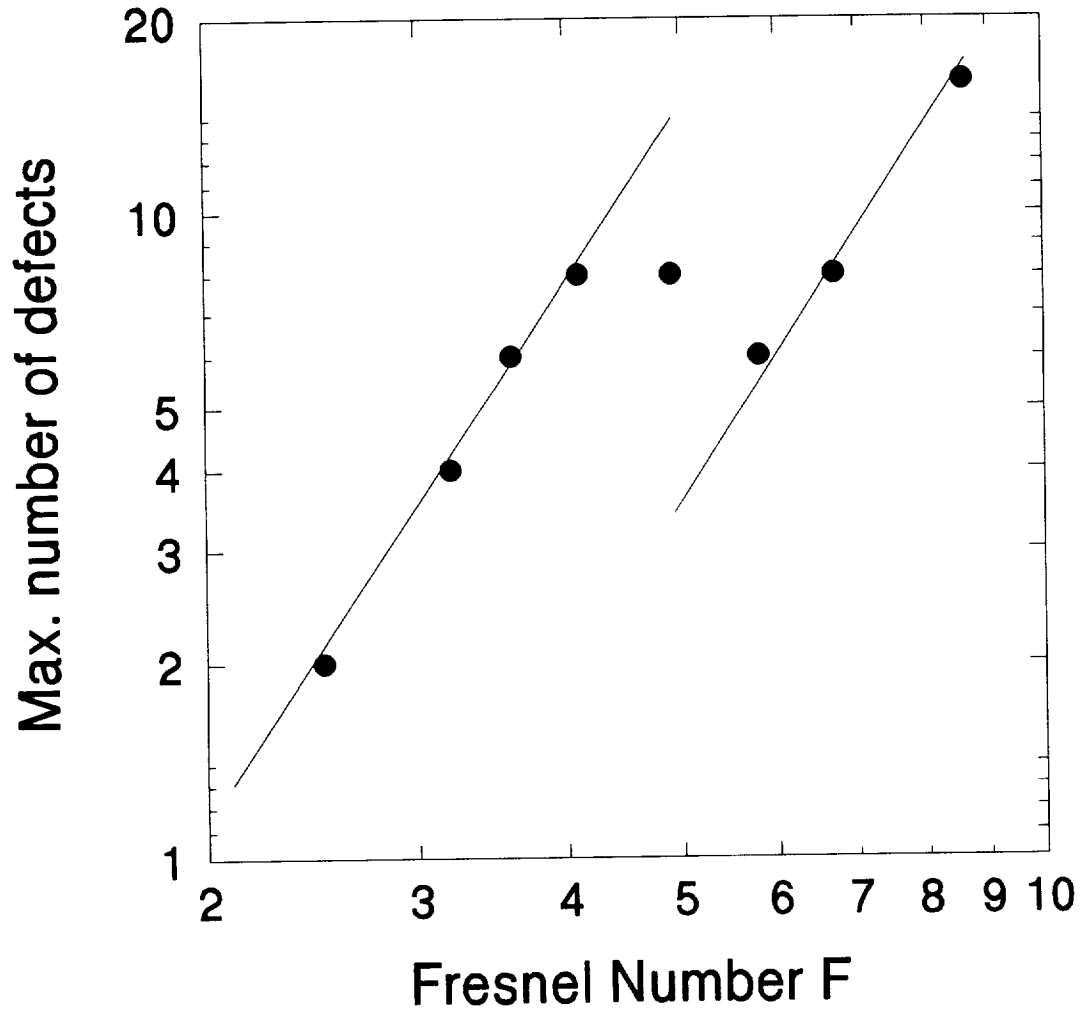
Figure 5.21: Maximum number N of defects observed in the transverse pattern at any given time versus Fresnel number F. The expected scaling law $N \propto F^2$ is interrupted in the region $4 < F < 6$.

numbers were video recorded with a standard CCD camera and examined frame by frame to determine the maximum number of defects appearing in the pattern at any instant of time. The result is shown in figure 5.21. There are two regions, $2 \leq F \leq 4$ and $F \geq 6$, where the maximum number of defects appears to grow as the square of the Fresnel number. This dependence is what is expected if, using simple diffraction arguments, F^2 is interpreted as being a measure of the maximum number of speckles (or of bright lobes) within a cross section of the beam. The number of true zeros between the bright speckles is expected to be of the same order as the number of speckles, at least for large numbers [91, 87].

In addition, the temporal fluctuations of the local intensity were recorded at two different locations in aperture H_1, and a spatial correlation index [98] was calculated.

The spatial correlation function is defined as

$$C(\vec{r}_1, \vec{r}_2, \Gamma) = \frac{\sum_{n=1}^{N} [I(\vec{r}_1, n) - \bar{I}(\vec{r}_1)][I(\vec{r}_2, n + \Gamma) - \bar{I}(\vec{r}_2)]}{S(\vec{r}_1) S(\vec{r}_2)}, \qquad (5.4)$$

with

$$S(\vec{r}_j) = \left\{ \sum_{n=1}^{N} [I(\vec{r}_j, n) - \bar{I}(\vec{r}_j)]^2 \right\}^{1/2}, \qquad (5.5)$$

where $\vec{r}_1$, $\vec{r}_2$ are the two locations in the wavefront where the local intensity fluctuations are measured, $\bar{I}(\vec{r}_j)$ is the time averaged intensity at $\vec{r}_j$, n and Γ are the running time and time delay, respectively, measured in units of the sampling interval τ.

In the experiments, the local intensity fluctuations were measured at two points only, distant by approximately one half the diameter of aperture H_1. A spatial correlation index can then be defined as

$$K(|\vec{r}_1 - \vec{r}_2|) = \text{Max} C(\vec{r}_1, \vec{r}_2, \Gamma), \qquad \forall \Gamma. \qquad (5.6)$$

The correlation index runs from 0 to 1. It is high when the fluctuations at $\vec{r}_1$ and $\vec{r}_2$ are highly correlated. It is equal to one when the fluctuations at $\vec{r}_1$ and $\vec{r}_2$ differ only by a time delay, as one would expect if a transverse wave sweeps through the pattern. It drops to small values as the fluctuations at $\vec{r}_1$ and $\vec{r}_2$ become decorrelated.
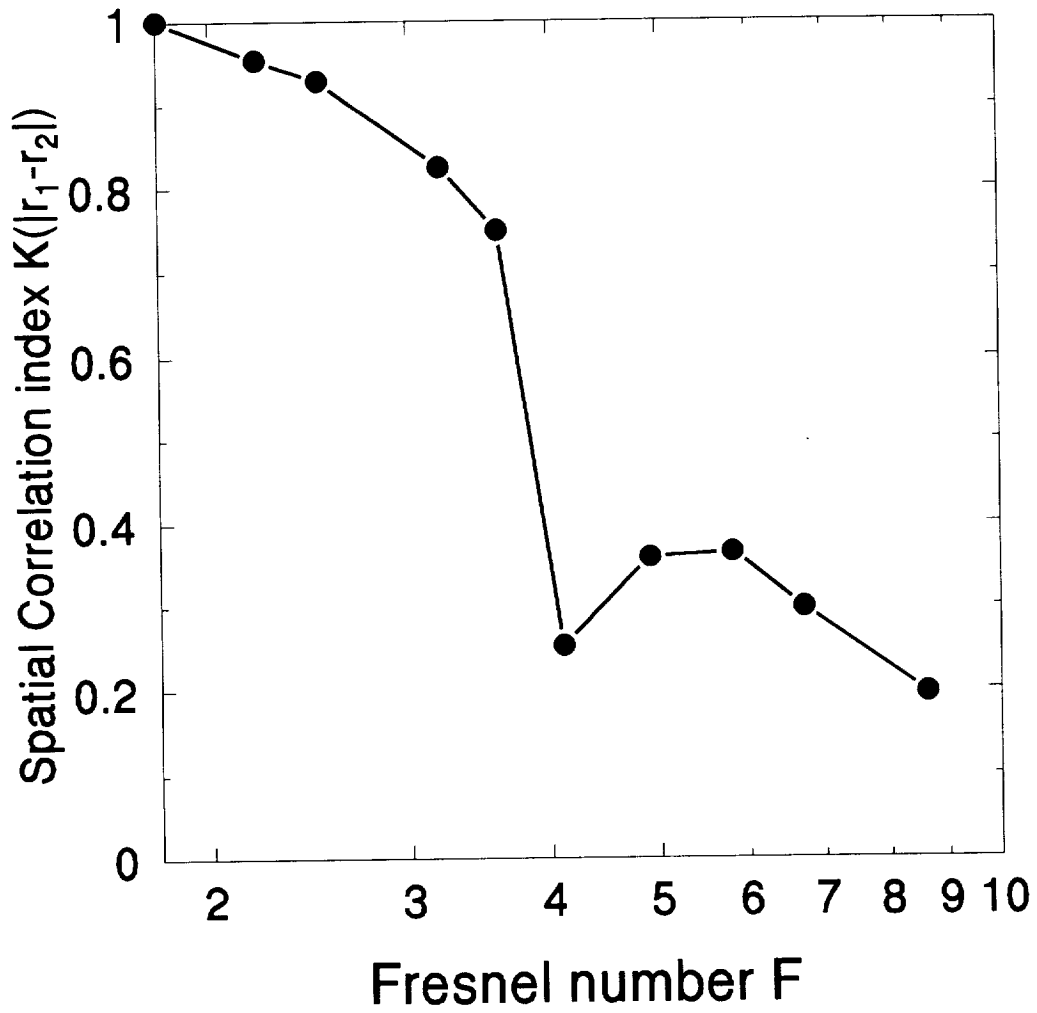
Figure 5.22: Spatial correlation index versus Fresnel number F. Comparison with Fig. 5.21 reveals the relationship between the spatial correlation and the number of defects.

The result is shown in figure 5.22. The interesting point is the correlation between the index K and the number of defects (which measures the degree of spatial complexity), as the Fresnel number increases (i.e. , as the confinement of the system is relaxed). At first (Fig. 5.22), the correlation index drops, as one would expect. Near $F \sim 4$, where the first chaotic state appears, the correlation index drops drastically to a small value. In the range $4 \le F \le 6$, where the spatial complexity, as measured by the number of defects decreases (Fig. 5.21), the spatial correlation index is seen to increase (Fig. 5.22). The correlation index reaches a local maximum at exactly the same Fresnel number (~ 5.8) that leads to a local minimum in the number of defects. These observations seem to indicate that the loss of spatiotemporal coherence and the subsequent onset of turbulence in the phase-conjugate resonator is indeed mediated by the dynamics of the phase defects appearing in the wavefronts.

5.6 Modes superposition

Some of the transverse patterns observed are reminiscent of the common transverse electro-magnetic modes of a laser cavity. It is interesting to try to correlate our observations with the dynamical behavior of a few superposed cavity modes. The simpler motions observed at low Fresnel numbers could be interpreted as a sequential succession of a few modes of low order similar to the alternation described in reference [99]. This interpretation seems to be confirmed by the high spatial correlation of these patterns. In addition, we have observed that the introduction of selective losses in the cavity can be used to suppress the oscillation of certain modes and lock the beam into an almost stationary pattern. At higher Fresnel numbers, when the motion becomes chaotic, the lack of spatial correlation seems to point to the coexistence of a number of uncorrelated modes as opposed to the alternation of modes of higher orders. The highly structured pattern observed at $F \sim 5.8$, with its higher spatial correlation and smaller number of defects, may however be due to the superposition or alternation of a small number of modes of higher orders.

It is intriguing to ask whether a superposition of several modes with different

frequencies could produce patterns in which the defects would move around in a manner similar to the motions described in section 5.4.

As an illustrative example we used a superposition of three Gauss-Hermite modes of the form

$$E_{mn}(x, y; t) = A_{mn} U_m \left(\frac{\sqrt{2}x}{w} \right) U_n \left(\frac{\sqrt{2}y}{w} \right) \exp \left\{ i(\delta_{mn}t + \phi_{mn}) - \frac{x^2 + y^2}{w^2} \right\}, \quad (5.7)$$

where the U_j's are Hermite polynomials, w is the beam "waist", $\phi_{mn} = (m + n + 1)\eta$ and $\eta = \pi/3$ (arbitrary choice), δ_{mn} is the frequency detuning and A_{mn} is the weight of mode mn [94].

We chose the three modes TEM 01, 10, and 20 with respective weights 1, 1, 1/3 and respective detuning 1/2, 1, $(\sqrt{5} + 1)/2$. A sequence showing the evolution of the pattern in time is shown in figure 5.23. The shaded regions are the bright spots and a and b indicate the position of the roots of Re(E)=Im(E)=0, where the defects are located. The arrows show the directions of their motions. Figure 5.24a shows the motion of the two conjugate defects projected on a plane. Starting at point A for defect a (solid dots) and B for defect b (empty squares), the following motions are observed. At first, defect a rotates slowly counterclockwise near the center the field, while defect b accelerates upward, disappears at the upper right, reappears at the upper left corner and swiftly moves down across the field. This motion is labeled 1 in Fig. 5.24a. Next (motion labeled 2), defect a, still moving slowly, changes direction and starts upward while defect b disappears at the bottom left and reappears at the bottom right. Defect a then accelerates out at the top left, reappears at the top right and rapidly crosses the field toward the bottom left, while defect b starts executing a slow clockwise rotation near the center of the field. In a certain sense, the two defects have exchanged their roles but with antisymmetrical motions. This type of motion continues, leading to the path diagram shown in figure 5.24b.

Another interesting illustration given here is a scalar wave $\psi(r, t)$ combining the three modes TEM 00, 01 and 20 with fixed relative phases. For example, $\psi = \alpha_1(t)U_{20} + \alpha_2(t)U_{00} + i\alpha_3(t)U_{01}$, where $\alpha_i(t)$'s are real functions of time. This example shows two opposite charge defects moving apart along the x-axis as seen in

132
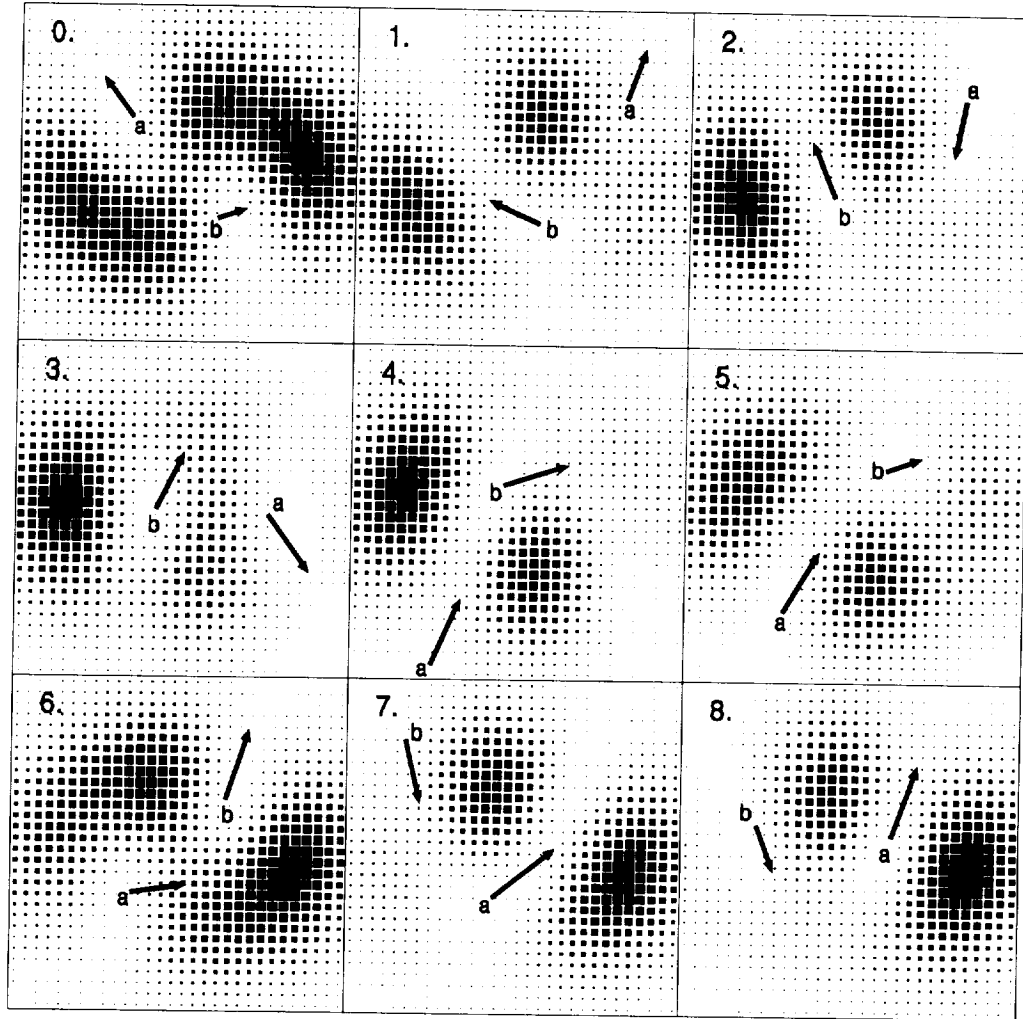
Figure 5.23: Sequence of patterns at equal intervals of time obtained by the superposition of three Gauss-Hermite modes of order 01, 10 and 20 with respective weighting coefficients 1, 1, 1/3 and respective detunings 0.5, 1, $(\sqrt{5}+1)/2$. Letters a and b indicate the locations of the two conjugate defects and the arrows show their directions of motion.
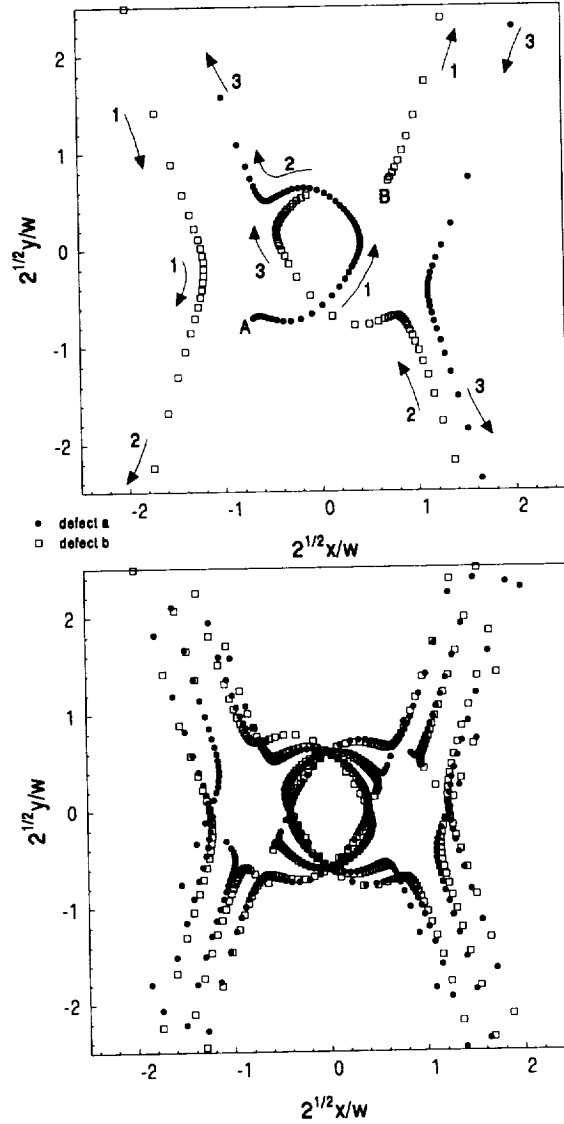
Figure 5.24: Motions of the two conjugate defects seen in fig. 5.23 projected on a plane. The defects locations are solutions of ReE=ImE=0 where E is the field amplitude resulting from the superspoition of the three modes of Fig 5.23. Short time motion (see text for details) in top diagram, long-time defect trajectories in bottom diagram.
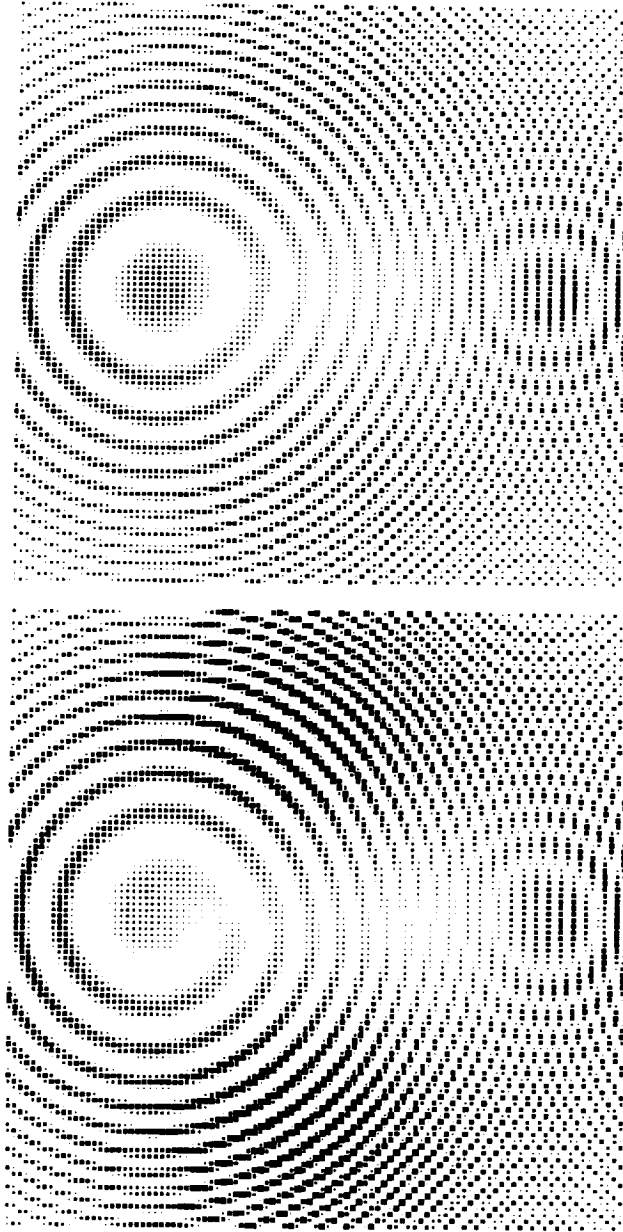
Figure 5.25: Computer-generated snapshots of an interferogram with a spherical reference wave: before the nucleation of the defects (top diagram); while a defect crosses the vertex of the spherical wave (bottom diagram).

experiments with a Fresnel number $F = 2.2$ (figure 5.11). Figure 5.25 shows a computer generated interferogram of the wavefront with a spherical wave. Figure 5.25a shows the interferogram of the uniform wavefront with no defect. It displays typical Newton's rings. A short while later, two defects appear at the center and move apart along the x-axis. Figure 5.25b shows the interferogram of the wavefront at the time when one of the defects crosses the reference spherical wave. The spiral fringes reveal the spiral nature of the wavefront. As the defect disappears at the boundary, the complete rings are recovered again. A similar behavior was observed in the experimental recordings for $F = 2.2$. Figure 5.26 shows snapshots of interferograms obtained by interfering the cavity beam with a spherical reference beam from the same laser. When one of the defects passes through the vertex of the spherical reference wave, it creates spiral fringes.

These examples are presented for illustrative purposes only. They show that the superposition of a few low order modes, with appropriate weights and detunings, can produce a great variety of patterns and defect motions, some of them resembling qualitatively what is being seen in the experiments, but they do not prove that this is the correct representation. We will explore this modal superposition approach to represent the spatiotemporal dynamics in a PCR in the next chapter.

5.7 Discussion and conclusion

As mentioned in chapter 1, phase conjugation via four-wave mixing in $BaTiO_3$ is known to be itself unstable in some regions of parameter space, leading to a pulsating or chaotic phase-conjugate beam [22, 27]. These instabilities appear to be related to the existence and competition of several gratings in the crystal. In addition, self-phase-conjugation of pump two, which is readily observed in $BaTiO_3$, produces a feedback to the laser which can also cause instabilities. Two different tests were made that lead us to believe that these two factors did not play a major role in the experiments.

Four-wave mixing without the cavity (mirror M removed) and with an external
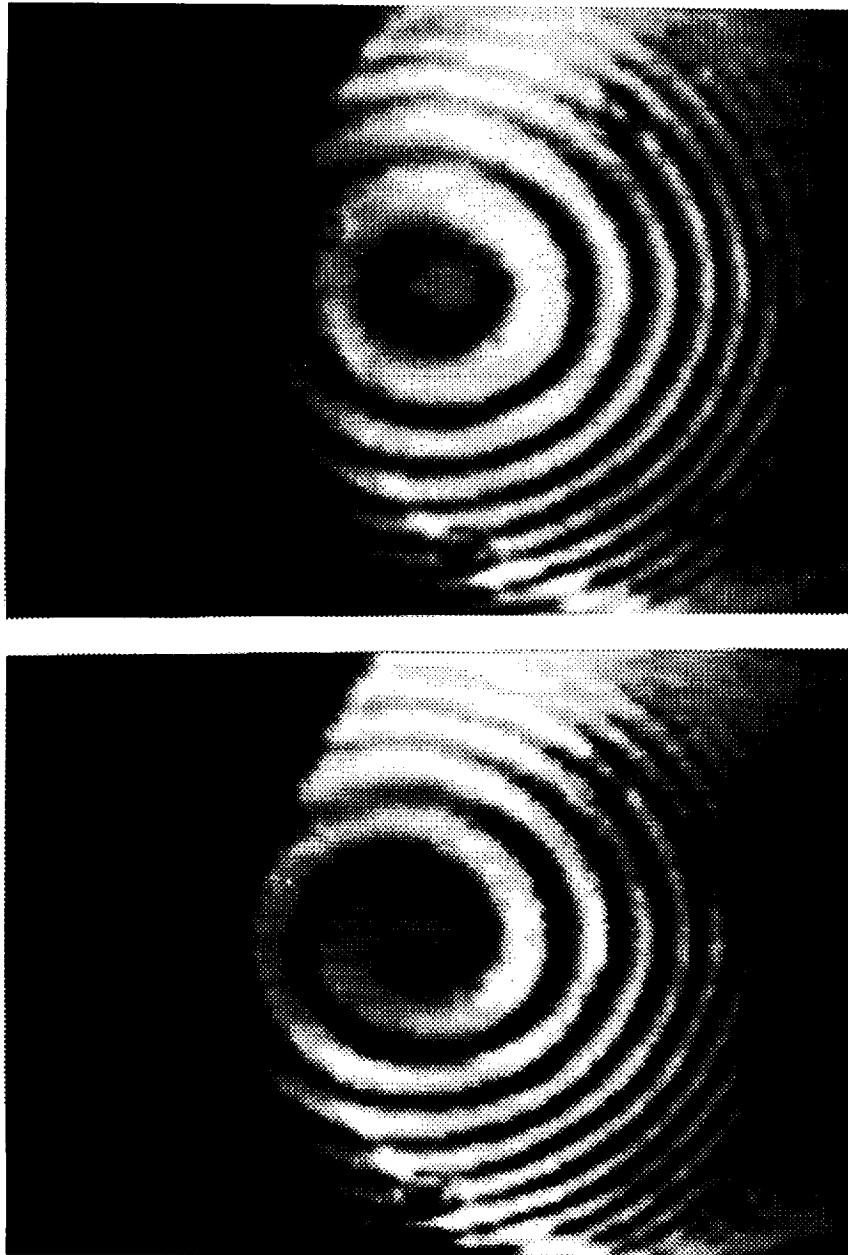
Figure 5.26: Experimental snapshots of the interferograms of wavefront containing a pair of defects with a spherical reference wave: before the nucleation of the defects (top diagram); while a defect crosses the vertex of the spherical reference wave (bottom diagram).

137

probe beam was tested for parameter values comparable to these used in the experiments. In all cases, the phase-conjugate beam was found to be quite stable. This appears to indicate that the observed dynamics is that of the phase-conjugate resonator, which of course involves a possibly complicated nonlinear interaction with feedback between the resonator and the photorefractive crystal, rather than that of the four-wave mixing process. Furthermore, PC instabilities often require a rather high coupling constant ($\gamma l \sim 6$ in Ref [22]). In our crystal, the coupling constant was estimated to be between 2 and 3 only (see chapter 3).

Tests were also made to detect the presence of self-pumping. With pump two alone incident on the crystal, strong self-phase-conjugation was observed. The presence of self-pumping is easily revealed by the usual beam fanning and internal reflections in the crystal. The feedback of the self-conjugated pump beam into the laser did cause some instability of its output. However, as soon as pump one was turned on, the fanning died out, the path of pump two straightened out inside the crystal and the self-conjugated beam intensity dropped to negligible values. Apparently, the presence of pump one did effectively erase all the extraneous gratings responsible for self-pumping. The same transverse patterns and dynamical behavior were observed, confirming that feedback due to self-pumping was negligible in our experiments and was not influential in our data.

In summary we have studied some aspects of the spatiotemporal dynamics of a phase-conjugate resonator. The control parameter was the resonator Fresnel number. Time series of the local intensity fluctuations were recorded and analysed by means of spectral analysis and embedded phase space portraits. A number of occurrences characteristic of low dimensional dynamical systems were observed, i.e. in order of increasing control parameter: a bifurcation from a stationary to a periodic state, followed by more subharmonic bifurcations; the occurrence of a chaotic state characterized by the appearance of a continuous background in the power spectrum; the appearance of an additional frequency unrelated to the fundamental frequency of the periodic motion; the occurrence of intermittency; and the final development of what appears to be a fully turbulent state.

The occurrences of these events were found to be quite reproducible, providing some evidence for the presence of a deterministic chaotic state of the cavity field. Further evidence is given by calculating the correlation exponent and the Kolmogorov entropy at a Fresnel number leading to a chaotic time series.

The spatial complexity of the pattern was studied by video recording and by interferometry, revealing the leading role played by the wavefront dislocations or vortices. The number of phase defects and the spatial correlation index of the wavefront were observed to follow similar trends as the transverse confinement of the system was relaxed. This suggests that the spatiotemporal chaos of the cavity field may be mediated by the phase defects.

Chapter 6

A model of spatiotemporal dynamics in PCRs

6.1 Introduction

In this chapter we present a truncated modal expansion approach to model the spatiotemporal dynamics of a PCR. Nonlinear dynamical problems that include the transverse dimensions and are described by systems of partial differential equations (PDEs) remain a theoretical challenge and do not benefit from well established experimental methodologies [100] as do systems of ordinary differential equations (ODE) [60, 101]. Furthermore, their numerical analyses require large computational budgets [56, 102]. We will test a relatively simple mathematical scheme to represent the transverse dynamics of the PCR without requiring prohibitive computational budgets.

This chapter has two aims. The first is to describe and establish the soundness of a somewhat arbitrary yet sensible modal decomposition approach to study the dynamics of PCRs with modest Fresnel numbers. This is done by comparing numerical results with actual experimental data. The hope is that this comparison, although complicated by the difficulty in measuring experimental control parameters exactly

140

and by the problematic effect of stochastic noise, will prove sufficiently convincing to confirm the usefulness of the approach. The second is to illustrate the relationship existing between the dynamics of the optical vortices observed in PCRs [87, 88, 86] and the spatial correlation of the oscillating beam.

The chapter is organized as follows: The PCR's equations and boundary conditions within approximations compatible with experimental conditions are stated in section 6.2.1. Arguments justifying the modal expansion approach are given in section 6.2.2 and the method is then used to arrive at a set of modal amplitude equations. In section 6.3, a particular set of parameter values is chosen and the system is integrated, using the off-Bragg detuning as a control parameter. Different dynamical behaviors are identified from local time series, power spectra and phase space portraits. Examples of vortices' motions and spatial correlation maps are given in section 6.3. Experimental results are presented and discussed in section 6.4 and a summary is given in section 6.5.

6.2 The modal expansion model

6.2.1 Phase-conjugate resonator

The PCR is sketched in fig. 6.1. Its active element is an externally pumped photorefractive medium acting as a PCM. Maxwell's equations for the optical field in the medium lead to the following coupled equations (see Appendix A):

$$\left(\frac{i\nabla_T^2}{2k} + \hat{k}_1 \cdot \nabla + \alpha + \frac{\partial}{v\partial t}\right) A_1(x,y,z,t) = -Q(x,y,z,t)A_4(x,y,z,t)e^{\ ibz}, \quad (6.1)$$

$$\left(-\frac{i\nabla_T^2}{2k} + \hat{k}_2 \cdot \nabla + \alpha + \frac{\partial}{v\partial t}\right) A_2(x,y,z,t) = Q(x,y,z,t)A_3(x,y,z,t), \quad (6.2)$$

$$\left(\frac{i\nabla_T^2}{2k} + \hat{k}_3 \cdot \nabla + \alpha + \frac{\partial}{v\partial t}\right) A_3(x,y,z,t) = -Q(x,y,z,t)A_2(x,y,z,t), \quad (6.3)$$

$$\left(-\frac{i\nabla_T^2}{2k} + \hat{k}_4 \cdot \nabla + \alpha + \frac{\partial}{v\partial t}\right) A_4(x,y,z,t) = Q(x,y,z,t)A_1(x,y,z,t)e^{\ ibz}, \quad (6.4)$$

141
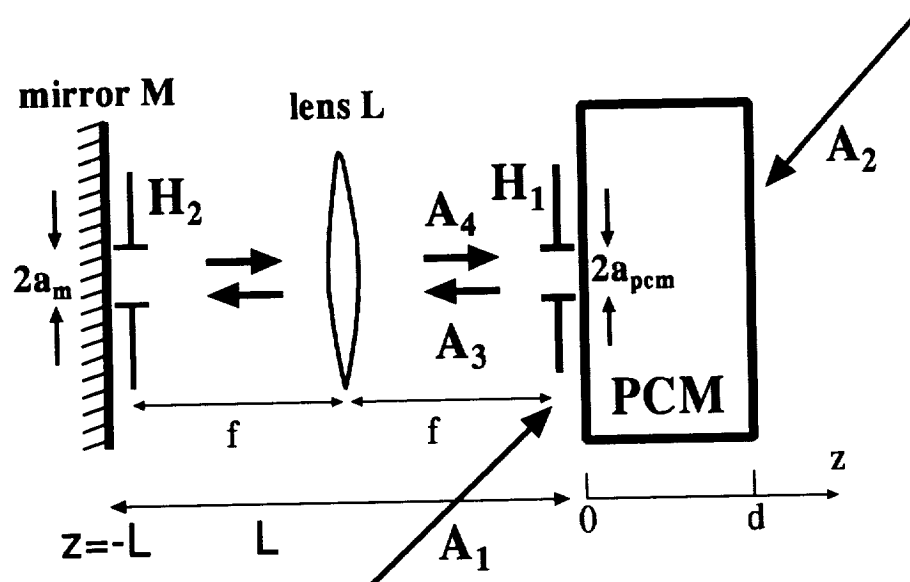
Figure 6.1: Four-wave mixing in a photorefractive phase-conjugate resonator (PCR): A_1, A_2 are two gaussian pump beams; A_3, A_4 are the left-going and the right-going beams inside the PCR; mirror M allows feedback of field back into the phase-conjugate mirror (PCM); apertures H_1,H_2 confine the transverse dimensions of the propagating beams.

where, in spirit of the slowly varying envelope approximation, the field in the medium is written as

$$E(x, y, z, t) = \sum_{i=1}^{4} A_i(x, y, z, t) e^{i(\omega t - \vec{k}_i \cdot \vec{r})} + \text{c.c.}, \tag{6.5}$$

$v = c/\bar{n}$ is the speed of light in the medium. $\bar{n}$ is the average refractive index. $\hat{k}_j$ are unit vectors pointing in the direction of the four wavevectors in the medium. The wavenumber is $k_j = \omega/v$, where ω is the angular frequency of the pump and α is the linear absorption coefficient. ∇_T is the transverse gradient operator. The parameter b is the wavevector mismatch (momentum mismatch along the z-axis) measuring the departure from the Bragg condition. This off-Bragg parameter is introduced as a means of varying the amount of phase transfer between the waves mixed in the nonlinear medium and is later taken as the control parameter.

The equation for the phase grating Q is derived from the standard band transport model of Kukhtarev [103] and reads, in the single grating approximation (see Appendix B),

$$\tau_I \frac{\partial Q(x, y, z, t)}{\partial t} + CQ(x, y, z, t) = \tag{6.6}$$

$$\gamma_o C \left(\frac{A_1(x, y, z, t) A_4^*(x, y, z, t) e^{ibz} + A_2^*(x, y, z, t) A_3(x, y, z, t)}{I_o(x, y, z, t)} \right),$$

where $C = [E_o + i(E_q + E_D)]/[E_o + i(E_M + E_D)]$.

The boundary conditions for the wave equation in the medium are determined by the cavity geometry. The transverse confinement of the cavity is controlled by two square apertures H_1 and H_2 of sides $2a_{pcm}$ and $2a_m$ respectively. The first aperture is located near the phase-conjugate mirror in the front focal plane of the lens (fig. 6.1). The second one is in the back focal plane of the lens next to the planar mirror. The transverse confinement is measured by the cavity Fresnel number defined as

$$F = 4a_m a_{pcm}/\lambda f, \tag{6.7}$$

where λ is the wavelength in vacuum and f the focal length of the lens.

One cavity round trip, starting at the PCM, consists of a truncation by H_1 and imaging in a 4-f afocal system with a pupil H_2. Thus, the amplitude A_4 is proportional

to the truncated convolution of A_3 with a point-spread-function which is the fourier transform of the aperture H$_2$. According to Fourier optics [104], the field at the plane of the mirror M, $\mathcal{E}(x, y, -L^+, t)$, is proportional to the convolution of the Fourier transform of the field $A_3(x, y, 0^+, t)$ at the exit plane of the crystal and the Fourier transform of the square aperture H$_1$, i.e.

$$\mathcal{E}(x, y, -L^+, t + \frac{L}{c}) = \frac{e^{ik_oL}}{i\lambda f}\left[F\{A_3(x, y, 0^+, t)\} \star F\{\text{rect}(\frac{x}{2a_{pcm}})\text{rect}(\frac{y}{2a_{pcm}})\}\right], \quad (6.8)$$

where $\text{rect}(x/2) = 1$ for $-1 \leq x \leq 1$ and $= 0$ otherwise. The field is then mirror reflected and truncated by the aperture H$_2$ such that

$$\mathcal{E}(x, y, -L^+, t + \frac{L}{c}) = r\mathcal{E}(-x, -y, -L^+, t + \frac{L}{c}) \cdot \text{rect}(\frac{-x}{2a_m})\text{rect}(\frac{-y}{2a_m}), \quad (6.9)$$

where r is mirror M's reflectance coefficient.

The field $\mathcal{E}(x, y, 0^-, t + \frac{2L}{c})$ is a multiplicative of the inverse Fourier transform of $\mathcal{E}(x, y, -L^+, t + \frac{L}{c})$, i.e.

$$
\begin{aligned}
\mathcal{E}(x, y, 0^-, t + \frac{2L}{c}) &= \frac{e^{ik_oL}}{j\lambda f}F^{-1}\{\mathcal{E}(x, y, -L^+, t + \frac{L}{c})\} \qquad (6.10) \\
&= \left[-\frac{e^{i2k_oL}}{\lambda^2 f^2}A_3(-x, -y, 0^+, t) \cdot \text{rect}(\frac{-x}{2a_{pcm}})\text{rect}(\frac{-y}{2a_{pcm}})\right] \\
&\quad \star \left[4a_m^2\text{sinc}(2a_mx)\text{sinc}(2a_my)\right],
\end{aligned}
$$

where $\text{sinc}(x) \equiv \sin(\pi x)/(\pi x)$.

Thus, we can write the input field $A_4(x, y, 0^+, t)$ in terms of the outgoing phase conjugate beam $A_3(x, y, 0^+, t)$ in the following way:

$$A_4(x, y, 0^+, t + \frac{2L}{c}) = -4a_m^2 r\frac{e^{i2k_oL}}{\lambda^2 f^2}\iint_{-a_{pcm}}^{+a_{pcm}} A_3(x', y', 0^+, t)\text{sinc}\left[\frac{2a_m(x' + x)}{\lambda f}\right] \quad (6.11)$$
$$\text{sinc}\left[\frac{2a_m(y' + y)}{\lambda f}\right] dx'dy',$$

144

Using the resonator Fresnel number $F = 4a_m a_{pcm}/\lambda f$ and normalizing the transverse coordinates to the aperture size a_{pcm}, we find

$$A_4(x, y, 0, t + \frac{2L}{c}) = -r(F/2)^2 e^{i2k_oL} \iint_{-1}^{+1} A_3(x', y', 0, t)\text{sinc}\,[F(x' + x)/2] \quad (6.12)$$
$$\text{sinc}\,[F(y' + y)/2]\,dx'dy',$$

where $x = \mathbf{x}/a_{pcm}, y = \mathbf{y}/a_{pcm}$ ($\mathbf{x}$ and $\mathbf{y}$ are the real physical dimensions).

6.2.2 Modal decomposition

The direct integration of equation 6.1- 6.6 requires a large computational budget. Furthermore, calculations taking only one transverse dimension into account, although showing interesting dynamical behaviors (e.g. ref. [105]), fail to reveal the crucial role played by the phase defects in mediating the spatiotemporal dynamics of the PCR [87, 88, 86].

Modal decomposition is a powerful tool for studying systems of PDEs [106]. This approach allows one to reduce an infinite dimensional problem to a finite (hopefully low) dimensional problem described by a system of ODEs for the modal coefficients. The success of the method relies on the assumption that the dynamics is fairly well described by the interaction of a small number of active spatial modes. The main difficulty resides in the choice of appropriate basis functions for the expansion. They must accurately represent the spatial structure of the active modes. However, this structure is generally difficult to identify a priori and one often relies on the choice of a "sensible" basis rather than trying to identify the exact optimal basis.

In optical resonators with relatively small Fresnel numbers, this assumption appears to be justified. The dynamics of these systems is indeed dominated by a few active modes and the Gauss-Laguerre or Gauss-Hermite modes of the empty resonator seem to be reasonable basis functions to replace the optimal ones [75]. Of course such a practice introduces a degree of arbitrariness since a small number of modes of the sensible basis may not be sufficient to adequately represent the spatial structure. Nevertheless, the resulting enormous reduction of computational budget

and the physical insight that can be gained justify further tests of the validity of this approach.

The cavity fields A_3 and A_4 in the nonlinear medium ($0 \leq z \leq d$) are thus expanded in series as

$$A_3(x,y,z,t) = \sum_{m,n} f_{3mn}(z,t) u_m^*(x,z;z_o) u_n^*(y,z;z_o) \tag{6.13}$$

$$A_4(x,y,z,t) = \sum_{m,n} f_{4mn}(z,t) u_m(x,z;z_o) u_n(y,z;z_o) \tag{6.14}$$

and the Gauss-Hermite modes are chosen as a sensible set for the decomposition:

$$u_m(x,z;z_o) \equiv \left(\frac{2}{\pi}\right)^{1/4} [2^m m! w(z)]^{-1/2} H_m\left(\frac{\sqrt{2}x}{w(z)}\right) \tag{6.15}$$
$$\exp\left[-\frac{x^2}{w^2(z)} - i\frac{kx^2}{2R(z)} + i(m+1/2)\tan^{-1}(z/z_o)\right],$$

where H_m are Hermite polynomials. The beam radius is $w(z) = w_o(1 + z^2/z_o^2)^{1/2}$, its radius of curvature is $R(z) = z(1 + z_o^2/z^2)$. $z_o = \pi w_o^2 \bar{n}/\lambda$ is the Rayleigh distance and $k = 2\pi\bar{n}/\lambda$ is the wavenumber in the medium. The waist w_o is located at the entrance face of the PCM ($z = 0$).

The pump beams are Gaussian, with a waist w_p chosen appreciably larger than w_o, and for simplicity are assumed to make a very small angle with the z-axis. Thus, the pump beams are

$$A_1(x,y,z,t) = f_1(z,t) U(x,z) U(y,z) \tag{6.16}$$

$$A_2(x,y,z,t) = f_2(z,t) U^*(x,z) U^*(y,z) \tag{6.17}$$

where $U(x,z) = u_o(x,z;z_p)$ and $z_p = \pi w_p^2 \bar{n}/\lambda$.

The series in equations 6.13, 6.14 are infinite and the problem remains infinite dimensional. Because of the cavity transverse confinement however, we expect that only the modes with indices smaller than some upper bound will take a significant part in the dynamics. The cavity Fresnel number defined by equation 6.7 is a measure of the amount of transverse spatial information that the cavity can accommodate (F^2 is the space-bandwidth product of the cavity). It is thus reasonable to assume that

only the modes with indices smaller than F will play a dominant role in the wave interaction in the PCM since they are the modes which are most likely to survive in the cavity. It must be stressed however that choosing which modes to include in the dynamics is somewhat arbitrary. Only a comparison with experiment can provide an *a posteriori* justification of this choice. The important point is that the series of equations 6.13, 6.14 can often be limited to a small number of terms while still giving results which agree at least qualitatively with observations, as will be shown in a later section.

Equations 6.13- 6.17 are substituted in 6.1- 6.6 and use is made of the fact that the Gauss-Hermite modes are solutions of the Helmholtz equation:

$$\left(\frac{i\nabla_T^2}{2k} + \frac{\partial}{\partial z}\right) u_m(x,z)u_n(y,z) = 0, \tag{6.18}$$

and satisfy the biorthogonality relation [94]

$$\iint_{-\infty}^{+\infty} dxdy\, u_m(x,z)u_n(y,z)u_p^*(x,z)u_q^*(y,z) = \delta_{mp}\delta_{nq}. \tag{6.19}$$

A final set of differential equations is then obtained for the modal amplitudes:

$$\frac{\partial f_1(z,t)}{\partial z} + \alpha f_1(z,t) = -e^{-ibz}\sum_{m,n} f_{4mn}(z,t)h_{mn}(z,t), \tag{6.20}$$

$$\frac{\partial f_2^*(z,t)}{\partial z} - \alpha f_2^*(z,t) = -\sum_{m,n} f_{3mn}^*(z,t)h_{mn}(z,t), \tag{6.21}$$

$$\frac{\partial f_{3mn}(z,t)}{\partial z} - \alpha f_{3mn}(z,t) = f_2(z,t)h_{mn}(z,t), \tag{6.22}$$

$$\frac{\partial f_{4mn}^*(z,t)}{\partial z} + \alpha f_{4mn}^*(z,t) = e^{-ibz}f_1^*(z,t)h_{mn}(z,t), \tag{6.23}$$

where

$$h_{mn}(z,t) = \iint_{-\infty}^{+\infty} dxdy\, Q(x,y,z,t)u_m(x,z)u_n(y,z)U^*(x,z)U^*(y,z) \tag{6.24}$$

is the overlap integral of the pump and the projection of the grating Q onto the mode (m,n).

147

The grating equation 6.6 is likewise projected onto the cavity modes to obtain

$$\tau\frac{\partial h_{mn}(z,t)}{\partial t} \quad + \quad Ch_{mn}(z,t) = \tag{6.25}$$

$$\gamma_o C\{e^{ibz}f_1(z,t)\sum_{k,l}f^*_{4kl}(z,t)G_{klmn}(z,t) + f^*_2(z,t)\sum_{k,l}f_{3kl}G_{klmn}(z,t)\},$$

with

$$G_{klmn}(z,t) = \iint_{-\infty}^{+\infty}\frac{u^*_k(x,z)u^*_l(y,z)u_m(x,z)u_n(y,z)|U(x,z)|^2|U(y,z)|^2}{I_o(x,y,z,t)}dxdy \tag{6.26}$$

and the total intensity $I_o(x,y,z,t)$ is calculated using equations 6.13, 6.14, 6.16, 6.17.

For the case of strong pumps and large pump width (we can call this the zeroth order approximation), G_{klmn} in equation 6.26 becomes approximately a delta function $\delta_{km}\delta_{ln}$ such that the grating equation becomes

$$\tau\frac{\partial h_{mn}(z,t)}{\partial t} + Ch_{mn}(z,t) \quad = \quad \gamma_o C \tag{6.27}$$

$$\{e^{ibz}f_1(z,t)f^*_{4mn}(z,t) + f^*_2(z,t)f_{3mn}\},$$

It seems that as the coupling terms in the sums of the right hand side of equation 6.25 have been taken out in this approximation, the projection of the grating Q onto each mode (m,n) contributes mainly to the corresponding mode (m,n). However, coupling still occurs through the factors f_1 and f^*_2 which are linked to all participating modes as shown in equations 6.20 and 6.21. Thus, in spite of the fact that coupling through G_{klmn} is eliminated in the strong pumps and large pump width approximation, coupling between modes remain in equation 6.27 due to factors f_1 and f_2, unless if the pumps are so strong that f_1 and f_2 are about constant. We may regard this so-called zeroth order approximation as appropriate to the spatiotemporal dynamics with weak coupling in PCR.

The integration of equations 6.20- 6.26 is greatly simplified if the interaction length in the PCM is shorter than all the beams' Rayleigh distances:

$$d \ll z_o, z_p. \tag{6.28}$$

In this case, diffraction can be neglected in the medium, and the interacting beams' modes, normalized to the aperture size a_{pcm}, take the simple form:

$$u_m(x,z;z_o) \simeq u_m(x) = \left(\frac{1}{\pi}\right)^{1/4}\left(\frac{\beta_o}{2^m m!}\right)^{1/2}H_m(\beta_o x)e^{-\beta_o^2 x^2/2}, \tag{6.29}$$

with $\beta_o = \sqrt{2}a_{pcm}/w_o$. The pumps are gaussian with a parameter $\beta_p = \sqrt{2}a_{pcm}/w_p$.

The boundary conditions for the modal amplitudes at $z = 0$ are found from equation 6.12 using the modal decompositions 6.13, 6.14. They read, without the unimportant phase factors in eq. 6.12,

$$f_{4mn}(0,t) = rF^2 \sum_{k,l} f_{3kl}(0,t) I_{km} I_{ln}, \tag{6.30}$$

with

$$I_{km} = \int_{-1}^{+1} dx \mathcal{H}_k(x) u_m(x), \tag{6.31}$$

and

$$\mathcal{H}_k(x) = \int_{-1}^{+1} dx' u_k(x') \text{sinc}[F(x'+x)/2]. \tag{6.32}$$

The algorithm of the adiabatic elimination method described in section 3.1.2 was used to solve the system of equations 6.20- 6.26 with the boundary conditions 6.30- 6.32. Some results are illustrated in the next section.

6.3   Numerical results

Phase transfer between interacting beams in the four-wave mixing process appears to be a desirable condition for the observation of non-trivial dynamics with reasonable values of the coupling parameter. For example, the onset of instabilities in ring resonators with injected signals has been shown to depend sensitively on this parameter [24]. In a material having a real coupling parameter and no external field, this phase transfer can be the result of an angular mismatch of the pump beams. For the simulation presented in this section, the control parameter was chosen to be the phase mismatch bd (off-Bragg parameter), where b is the momentum mismatch along z and d is the length of the nonlinear medium.

We have shown in the last chapter that the dynamics of the PCR strongly depends on the cavity Fresnel number. Increasing the Fresnel number relaxes the transverse confinement of the system and allows higher order modes to take part in the dynamics. As a result, the spatial complexity of the beam increases. In particular, the number

of vortices increases and their motion becomes more complex, eventually leading to chaotic states and, in the limit of large Fresnel numbers, to spatiotemporal turbulence. The example shown in the next section is for a Fresnel number $F = 3.5$. This is small enough so that only a few modes are expected to take part in the dynamics, yet it is large enough to exhibit a wide range of behaviors.

Experiments carried out with Fresnel numbers between 3 and 4 reveal a transverse pattern in which two pairs of defects of opposite charges repetitively nucleate, move along symmetrical trajectories, spending much time in some circular zone centered on the beam and disappear at boundaries or collide and annihilate each other [88]. Based on these observations and in order to keep the computational budget to a minimum, it was decided to limit the expansions in eqs. 6.13, 6.14 to four modes only, namely, $(m, n) = (0, 0), (1, 1), (2, 0)$, and $(0, 2)$ with a beam waist $w_o = a_{pcm} = 1$.

As already mentioned, there is a certain degree of arbitrariness in this choice. However, with a Fresnel number of 3.5, it is unlikely that modes with indices higher than 3 can survive in the cavity and play a significant role in the dynamics. Indeed, when a mode of higher index $(8, 0)$ was initially added to the series of $(0, 0), (1, 1), (2, 0), (0, 2)$, the simulation showed that the amplitude of mode $(8, 0)$ decays and vanishes with the other transients. Another reason for limiting the expansion to these particular four modes is that it allows the calculation of the vortices' positions to be done algebraically rather than numerically, thus saving CPU time. Finally, simulations run with different choices of modes, although giving results which differ in details, revealed the same generic range of behaviors.

The other parameters of the model are chosen as follows: $\gamma d = -10, \alpha d = 0.15, \beta_o = \sqrt{2}, \beta_p = \sqrt{2}/10, E_D = 1kV/cm, E_q = 5kV/cm, E_M = 100kV/cm, E_o = 0$, and the pump beam intensity coefficients are $f_1^2(z = 0) = f_2^2(z = 0) = 0.5$. As an initial condition, it is assumed that the four modes are excited from white noise and have initial modal amplitudes $f_{4mn}(t = 0) = 10^{-4}$.

6.3.1 Local intensity fluctuations

The local intensity of the cavity field A_4 measured at the exit face of the PCM was chosen as a variable because it is easily accessible experimentally. The local intensity $I_4(x_o, y_o, d)$ was calculated at $(x_o, y_o) = (0.75, 0.15)$ in a region where experiments indicate that the intensity fluctuations have a deep modulation. Figure 6.2 shows short sections of time series of the local intensity fluctuations for different values of the off-Bragg parameter. Time in fig. 6.2 is normalized to the relaxation time τ' of the photorefractive grating $(\tau' = |[E_o + i(E_M + E_D)]/[E_o + i(E_q + E_D)]|\tau_I$, see eq. 6.6).

After the transients have vanished and a stationary state has been reached, the local extrema of these time series were recorded and used to construct the bifurcation diagram of fig. 6.3. For small Bragg mismatch ($|bd| < 2.4$) the motion is periodic. Unstable oscillations occur in a wide range of parameter values ($2.4 < |bd| < 3.6$). In most of this range the motion appears to be quasiperiodic. Some regions of the bifurcation diagram seem to be more chaotic than others and there exist narrow windows in which the motion appears to be periodic, usually with a large number of subharmonics. For $|bd| > 3.6$, the motion is periodic again and eventually, with a sufficiently large mismatch, the only stable state is $I_4 = 0$.

The time series of fig. 6.2 were chosen to illustrate these various types of motion. The corresponding power spectra shown in fig. 6.4 give a fair indication of the dynamics of the system. Additional information can be gained by reconstructing pseudo phase space portraits such as these shown in fig. 6.5, which are plots of the imaginary part of the field $A_4(x_o, y_o, d)$ versus its real part.

At $bd = -2.3$, the motion is clearly periodic with a frequency f_1 slightly larger than 1/2 of the relaxation rate of the grating (fig. 6.4a), and the phase space portrait (fig. 6.5a) is a limit cycle. At $bd = -2.45$, a second characteristic frequency f_2, about 1/10 of the grating relaxation rate, appears and modulates the time series (figs 6.2b and 6.4b). For this value of the off-Bragg parameter, the two frequencies are (relatively) incommensurate and the motion is quasiperiodic with the phase space portrait shown in fig. 6.5b. At $bd = -2.55$, the low frequency modulation deepens (fig. 6.4c)
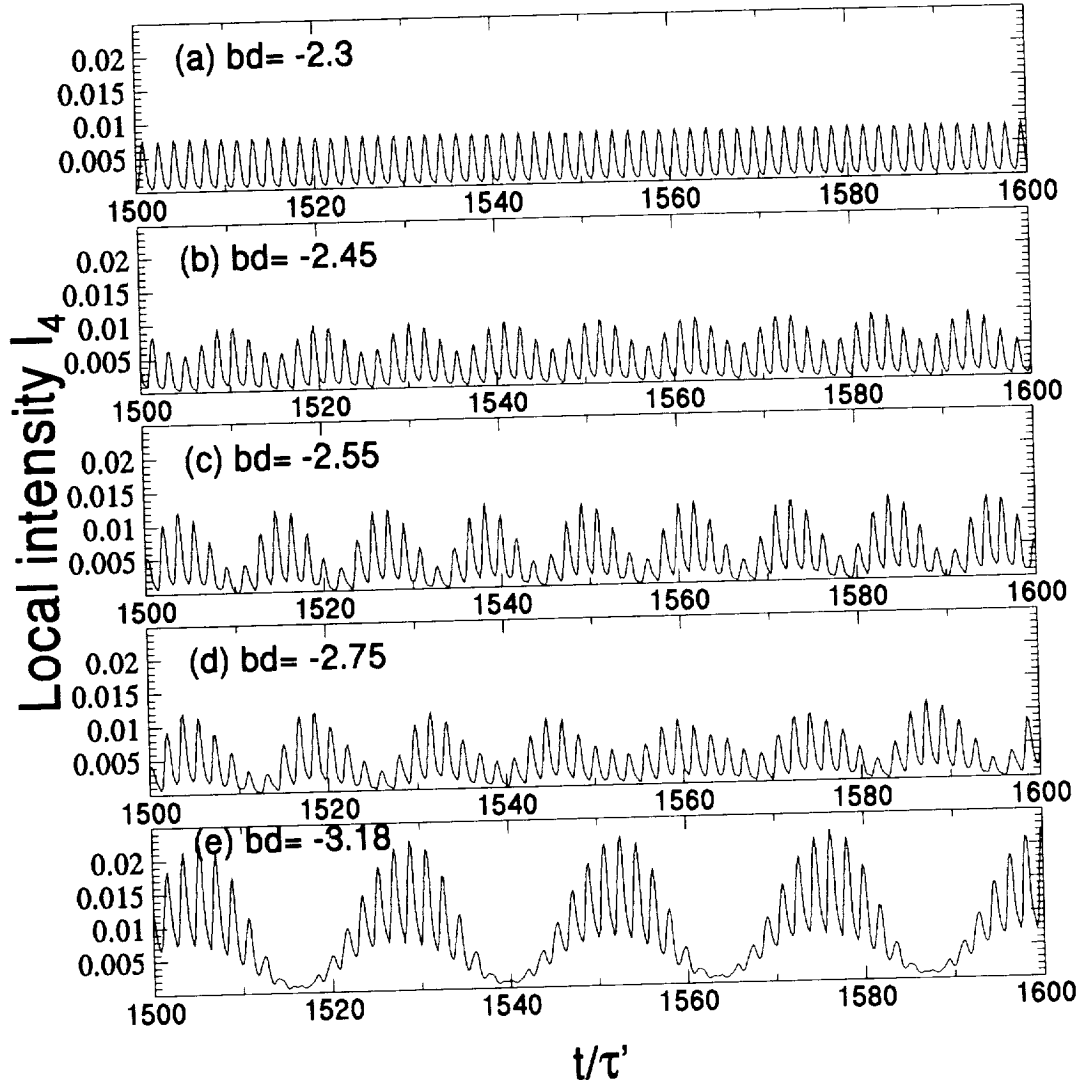
Figure 6.2: Time series of local intensity I_4 for different values of the off-Bragg parameter bd showing a sequence of dynamical states including periodic, quasiperiodic and chaotic states.
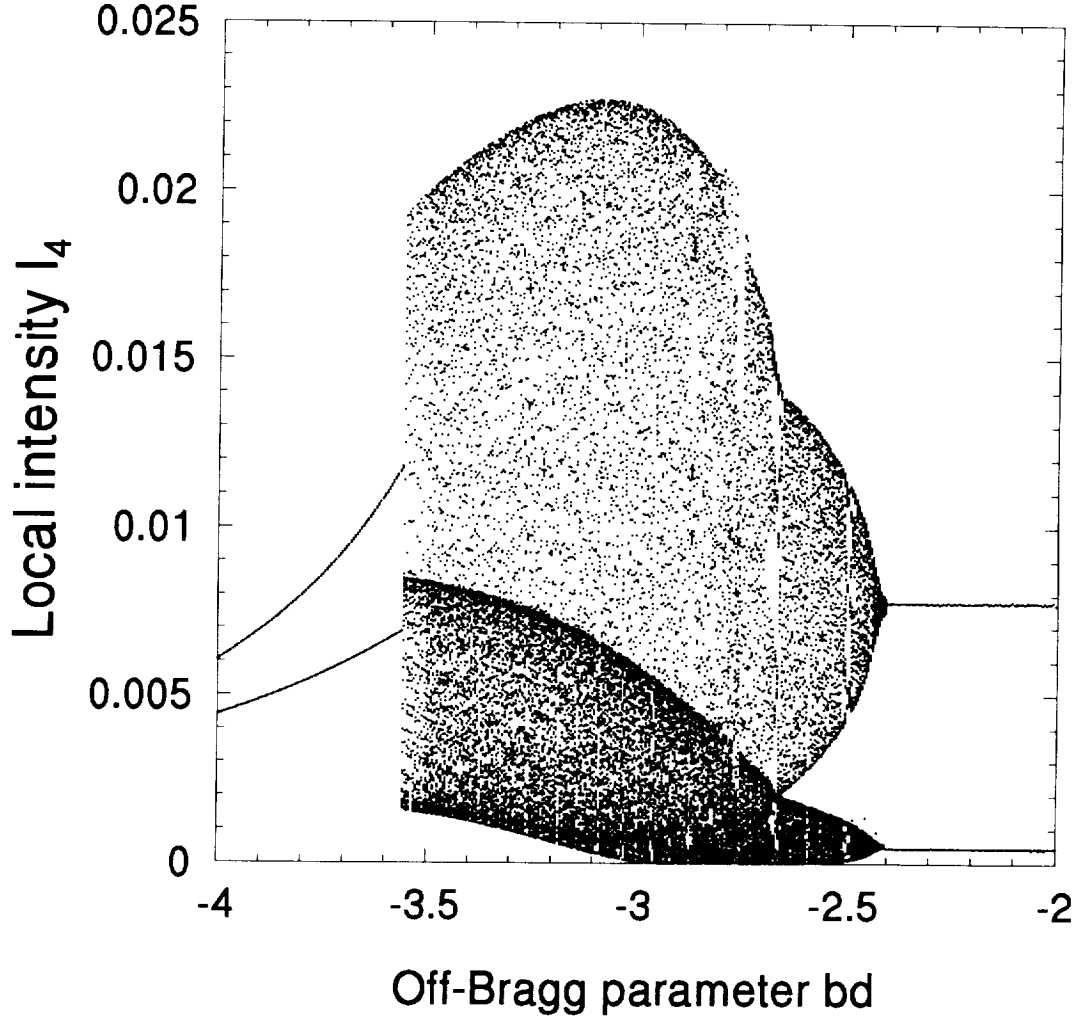
Figure 6.3: Bifurcation diagram of the local intensity I_4 at a point of the beam cross-section in the exit plane ($z = d$) as a function of the off-Bragg parameter bd. Other parameter values used are: $\gamma d = -10, \alpha d = 0.15, F = 3.5, \beta_o = 1, \beta_p = 0.1, f_1^2(z = 0) = f_2^2(z = d) = 0.5, f_{4mn}^2(t = 0) = 10^{-4}, (m, n) = (0, 0), (1, 1), (2, 0), (0, 2)$.
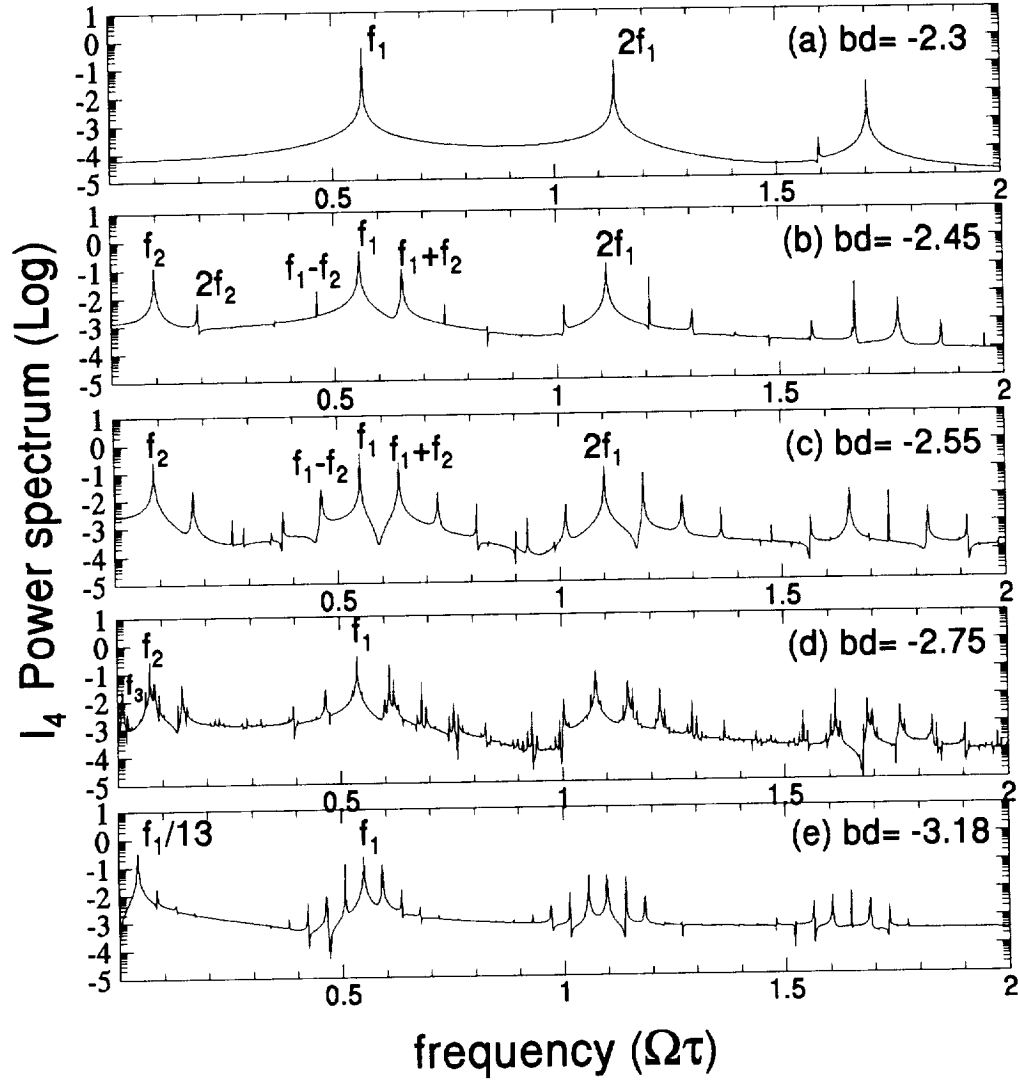
Figure 6.4: Power spectra of the time series of fig. 6.2 illustrating the dynamics as the off-Bragg parameter bd is varied. (a) a periodic motion with a single frequency, (b) quasiperiodic motion with two (relatively) incommensurate frequencies, (c) same with more energy in the side bands, reflecting the deeper modulation of fig. 6.2c, (d) broadening of the two frequency peaks and their harmonics with the appearance of an additional low frequency leading to chaotic motion, (e) two frequency peaks of commensurate ratio corresponding to frequency locking at period 13.
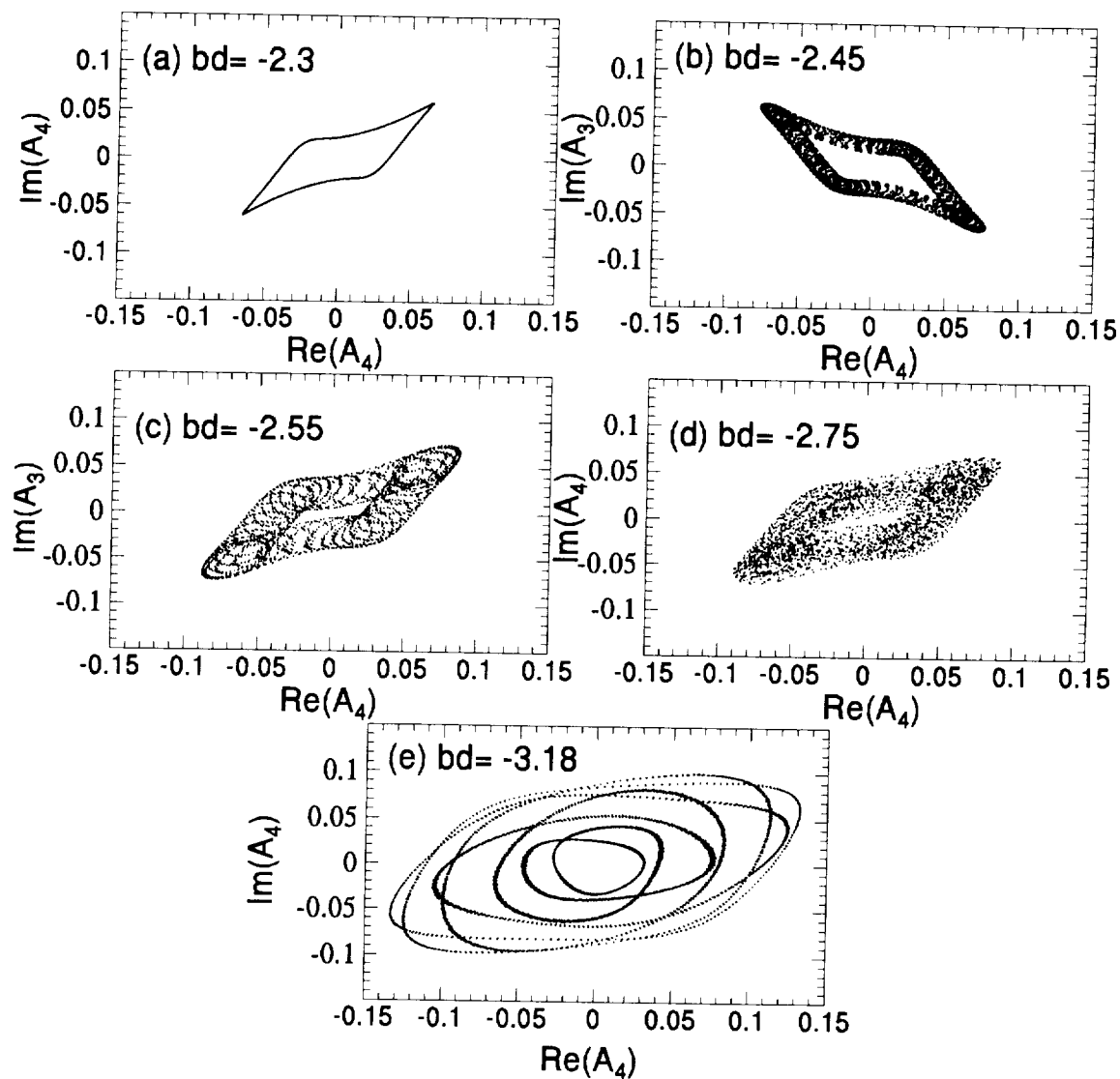
Figure 6.5: Phase space portraits corresponding to the local time series of fig. 6.2 with the real part of the field amplitude A_4 plotted versus its imaginary part. It shows (a) a limit cycle, (b) a two frequency torus, (c) a thicker two frequency torus, (d) a diffuse broken torus, (e)a 13 loops limit cycle indicating frequency locking.

and more energy shifts toward higher harmonics of f_1 and linear combinations of the two main frequencies (fig. 6.4c). The phase space portrait still shows some structures although it will eventually densely fill a region of phase space since the two frequencies are still incommensurate. At $bd = -2.75$, the time series is more irregular, possibly chaotic (fig. 6.2d). There are still two main frequencies but the spectrum is broadened and shows a number of additional peaks indicating the presence of a third frequency about $1/100$ grating relaxation rate (fig. 6.4d). The phase space portrait of fig. 6.5d is diffuse and shows no apparent structure. At $bd = -3.18$ a phenomenon akin to frequency locking occurs. The two larger frequencies pull each other so as to become rational. The very low frequency, which seems to have appeared only to allow this locking to occur, disappears. The spectrum of fig. 6.4e shows a ratio $f_1/f_2 = 13$. The periodic motion with 13 subharmonics is confirmed by the closed loop phase space trajectory of fig. 6.5e.

6.3.2 Vortices and spatial correlation

The local intensity fluctuations offer a convenient means of comparing model predictions with experimental data but this information is not sufficient to fully characterize the spatiotemporal dynamics. The aim of this section is to illustrate the role played by the phase defects (vortices) in mediating the dynamics.

The vortices appear where the real and imaginary parts of the field amplitude vanish simultaneously. For example, fig. 6.6 shows a snapshot of the beam amplitude cross-section $|A_4(x, y, d)|$ for $bd = -2.45$, which exhibits four dark spots. The corresponding phase contour diagram of fig. 6.7 clearly identifies these spots as two pairs of vortices of opposite charges (± 1). In time, these vortices nucleate, move around, annihilate each other or disappear at boundaries. This is the motion of the vortices which gives rise to the local intensity fluctuations described in the previous section. This section gives a more detailed illustration of the spatial aspect of the dynamics and attempts to identify the spatial features responsible for the characteristic frequencies observed in the local times series.

bd= -2.45, t=1502.8τ'
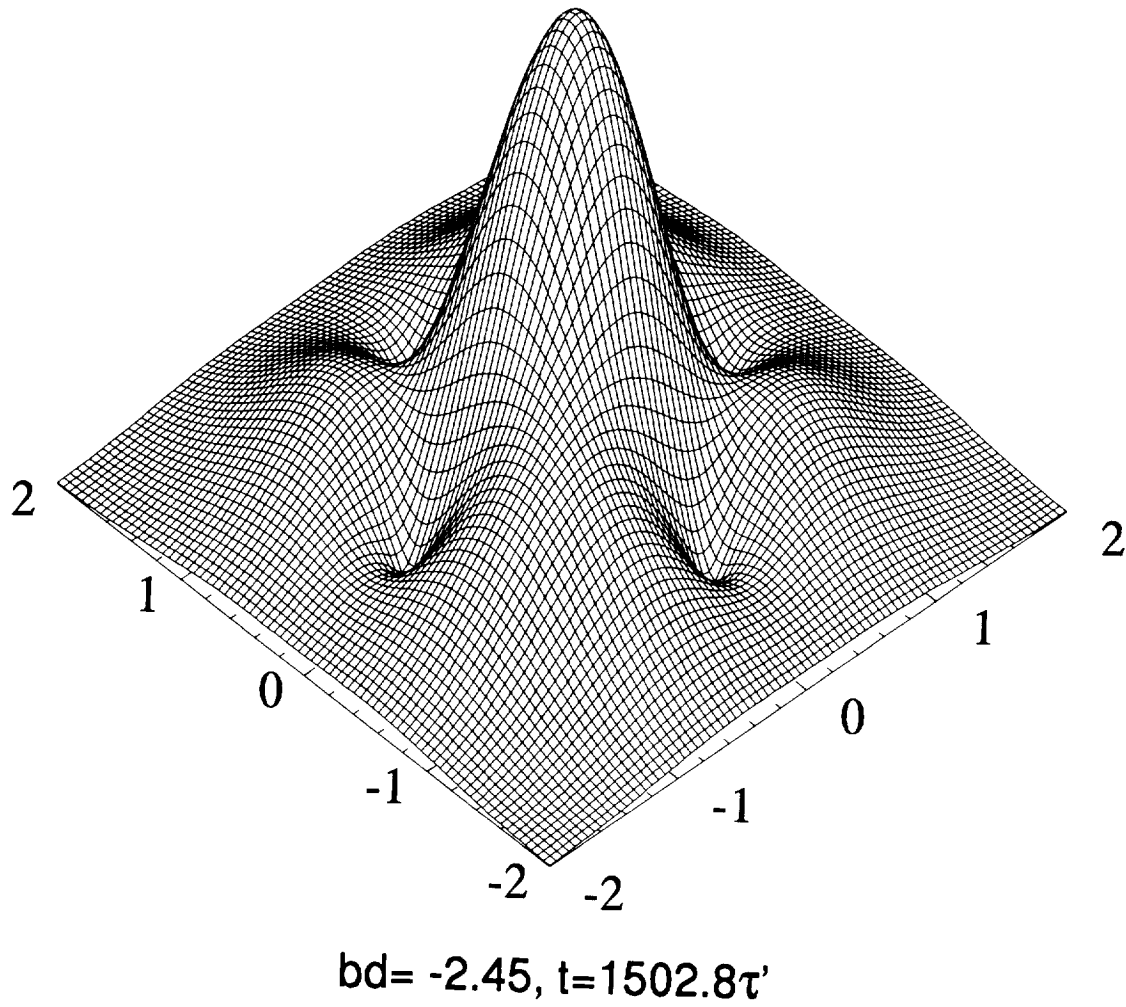
Figure 6.6: The profile of the absolute value of the field amplitude $|A_4|$ showing four holes in the beam cross-section.
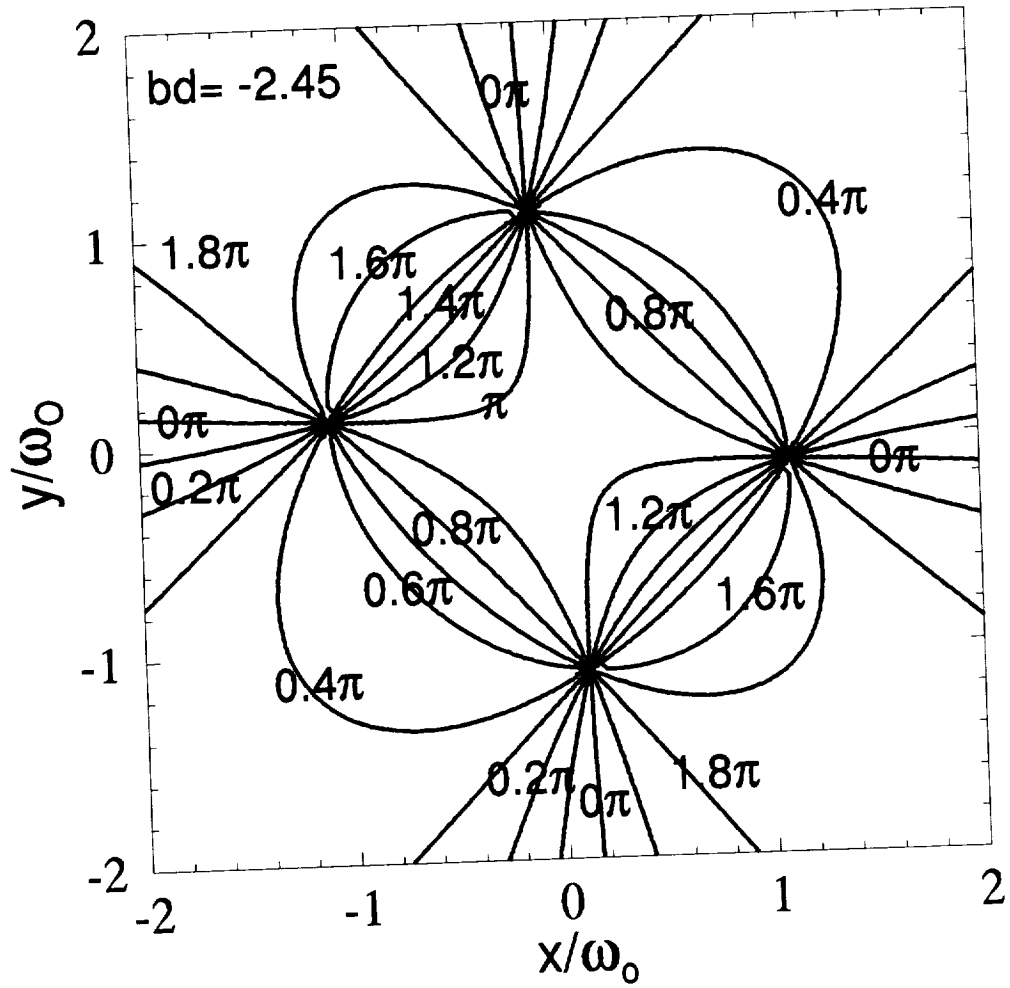
Figure 6.7: Phase contour map corresponding to the amplitude map of fig. 6.6 clearly identifies the four holes in the wavefront as two pairs of vortices of opposite charges (±1).
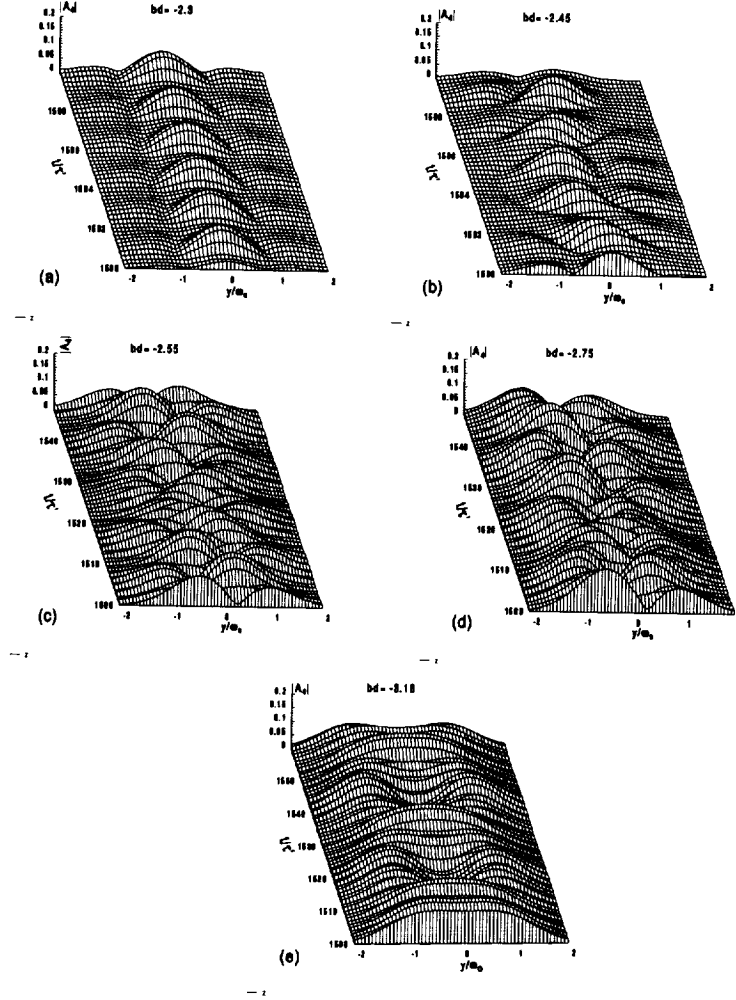
Figure 6.8: Time evolution of the modulus of the field amplitude A_4 along a line $x = 1$ for different values of the off-Bragg parameter bd, showing (a) a synchronized periodic motion, (b) a periodic motion with transverse modulation, (c) a quasiperiodic motion, (d) a turbulent flow, (e) another periodic flow.

Figure 6.8a to e shows the temporal evolution of the modulus of the field amplitude $A_4(x = 0.75, y, d)$ along a line across the beam for the same off-Bragg parameter values used in figs. 6.2, 6.4, 6.5. For a small offset ($bd = -2.3$), all points across the line execute synchronized periodic motions with a period a bit smaller than two grating time constants (fig 6.8a). In 2-D, the phase of the wavefront is observed to breathe periodically together with the amplitude but the phase gradients produced are not steep enough to trigger the nucleation of defects.

At $bd = -2.45$ (fig 6.8b), the periodic motion is transversely modulated with a period of the order of 10 grating time constants. This spatial motion gives rise to the quasiperiodic time series of fig. 6.2b. In 2-D, the phase gradients are locally steep enough to tear the wavefront at locations where two pairs of defects of opposite charges nucleate. The four vortices then travel across the wavefront, and pairs of opposite charge collide and annihilate. The higher frequency of the time series seems to correspond to the recovery rate of the local wavefront after a vortex has moved through it, while the lower frequency corresponds to the full cycle of vortex nucleation, motion and annihilation. At $bd = -2.55$, the motion is similar to that just described but with deeper modulation (fig. 6.8c, which is plotted with a different time scale).

At $bd = -2.75$ (fig. 6.8d), the transverse modulation is irregular, possibly due to the occurrence of a third incommensurate frequency. In 2-D, in contrast with the previous case where the vortices' trajectories were confined to a fairly well defined area, they now seem to visit the whole beam cross-section irregularly. At $bd = -3.18$ (fig. 6.8e) the motion is periodic again. The transverse modulation has a period of ~ 23 grating time constants, which is 13 times the period of $\sim 9/5$ time constant of the fast oscillations measured in fig. 6.8a.

The remainder of this section gives a more detailed illustration of the relationship between the vortices' trajectories and the spatiotemporal coherence of the beam. The dynamics of the fluctuating beam can be characterized by a correlation index distribution calculated from the spatial correlation function defined in eq. 5.4.

To illustrate the usefulness of this concept, the correlation index distribution with

respect to the origin, $C(0,0;x,y)$, was calculated for the five off-Bragg parameter values used in the previous examples. The spatial correlation diagram thus obtained can then be compared with the vortices' trajectories. For this, the positions of the vortices were calculated at regular intervals of time by solving for $\mathrm{Re}A_4(x,y,t) = \mathrm{Im}A_4(x,y,t) = 0$, and they are represented by dots on a 2-D plot. Note in passing that, with the particular choice of modes adopted for the expansion of A_4, these positions could be solved for algebraically.

Figure 6.9 shows the correlation index distribution for a small value of the off-Bragg parameter $(bd = -2.3)$. No vortices appear in the field but the amplitude and phase of the wavefront oscillate periodically as if waves were travelling along an annular area centered on the beam.

At $bd = -2.45$, the motion is characterized by the nucleation of two pairs of defects at two diagonal ends. The vortices move along circular trajectories and the members with opposite charges from each different pair collide and annihilate near the two diagonal ends on the other side. This motion is then repeated periodically with alternating directions. A sequence of interferogram snapshots illustrating this motion is shown in fig. 6.10. A plot showing the distribution of vortice's positions in time is shown in fig. 6.11a. The vortices' trajectories are clearly confined to a narrow annular area in the beam. Figure 6.11b shows the corresponding correlation index distribution. Its particular shape can be explained by the fact that the intensity fluctuations at some location in the beam are due to the passage of a vortex nearby, that no vortex ever appears near the origin (the fixed point for calculating C) and that the vortices' trajectories are confined to a narrow annular region of space. It is only near this region that the correlation index is expected to drop sharply. The correlation index distribution was also calculated with a fixed point chosen at a location frequently visited by a vortex. The relationship between the distributions of fig. 6.11a and b is analogous to that between a photographic print and its negative. The correlation index is high in the annular area visited by the vortices and low everywhere else. This confirms that the four vortices appearing in the pattern are highly correlated, as is expected since they nucleate simultaneously and produce intensity fluctuations near
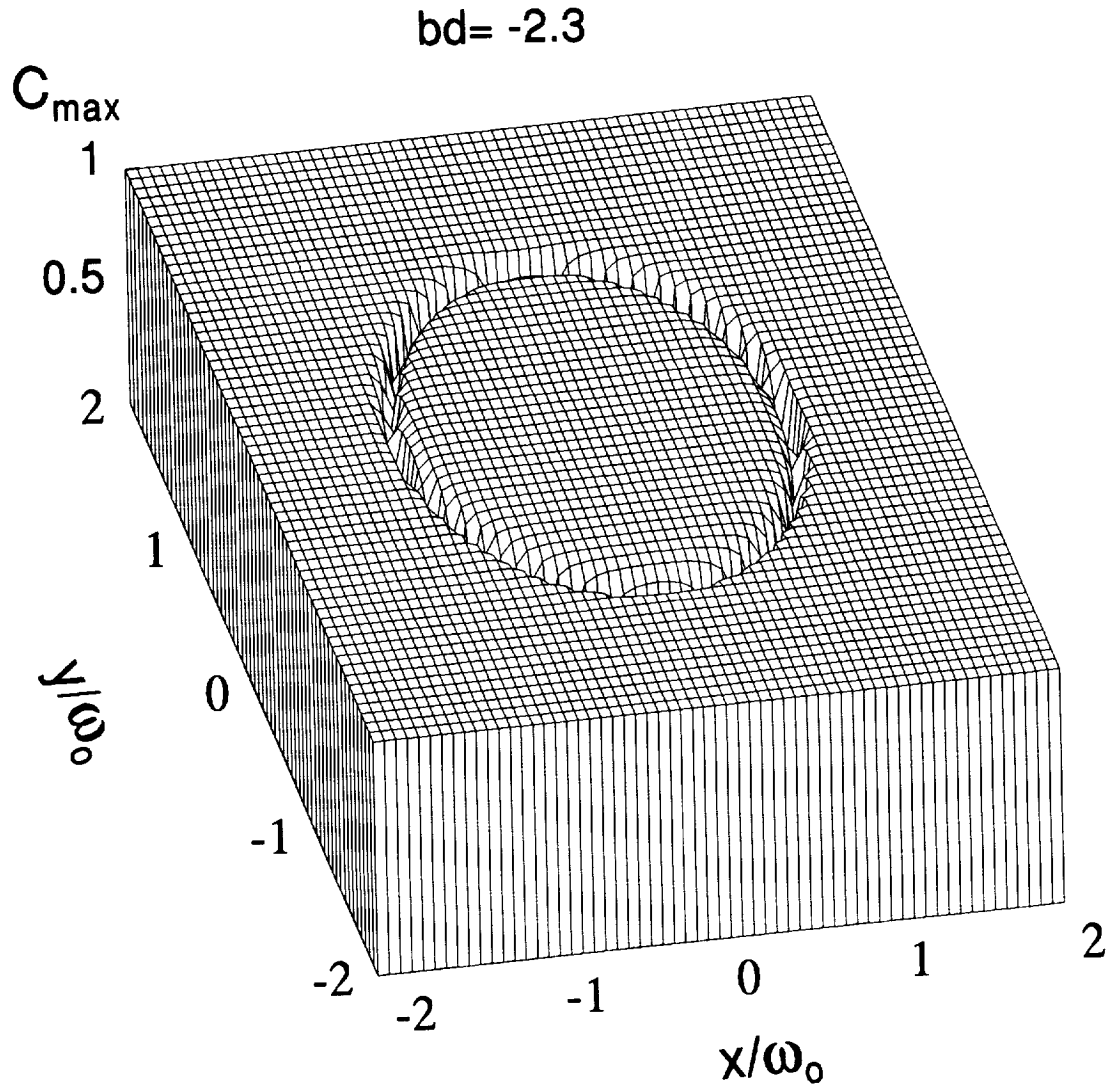
Figure 6.9: Correlation index distribution calculated with respect to the center point shows that the spatial coherence remains high in most parts of the wavefront except near an annular area where phase instability is found to occur.
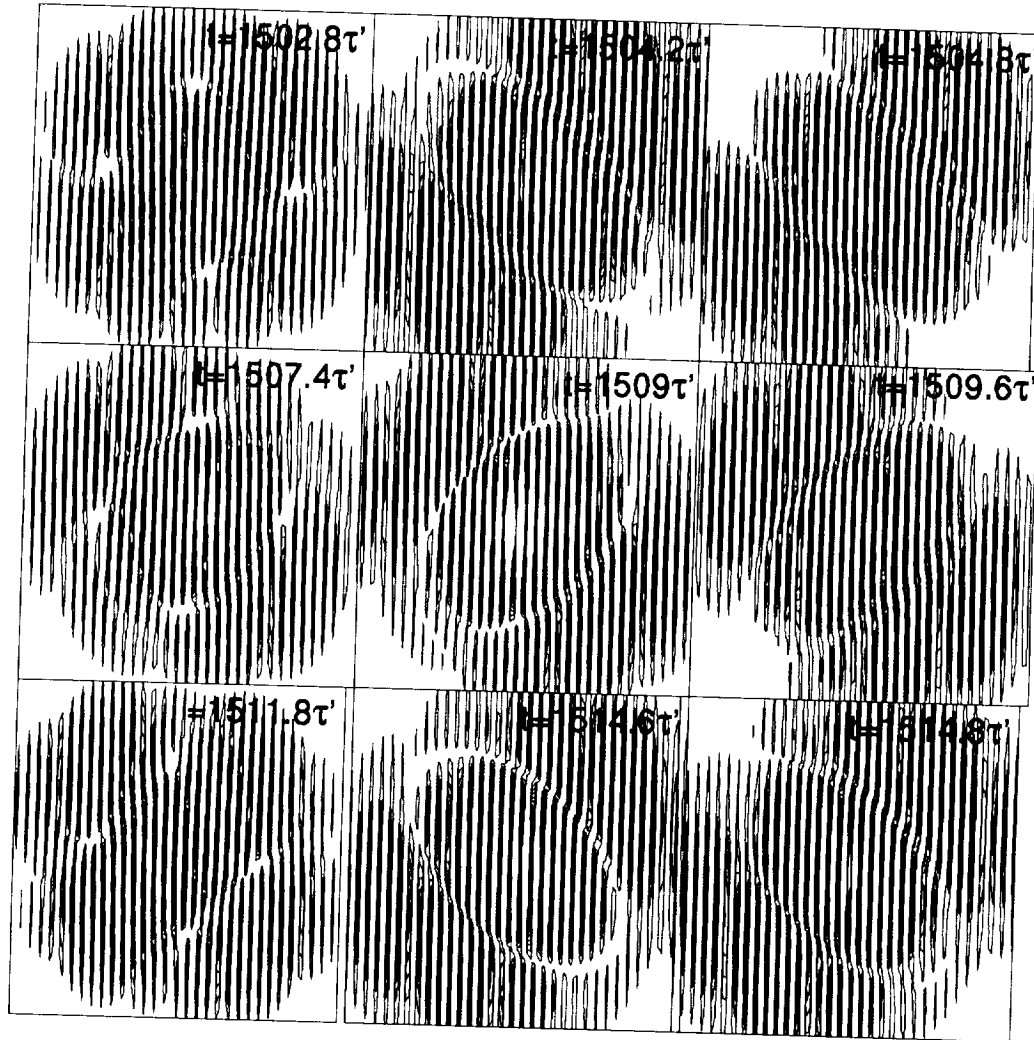
Figure 6.10: Sequence of interferogram snapshots revealing the motions of two pairs of defects in the beam cross-section for the off-Bragg parameter $bd = -2.45$. The two pairs of defects of opposite charge move along circular trajectories, collide and then annihilate near the two diagonal ends. The rotating motions of the defects are alternate in handedness.
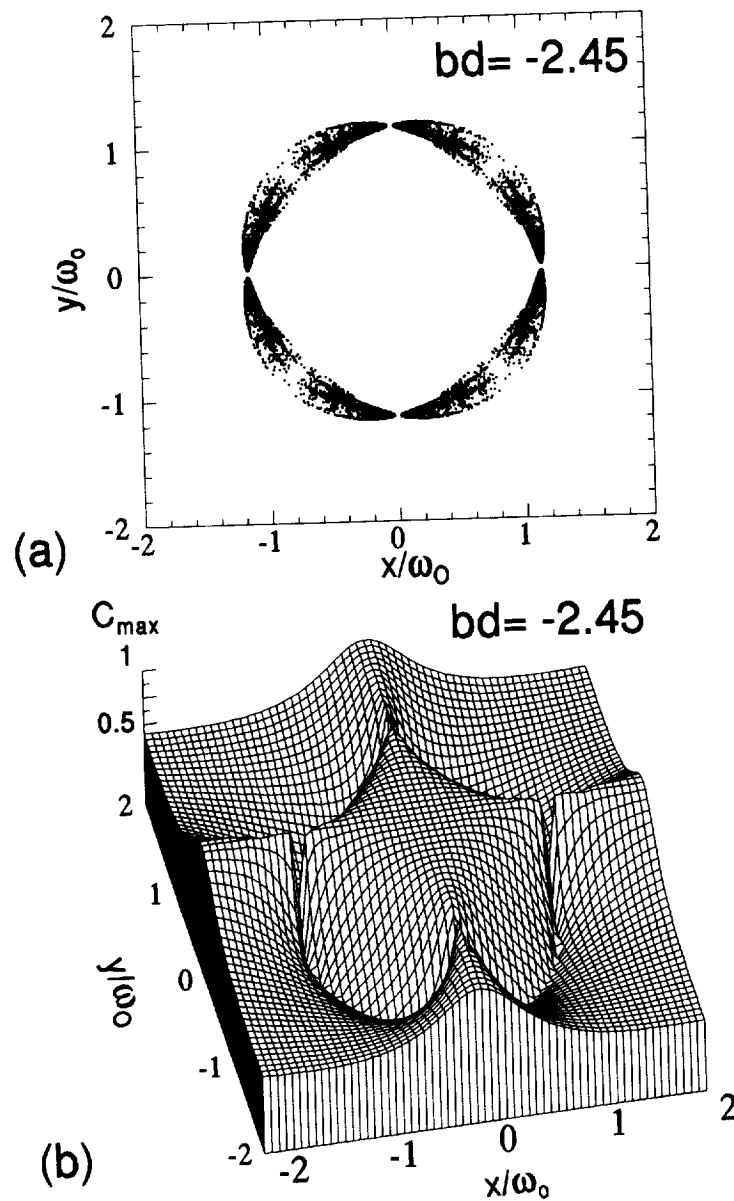
Figure 6.11: (a) Trajectories of defects in the wavefront for the off-Bragg parameter $bd = -2.45$, localized on an annular ring. (b) The correlation index with respect to a point at beam center drops sharply near the defects' trajectories.

their trajectories which are only delayed in time. A qualitatively similar behavior of the vortices was observed for $bd = -2.55$, as illustrated in fig. 6.12a and b.

An apparently chaotic time series was observed for $bd = -2.75$. Figure 6.13a shows that the vortices' position distribution is diffuse, indicating that their trajectories do not remain confined to narrow regions of space. In fact, the defects can visit about any place in the beam except near the origin and this is only because of the peculiar set of modes chosen for the decomposition. The corresponding correlation index distribution shown in fig. 6.13b is low in all regions visited by the vortices. Figure 6.13c shows the correlation index distribution with a fixed point $(x_1, y_1) = (1, 0.3)$ frequently visited by a vortex. It shows that even though the vortices trajectories have become more random, the intensity fluctuations in the regions they visit remain highly correlated.

At $bd = -3.18$, an apparent frequency locking was observed in the local intensity time series, leading to a quieter dynamics. For this value of the off-Bragg parameter, the wavefront phase and amplitude oscillate periodically but no defect nucleates. The regions in space where these fluctuations occur are identified as two concentric rings in the interferogram snapshots of fig. 6.14 and in the corresponding correlation index distribution of fig. 6.15.

6.4 Experimental results

The experimental apparatus has been described in detail in section 5.1. The PCM is an externally pumped single crystal of $BaTiO_3$. The source for the pumps is a single mode Ar ion laser ($\lambda = 514nm$) optically isolated from the setup by a Faraday rotator. The cavity ends with a planar dielectric mirror (R=0.95%) and contains a 16cm focal length lens. Two intra-cavity circular apertures of diameter $d_{pcm} = 0.79$mm and $d_m = 0.38$mm give a Fresnel number $F = 3.7$. The off-Bragg parameter was varied by tilting the mirror directing the pump A_1 toward the PCM and its values were calculated as the product of the momentum mismatch along the cavity axis with the interaction length. The change in pump overlap due to the tilting was measured and found negligible.
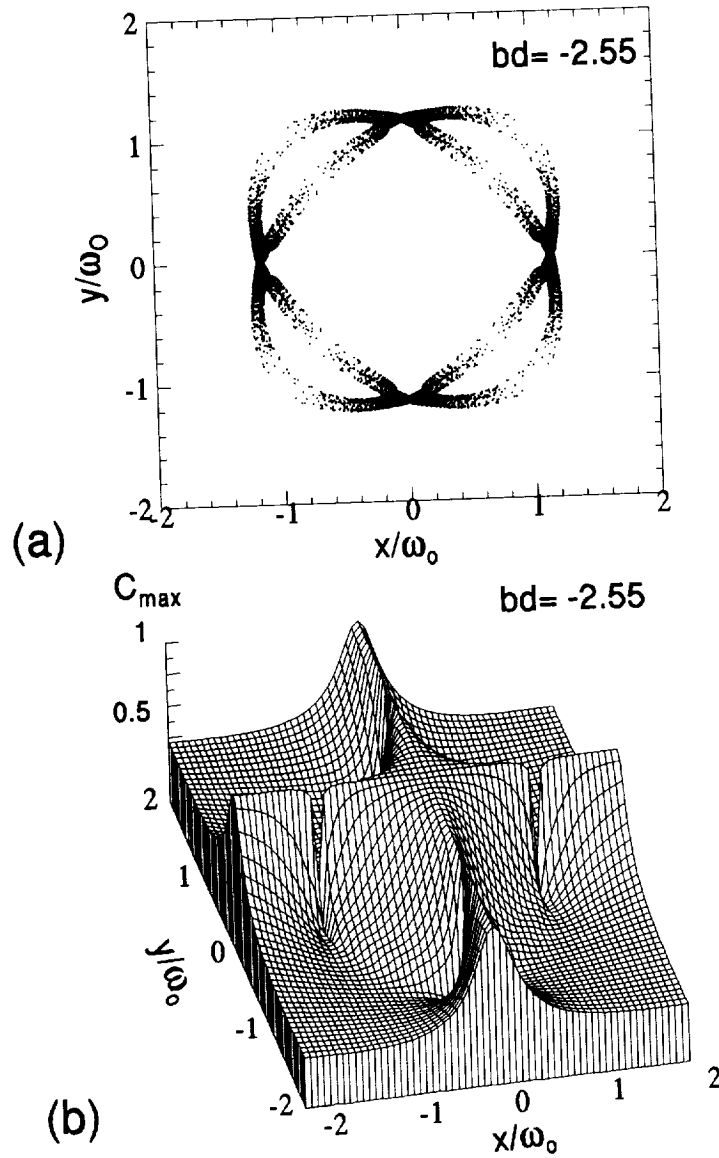
Figure 6.12: (a) Defect trajectories for $bd = -2.55$ showing defects still confined to certain regions of space but with more paths appearing. (b) The corresponding correlation index distribution shows the sharp drops of the spatial coherence in the area of the paths of defects.
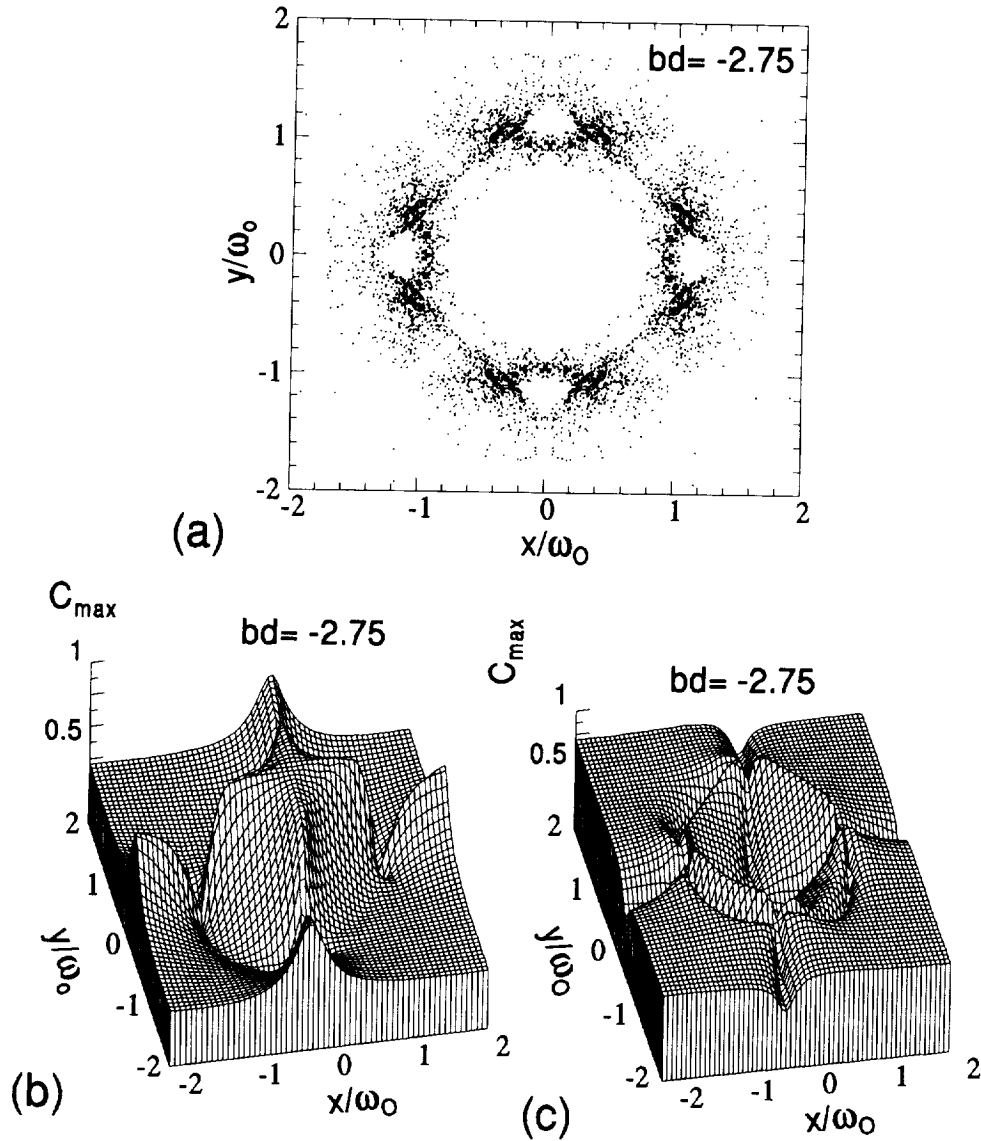
Figure 6.13: (a) At $bd = -2.75$, the defect trajectories become more diffuse and occupy larger regions of space in the wavefront. (b) The correlation index distribution with respect to the center point drops to small values at places where the defects concentrate. (c) The correlation index distribution with respect to a point $(1, 0.5)$ shows a high spatial coherence in all areas visited by the defects.
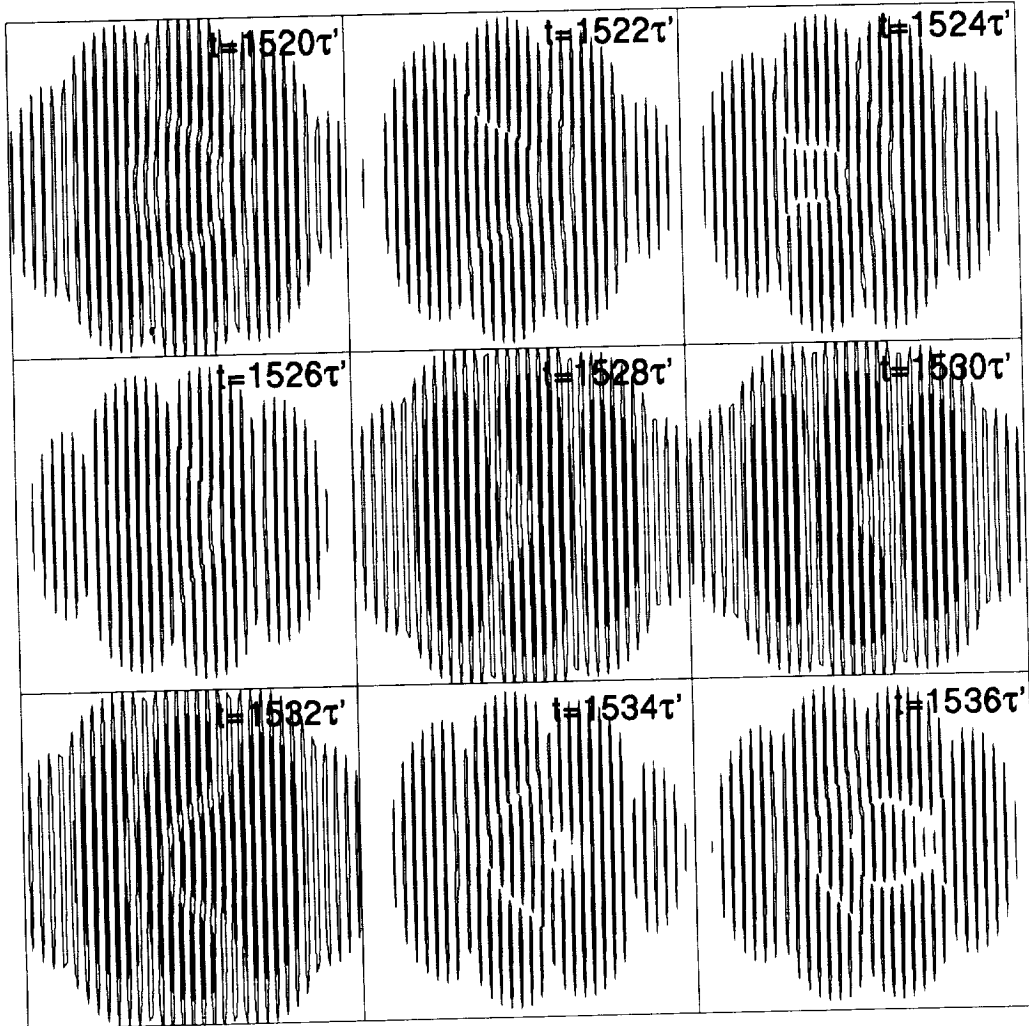
Figure 6.14: Sequence of snapshots of interferograms showing the time evolution of structures in the beam cross-section at $bd = -3.18$. It shows fringes bending with no defect nucleation. The phase breathes periodically in two concentric annular areas.
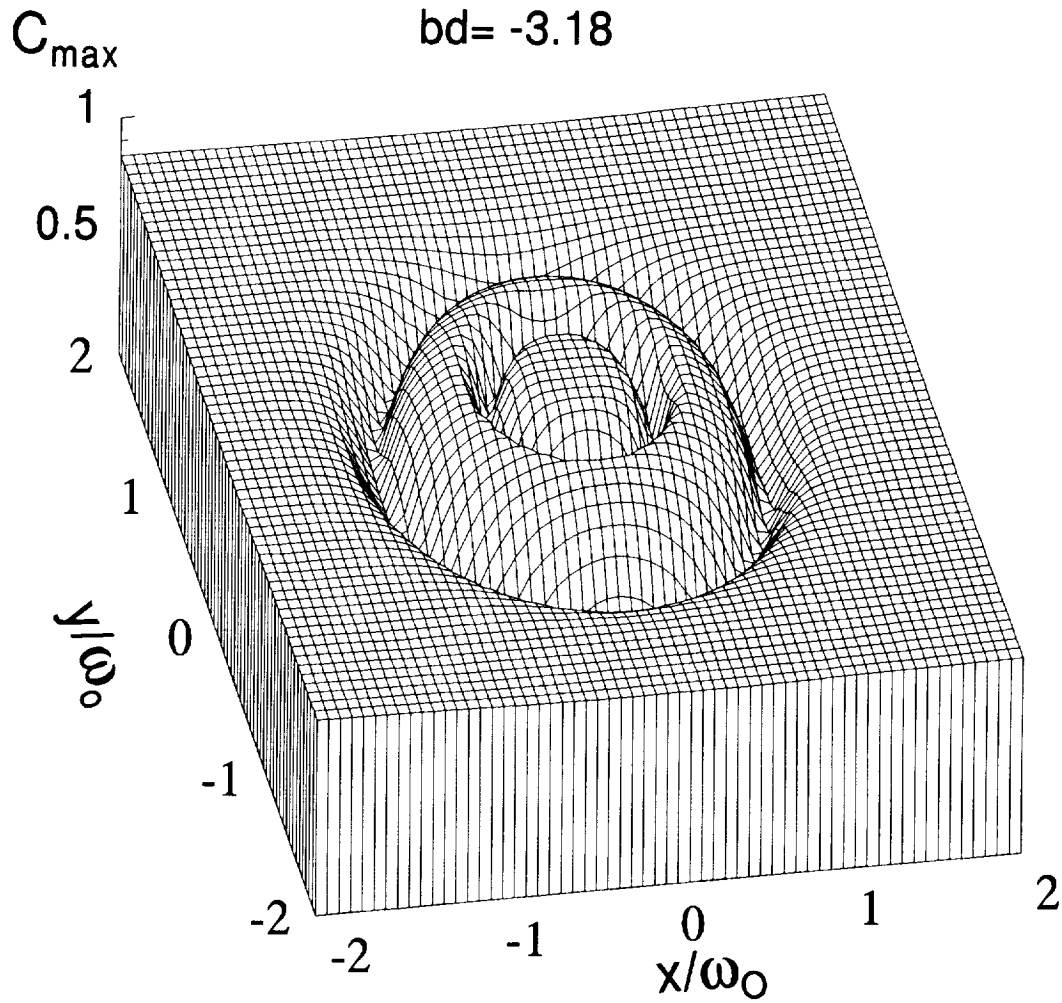
Figure 6.15: The correlation index distribution with respect to the center point show a structure with two concentric rings. The regions of low values of the correlation index are the places where fringe bendings are observed.

The aim of the experiments is to show, by way of illustration, that the range of behaviors predicted by the model and described in section 6.3 is indeed observed in the physical system. It would be unrealistic to expect a quantitative match between the experimental data and the results of numerical simulations if only because it is not possible to control experimentally which modes are actually taking part in the dynamics. A qualitative match, however, would at least indicate that the truncated modal expansion approach gives a fair representation of the actual dynamics of the PCR.

Figure 6.16 shows an interferogram snapshot of the beam exiting the PCM. It exhibits four vortices located at the corners of a quadrangle in an arrangement similar to that predicted by the model in figs. 6.6 and 6.10.

The off-Bragg parameter was scanned between two extreme values at which the momentum mismatch is large enough to reduce the gain below cavity losses and prevent oscillation. Local time series were recorded within that range and analyzed using power spectra and delayed-time phase space portraits. Near the center of the covered range of parameter values, a region where the motion was clearly periodic could be identified. On both sides of this region, similar sequences of various dynamical behaviors were observed, up to large mismatches at which the cavity stops oscillating. Before reaching these limits, simple periodic oscillations at reduced amplitudes were again observed. The sequence of behaviors just described is exactly what the bifurcation diagram of fig. 6.3 would predict (note that within the approximations of the model, this bifurcation diagram is symmetrical around $bd = 0$, but in the actual setup this symmetry is broken). By analogy with the model, the origin of parameter space ($bd_r = 0$) was chosen as the midpoint of the central region showing periodic oscillations. Other values of the off-Bragg parameter mentioned below are relative to this point. Some examples of time series are shown in fig. 6.17 and the corresponding power spectra are displayed in fig. 6.18. These examples were chosen to illustrate the variety of dynamical behaviors exhibited by the PCR and to compare them with the characteristic behaviors predicted by the model.

Figures 6.17a, 6.18a show the periodic motion expected for the off-Bragg parameter
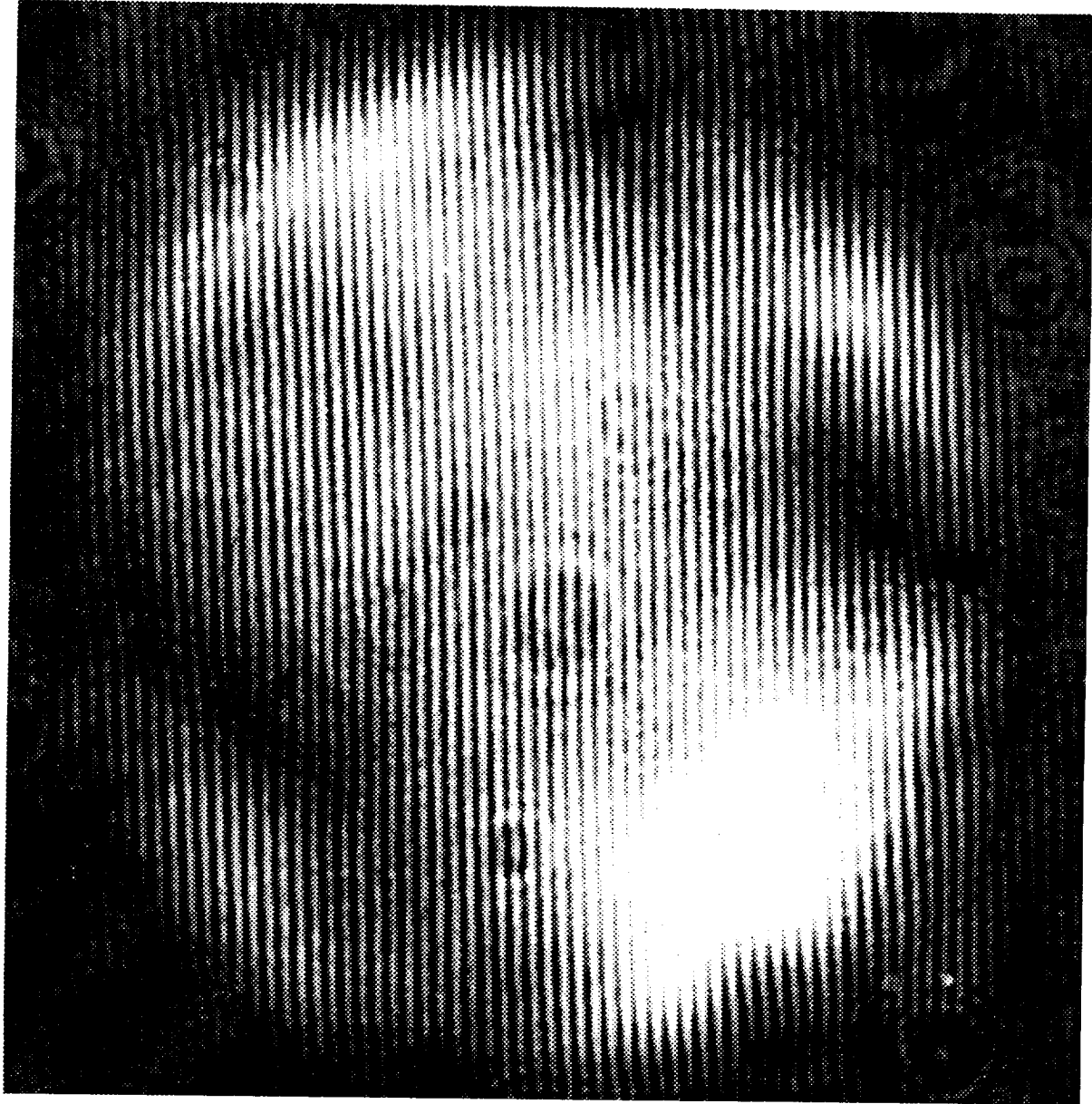
Figure 6.16: Interferogram snapshot at the output of the PCM revealing the presence of two pairs of vortices of opposite charges (experimental result).
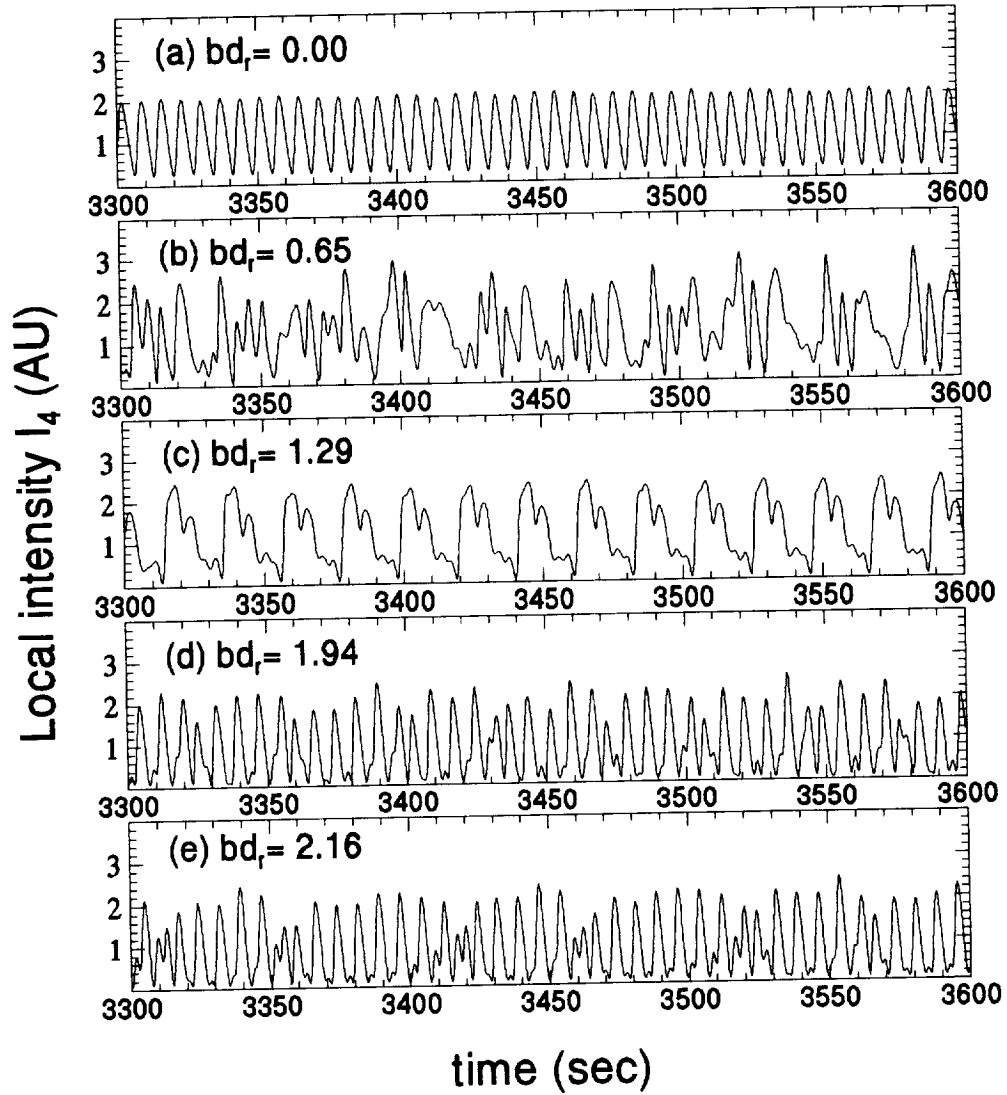
Figure 6.17: Local time series of I_4 measured at a point in the beam cross-section showing the variation of the dynamics for different values of the off-Bragg parameter: (a) simple periodic motion, (b) irregular motion, (c) frequency locking, (d) quasiperiodic motion, (e) another quasiperiodic motion.
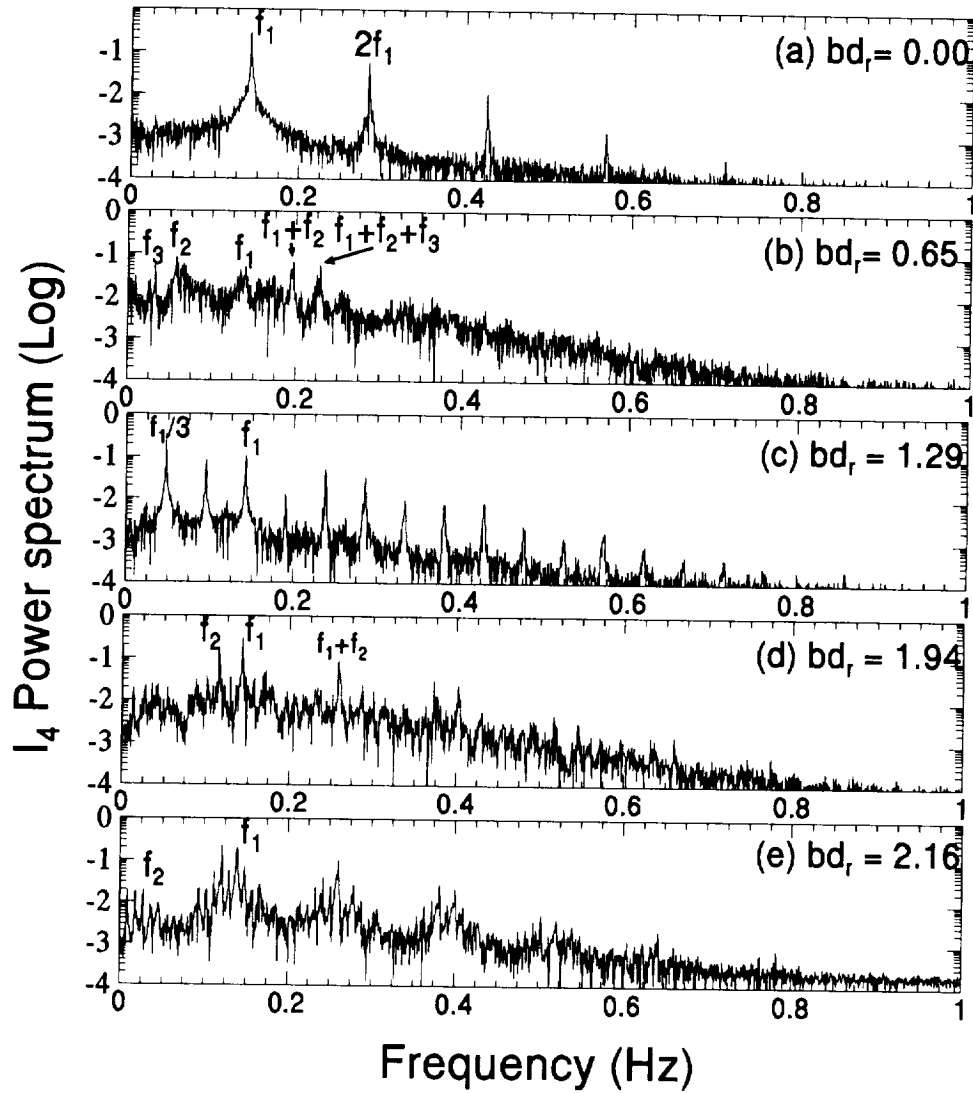
Figure 6.18: Power spectra of the local time series of fig. 6.17 showing (a) a fundamental frequency for a simple periodic motion, (b) three frequencies and a continuum for an irregular motion, (c) a frequency and it subharmonics for the frequency locked motion, (d) two incommensurate frequencies for a quasiperiodic motion, (e) another quasiperiodic motion with at least two incommensurate frequencies in the spectrum.

173

$bd = 0$. The corresponding delayed-time phase space portrait (fig. 6.19a) shows broadening which may give an indication of the level of stochastic noise.

Figures 6.17b, 6.18b obtained with $bd_r = 0.65$ show a chaotic state with an irregular time series and a spectrum containing at least two or three incommensurate frequencies, including the main frequency of about 0.14Hz, and a broad continuum, a signature of chaos. The exponential decay of the power spectrum (linear on the semilog scale of fig. 6.18) may be indicative of deterministic chaos. The corresponding phase space portrait of fig. 6.19b is diffuse and essentially featureless.

Figures 6.17c, 6.18c give a typical example of frequency locking obtained at $bd_r = 1.29$. The locking at period three is confirmed by the closed-loop phase space trajectory shown in fig. 6.19c. Note that the width of this limit cycle is about the same as that of fig. 6.19a and is probably due to stochastic noise.

At $bd_r = 1.94$ (figs. 6.17d, 6.18d) the motion is quasiperiodic with a spectrum containing only two incommensurate frequencies and their linear combinations. Another quasiperiodic motion obtained at $bd_r = 2.16$ is shown in fig. 6.17e, 6.18e. Here the lower frequency appears as sidebands of the higher one. For larger values of the off-Bragg parameter, e.g. $bd_r > 2.37$, the motion is periodic again with the same dominant frequency of ~ 0.14Hz but with decreasing amplitude. When $bd_r > 3$, the gain is lower than the cavity losses and no oscillation occurs.

6.5 Summary and conclusions

A model based on a truncated modal expansion of the cavity modes has been tested to describe the spatiotemporal dynamics of a phase-conjugate resonator. The Gauss-Hermite modes of the empty cavity are chosen as sensible basis functions to represent the fields in the nonlinear medium. Although the choice of the modes which take part in the dynamics is arbitrary in this method, justifications are given for truncating the series at a mode index of the order of the cavity Fresnel number. Verification of the validity of this choice are later given by comparison with
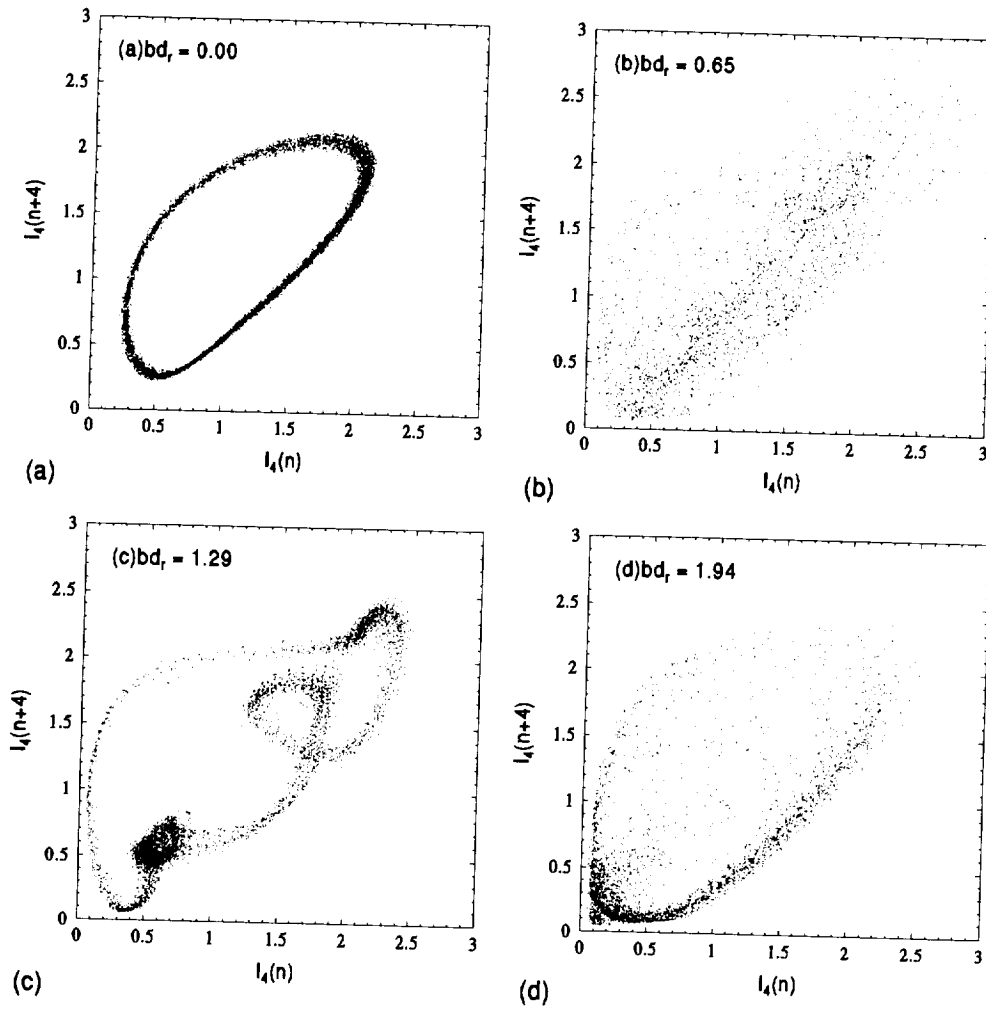
Figure 6.19: Time delayed phase-space portraits obtained from the data of the time series in fig. 6.17 showing (a) a limit cycle, (b) an irregular distribution, (c) a cycle-three motion, (d) smeared trajectories for the quasiperiodic motion.

experimental data. Numerical examples, using the off-Bragg parameter (momentum mismatch) as a control parameter, reveal a rich variety of dynamical behaviors illustrated by the local intensity fluctuations and ranging from simple periodic oscillations to quasiperiodic motions and chaotic states.

The modal decomposition method is particularly well suited to studying the spatial aspect of the dynamics without requiring prohibitive computational budgets. Numerical results indicate that the spatiotemporal dynamics of the PCR is mediated by the nucleation of pairs of defects of opposite charges in the beam and by their subsequent motion and annihilation. Maps of the spatial coherence function of the beam are found to be templates of the corresponding maps of the vortices' trajectories, establishing a strong correlation between these two quantities. The loss of temporal coherence and the onset of temporal chaos in the local intensity fluctuations is likewise correlated to the loss of spatial confinement of the vortices' trajectories and to the loss of spatial coherence.

Experimental data obtained with a PCR, using an externally pumped $BaTiO_3$ photorefractive PCR, reveal a range of dynamical behaviors similar to those shown by the simulation. These results confirm and complete the findings of the earlier experimental study of the PCR's dynamics at various Fresnel number, given in chapter 5. The arbitrariness of choice of the modes to include in the dynamics is the main shortcoming of the truncated modal expansion approach. Nevertheless it appears to be a convenient and computationally nondemanding tool to use to study and predict qualitatively the spatiotemporal behavior of phase-conjugate resonators and perhaps of other nonlinear optical devices as well.

Chapter 7

Conclusion

7.1 Discussion and summary

The material presented in this thesis is the result of an inquiry about the possible use of a phase conjugate resonator (PCR) as an image storage as well as a processing element in structural control (e.g. for the real time monitoring of the deformation of large structures). The dynamics of the PCR has been studied in two distinct regimes. Below threshold (gain < loss), the PCR cannot self-oscillate. In this regime, the output beam is always stationary in space and time, after the transients have died out. This stability makes it possible to use the PCRs in image processing applications. When the gain threshold is exceeded (above threshold), the PCR self-oscillates and spatiotemporal instabilities in the output beam set in.

This thesis was thus organized in two parts. In the first part, we have investigated the transient behavior and stability properties of a PCR below threshold. In the second part, we have studied experimentally and theoretically the PCR's spatiotemporal dynamics above threshold.

We have presented the transient dynamics of a PCR below threshold based on time-dependent coupled wave equations for FWM in a photorefractive crystal with two distinct interaction regions caused by the feedback from a slightly tilted ordi-

nary mirror. First, we have solved the steady state equations for the cavity's fields analytically, assuming nondepleted pumps and an absorption free medium. The solutions predict that the PCR self-oscillates (reaches threshold) in a broader range of values of pump ratios if the PCM has a higher values of the coupling parameter. The PCR's transfer function (below threshold) is obtained through applying a simple frequency-domain transformation technique to the steady state equations. The transfer function is shown to be largely dependent on the coupling parameter and the pump ratio. Contour plots of the transfer function as a function of complex angular frequency indicate that there is no sign of instability before the PCR can self-oscillate, while unstable poles quickly develop once the PCR is above threshold.

In the transient regime of the PCR, we have successfully applied a numerical scheme for integrating the photorefractive FWM equations separately in the space and the time domains using the adiabatic elimination process. Numerical calculations of the cavity's buildup and decay times as well as of the specularly reflected and phase conjugate reflected intensities as functions of a number of system parameters confirm that the parameters affecting the threshold most directly are the coupling parameter and the pump ratio. We have presented results which indicate that the cavity buildup and decay times can be tailored by varying several system parameters. Results predict the possible use of the PCR as an image processing element. For example, the PCR could, in principle, perform constrast enhancement during buildup and contrast reduction during decay. This same feature could be used to implement a time varying spatial filtering if the projected field in the PCM is the spatial spectrum of an image rather than the input image itself. Experimental measurements of the cavity's buildup and decay times confirm qualitatively the result of the numerical simulations.

In the above-threshold regime, we have studied experimentally some aspects of the spatiotemporal behaviors of the PCR as a function of the Bragg detuning bd achieved by misaligning one of the two pump beams, and as a function of the degree of transverse confinement controlled by varying the resonator's Fresnel number F. Temporal aspects of the beams' complexity were revealed by analysing the local intensity time

series, power spectra, and embedded phase space portraits. In the case of varying F, we observed bifurcation phenomena typical of low dimensional dynamical systems, i.e. in order of increasing control parameter, a bifurcation from a stationary to a periodic state, followed by more subharmonic bifurcations, the occurrence of a chaotic state, the occurrence of intermittency, and finally a fully turbulent state. For a particular case of irregular oscillations, the correlation dimension of the attractor constructed from the embedded phase space was calculated to be approximately 5.2, indicating that the attractor may be strange. Furthermore, a positive finite lower bound value of the Kolmogorov entropy can be extracted from the same time series, indicating the existence of a deterministic chaos. In the case of varying bd, the temporal aspects of the dynamics in the local time series range from simple periodic oscillations, followed by quasiperiodic states interrupted by chaotic states. All experimental results thus far have consistently revealed the presence of two distinct frequencies in the power spectra in some regions of parameter space.

Regarding the spatial aspects of the beams' complexity, we have demonstrated the existence of wavefront dislocations or vortices in the optical fields by video recording and by interferometry. A rich variety of defect movements has been recorded and analysed. The spatial complexity was characterized by the number of optical vortices and their variety of movements, as well as by their relationship with the beam's spatial coherence. The number of defects and the spatial correlation index have been shown to follow similar trends as the transverse confinement of the system is relaxed, pointing to the role played by the wavefront dislocations in the dynamics.

We have also tested a model based on a truncated modal expansion of the cavity modes, to investigate the spatiotemporal dynamics of the PCR. We have clearly shown that the optical vortices in the wavefront are also present in the numerical solutions. Simulations using the Bragg detuning as a control parameter have shown that optical vortices begin to appear under conditions of increased local gain which appears to be obtained by the small misalignment of one of the pump beams from the Bragg angle. Power spectra of simulated time series also contain two distinctive frequencies for a certain range of the off-Bragg parameter, indicating that the dynamics is governed

C'-3

by two different time scales. The short one, on the order of the material's damping time, seems to correspond to the recovery rate of the local wavefront after a vortex has moved through it, while the long one is associated with the alternation from one mode to another in the competition process and seems to correspond to the full cycle of the vortices' nucleation, motion and annihilation. Numerical results also indicate that the loss of temporal coherence and the onset of temporal chaos in the local intensity fluctuations is likewise correlated to the loss of spatial confinement of the vortices' trajectories and the spatial coherence.

Thus far, several reports have been published in the literature concerning temporal instabilities in photorefractive oscillators. Each of these systems has provided a physical picture of how chaotic oscillations can occur. Our study shows that the spatiotemporal chaotic behaviors in a PCR may possibly be attributed to the mechanisms of the competition among various cavity modes and the gain enhancement which arises from off-Bragg FWM. As we have seen in chapter 2, the steady state solution predicts that the range of pump ratios R_p, within which the feedback parameter β can be greater than one, becomes wider and wider as the coupling parameter $\gamma_o d$ is increased. The direct numerical integration of the FWM equations in chapter 3 confirms that the PCR can fall into the above-threshold regime in a wider range of pump ratios with increasing values of the coupling parameter. In chapter 6, we presented the three dimensional FWM equations in order to account for the transverse dynamics in the PCR. We introduced a modal decomposition method in which cavity fields are basically described by a set of participating cavity modes. Numerical results show that chaotic oscillations set in for a large enough coupling parameter (e.g. $|\gamma_o d| > 8$). In the modal decomposition method, we have seen how the modal amplitudes of the cavity fields are coupled to each other in eqs. 6.20–6.23. It is this complex coupling that brings about the unstable oscillations which would otherwise not be seen in the plane-wave FWM model even in cases of quite large coupling parameters. The off-Bragg parameter bd obtained by tilting one of the two pumps away from the Bragg angle is another significant factor in lowering the threshold for the instabilities observed in PCR. When $bd = 0$ (no Bragg detuning), only periodic os-

180

cillations are seen in the output. When $bd \neq 0$ (with Bragg detuning), quasiperiodic and irregular oscillations appear in the output.

With no Bragg detuning, the coupling between cavity modes provides only channels for energy exchange between modes. This "beating" between oscillating modes leads to periodic changes in the output beam. With Bragg detuning, there is an additional phase transfer between the interacting modes due to the additional phase shifts of the individual mode gratings. It is this coupling of the phases which makes possible the occurrence of chaotic behavior. An intuitive explanation for this behavior is the following. Consider what happens inside the crystal as the FWM process progresses in time. Initially pump 2 illuminates the crystal and at time $t = 0$ pump 1 is turned on and scattered noise in the cavity forms beam 4. Then, beam 1 and beam 4 start to write various mode gratings and beam 2 is scattered from these gratings and the scattered beam is fed back from the dielectric mirror. However, as the gratings start to form, they change the phase of the individual mode. This in turn causes a new mode grating to be written, which again changes the phases of the participating modes, and so on. This constant change in phases of the interacting beams leads to constantly writing new gratings and washing out old gratings. It is these dynamic gratings together with the feedback of the cavity that gives rise to chaotic oscillations once some gain threshold is exceeded.

A final remark should be given. The arbitrariness of choice of the participating modes is the main shortcoming of the truncated modal expansion approach used in this work, despite the fact that justifications are given for truncating the series at a mode index of the order of the cavity Fresnel number. Yet, the method is shown to be a particularly convenient and computationally nondemanding tool for study of the spatiotemporal behavior of the PCR and perhaps of other nonlinear systems as well. Thus far, experimental results are supportive of the validity of this approach.

In conclusion, this the first time to the author's best knowledge that the spatiotemporal dynamics has been both experimentally and theoretically explored in a photorefractive PCR, and also that direct physical evidence of optical vortices has been unveiled in detail in the wavefronts of the optical fields from the PCR. Our re-

sults should prove useful in the study of photorefractive devices and in the assessment of their practical usefulness. They may also add a small contribution to the growing area of research in nonlinear dynamics in general.

7.2 Possible future investigations

One of the interesting properties of a PCR is that a great number of transverse modes is allowed to oscillate if the transverse extent of the cavity is opened up. This means that an optical processing device utilizing a PCR can have a high spatial resolution. Yet, the spatiotemporal instabilities due to the transverse mode competition reported in this thesis may impose limitations on the spatial and temporal performance of the device. To make a device pratical, methods for eliminating these instabilities are definitely needed. Some efforts have been recently made to alleviate the spatial and temporal instabilities in a PCR with $BaTiO_3$ as the PCM, by using an intracavity mode homogenizer such as a multimode fiber taper or light pipe [107]. The demonstrated improvement in the spatial and temporal stability, and also the overall increase in the transverse extent of the oscillating mode, will undoubtedly make possible many new processing techniques based on PCR in the above threshold regime.

The mode competition process in the PCM may be favorable for other applications. For example, associative recall and processing of images using photorefractive oscillators have already been demonstrated [9, 10, 11]. In these applications, competition between modes is fundamental for the discrimination capability of the memory. A recent investigation to explore the possibility of using a laser as a nonlinear element in an associative memory architecture [108] may be an important new approach utilizing the continuous field distributions in a cavity rather than a discrete array of elements as in many neural networks. One basic requirement for this approach to be successful is the coexistence of many stable states, or "spatial multistability". In isolated multistable systems the final state is completely unpredictable because initial fluctuations determine its evolution. Yet, different behavior is expected when the

system is driven externally by an identical system. In this case, a weak signal from the driving system is injected into the system while it is below threshold. As soon as the injected signal is switched off, the main system is switched above threshold. The system then starts with the seed left by the signal, and the evolution toward a stationary state is no longer random but is a function of the spatial configuration of the initial seed. Still, more demonstrations of practical architectures of such kinds are definitely needed. It seems that a PCR with high mode volume may be a candidate for the nonlinear element of an optical associative memory. Nevertheless, the first question to answer is whether spatial multistability can be achieved in systems based on photorefractive oscillators. To this end, the PCR patterns must be stabilized and simultaneously some process must be found to switch from pattern to pattern. Perhaps the example of using an intracavity mode homogenizer in PCR is a first step toward achieving these goals.

Another aspect of the spatiotemporal dynamics concerns the behaviors of the cavity fields in other PCR geometries. The similarities and differences obtained with different setups may be important. At least, with such a comparison we could have some ideas of what is generic or geometric-specific in the observed dynamics. Furthermore, other new methods for the study of extended systems such as subspace Lyapunov spectra. [84] could also be applied to the diagnosis of experimental data from the PCR.

Appendix A

Derivation of the four-wave mixing equations

In this appendix we derive the set of coupled wave equations for waves propagating in the PCM that are used in studying the dynamics of the PCR. At first we consider the optical fields as uniform plane waves of infinite extent, then we allow the optical fields to have transverse spatial variations.

We start with the Maxwell's equations for the macroscopic variables of the fields. In general these equations take the form:

$$\nabla \times \vec{\mathcal{E}} = -\frac{1}{c}\frac{\partial \vec{\mathcal{H}}}{\partial t}, \tag{A.1}$$

$$\nabla \times \vec{\mathcal{H}} = \frac{1}{c}\frac{\partial \vec{\mathcal{D}}}{\partial t} + \frac{4\pi}{c}\vec{\mathcal{J}}, \tag{A.2}$$

$$\nabla \cdot \vec{\mathcal{D}} = 4\pi \rho_f, \tag{A.3}$$

$$\nabla \cdot \vec{\mathcal{B}} = 0, \tag{A.4}$$

with

$$\vec{\mathcal{D}} = \vec{\mathcal{E}} + 4\pi\vec{\mathcal{P}} = \epsilon_o(\epsilon_{r_o} + \Delta\epsilon_r)\vec{\mathcal{E}}, \tag{A.5}$$

$$\vec{\mathcal{H}} = \vec{\mathcal{B}} - 4\pi\vec{\mathcal{M}}, \tag{A.6}$$

184

$$\vec{\mathcal{J}} = \sigma \vec{\mathcal{E}}, \tag{A.7}$$

where $\vec{\mathcal{E}}$ is the total optical electric field, $\vec{\mathcal{D}}$ is the electric displacement, $\vec{\mathcal{P}}$ is the induced polarization, $\vec{\mathcal{H}}$ is the magnetic field, $\vec{\mathcal{B}}$ is the magnetic induction, $\vec{\mathcal{M}}$ is the magnetization, ρ_f is the free charge density, $\vec{\mathcal{J}}$ is the current density, c is the speed of light in vacuum, ϵ_o is the permittivity in vacuum, ϵ_{ro} is the background (average) relative dielectric constant when only the pump beams are present, $\Delta \epsilon_r$ is the relative induced dielectric constant which is slowly varying in both time and space when both the pump beams and the probe beams are present, and σ is the conductivity.

For ferroelectric oxides, $\vec{\mathcal{H}} = \vec{\mathcal{B}}$ and $\rho_f = 0$. Taking the curl of eq. A.1 and combining with eq. A.2, we obtain the wave equation:

$$\nabla^2 \vec{\mathcal{E}} - \frac{\epsilon}{c^2} \frac{\partial^2 \vec{\mathcal{E}}}{\partial t^2} = \frac{\Delta \epsilon}{c^2} \frac{\partial^2 \vec{\mathcal{E}}}{\partial t^2} + \frac{4\pi\sigma}{c^2} \frac{\partial \vec{\mathcal{E}}}{\partial t}, \tag{A.8}$$

where $\epsilon = \epsilon_o \epsilon_{ro}$ and $\Delta\epsilon(r,t) = \epsilon_o \Delta\epsilon_r$. It is assumed that $\Delta\epsilon(r,t)$ is smooth in space and time. Suppose that the fields inside the PCM are uniform plane waves of the same polarization, say the extraordinary polarization (see figure A.1). We also assume that all waves are propagating with small angles to the z-axis and the total intensity profile as well as the resultant refractive index vary periodically in x with frequency k_x. Thus, we can write down the scalar total optical field in fourier expansion as

$$\mathcal{E}(x, z, t) = \sum_{l=-\infty}^{\infty} A_l(z,t) e^{i(\omega t \mp k_z z + l k_x x)}, \tag{A.9}$$

and the induced dielectric constant as

$$\Delta\epsilon(x, z, t) = \sum_{l=-\infty}^{\infty} \epsilon_l(z,t) e^{i l k_x x}, \tag{A.10}$$

with $k_x = k_o \sqrt{\epsilon} \sin\theta$, $k_z = k_o \sqrt{\epsilon} \cos\theta$, $k_o = 2\pi/\lambda_o = \omega/c$, where λ_o is the light wavelength in vacuum.

In the following, we use the slowly varying envelope approximation (SVEA) which assumes that $A_l(z,t)$ and $\epsilon_l(z,t)$ are smooth functions of z and t, i.e.

$$\frac{\partial^2 A_l}{\partial t^2} \ll 2\omega \frac{\partial A_l}{\partial t} \quad \text{and} \quad \frac{\partial^2 A_l}{\partial z^2} \ll 2k_z \frac{\partial A_l}{\partial z}. \tag{A.11}$$

185
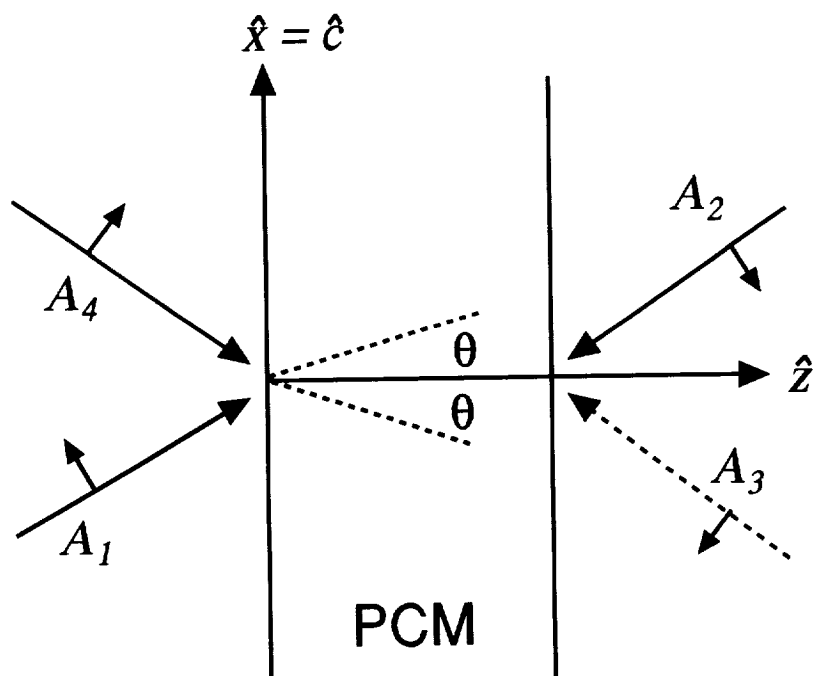
Figure A.1: Schematic diagram for the four-wave mixing geometry. A_1 and A_2 are the two external pumps. A_4 is the probe beam and A_3 is the phase conjugate beam. Arrows show the beams' polarization and direction of propagation. Beams are symmetrical about $\hat{Z}$ and θ is the angle inside the crystal. $\hat{c}$ denotes the crystal's axis.

Substituting eq. A.9 and A.10 with A.11 in A.8 and equating the lth component of the optical field on both sides, we obtain

$$\frac{\partial A_l}{\partial z} \pm \frac{\omega\epsilon}{c^2 k_z}\frac{\partial A_l}{\partial t} \pm \frac{i(1-l^2)k_x^2}{2k_z}A_l \pm \frac{2\pi\omega\sigma}{c^2 k_z}A_l = \mp\frac{ik_o^2}{2k_z}\sum_{l'}\epsilon_{l'}A_{l-l'}. \qquad (A.12)$$

In four-wave mixing, without Bragg missmatch, beam 1 is collinear with beam 2 and beam 4 is collinear with beam 3 (see figure A.1), we have

$$\vec{k_1} + \vec{k_2} = \vec{k_3} + \vec{k_4} = 0. \qquad (A.13)$$

The total optical field as a sum of four beams takes the form

$$\mathcal{E}(x,z,t) = \sum_{j=1}^{4} A_j(z,t)e^{i(\omega t - \vec{k_j}\cdot\vec{r})} \qquad (A.14)$$

Next, for the Bragg's condition in a thick volume hologram situation, i.e. $A_l = 0$ for $|l| > 1$ and $A_{\pm 1} \neq 0$, eq. A.12 becomes

$$\frac{\partial A_{\pm 1}}{\partial z} + \frac{\omega\epsilon}{c^2 k_z}\frac{\partial A_{\pm 1}}{\partial t} = -\frac{ik_o^2}{2k_z}\epsilon_{\pm 2}A_{\mp 1} - \frac{\alpha}{\cos\theta}A_{\pm 1}, \qquad (A.15)$$

for waves propagating to the right, and

$$\frac{\partial A_{\pm 1}}{\partial z} - \frac{\omega\epsilon}{c^2 k_z}\frac{\partial A_{\pm 1}}{\partial t} = +\frac{ik_o^2}{2k_z}\epsilon_{\pm 2}A_{\mp 1} + \frac{\alpha}{\cos\theta}A_{\pm 1}, \qquad (A.16)$$

for waves propagating to the left, where $\alpha \equiv 2\pi\sigma/c\sqrt{\epsilon}$. Thus we can write down the coupled differential equations for waves propagating inside the PCM in the notation of figure A.1 as follows:

$$\frac{\partial A_1}{\partial z} + \frac{1}{v\cos\theta}\frac{\partial A_1}{\partial t} = \frac{-ik_o}{2\sqrt{\epsilon}\cos\theta}\epsilon_2 A_4 - \frac{\alpha}{\cos\theta}A_1, \qquad (A.17)$$

$$\frac{\partial A_2}{\partial z} - \frac{1}{v\cos\theta}\frac{\partial A_2}{\partial t} = \frac{ik_o}{2\sqrt{\epsilon}\cos\theta}\epsilon_{-2} A_3 + \frac{\alpha}{\cos\theta}A_2, \qquad (A.18)$$

$$\frac{\partial A_3}{\partial z} - \frac{1}{v\cos\theta}\frac{\partial A_3}{\partial t} = \frac{ik_o}{2\sqrt{\epsilon}\cos\theta}\epsilon_2 A_2 + \frac{\alpha}{\cos\theta}A_3, \qquad (A.19)$$

$$\frac{\partial A_4}{\partial z} + \frac{1}{v\cos\theta}\frac{\partial A_4}{\partial t} = \frac{-ik_o}{2\sqrt{\epsilon}\cos\theta}\epsilon_{-2} A_1 - \frac{\alpha}{\cos\theta}A_4, \qquad (A.20)$$

APPENDIX A.

with $v = c/\sqrt{\epsilon}$. From eq. A.14, the total intensity is

$$
\begin{aligned}
I(x, z, t) &= |\mathcal{E}|^2 &&\text{(A.21)} \\
&= I_o(z, t) + (A_1 A_4^* e^{-i(\vec{k}_1 - \vec{k}_4) \cdot \vec{r}} + A_2 A_3^* e^{-i(\vec{k}_2 - \vec{k}_3) \cdot \vec{r}} \\
&\quad + A_1 A_3^* e^{-i(\vec{k}_1 - \vec{k}_3) \cdot \vec{r}} + A_2^* A_4 e^{-i(\vec{k}_4 - \vec{k}_2) \cdot \vec{r}}) + c.c.
\end{aligned}
$$

with $I_o(z, t) = \sum_{j=1}^{4} |A_j(z, t)|^2$. Because of the small incident angle to the z-axis for all fields, the exponentials in the 4th and 5th terms are fast changing phase factors with respect to the slowly varying amplitudes so that they becomes insignificant in space averaging. Now we let $\vec{k}_1 - \vec{k}_4 = \vec{k}_2 - \vec{k}_3 = \vec{K}_x$ with $|K_x| \sim 2k_x$. Then the light intensity can be written as

$$
I(x, z, t) = I_o(z, t) + \left[I_2(z, t) e^{-iK_x x} + c.c. \right], \tag{A.22}
$$

with

$$
I_2(z, t) = A_1(z, t) A_4^*(z, t) + A_2^*(z, t) A_3(z, t). \tag{A.23}
$$

The induced dielectric constant is related to a space-charge field via the linear electro-optic effect (see Appendix B) and is given by

$$
\Delta\epsilon(x, z, t) = \frac{1}{2} \sqrt{\epsilon} \bar{n}_o^3 r_{eff} E_{sc}(x, z, t), \tag{A.24}
$$

where $\bar{n}_o$ is the bulk refractive index, r_{eff} is the electrooptic coefficient, and E_{sc} is the space-charge field determined by the transport equations B.1–B.4. Also we can expand the space-charge field in the same form as $\Delta\epsilon$ in eq. A.10:

$$
E_{sc} = E_o + \left[E_2(z, t) e^{-iK_x x} + c.c. \right]. \tag{A.25}
$$

Thus, comparing eq. A.25 with A.10 and equating the coefficients of $e^{-iK_x x}$ on both sides of eq. A.24, we have

$$
\epsilon_{+2}(z, t) = \frac{\sqrt{\epsilon}}{2} \bar{n}_o^3 r_{eff} E_2(z, t), \tag{A.26}
$$

and

$$
\epsilon_{-2}(z, t) = \epsilon_{+2}^*(z, t). \tag{A.27}
$$

188

APPENDIX A.

Taking $\theta \ll 1$, and using eqs. A.17–A.20 with eqs. A.26 and A.27, we obtain a set of coupled wave equations having the form:

$$\frac{\partial A_1}{\partial z} + \frac{1}{v}\frac{\partial A_1}{\partial t} = -QA_4 - \alpha A_1,$$ (A.28)

$$\frac{\partial A_2^*}{\partial z} - \frac{1}{v}\frac{\partial A_2^*}{\partial t} = -QA_3^* + \alpha A_2^*,$$ (A.29)

$$\frac{\partial A_3}{\partial z} - \frac{1}{v}\frac{\partial A_3}{\partial t} = QA_2 + \alpha A_3,$$ (A.30)

$$\frac{\partial A_4^*}{\partial z} + \frac{1}{v}\frac{\partial A_4^*}{\partial t} = QA_1^* - \alpha A_4^*,$$ (A.31)

with the index grating

$$Q \equiv \frac{i\omega \bar{n}_o^3}{4c}r_{eff}E_2,$$ (A.32)

where E_2 is given in eq. B.32.

Next, we consider the possible transverse spatial variations of the optical fields. It means that the fields' amplitudes depend in general on x and y as well as z, i.e.,

$$\mathcal{E}(x,y,z,t) = \sum_{j=1}^{4} A_j(x,y,z,t)e^{i(\omega t - \vec{k}_j \cdot \vec{r})} + c.c.$$ (A.33)

The wave equation A.8 can be written as

$$\nabla^2 \mathcal{E}(x,y,z,t) - \frac{n^2(x,y,z,t)}{c^2}\frac{\partial^2 \mathcal{E}}{\partial t^2} - \frac{4\pi\sigma}{c^2}\frac{\partial \mathcal{E}}{\partial t} = 0,$$ (A.34)

where $n^2 = \epsilon + \Delta\epsilon$. Also when considering weak modulation in a photorefractive medium, we can expand n in the same form as the induced dielectric constant:

$$n(x,y,z,t) = \bar{n}(x,y,z) + n_1 e^{i\phi}m(x,y,z,t)e^{i\vec{K}\cdot\vec{r}} + c.c.$$ (A.35)

$$= \bar{n} + \Delta n(x,y,z,t),$$

where $m(x,y,z,t)$ is the first order perturbation which is given by the ratio

$$m(x,y,z,t) \equiv \frac{I_2(x,y,z,t)}{I_o(x,y,z,t)}$$ (A.36)

$$= \frac{A_1 A_4^* + A_2^* A_3}{I_o}$$

189

and $\bar{n}$ is the bulk refractive index, Δn is the induced refractive index. Here $\vec{K}_x \equiv \vec{k}_4 - \vec{k}_1 = \vec{k}_2 - \vec{k}_3$. We assume a small modulation in the refractive index, i.e., $|\Delta n| \ll \bar{n}$. Then the wave equation A.34 can be reduced to

$$\nabla^2 \mathcal{E}(x,y,z,t) - \left(\frac{\bar{n}^2}{c^2} + 2\bar{n}\frac{\Delta n}{c^2}\right)\frac{\partial^2 \mathcal{E}}{\partial t^2} - \frac{4\pi\sigma}{c^2}\frac{\partial \mathcal{E}}{\partial t} = 0. \qquad (A.37)$$

Substituting eqs. A.33 and A.35 in eq. A.37 and using the SVEA, we obtain

$$\sum_{i=1}^{4}\left\{\left[\nabla_T^2 - k_i^2 - 2i\vec{k}_i \cdot \nabla\right]A_i \quad - \quad \left[\frac{\bar{n}^2}{c^2} + \frac{\bar{n}n_1 e^{i\varphi}}{c^2}me^{i\vec{K}_x\cdot\vec{r}}\right]\left(-\omega^2 + 2i\omega\frac{\partial}{\partial t}\right)A_i\right.$$
$$\left.-\frac{4\pi\sigma}{c^2}\left(\frac{\partial}{\partial t} + i\omega\right)A_i\right\}e^{-i\vec{k}_i\cdot\vec{r}} + \text{c.c.} = 0, \quad (A.38)$$

where

$$\nabla_T^2 \equiv \frac{\partial^2}{\partial x^2} + \frac{\partial^2}{\partial y^2} \qquad (A.39)$$

is the transverse Laplacian operator. Equating the coefficients of $e^{-i\vec{k}_i\cdot\vec{r}}$ separately, we obtain the following set of equations for waves propagating inside the PCM including the transverse spatial variations in the fields' amplitudes:

$$\left(\frac{i\nabla_T^2}{2k} + \hat{k}_1 \cdot \nabla + \alpha + \frac{\partial}{v\partial t}\right)A_1 = -QA_4, \qquad (A.40)$$

$$\left(-\frac{i\nabla_T^2}{2k} + \hat{k}_2 \cdot \nabla + \alpha + \frac{\partial}{v\partial t}\right)A_2^* = QA_3^*, \qquad (A.41)$$

$$\left(\frac{i\nabla_T^2}{2k} + \hat{k}_3 \cdot \nabla + \alpha + \frac{\partial}{v\partial t}\right)A_3 = -QA_2, \qquad (A.42)$$

$$\left(-\frac{i\nabla_T^2}{2k} + \hat{k}_4 \cdot \nabla + \alpha + \frac{\partial}{v\partial t}\right)A_4^* = QA_1^* \qquad (A.43)$$

where we have ignored the products of two small quantities viz $n_1 \partial A_i/\partial t$ as well as the terms $(1/\omega)\partial A_i/\partial t$; $\alpha = 2\pi\sigma/c\sqrt{\epsilon}$ and $v = c/\sqrt{\epsilon}$. The grating Q is given by

$$Q(x,y,z,t) \equiv \gamma_o m(x,y,z,t), \qquad (A.44)$$

where the coupling coefficient γ_o is

$$\gamma_o \equiv \frac{i\omega n_1 e^{i\phi}}{2c}. \qquad (A.45)$$

The expressions for the amplitude n_1 and the phase ϕ of the refractive index modulation are given in eqs. B.55 and B.56 of Appendix B.

Appendix B

The Kukhtarev equations

In this appendix we use Kukhtarev band transport model [42] to derive the basic equations governing the hologram formation process in photorefractive media. In Kukhtarev model, the photorefractive materials are assumed to contain donor and acceptor traps which arise from the crystals' impurities. These traps introduce intermediate electronic energy states in the bandgap of the insulators. When photons of sufficient energy are present, electronic transitions by photoexcitation take place. As a result of the transitions, charge carriers are excited into the conduction band and the ionized donors become empty trap sites. Furthermore, movements of the charge carriers are generally described by diffusion, drift and the photovoltaic effect [16]. The migration of the charge carriers from bright regions where they are photoexcited to dark regions where they are recombined with acceptors builds up a space-charge field inside the crystal. The space-charge field modulates the material's refractive index via the linear electrooptic effect [40] (Pockel effect).

The space-charge field created by the migration and trapping of the charge carriers is determined by the following set of transport equations:

$$\frac{\partial n}{\partial t} = \frac{\partial N_D^+}{\partial t} - \frac{1}{q}\nabla \cdot \vec{j} \qquad \text{(continuity)}, \qquad (B.1)$$

$$\frac{\partial N_D^+}{\partial t} = (SI + \beta)(N_D - N_D^+) - \gamma_R n N_D^+ \qquad \text{(rate equation)}, \qquad (B.2)$$

APPENDIX B.

$$\vec{j} = q\mu n\vec{E} - k_B T\mu\nabla n + pI\hat{e}_c \qquad \text{(current equation)}, \qquad (B.3)$$

$$\nabla \cdot \vec{E} = \frac{q}{\epsilon}\left(n + N_A - N_D^+\right) \qquad \text{(Poisson's law)}, \qquad (B.4)$$

where $(SI+\beta)(N_D-N_D^+)$ is the rate of charge carrier generation, $\gamma_R n N_D^+$ is the rate of trap capture. Here S is the cross-section of photoionization, β is the rate of thermal generation, γ_R is the carrier-ionized trap recombination rate coefficient and n and N_D^+ are the concentrations of the carriers and ionized traps, N_D is the concentration of the donor traps, I is the light intensity, N_A is the acceptor concentration, μ is the mobility, T is the temperature, k_B is the Boltzman constant, ϵ is the dielectric constant, pI is the photovoltaic current and p is the photovoltaic constant, $\hat{e}_c$ is the unit vector along the c axis of the crystal, $\vec{E}$ is the total field which includes the induced space-charge field $\vec{E}_{sc}$ and any external or internal fields such as internal ferroelectric fields; and q is the charge of the charge carrier.

In general μ and ϵ are tensors and N_D and N_A could vary with position. For simplicity we will assume that μ and ϵ are scalars and N_D and N_A are constant throughout the material. Eqs. B.1–B.4 are nonlinearly coupled and generally difficult to solve without some approximations. In the following we will simplify the band transport equations using various approximations to solve for the space-charge field and obtain the basic equation that governs it.

We begin with a perturbation scheme to linearize the above coupled equations. To this end, we let (see figure B.1)

$$I(x,z,t) = I_o(z,t) + \left[I_2(z,t)e^{-iK_x x} + \text{c.c.}\right] \qquad (B.5)$$

$$E(x,z,t) = E_o(z,t) + \left[E_2(z,t)e^{-iK_x x} + \text{c.c.}\right], \qquad (B.6)$$

$$n(x,z,t) = n_o(z,t) + \left[n_2(z,t)e^{-iK_x x} + \text{c.c.}\right], \qquad (B.7)$$

$$N_D^+(x,z,t) = N_{Do}^+(z,t) + \left[N_{D2}^+(z,t)e^{-iK_x x} + \text{c.c.}\right], \qquad (B.8)$$

$$j(x,z,t) = j_o(z,t) + \left[j_2(z,t)e^{-iK_x x} + \text{c.c.}\right]. \qquad (B.9)$$

Here $E(x,z,t)$ is the overall electric field in the photorefractive material, which is the sum of any external field E_o and the induced space-charge field E_2, and we assume

192
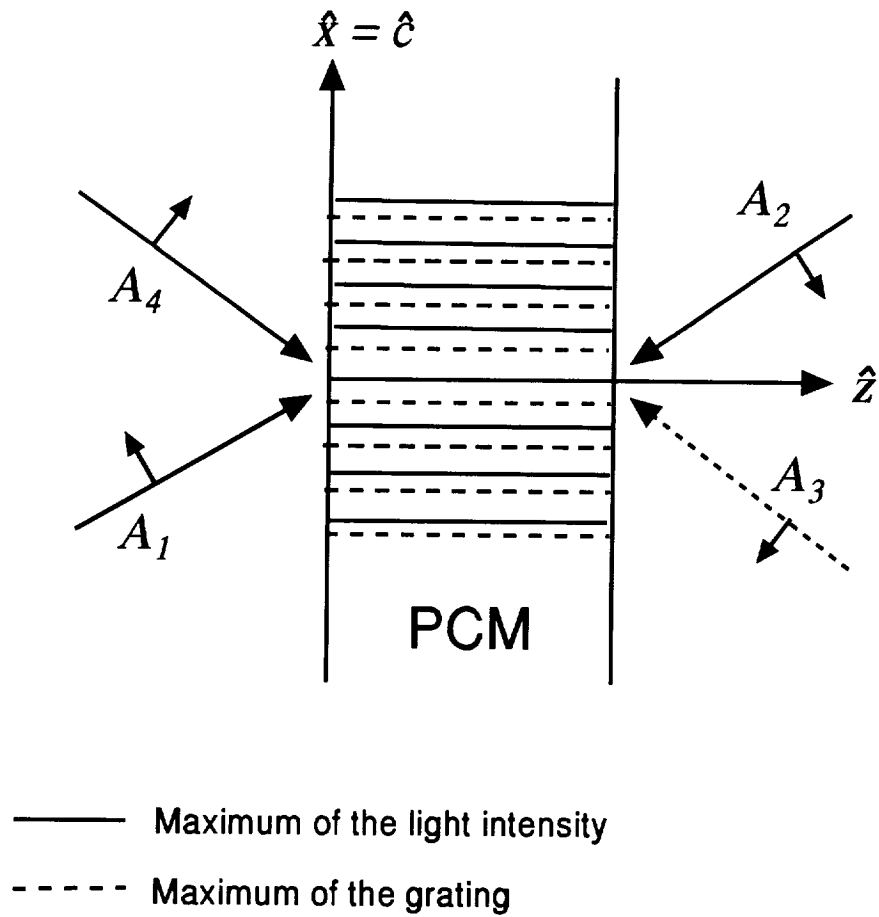
Figure B.1: Hologram formation in a photorefractive material using the four-wave mixing scheme

APPENDIX B.

that $I_2(z,t)$ varies relatively slowly along the z-axis as compared to the fast change of $e^{-iK_x x}$ along the x-axis, etc. (SVEA).

At first we consider the quasi-steady static case, i.e. $\partial n_o/\partial t \sim \partial N_{Do}^+/\partial t \sim 0$. We also assume that there are a lot of available donors and acceptors to linearize the generation and recombination rates, i,e., $N_D \gg N_D - N_D^+$ and $N_A \gg n$. From now on, we also ignore the small thermal factor, i.e. $\beta \ll SI$. Then, from eq. B.4 and assuming the SVEA, we have

$$\frac{\partial E_{sc}}{\partial x} \simeq \frac{q}{\epsilon}(n + N_A - N_D^+). \tag{B.10}$$

We obtain the following equations upon equating the zeroth order terms and the coefficients of $e^{-iK_x x}$:

$$N_{Do}^+ = N_A + n_o \sim N_A, \tag{B.11}$$

$$E_2 = \frac{iq}{K_x \epsilon}(n_2 - N_{D2}^+). \tag{B.12}$$

Consider a maximum space-charge field with charge separation comparable to the grating period such that

$$K_x E_q' = \frac{qN_D}{\epsilon}. \tag{B.13}$$

Then, in eq. B.12

$$E_2 = \frac{iE_q'}{N_D}(n_2 - N_{D2}^+). \tag{B.14}$$

Now, from eq. B.2, we have

$$\left[\frac{\partial N_{D2}^+}{\partial t}e^{-iK_x x} + \text{c.c.}\right] \simeq S\left[I_o + I_2 e^{-iK_x x} + \text{c.c.}\right]N_D \tag{B.15}$$

$$-\gamma_R\left[n_o + n_2 e^{-iK_x x} + \text{c.c.}\right]\left[N_{Do}^+ + N_{D2}^+ e^{-iK_x x} + \text{c.c.}\right],$$

which gives us

$$n_o = \frac{SI_o N_D}{\gamma_R N_{Do}^+} \sim \frac{SI_o N_D}{\gamma_R N_A}, \tag{B.16}$$

and

$$\frac{\partial N_{D2}^+}{\partial t} = SI_2 N_D - \gamma_R[n_2 N_{Do}^+ + n_o N_{D2}^+]. \tag{B.17}$$

APPENDIX B.

For the quasi-steady state, or when the generation rate equals the recombination rate, i.e. $\partial N_{D2}^+/\partial t \sim 0$, we have

$$N_{D2}^+ \sim \frac{SI_2 N_D}{\gamma_R n_o} - \frac{N_A}{n_o} n_2.$$
(B.18)

Combinding eqs. B.1 and B.3, we get

$$\left[\frac{\partial n_2}{\partial t} e^{-iK_x x} + \text{c.c.}\right] \sim \left[\frac{\partial N_{D2}^+}{\partial t} e^{-iK_x x} + \text{c.c.}\right]$$
(B.19)

$$-\mu \left[n_o + n_2 e^{-iK_x x} + \text{c.c.}\right] \left[(-iK_x) E_2 e^{-iK_x x} + \text{c.c.}\right]$$

$$-\mu \left[(-iK_x) n_2 e^{-iK_x x} + \text{c.c.}\right] \left[E_o + E_2 e^{-iK_x x} + \text{c.c.}\right]$$

$$+\frac{k_B T \mu}{q} \left[(-iK_x)^2 n_2 e^{-iK_x x} + \text{c.c.}\right]$$

$$-\frac{p}{q} \left[(-iK_x) I_2 e^{-iK_x x} + \text{c.c.}\right].$$

As $\partial n_2/\partial t - \partial N_{D2}^+/\partial t \sim 0$, we get

$$\left(E_o + \frac{ik_B T K_x}{q}\right) n_2 = -\left[E_2 + \frac{pI_o}{q\mu n_o}\left(\frac{I_2}{I_o}\right)\right] n_o.$$
(B.20)

We recognize the diffusion field $E_D \equiv k_B T K_x/q$ and the photovoltaic field $E_p \equiv pI_o/q\mu n_o$. Then we rewrite n_2 as

$$n_2 = -\frac{E_2 + E_p I_2/I_o}{E_o + iE_D} n_o.$$
(B.21)

Now, substituting eqs. B.18 and B.21 in eq. B.14, we have the following static space-charge field:

$$E_2^S = -iE_q' \left(\frac{N_A + n_o}{N_D}\right) \left[\frac{E_2^S + E_p I_2/I_o}{E_o + iE_D} + \frac{I_2}{I_o}\right].$$
(B.22)

Since

$$E_q' \left(\frac{N_A + n_o}{N_D}\right) \sim \frac{qN_A}{\epsilon K_x} \sim \frac{q(N_D - N_A)}{\epsilon K_x N_D} N_A \equiv \frac{qN_e}{\epsilon K_x} \equiv E_q,$$
(B.23)

where N_e is the effective trap density, we can simplify eq. B.22 such that the modulation of the static space-charge field is

$$E_2^S = -iE_q \left[\frac{(E_o + E_p) + iE_D}{E_o + i(E_q + E_D)}\right] \left(\frac{I_2}{I_o}\right).$$
(B.24)

195

APPENDIX B.

Next, we examine the time development of the space-charge field. In the short writing time limit, i.e. shortly after illumination, N_D^+ will not change greatly from its dark values (i.e. $N_D^+ \sim N_A$). Then eq. B.2 may be written as

$$\frac{\partial N_D^+}{\partial t} = SI(N_D - N_A) - \frac{n}{\tau_R}, \tag{B.25}$$

with $\tau_R \equiv 1/\gamma_R N_A$. Substituting this in eq. B.1,

$$\frac{\partial n}{\partial t} = SI(N_D - N_A) - \frac{n}{\tau_R} \tag{B.26}$$
$$- \frac{\partial}{\partial x}\left(\mu n E_{sc} - \frac{k_B T \mu}{q}\frac{\partial n}{\partial x} + \frac{p}{q}I\right).$$

As we expect $\partial n/\partial t = O(n/\tau_{di})$, whereas τ_{di} is the dielectric relaxation time, for illluminating times greater than a few τ_R we can then make the approximation that $\tau_R \partial n/\partial t \sim 0$. Also, for times short compared to τ_{di}, the space-charge field will not change greatly and we may make the further approximation $E_{sc} \simeq E_o$. Then eq. B.26 will reduce to

$$0 \sim \tau_R S\left[I_o + I_2 e^{-iK_x x} + \text{c.c.}\right](N_D - N_A) - n - \mu \tau_R E_o \frac{\partial n}{\partial x} \tag{B.27}$$
$$\tau_R \frac{k_B T \mu}{q}\frac{\partial^2 n}{\partial x^2} - \tau_R \frac{p}{q}\left[\frac{\partial I_2}{\partial x}e^{-iK_x x} + \text{c.c.}\right],$$

which, after equating the coefficients of $e^{-iK_x x}$, gives

$$n_2 = \frac{1 + iE_p/E_M}{1 + E_D/D_M - iE_o/E_M}n_o\left(\frac{I_2}{I_o}\right) \tag{B.28}$$
$$= \left[\frac{E_M + iE_p}{(E_M + E_D) - iE_o}\right]n_o\left(\frac{I_2}{I_o}\right),$$

with $E_M \equiv 1/(\mu \tau_R K_x)$. In eq. B.24, as $N_D^+ \sim N_A$, then we have for short time

$$N_D^+ \simeq N_A + \left(SIN_D - \frac{n}{\tau_R}\right)t. \tag{B.29}$$

So, from eq. B.4, and with $N_A, N_D - N_A \gg n$, we have

$$\frac{\partial E_{sc}}{\partial x} = \frac{q}{\epsilon}\left(\frac{n}{\tau_R} - SIN_D\right)t, \tag{B.30}$$

which gives, by equating the coefficients of $e^{-iK_x x}$,

$$E_2 = \frac{iq}{\epsilon K_x}\left(\frac{n_2}{\tau_R} - SI_2 N_D\right)t. \tag{B.31}$$

196

APPENDIX B.

Therefore, combining eq. B.28 and eq. B.31 we have

$$E_2 = \frac{q\mu n_o E_M}{\epsilon} \left[\frac{E_D - i(E_o + E_p)}{E_o + i(E_M + E_D)} \right] \left(\frac{I_2}{I_o} \right) t \tag{B.32}$$

$$= \frac{E_M}{\tau_{di}} \left[\frac{E_D - i(E_o + E_p)}{E_o + i(E_M + E_D)} \right] \left(\frac{I_2}{I_o} \right) t,$$

with $\tau_{di} \equiv \epsilon/(q\mu n_o)$. If we assume that the space-charge field builds up exponentially such that

$$E_2 = E_2^S(1 - e^{-\eta t}) \tag{B.33}$$

$$\simeq E_2^S \eta t$$

for the short time limit, then, comparing this with eq. B.31 and using eq. B.24, we have

$$\eta = \frac{E_M}{E_q} \left[\frac{E_o + i(E_q + E_D)}{E_o + i(E_M + E_D)} \right] \frac{1}{\tau_{di}} \tag{B.34}$$

$$= \frac{1}{\tau_{di}} \left[\frac{\left(1 + \frac{E_D}{E_q}\right)\left(1 + \frac{E_D}{E_M}\right) + \frac{E_o^2}{E_q E_M}}{\left(\frac{E_o}{E_M}\right)^2 + \left(1 + \frac{E_D}{E_M}\right)^2} + \frac{i\left(\frac{E_o}{E_M} - \frac{E_o}{E_q}\right)}{\left(\frac{E_o}{E_M}\right)^2 + \left(1 + \frac{E_D}{E_M}\right)^2} \right]$$

$$\equiv \frac{1}{\tau_{di}}(\eta_R + i\eta_I).$$

Therefore, we have a complex time constant for the material. Thus,

$$e^{-\eta t} = e^{-t/\tau_e} e^{i\omega_g t}, \tag{B.35}$$

with

$$\tau_e \equiv \frac{\tau_{di}}{\eta_R} = \tau_{di} \left[\frac{\left(1 + \frac{E_D}{E_M}\right)^2 + \left(\frac{E_o}{E_M}\right)^2}{\left(1 + \frac{E_D}{E_q}\right)\left(1 + \frac{E_D}{E_M}\right) + \frac{E_D^2}{E_q E_M}} \right], \tag{B.36}$$

and

$$\omega_g \equiv -\frac{\eta_I}{\tau_{di}} = -\frac{1}{\tau_{di}} \left[\frac{\frac{E_o}{E_M} - \frac{E_o}{E_q}}{\left(\frac{E_o}{E_M}\right)^2 + \left(1 + \frac{E_D}{E_M}\right)^2} \right]. \tag{B.37}$$

In the following we define various time scales of the material:

$$\tau_D \equiv \frac{1}{\mu K_x E_D} \qquad \text{(diffusion time)}, \tag{B.38}$$

APPENDIX B.

$$\tau_E \equiv \frac{1}{\mu K_x E_o} \qquad \text{(drift time due to external field)}, \qquad (B.39)$$

$$\tau_I \equiv \frac{1}{S I_o} \qquad \text{(inverse of photoexcitation rate)}, \qquad (B.40)$$

$$\tau_R \equiv \frac{1}{\gamma_R N_A} \qquad \text{(recombination time)}, \qquad (B.41)$$

$$\tau_{di} \equiv \frac{\epsilon}{q \mu n_o} \qquad \text{(dielectric relaxation time)}. \qquad (B.42)$$

From the above definitions, we also notice that

$$\frac{E_D}{E_M} = \frac{\tau_R}{\tau_D}, \qquad (B.43)$$

$$\frac{E_o}{E_M} = \frac{\tau_R}{\tau_E}, \qquad (B.44)$$

$$\frac{E_D}{E_o} = \frac{\tau_E}{\tau_D}, \qquad (B.45)$$

$$\frac{E_M}{E_q} = \frac{\tau_{di}}{\tau_I}. \qquad (B.46)$$

Then the material response time and the grating natural frequency can be expressed in terms of these various time scales as

$$\tau_e = \tau_{di} \frac{\left(1 + \frac{\tau_R}{\tau_D}\right)^2 + \left(\frac{\tau_R}{\tau_E}\right)^2}{\left(1 + \frac{\tau_R \tau_{di}}{\tau_D \tau_I}\right)\left(1 + \frac{\tau_R}{\tau_D}\right) + \left(\frac{\tau_R}{\tau_E}\right)^2 \left(\frac{\tau_{di}}{\tau_I}\right)}, \qquad (B.47)$$

and

$$\omega_g = \frac{1}{\tau_{di}} \frac{\left(\frac{\tau_R}{\tau_E}\right)\left(\frac{\tau_{di}}{\tau_I} - 1\right)}{\left(1 + \frac{\tau_R}{\tau_D}\right)^2 + \left(\frac{\tau_R}{\tau_E}\right)^2}. \qquad (B.48)$$

Here we can see that $\omega_g = 0$ when $E_o = 0$, i.e. the material time constant becomes real when there is no applied field. Now we consider eq. B.33 as a solution for E_2 of a differential equation of the form

$$\frac{\partial E_2}{\partial t} + \eta E_2 = \eta E_2^S. \qquad (B.49)$$

With eq. B.34, the above equation can be rewritten as

$$\tau_{di} \frac{\partial E_2}{\partial t} + \left(\frac{E_M}{E_q}\right) \left[\frac{E_o + i(E_q + E_D)}{E_o + i(E_M + E_D)}\right] E_2 \qquad (B.50)$$

$$= \left(\frac{E_M}{E_q}\right) \left[\frac{E_o + i(E_q + E_D)}{E_o + i(E_M + E_D)}\right] E_2^S.$$

198

APPENDIX B.

Using eq. B.46 we have

$$\tau_I \frac{\partial E_2}{\partial t} \;+\; \left[\frac{E_o + i(E_q + E_D)}{E_o + i(E_M + E_D)}\right] E_2 \tag{B.51}$$

$$=\; \left[\frac{E_o + i(E_q + E_D)}{E_o + i(E_M + E_D)}\right] E_2^S .$$

From eq. A.32 of Appendix A we know that the grating is directly proportional to E_2. Thus we can write down the time equation for the grating as

$$\tau_I \frac{\partial Q}{\partial t} + CQ = \frac{\gamma_o}{I_o} C(A_1 A_4^* + A_2^* A_3), \tag{B.52}$$

with

$$C = \frac{E_o + i(E_q + E_D)}{E_o + i(E_M + E_D)}, \tag{B.53}$$

and

$$\gamma_o \;=\; \frac{i\omega \bar{n}_o^3}{4c} r_{eff}(-iE_q) \left[\frac{(E_o + E_p) + iE_D}{E_o + i(E_q + E_D)}\right] \tag{B.54}$$

$$\equiv\; \frac{i\omega n_1}{2c} e^{i\phi}$$

where

$$n_1 = -\frac{1}{2} r_{eff} \bar{n}_o^3 E_q \left[\frac{(E_o + E_p)^2 + E_D^2}{E_o^2 + (E_q + E_D)^2}\right]^{1/2}, \tag{B.55}$$

and

$$\phi = \tan^{-1}\left[\frac{E_D(E_q + E_D) + E_o(E_o + E_p)}{E_o E_q + E_p(E_q + E_D)}\right]. \tag{B.56}$$

When $E_o = E_p = 0$, $\phi = \pi/2$. Thus, γ_o is real. From eq. B.52, this means that when there is no external applied field, the grating does not have a natural oscillation frequency and it is always $\pi/2$ phase shifted with respect to the interference fringes of the optical fields. In addition, the response time is just inversely proportional to the intensity.

REFERENCES

[1] J. N. Cederquist, "Optical Feedback Processing," in *Optical Signal Processing*, (J. L. Horner, ed.), London: Academic Press, 1983.

[2] P. De Santis, F. Gori, G. Guttari, and C. Palma, "Optical systems with feedback," *Optica acta*, **23**, pp. 505–518, 1976.

[3] R. J. Marks, "Coherent optical extrapolation of 2-D band-limited signals: processor theory," *Appl. Opt.*, **19**, pp. 1670–1672, 1980.

[4] T. W. Hansch, F. Varsanyi, and A. L. Schawlow, "Image amplification by dye lasers," *Appl. Phys. Lett.*, **18**, pp. 108–110, 1971.

[5] R. P. Akins and S. H. Lee, "Two-stage injection-locked ring dye laser/amplifier for coherent image amplification," *J. Opt. Soc. Am.*, **A 7**, pp. 533–538, 1984.

[6] P. Pellat-Finet and J. L. De Bougrenet De La Tocnaye, "Optical generator of spheroidal wave functions, using a BSO crystal," *Opt. Commun.*, **55**, pp. 305–310, 1985.

[7] Y. Fainman, E. Klancnik, and S. H. Lee, "Optimal coherent image amplification by two-wave coupling in photorefractive BaTiO₃," *Opt. Eng.*, **25**, pp. 228–234, 1986.

[8] J. Feinberg and R. W. Hellwarth, "Phase conjugating mirror with continuous wave gain," *Opt. Lett.*, **5**, pp. 519–521, 1980.

[9] B. H. Soffer, G. J. Dunning, Y. Owechko, and E. Marom, "Associative holographic memory with feedback using phase-conjugate mirrors," *Opt. Lett.*, **11**, pp. 118–120, 1986.

[10] D. Z. Anderson, "Coherent optical eigenstate memory," *Opt. Lett.*, **11**, pp. 56–58, 1986.

[11] A. Yariv and S. K. Kwong, "Associative memories based on message-bearing optical modes in phase-conjugate resonators," *Opt. Lett.*, **11**, pp. 186–188, 1986.

REFERENCES

[12] T. Kohonen, *Self organization and associative memory*. Springer-Verlag, 1984.

[13] J. J. Hopfield, "Neural networks and physical systems with emergent collective computational abilities," *Proc. Nat. Acad. Sci.*, **79**, pp. 2554–2562, 1982.

[14] N. H. Farhat and D. Psaltis, "Optical implementation of associative memory based on models of neural networks," in *Optical Signal Processing*, (J. L. Horner, ed.), London: Academic Press, 1983.

[15] T. J. Hall, R. Jaura, L. M. Connors, and P. D. Foote, "The photorefractive effect –A review," *Prog. Quant. Electr.*, **10**, pp. 77–146, 1985.

[16] P. Günter and J. P. Huignard, *Photorefractive Materials and Their Applications I & II*. Springer-Verlag, 1988.

[17] J. M. Heaton and L. Solymar, "Transient energy transfer during hologram formation in photorefractive crystals," *Optica Acta*, **32**, pp. 397–408, 1985.

[18] G. C. Papen, B. E. A. Saleh, and J. A. Tataronis, "Analysis of transient phase conjugation in photorefractive meida," *J. Opt. Soc. Am.*, **B 5**, pp. 1763–1774, 1988.

[19] W. Krolikowski, K. D. Shaw, M. Cronin-Golomb, and A. Bledowski, "Stability analysis in photorefractive crystals," *J. Opt. Soc. Am.*, **B 6**, pp. 1828–1833, 1989.

[20] P. Günter, E. Volt, M. Z. Zha, and J. Albers, "Self-pulsation and optical chaos in self-pumped photorefractive $BaTiO_3$," *Opt. Commun.*, **55**, pp. 210–214, 1985.

[21] A. M. C. Smout and R. W. Eason, "Regular oscillations and self-pulsating in self-pumped $BaTiO_3$," *Opt. Commun.*, **59**, pp. 77–82, 1986.

[22] D. J. Gauthier, D. Narum, and R. W. Boyd, "Observation of deterministic chaos in a phase conjugate mirror," *Phys. Rev. Lett.*, **58**, pp. 1640–1643, 1987.

[23] J. P. Jiang and J. Feinberg, "Dancing modes and frequency shifts in a phase conjugator," *Opt. Lett.*, **12**, pp. 48–50, 1987.

[24] W. Krolikowski, B. S. Chen, and M. Cronin-Golomb, "Temporal instabilities in an externally driven ring phase conjugator," *J. Opt. Soc. Am.*, **B 8**, pp. 1455–1460, 1991.

[25] G. Hussain, S. W. James, and R. W. Eason, "Observation and Modeling of dynamic instabilities in the mutually pumped bird-wing phase conjugator in $BaTiO_3$," *J. Opt. Soc. Am.*, **B 7**, pp. 2294–2298, 1990.

REFERENCES

[26] D. Wang, Z. Zhang, X. Wu, and P. Ye, "Instabilities in a mutually pumped phase conjugator of $BaTiO_3$," *J. Opt. Soc. Am.*, **B 7**, pp. 2289–2293, 1990.

[27] G. Valley and G. Dunning, "Observation of optical chaos in a phase conjugate resonator," *Opt. Lett.*, **9**, pp. 513–515, 1984.

[28] J. L. Bougrenet, P. Pellat-Finet, and J. P. Huignard, "Effect of using a $B_{12}SiO_{20}$ light amplifier on the formation and competition of modes in optical resonators," *J. Opt. Soc. Am.*, **B 3**, pp. 315–319, 1986.

[29] A. Bledowski, W. Krolikowski, and A. Kujawski, "Temporal instabilities in single photorefractive four-wave mixing," *J. Opt. Soc. Am.*, **B 6**, pp. 1544–1547, 1989.

[30] K. D. Shaw and M. Cronin-Golomb, "Stability of multiple solutions in photorefractive four-wave mixing with external electric field," *Opt. Commun.*, **76**, pp. 151–156, 1990.

[31] W. Krolikowski, M. R. Belic, M. Cronin-Golomb, and A. Bledowski, "Chaos in photorefractive four-wave mixing with a single grating and a single interaction region," *J. Opt. Soc. Am.*, **B 7**, pp. 1204–1209, 1990.

[32] M. R. Belic, D. Timotijevic, and W. Krolikowski, "Multigrating phase conjugation:chaotic results," *J. Opt. Soc. Am.*, **B 8**, pp. 1723–1731, 1991.

[33] M. Horowitz, D. Kligler, and B. Fischer, "Time-dependent behavior of photorefractive two and four-wave mixing," *J. Opt. Soc. Am.*, **B 8**, pp. 2204–2217, 1991.

[34] S. R. Liu and G. Indebetouw, "Dynamics of a phase conjugate resonator: transient buildup and decay rates," *Appl. Phys. B*, **54**, pp. 247–258, 1992.

[35] L. K. Dai, Y. S. Gou, C. Gu, and P. Yeh, "Instabilities in coupled photorefractive ring cavities and self-pumped phase conjuators: I & II," *Appl. Phys. B*, **54**, pp. 57–70,156–166, 1992.

[36] H. Kogelnik, "Coupled wave theory for thick hologram gratings," *Bell Syst. Tech. J.*, **48**, pp. 2909–2947, 1969.

[37] V. V. Eliseev, V. T. Tikhonchuk, and A. A. Zozulya, "One-mirror self-pumped phase conjugator: three-dimensional analysis," *Opt. Commun.*, **85**, pp. 520–526, 1991.

[38] W. Krolikowski and M. Cronin-Golomb, "Photorefractive wave mixing with finite beams," *Opt. Commun.*, **89**, pp. 88–98, 1992.

REFERENCES

[39] "Transverse effects in nonlinear optical systems", *J. Opt. Soc. Am.* B 7, Special issues (June and July, 1990).

[40] A. Yariv, *Optical electronics.* Holt, Rinehart and Winston, Inc., 1985.

[41] N. V. Kukhtarev, V. B. Markov, and S. G. Odulov, "Transient energy transfer during hologram formation in $LiNbO_3$ in external electric field," *Opt. Commun.*, **23**, pp. 338–343, 1977.

[42] N. V. Kukhtarev, V. B. Markov, S. G. Odulov, M. S. Soskin, and V. L. Vinetskii, "Holographic storage in electro-optic crystals. II. Beam coupling - light amplification," *Ferroelectrics*, **22**, pp. 961–964, 1979.

[43] V. L. Vinetskii, N. V. Kukhtarev, S. G. Odulov, and M. S. Soskin, "Dynamic self-diffraction of coherent light beams," *Sov. Phys. Usp*, **22**, pp. 742–756, 1979.

[44] H. Kogelnik, "Holographic image projection through imhomogeneous media," *Bell Syst. Tech. J.*, **44**, pp. 2451–2455, 1965.

[45] A. E. Siegman, P. A. Belanger, and A. Hardy, "Optical resonators using phase-conjugate mirrors," in *Optical Phase Conjugation*, (R. Fisher, ed.), pp. 465–535, Academic Press, New York, 1983.

[46] K. P. Lo and G. Indebetouw, "Iterative image processing using a cavity with a phase conjugate mirror," *Appl. Opt.*, **31**, pp. 1745–1753, 1992.

[47] M. F. Barsky, *Holographic sensing for control of flexible structures.* PhD thesis, Electrical Engineering, Virginia Polytectnic Institute & State University, 1990.

[48] P. D. Drummond and A. T. Friberg, "Specular reflection cancellation in an interferometer with a phase-conjugate mirror," *J. Appl. Phys.*, **54**, pp. 5618–5625, 1983.

[49] A. T. Friberg, M. Kauranen, and R. Salomaa, "Dynamics of Fabry-Perot resonators with a phase-conjugate mirror," *J. Opt. Soc. Am.*, **B 3**, pp. 1656–1672, 1986.

[50] M. Cronin-Golomb, F. Baruch, S. K. Kwong, J. O. White, and A. Yariv, "Non-degenerate optical oscillation in a resonator formed by two phase-conjugate mirrors," *Opt. Lett.*, **10**, pp. 353–355, 1985.

[51] S. S. Lafleur and R. C. Montgomery, "Real-time dynamic holographic image storage device," *Appl. Opt.*, **29**, p. p.3976, 1990. U.S. patent 4,913,534.

[52] A. M. Glass, D. Von der Linde, and T. D. Negran, "High-voltage bulk photovoltaic effect and the photorefractive process in $LiNbO_3$," *Appl. Phys. Lett.*, **25**, pp. 233–235, 1974.

REFERENCES

[53] G. C. Valley and M. B. Klein, "Optimal properties of photorefractive materials for optical data processing," *Opt. Eng.*, **22**, pp. 704–711, 1983.

[54] G. A. Brost and R. A. Motes, "Origin of the sublinear photorefractive response time in BaTiO₃," *Opt. Lett.*, **15**, pp. 1194–1196, 1990.

[55] V. Kalinin and L. Solymar, "Transient effects in four-wave mixing in photorefractive passive phase conjugate mirrors," *Applied Physics*, **B 45**, pp. 129–135, 1988.

[56] N. B. Abraham, A. M. Albano, and N. B. Tufillaro, "Complexity and chaos," in *Measures of Complexity and Chaos*, (Abraham, N.B. et als, ed.), pp. 1–27, Plenum Press, New York, 1990.

[57] F. C. Moon, *Chaotic Vibrations: An introduction for applied scientists and engineers.* N.Y., N.Y.: Wiley, 1987.

[58] E. N. Lorenz, "Deterministic nonperiodic flow," *J. Atmos. Sci.*, **20**, pp. 130–144, 1963.

[59] C. Corduneanu, *Almost Periodic Functions.* Interscience Publishers, N.Y., 1968.

[60] P. Berge, Y. Pomeau, and C. Vidal, *Order within Chaos.* John Wiley and Sons, New York, 1984.

[61] S. N. Rasband, *Chaotic dynamics of nonlinear systems.* Wiley, 1990.

[62] G. L. Baker and J. P. Gollub, *Chaotic dynamics: an introduction.* Cambridge Univ. Press, 1990.

[63] P. Grassberger and I. Procaccia, "Estimation of the Kolomogrov entropy from a chaotic signal," *Phys. Rev. A*, **28**, pp. 2591–2593, 1983.

[64] F. Takens, "Detecting strange attractors in turbulence," in *Dynamical systems and Turbulence, 898 of Lecturer Notes in Mathematics*, (Rand, D. A. and Young, L-S, ed.), pp. 366–381, Berlin: Springer-Verlag, 1981.

[65] G. Nicolis and I. Prigogine, *Self-organization in nonequilibrium systems.* New York: Wiley, 1977.

[66] S. Chandrasekhar, *Hydrodynamic and hydromagnetic stability.* Clarendon Press, 1961.

[67] A. Libchaber and J. Maurer, "A Rayleigh-Benard experiment: helium in a small box," in *Nonlinear phenomena at phase transitions and instabilities*, (Riste, T., ed.), pp. 259–86, Plenum Press, New York, 1982.

REFERENCES

[68] P. Manneville, *Dissipative structures and weak turbulence*. San Dieao, CA: Appl. Phys., 1990.

[69] T. B. Benjamin and J. E. Feir, "The disintegration of wavetrains on deep water," *J. Fluid Mech.*, **27**, pp. 417–430, 1967.

[70] L. A. Lugiato, C. Oldano, and L. M. Narducci, "Cooperative frequency locking and stationary spatial structures in lasers," *J. Opt. Soc. Am.*, **B 5**, pp. 879–888, 1988.

[71] L. A. Lugiato, G. L. Oppo, M. A. Pernigo, J. R. Tredicce, L. M. Narducci, and D. K. Bandy, "Spontaneous spatial pattern formation in lasers and cooperative frequency locking," *Opt. Commun.*, **68**, pp. 63–68, 1988.

[72] L. A. Lugiato, F. Frati, L. M. Narducci, P. Ru, J. R. Tredicce, and D. K. Bandy, "Role of transverse effects in laser instabilities," *Phys. Rev. A*, **37**, pp. 3847–3866, 1988.

[73] L. A. Lugiato, F. Frati, L. M. Narducci, and G. L. Oppo, "Spontaneous breaking of the cylindrical symmetry in lasers," *Opt. Commun.*, **69**, pp. 387–392, 1989.

[74] L. A. Lugiato, G. L. Oppo, J. R. Tredicce, and L. M. Narducci, "Instabilities and spatial complexity in a laser," *J. Opt. Soc. Am.*, **B 7**, pp. 1019–1033, 1990.

[75] G. D'Alessandro and G. L. Oppo, "Gauss-Laguerre modes: a "sensible" basis for laser dynamics," *Opt. Commun.*, **88**, pp. 130–136, 1992.

[76] M. Brambilla, F. Battipede, L. A. Lugiato, V. Penna, F. Prati, C. Tamm, and C. O. Weiss, "Transverse laser patterns. I. Phase singularity crystals," *Phys. Rev. A*, **43**, pp. 5090–5113, 1991.

[77] M. Brambilla, F. Battipede, L. A. Lugiato, V. Penna, F. Prati, C. Tamm, and C. O. Weiss, "Transverse laser patterns. II. Variational principle for pattern selection, spatial multistability and laser hydrodynamics," *Phys. Rev. A*, **43**, pp. 5113–5120, 1991.

[78] P. Coullet, L. Gil, and F. Rocca, "Optical vortices," *Opt. Commun.*, **73**, pp. 403–407, 1989.

[79] P. Coullet and J. Lega, "Defect-mediated turbulence in wave patterns," *Europhys. Letters*, **7**, pp. 511–516, 1988.

[80] P. Coullet, L. Gil, and J. Lega, "Defect-mediated turbulence," *Phys. Rev. Lett.*, **62**, pp. 1619–1622, 1989.

[81] Balian, R. et al, ed., *Physics of defects*, (Amsterdam), North-Holland, 1981.

REFERENCES

[82] W. A. Burke, ed., *Theory of self-reproducing automatoa.* University of Illinois Press, 1966.

[83] K. Kaneko, "Transition from torus to chaos accompanied by frequency lookings with symmetry breaking," *Prog. Theor. Phys.*, **69**, pp. 1427–1442, 1983.

[84] K. Kaneko, "Towards thermodynamics of spatiotemporal chaos," *Prog. Theoret. Phys. Suppl.*, **99**, pp. 262–287, 1989.

[85] P. Procaccia, "Weak turbulence and dynamics of topological defects," in *Measures of Complexity and Chaos*, (Abraham, N.B. et als, ed.), Plenum Press, New York, 1990.

[86] F. T. Arecchi, G. Giacomelli, P. L. Ramazza, and S. Residori, "Vortices and defect statistics in two-dimensional optical chaos," *Phys. Rev. Lett.*, **67**, pp. 3749–3752, 1991.

[87] G. Indebetouw and S. R. Liu, "Defect-mediated spatial complexity and chaos in a phase-conjugate resonator," *Opt. Commun.*, **91**, pp. 321–330, 1992.

[88] S. R. Liu and G. Indebetouw, "Periodic and chaotic spatiotemporal states in a phase-conjugate resonator using a photorefractive $BaTiO_3$ phase-conjugate mirror," *J. Opt. Soc. Am.*, **B 9**, pp. 1507–1520, 1992.

[89] M. Berry, "Singularities in waves and rays," in *Physics of defects*, (Balian, R. et als, ed.), (Amsterdam), pp. 455–543, North-Holland, 1981.

[90] J. F. Nye and M. V. Berry, "Dislocations in wavetrains," *Proc. Roy. Soc. Lond.*, **336**, pp. 156–190, 1974.

[91] N. B. Baranova, A. V. Mamaev, N. F. Pilipetsky, V. V. Shkunov, and B. Y. Zeldovich, "Wave-front dislocations: topological limitations for adaptive systems with phase conjugation," *J. Opt. Soc. Am.*, **B 5**, pp. 525–528, 1983.

[92] J. Nye, "Dislocations and disclinations in transverse electromagnetic waves," in *Physics of defects*, (Balian, R. et. al, ed.), pp. 122–155, North Holland, Amsterdam, 1981.

[93] F. J. Wright, "Wavefront dislocations and their analysis using catastrophe theory," in *Structural stability in Physics*, pp. 141–156, Heidelberg: Springer-Verlag, 1979.

[94] *Laser.* University Science Book, Mill Valey, 1986.

[95] A. Brandstater and H. L. Swinney, "Strange attractors in weakly turbulent Couette-Taylor flow," *Phys. Rev. A*, **35**, pp. 2207–2220, 1987.

REFERENCES

[96] P. Grassberger and I. Procaccia, "Characterization of strange attractors," *Phys. Rev. Lett.*, **50**, pp. 346–349, 1983.

[97] P. Coullet, "Defect-induced spatio-temporal chaos," in *Measures of Complexity and Chaos*, (Abraham, N.B. et als , ed.), (N. Y.), pp. 367–373, Plenum Press, 1989.

[98] G. Oppo, M. A. Pernigo, and L. M. Narducci, "Characterization of spatiotemporal structures in lasers: A progress report," in *Measures of Complexity and Chaos*, (Abraham, N.B. et als, ed.), (N.Y.), pp. 395–404, Plenum Press, 1989.

[99] F. T. Arecchi, G. Giacomelli, P. L. Ramazza, and S. Residori, "Experimental evidence of chaotic itinerancy and spatiotemporal chaos in optics," *Phys. Rev. Lett.*, **65**, pp. 2531–2534, 1990.

[100] A. Aceves, H. Adachihara, C. Jones, J. C. Lerman, D. W. McLaughlin, J. V. Moloney, and A. C. Newell, "Chaos and coherent structures in partial differential equations," *Physica D*, **18**, pp. 85–112, 1986.

[101] C. O. Weiss and R. Vilaseca, *Dynamics of lasers*. VCH Pulbisher Inc. Weinheim, 1991.

[102] J. P. Crutchfield and K. Kaneko, "Phenomenology of spatio-temporal chaos," in *Directions in chaos*, (B. L. Hao, ed.), pp. 272–353, World Scientific, Singapore, 1987.

[103] V. L. Vinetskii, N. V. Kukhtarev, S. G. Odulov, and M. S. Soskin, "Dynamic self-diffraction of coherent light beams," *Sov. Phys. Usp*, **22**, pp. 742–756, 1979; and N. V. Kukhtarev, V. B. Markov, S. G. Odulov, M. S. Soskin, and V. L. vinetskii, "Holographic storage in electro-optic crystal. II. Beam coupling-light-amplication," *Ferroelectrics*, **22**, pp. 961–964, 1979.

[104] J. Goodman, *Introduction to Fourier Optics*. McGraw-Hill, 1968.

[105] G. Reiner, P. Meystre and E. M. Wright, "Transverse dynamics of a phase-conjugate resonator," *J. Opt. Soc. Am.* **B 4**, pp. 675–686, 1987 and *J. Opt. Soc. Am.* **B 4**, pp. 865–874, 1987; G. Reiner, M. R. Belic and P. Meystre, "Optical turbulence in phase-conjugate resonators," *J. Opt. Soc. Am* **B 5**, pp. 1193–1210, 1988.

[106] A. C. Newell, "The dynamics of patterns: A survey," in *Propagation in systems far from equilibrium*, (J. W. Wesfried et. als., ed.), pp. 122–155, Springer-Verlag, Berlin, 1988.

[107] G. J. Dunning, "Improved spatial and temporal performance of a phase conjugate resonator by using an intracavity fiber optic taper", (Presented at OSA Annual Meeting, Albuquerque, NM 1992).

207

REFERENCES

[108] M. Brambilla, L. A. Lugiato, M. V. Pinna, F. Prati, P. Pagani, P. Vanotti, M. Y. Li, and C. O. Weiss, "The laser as nonlinear element for an optical associative memory," *Opt. Commun.*, **92**, pp. 145–164, 1992.

REPORT DOCUMENTATION PAGE

Public reporting burden for this collection of information is estimated to average 1 hour per response, including the time for reviewing instructions, searching existing data sources, gathering and maintaining the data needed, and completing and reviewing the collection of information. Send comments regarding this burden estimate or any other aspect of this collection of information, including suggestions for reducing this burden, to Washington Headquarters Services, Directorate for Information Operations and Reports, 1215 Jefferson Davis Highway, Suite 1204, Arlington, VA 22202-4302, and to the Office of Management and Budget, Paperwork Reduction Project (0704-0188), Washington, DC 20503.

1. AGENCY USE ONLY (Leave blank)	2. REPORT DATE	3. REPORT TYPE AND DATES COVERED
	December 1993	Contractor Report

4. TITLE AND SUBTITLE	5. FUNDING NUMBERS
Spatiotemporal Behavior and Nonlinear Dynamics in a Phase Conjugate Resonator	G NAG1-1363 WU 233-03-01-01

6. AUTHOR(S)

Siuying Raymond Liu

7. PERFORMING ORGANIZATION NAME(S) AND ADDRESS(ES)	8. PERFORMING ORGANIZATION REPORT NUMBER
Virginia Polytechnic Institute and State University Physics Department Blacksburg, Virginia 24061	

9. SPONSORING / MONITORING AGENCY NAME(S) AND ADDRESS(ES)	10. SPONSORING / MONITORING AGENCY REPORT NUMBER
National Aeronautics and Space Administration Langley Research Center Hampton, VA 23681-0001	NASA CR-4567

11. SUPPLEMENTARY NOTES

Langley Technical Monitor: Sharon S. Welch
Dissertation submitted in partial fulfillment of the requirements for the Degree of Doctor of Philosophy in Physics, Virginia Polytechnic Institute and State University, Blacksburg, Virginia, April 1993.

12a. DISTRIBUTION / AVAILABILITY STATEMENT	12b. DISTRIBUTION CODE
Unclassified-Unlimited Subject Category 74	

13. ABSTRACT (Maximum 200 words)

The work described in this report can be divided into two parts. The first part is an investigation of the transient behavior and stability property of a phase conjugate resonator (PCR) below threshold. The second part is an experimental and theoretical study of the PCR's spatiotemporal dynamics above threshold.

The time-dependent coupled wave equations for four-wave mixing (FWM) in a photorefractive crystal, with two distinct interaction regions caused by feedback from an ordinary mirror, was used to model the transient dynamics of a PCR below threshold. The conditions for self-oscillation were determined and the solutions were used to define the PCR's transfer function and analyze its stability. Experimental results for the buildup and decay times confirmed qualitatively the predicted behavior.

Experiments were carried out above threshold to study the spatiotemporal dynamics of the PCR as a function of Bragg detuning and the resonator's Fresnel number. The existence of optical vortices in the wavefront were identified by optical interferometry. It was possible to describe the transverse dynamics and the spatiotemporal instabilities by modeling the three-dimensional-coupled wave equations in photorefractive FWM using a truncated modal expansion approach.

14. SUBJECT TERMS	15. NUMBER OF PAGES
Photorefractive, Resonators, Nonlinear optics, Holographic, Phase conjugation, Nonlinear dynamics	228
	16. PRICE CODE A11

17. SECURITY CLASSIFICATION OF REPORT	18. SECURITY CLASSIFICATION OF THIS PAGE	19. SECURITY CLASSIFICATION OF ABSTRACT	20. LIMITATION OF ABSTRACT
Unclassified	Unclassified		